Geoptimaliseerde 'Power Take-Off'-configuratie voor golfenergieconvertoren

Optimised Power Take-Off Configuration for Wave Energy Converters

Kristof De Koker

Promotoren: prof. dr. ir. L. Vandevelde, prof. dr. ir. M. Vantorre
Proefschrift ingediend tot het behalen van de graad van
Doctor in de ingenieurswetenschappen: werktuigkunde-elektrotechniek

Vakgroep Elektrische Energie, Metalen, Mechanische Constructies en Systemen
Voorzitter: prof. dr. ir. L. Dupré

Vakgroep Civiele Techniek
Voorzitter: prof. dr. ir. P. Troch

UNIVERSITEIT
GENT

Faculteit Ingenieurswetenschappen en Architectuur
Academiejaar 2017 - 2018

ISBN 978-94-6355-050-5
NUR 961, 969
Wettelijk depot: D/2017/10.500/85

Ghent University
Faculty of Engineering and Architecture (FEA)

Department of Electrical Energy, Metals,
Mechanical Constructions & Systems (EEMMeCS)
Electrical Energy Laboratory (EELAB)

Department of Civil Engineering
Maritime Technology Division

Geoptimaliseerde 'Power Take-Off'-configuratie voor golfenergieconvertoren

Optimised Power Take-Off Configuration for Wave Energy Converters

Kristof De Koker

Promoters
Prof. dr. ir. Lieven Vandevelde (UGent - EEMMeCS)
Prof. dr. ir. Marc Vantorre (UGent - Maritime Technology Division)

Chairman of the examination board
Prof. dr. ir. Daniël De Zutter (UGent)

Examination board
Prof. dr. ir. Jan Cappelle (KU Leuven - ESAT)
Prof. dr. ir. Guillaume Crevecoeur (UGent - EEMMeCS)
dr. ir. Joris Degrieck (UGent - MATCH)
Prof. dr. ir. Mia Loccufier (UGent - EEMMeCS)
dr. ir. Bart Meersman (S^2ENSO)
Prof. dr. ing. Kurt Stockman (UGent - EEMMeCS)
Prof. dr. Elisabetta Tedeschi (NTNU - Elkraft)
Prof. dr. ir. Lieven Vandevelde (UGent - EEMMeCS)
Prof. dr. ir. Marc Vantorre (UGent - Maritime Technology Division)

The research presented in this work has been funded by the Agency for Innovation by Science and Technology in Flanders (IWT) and the Special Research Fund (BOF) of Ghent University.

voor Suze
en haar generatie

for Suze
and her generation

Dankwoord

Golven ontstaan niet uit het niets, maar door de samenwerking van wind en van water, van water en wind. De wind op zijn beurt heeft zijn energie te danken aan de zon. Zo ook stond ik er gelukkig niet alleen voor. Er waren vele mensen waarbij ik eens kon uitwaaien, of die me een zonnebad aan energie gaven. Want zoals de golfbeweging op zee op en neer gaat, zo gaat ook het schrijven van een doctoraat in ups en downs. Het stormde al eens, of soms was de zee zo kalm dat ik wel een beetje wind in de rug kon gebruiken.

Mijn promotoren professor Lieven Vandevelde en professor Marc Vantorre dank ik om me de kans te geven dit pad af te leggen.

Lieven, bedankt voor de geduldige vrijheid waarin ik mocht werken. Maar het zijn de momenten waarop we onze tanden zetten in de materie (zoals de werking van de PST) waaraan ik met plezier zal terugdenken.

Marc, op de 'natte' vragen die ik had, antwoordde jij met droge humor. Je nam steeds de tijd om me de hydrodynamische principes op een begrijpelijke manier bij te brengen, en heel waardevolle aanvullingen en feedback te geven op mijn papers en de tekst van dit werk.

I would like to thank the members of the examination board for the effort they put in the evaluation of my work.

Guillaume Crevecoeur, dankjewel om de drempel van mijn eerste paper te helpen verlagen, om me het nodige zelfvertrouwen te geven in moeilijke momenten en om me ook inhoudelijk bij te staan.

Had ik ooit gedacht dat ik iemand zou bedanken om een dwingende context voor me te creëren? Bart Meersman: dankjewel. Je daagde me uit om op geregelde tijdstippen een hoofdstuk naar je door te sturen en nam ook de tijd om het te overlezen en feedback te geven.

Het FlanSea team en partners wil ik danken om samen in zee te gaan en de Wave Pioneer te ontwerpen en te bouwen, ook al waren er soms wisselende weersomstandigheden... De ontwikkeling van deze test-golfenergieconvertor heeft ons

veel kennis en ervaring laten opbouwen die aan de basis lag van het onderzoek in dit werk.

Dank aan de UGent FlanSea collega's Dennis, Mathias, Maxim, Tom, Enrique, Joris, Sridhar, Hannes, Florent, Ellen, Lien, om samen de golven letterlijk en figuurlijk te trotseren. Frederik, bedankt om me in te wijden in de wereld van Matlab-Simulink en om het hydrodynamische model erin te implementeren.

Joris Degrieck, dank voor je deskundige bijdrages en bijsturingen zowel tijdens het FlanSea project, maar vooral tijdens het WES project. En natuurlijk ook dank voor je boeiende idee om een PST in een PTO te gebruiken.

Jeroen De Maeyer, bedankt voor het helpen opstarten van zovele projecten, waaronder FlanSea en het WES-project. Ook inhoudelijk hebben onze besprekingen over de PST mij goed vooruit geholpen.

Florian Verbelen, het was fijn om zo snel met jou op dezelfde golflengte te zitten tijdens het uitwerken van het PST model, dankjewel. Tim Verbrugghe, dankzij jou waren de hydrodynamische input die ik nodig had steeds maar een telefoontje en een mail van me verwijderd. Wim Verheirstraeten, de uitbreiding met extra metingen en je onderzoek erover tijdens je masterthesis maakten van de lab setup een nog betere tool voor mijn onderzoek, dank daarvoor.

Alle EELAB collega's wil ik graag bedanken voor de collegialiteit in vele vormen, voor de leuke middagpauzes, de droge, flauwe en andere humor, maar ook om paraat te staan als ik vragen had die binnen jullie specialisatie vielen. Mitko om een kantoor te delen in peis en vree (en m'n planten water te geven als ik er niet was) in Zwijnaarde, en in het Technicum afwisselend: Jan, Thomas, Joachim, Bart, Michiel, Enrique. Tony, Nic, Vincent, Marilyn en Ingrid voor de ondersteuning van allerlei aard.

Eddy, Christine, Steven S, Gwen, Katrien, Luc, Winne wil ik graag danken voor hun warm professionalisme dat ze telkens aan boord legden.

En in de branding waar de golven breken, waren gelukkig mijn vrienden om samen pootje te baden, een duikje te nemen, maar vooral om gewoon aan te komen en te zijn. Dankjewel Dries en Frauke, Lieven en Linds, de Cavia's, Kurt, Leentje, Laura en Koen, Norman en Lien, Krakelers, om jullie fantastische zelve te zijn en er voor mij te zijn.

Mama en papa, dat jullie uitzonderlijk zijn in vele facetten is niets nieuw. Geen moeite was jullie te veel om ons op te vangen zodat ik rustig kon werken. Dankjewel om er te zijn en in mij te geloven.

Mijn broer, zussen en partners: Bieke, Steven, Petra en Estelle, Karolien en Xavier, bedankt om dat gezellige zootje ongeregeld te zijn. En de neefjes Jotte en Korneel, Moris, Pieter en Tijs om mee het kot op stelten te zetten.

Trees en Rik: Meetse, dankjewel om zoveel Meetse te zijn.

Anne en Hugo, men zegt wel eens 'je familie kan je niet kiezen, maar je schoonfamilie wel'. Ik ben heel blij met m'n keuze! Dankjewel dat we zo vaak bij jullie terecht konden.

En als het water me al eens aan de lippen stond, was daar steeds m'n vrouwtje Lientje. Dankjewel vrouwtie om golfbreker te zijn, om een baai te bieden met zonovergoten strand als thuishaven, of om juist samen te surfen op de golven. Maar vooral om zo'n prachtig persoontje te zijn, en de zaligste mama voor Suze.

Suze, jouw komst leerde me te relativeren en te beseffen wat echt belangrijk is in het leven, en daardoor hielp je me dit boek af te werken. Ik doe onderzoek naar hernieuwbare energie om jouw en volgende generaties ook nog wat aarde te gunnen. En ook al vind ik dat belangrijk, en ook al krijg ik er met dit boek een titel bij, het is de titel 'papa' die ik het fierste draag. Suze, dankjewel om zo'n fantastisch klein mensje te zijn.

En u, beste lezer, dank ik om dit boek ter hand te nemen. Ik hoop dat het u iets kan bijbrengen.

Gent, oktober 2017
Kristof De Koker

Table of Contents

Dankwoord **iii**

Nederlandse samenvatting **xxiii**

English summary **xxvii**

1 Introduction **1**

2 Hydrodynamic Model **7**
2.1 Working principle of a heaving point absorber 7
2.2 Terminology 9
2.3 Hydrodynamic simulation model 12
2.3.1 Hydrodynamic force 13
2.3.1.1 Exciting wave force 14
2.3.1.2 Hydrostatic restoring force 14
2.3.1.3 Radiation force 14
2.4 PTO Control 15
2.4.1 Spring-mass-damper principle 15
2.4.2 Reactive control 16
2.5 Shape and dimensions of used WEC 17
2.6 Constraints of the buoy dimensions and simulation model 17
2.6.1 Sinkage constraint 18
2.6.2 Lift or slamming constraint 18
2.6.3 Consequences towards power production 18
2.7 Conclusion 19

3 Modelling of electrical machine and drive characteristics **21**
3.1 Machine dynamics 22
3.2 Machine working region 23
3.2.1 Super-rated torque usage 23
3.2.2 Super-rated speed usage 24
3.2.3 Practical implementation 24
3.3 Machine efficiency 24
3.3.1 Implementation of an efficiency map in the simulation . . 26
3.3.2 Static efficiency map validation for dynamic operation . . 28
3.3.2.1 Using the setup as benchmark 28

3.3.2.2 Comparison of net energy . . . 30
3.3.3 Efficiency maps used in the simulations of this work . . . 32
3.4 Variable frequency drive efficiency . . . 32
3.5 Resulting machine and drive model . . . 34
3.6 Conclusion . . . 35

4 A Wave Emulator for Ocean Wave Energy 37
4.1 Introduction . . . 37
4.2 Importance of real-time emulation of the hydrodynamic force . . . 39
4.3 Lab setup . . . 41
4.3.1 Representation of the floater and sea in the setup . . . 41
4.3.1.1 Hydrodynamic force and mass . . . 41
4.3.1.2 Emulator torque and inertia . . . 42
4.3.2 Configuration . . . 42
4.3.2.1 Control . . . 43
4.3.2.2 Grid connection of the setup . . . 44
4.4 Scaling . . . 44
4.4.1 Froude scaling . . . 44
4.4.2 Compensation by inertia to adapt speed after Froude scaling 46
4.4.2.1 Consequences of the compensation towards the emulator control . . . 47
4.4.2.2 Consequences of the compensation towards interpreting the results . . . 47
4.5 Sizing the Setup . . . 48
4.5.1 PTO torque . . . 48
4.5.2 PTO inertia . . . 48
4.5.3 Wave Emulator torque . . . 49
4.5.4 Wave Emulator inertia . . . 51
4.5.5 Overview of lab setup electrical machines and drives . . . 51
4.6 Validation of the Emulator . . . 51
4.7 Conclusions . . . 53

5 A drum and cable based PTO 57
5.1 Working principle and mathematical model . . . 58
5.1.1 PTO model . . . 59
5.1.1.1 Equivalent linear PTO model . . . 60
5.1.1.2 Gearbox efficiency . . . 61
5.2 PTO control . . . 62
5.2.1 Specific control for a drum and cable PTO . . . 62
5.2.1.1 Unidirectional forces due to cable . . . 62
5.2.1.2 Keeping the cable under tension . . . 63
5.2.2 Influence of control parameters on power absorption . . . 63
5.2.3 Time course of power and buoy movement . . . 67
5.3 Introducing PTO dynamics and efficiency . . . 68
5.3.1 Influence of PTO dynamics . . . 69

5.3.2 Influence of PTO efficiency . . . 69
5.3.2.1 Effect on control parameters . . . 72
5.3.2.2 Effect on produced power . . . 72
5.4 Influence of PTO installed power . . . 76
5.5 Influence of location . . . 79
5.5.1 Yearly energy yield vs. installed power per location . . . 83
5.5.1.1 Capacity factor . . . 83
5.5.1.2 Influence of the PTO efficiency on the yearly yield per location . . . 85
5.6 Electromechanical optimisation of PTO sizing . . . 89
5.6.1 Optimising the available speed . . . 89
5.6.2 Optimizing rated torque and speed . . . 91
5.6.2.1 Mean electrical power - $A1$ map . . . 93
5.6.2.2 Constraints - $A1$ map . . . 95
5.6.2.3 Yearly yield - $A1$ map . . . 96
5.6.2.4 Yearly yield - $B3$ . . . 99
5.6.3 Direct drive machine . . . 101
5.6.4 Optimizing the PTO inertia . . . 104
5.7 Conclusion . . . 106

6 Rack and Pinion PTO **111**
6.1 Working principle and mathematical model . . . 112
6.1.1 PTO model . . . 113
6.2 PTO control . . . 113
6.2.1 Specific control for a rack and pinion PTO . . . 113
6.2.2 Influence of control parameters on power absorption . . . 114
6.2.3 Time course of power and buoy movement . . . 117
6.3 Introducing PTO dynamics and efficiency . . . 118
6.3.1 Influence of PTO dynamics . . . 118
6.3.2 Influence of PTO efficiency . . . 120
6.3.2.1 Effect on control parameters . . . 121
6.3.2.2 Effect on produced power . . . 121
6.4 Influence of PTO installed power . . . 124
6.5 Influence of location . . . 127
6.5.1 Yearly energy yield vs. installed power per location . . . 128
6.5.1.1 Capacity factor . . . 128
6.5.1.2 Influence of the PTO efficiency on the yearly yield per location . . . 129
6.6 Electromechanical optimisation of PTO sizing . . . 131
6.6.1 Optimising the available speed . . . 131
6.6.2 Optimizing rated torque and speed . . . 131
6.6.2.1 Mean electrical power - $A1$ map . . . 132
6.6.2.2 Constraints - $A1$ map . . . 134
6.6.2.3 Yearly yield - $A1$ map . . . 134
6.6.2.4 Yearly yield - $B3$ . . . 138

6.6.3 Direct drive machine . . . 140
6.6.4 Optimizing the PTO inertia . . . 142
6.6.5 Introducing negative motor tuning . . . 144
6.7 Conclusion . . . 147

7 Power Split Transmission PTO 151
7.1 Working principle . . . 152
7.2 Modelling . . . 153
7.2.1 Shaft to the buoy . . . 154
7.2.2 Auxiliary machine . . . 154
7.2.3 Main generator with flywheel . . . 155
7.2.4 Model of the PST . . . 155
7.2.5 Additional speed conversions and transmission ratio of the planetary gear PST . . . 156
7.2.6 PTO efficiency . . . 157
7.3 Control . . . 158
7.4 First simulation results . . . 159
7.4.1 Bidirectional to unidirectional conversion . . . 159
7.4.2 Efficiency at operating points . . . 160
7.4.3 Sensitivity of the parameters towards power absorption . . . 161
7.4.3.1 Influence of auxiliary machine damping . . . 162
7.4.3.2 Influence of main generator damping . . . 162
7.4.3.3 Influence of auxiliary inertia . . . 165
7.4.3.4 Influence of main generator inertia . . . 165
7.5 Update of the control . . . 165
7.5.1 Variable inertia . . . 168
7.5.2 Reactive control . . . 168
7.5.3 Auxiliary speed range . . . 169
7.6 Power smoothness . . . 169
7.6.1 Time course of power as a function of control choices . . . 171
7.6.2 Potential power averaging with the PST topology . . . 171
7.7 System definition for further analysis . . . 173
7.8 Influence of PTO installed power . . . 173
7.9 Influence of location . . . 179
7.10 Optimising rated torque and speed . . . 181
7.10.1 Mean power . . . 182
7.10.2 Constraints . . . 183
7.10.3 Yearly yield . . . 183
7.10.4 Yield comparison between $B3$ map and $A1$ map . . . 189
7.11 Conclusion . . . 190

8 Conclusion and suggestions for future research 193

Bibliography 205

List of Figures

2.1 Point absorber buoy with a drum and cable PTO 8
2.2 Point absorber buoy around a pile with a rack and pinion PTO . . 8
2.3 Point absorber buoy around a pile with a rack and pinion PTO based on a platform 9
2.4 A buoy in still water 10
2.5 Buoy position z, relative position and actual wave elevation ζ . . . 10
2.6 Wave amplitude, height, crest and trough 10
2.7 A partially decomposed representation of a buoy with the hydrodynamic force F_{hyd} and the PTO force F_{PTO} 13
2.8 Dimensions of the WEC used in the simulations 17
2.9 Colorplot of produced electrical power as a function of the control parameters m_{sup} and b_{ext} and contours of WEC contraints lift (blue), sinkage (black) and PTO constraints RMS torque (magenta), speed (white) 19

3.1 Schematic of the PTO drive train with electrical machine and variable frequency drive 22
3.2 Limitation of torque in the super-rated speed region due to field weakening 24
3.3 Machine motoring efficiency vs. normalised power output 25
3.4 Efficiency map as a function of normalised speed and torque . . . 25
3.5 Machine motoring efficiency vs normalised torque at 100%, 75%, 50% and 25% of nominal speed 26
3.6 Machine motoring efficiency vs normalised power output at 100%, 75%, 50% and 25% of nominal speed 27
3.7 Scatter of the operating points of the first 5 minutes of the 30 minutes test. 27
3.8 Power flows in the wave emulator PTO test setup 29
3.9 Scatter of operation points of a +/- 30 minute SS3 run on the setup above the efficiency map 29
3.10 Cumulative energy for measured and calculated cases 31
3.11 Ratio of calculated over measured cumulative sum of energy . . . 31
3.12 Efficiency map for the $A1$ map variant vs. normalised speed and torque. The white line represents the 200% maximum power limit in the field-weakening region. (Based on [1]) 33

3.13 Efficiency map for the $B3$ map variant vs. normalised speed and torque. The white line represents the 200% maximum power limit in the field-weakening region. (Based on [1]) 33
3.14 Simplified block diagram of the machine submodel in the PTO model with the connection with the hydrodynamic sub model . . . 34

4.1 Plot of the total hydrodynamic force and its components for a control consisting of reactive control (m_{sup} = 60 000 kg, b_{ext} = 80 000 kg/s) in a SS3 with a 4.4m diameter buoy with a drum & cable PTO. 40
4.2 Plot of the total hydrodynamic force and its components for a control without reactive control, i.e. pure damping (m_{sup} = 0 kg, b_{ext} = 80 000 kg/s) in a SS3 with a 4.4m diameter buoy with a drum & cable PTO. 40
4.3 Schematic presentation of the correspondence between the floater at sea and PTO drive train with the setup 42
4.4 Schematic of the configuration of the setup 43
4.5 Applied torque-speed path (blue dashed) for the full scale (upper figure) and for the Froude scale model (lower figure) with the nominal (black) and 200% of nominal working range (green) 46
4.6 Torque-speed 200% working regions for three different machine sizes fitted above the most demanding load plots. Machine sizes of 18.5 kW (purple -.), 22 kW (green –) and 30 kW (red solid line). Load curves in blue solid line. 50
4.7 Plots of 100s of the rotational speed of setup (blue), simulation (green) and the speed error (red) for sea state 1 up to 6 54
4.8 Histograms number of occurrence vs. relative rpm error per sea state 55

5.1 Schematic overview of the Wave Pioneer and the drum and cable PTO system: two electrical machines are connected to a drum by means of a gearbox. 58
5.2 Schematic overview of the drum and cable PTO in the floater and the resulting PTO force together with the hydrodynamic force on the buoy 59
5.3 Linear representation of the PTO inertia and electromagnetic force. 60
5.4 Efficiency map of a 2 stage helical bevel transmission as a function of normalised speed and normalised torque (Source: [2]) 62
5.5 Absorbed power [kW] vs. control parameters m_{sup} and b_{ext} for an unlimited available PTO force, contours for maximum sinkage (black). (Note the different axis scales for some of the plots.) . . . 65
5.6 Optimal values for the control parameters m_{sup} and b_{ext} to maximise the absorbed power for the different sea states for an unlimited PTO force without inertia 66

5.7 The absorbed power with a tuning strategy compared with the absorbed power with a purely damping control strategy for an unlimited PTO (left axis in [kW]), together with the ratio between the two (right axis in [%]). 67
5.8 Plots of the buoy position, speed and acceleration together with the absorbed power vs. time for 200 seconds of the simulation for SS3. 68
5.9 Absorbed power [kW] vs. control parameters m_{sup} and b_{ext} for a 280kW PTO, contours for maximum sinkage (black). 70
5.10 Optimal values for the control parameters m_{sup} and b_{ext} to maximise the absorbed power for the different sea states for a 280kW PTO 70
5.11 Buoy movement and PTO force together with the electromagnetic force. 71
5.12 Electrical power [kW] vs. control parameters m_{sup} and b_{ext} for a 280kW PTO with gearbox and $A1$ machine efficiency map, contours for maximum sinkage (black). 73
5.13 Optimal values for the control parameters m_{sup} and b_{ext} to maximise the electrical power for the different sea states for a 280kW PTO with gearbox and $A1$ machine efficiency map 73
5.14 The electrical power with a tuning strategy compared with the electrical power with a purely damping control strategy, together with the ratio between the two, both for an $A1$ machine. 74
5.15 Mean electrical power vs. sea state for the 8 efficiency map variants for a 280kW PTO with gearbox 75
5.16 Optimal values for the control parameters m_{sup} and b_{ext} to maximise the electrical power for the different sea states for a 280 kW PTO with gearbox and $B3$ machine efficiency map 76
5.17 Electrical power [kW] vs. control parameters m_{sup} and b_{ext} for the 6 steps of PTO power with gearbox and $A1$ machine efficiency map, contours for maximum sinkage (black), maximum speed (white), maximum RMS torque (magenta) and lift (blue). . . 78
5.18 Mean electrical power per sea state vs. installed power with normalised values in relation to the constraint limits for sinkage, lift, RMS torque and rpm, for an $A1$ machine and gearbox. 80
5.19 Occurence frequencies for SS1 to SS6 for locations Location 1, 2 and 3. 82
5.20 Yearly available energy per meter wave crest in MWh per sea state for the 3 locations 82
5.21 Yearly energy yield vs. the installed power for the 3 locations together with the energy fractions per sea state for the $A1$ efficiency map and gearbox. 84

5.22 The yearly yield per installed power [kWh/kW], or full load hours [h] on the left y-axis, and the capacity factor [%] on the right y-axis vs. the installed power for the three locations, with an $A1$ efficiency map and gearbox. 85
5.23 Yearly energy yield vs. the installed power for the A and B variants efficiency map also including a gearbox map for Location 1, 2 and 3. 86
5.24 The yearly yield per installed power [kWh/kW], or full load hours [h] on the left y-axis, and the capacity factor [%] on the right y-axis vs. the installed power for the three locations, with a $B3$ efficiency map and gearbox 88
5.25 Scatter of the operating points for a SS6 simulation for a 1500 rpm rated machine (top), and a 1200 rpm rated machine (bottom), showing the increase of speed due to the lack of damping at field weakening. 90
5.26 Scatter of the operating points for a SS6 simulation for a 1350rpm rated machine. 90
5.27 Mean electrical power [kW] for SS6 with a $P5$-$A1$ machine, contour lines for the buoy speed [m/s] in yellow, for the sinkage in black, and RMS torque in cyan. 92
5.28 Mean electrical power ($A1$ map & gearbox) vs. rated torque and speed for sea states 1 to 6, contour lines for the rated power [kW]. 94
5.29 Scatter of the operating points for SS4 (left) and SS6 (right) on a merged efficiency map of $A1$ machine and gearbox for a $T6$-1500 rpm (upper) and a $T6$-1200 rpm (bottom) rated machine. . . 95
5.30 Normalised values in relation to the constraint limits for sinkage, lift, RMS torque and speed, for an $A1$ machine and gearbox. . . . 97
5.31 The yearly yield [MWh] vs. the rated torque and speed (left column), and the yearly yield per installed power [kWh/kW], or equivalent full load hours [h] vs. the rated torque and speed (right column), for the three locations, with an $A1$ efficiency map and gearbox. 98
5.32 The yearly yield [MWh] vs. the rated torque and speed (left column), and the yearly yield per installed power [kWh/kW], or equivalent full load hours [h] vs. the rated torque and speed (right column), for the three locations, with a $B3$ efficiency map and gearbox. 100
5.33 Scatter of the operating points for SS4 (left) and SS6 (right) on a merged efficiency map of $B3$ machine and gearbox for a $T6$-1500 rpm (upper) and a $T6$-1200 rpm (bottom) rated machine. . . 102
5.34 Supplementary mass m_{sup} [kg] vs. rotor inertia [kgm^2] for an $A1$ $T4$-$n5$ machine. 106

6.1 Schematic overview of the rack and pinion PTO in the floater and the resulting PTO force together with the hydrodynamic force on the buoy 112

6.2 Absorbed power [kW] for SS1-6 vs. control parameters m_{sup} and b_{ext} for an unlimited available PTO force, contours for maximum lift (blue) and sinkage (black). 115
6.3 Optimal values for the control parameters m_{sup} and b_{ext} to maximise the absorbed power for the different sea states for an unlimited PTO force without inertia. 116
6.4 The absorbed power with a tuning strategy compared with the absorbed power with a purely damping control strategy for an unlimited PTO (left axis in [kW]), together with the ratio between the two (right axis in [%]). 116
6.5 Plots of the buoy position, speed and acceleration together with the absorbed power vs. time for 200 seconds of the simulation for SS3. 117
6.6 Absorbed power [kW] vs. control parameters m_{sup} and b_{ext} for a 200 kW 1500 rpm PTO, contours for maximum lift (blue). (Please note the different range for the x axis of SS6) 119
6.7 Optimal values for the control parameters m_{sup} and b_{ext} to maximise the absorbed power for the different sea states for a 200 kW PTO. 119
6.8 Buoy movement and PTO force together with the electromagnetic force for SS4 with a 200 kW 1500 rpm machine. 120
6.9 The electrical power with a tuning strategy compared with the electrical power with a purely damping control strategy, together with the ratio between the two, both for an $A1$ machine with gearbox. 121
6.10 Mean electrical power vs. sea state for the 8 efficiency map variants for a 200 kW PTO with gearbox. 123
6.11 Electrical power [kW] vs. control parameters m_{sup} and b_{ext} for the 6 steps of PTO power with gearbox and $A1$ machine efficiency map, contours for maximum sinkage (black), speed (yellow), RMS torque (magenta) and lift (blue). 125
6.12 Mean electrical power per sea state vs. installed power with normalised values in relation to the constraint limits for sinkage, lift, RMS torque and rpm, for an $A1$ machine and gearbox. 126
6.13 Yearly energy yield vs. the installed power for the 3 locations together with the energy fractions per sea state for the $A1$ efficiency map and gearbox. 127
6.14 The yearly yield per installed power [kWh/kW], or full load hours [h] on the left y-axis, and the capacity factor [%] on the right y-axis vs. the installed power for the three locations, with an $A1$ efficiency map and gearbox. 128
6.15 Yearly energy yield vs. the installed power for the A and B variants efficiency map also including a gearbox map for Location 1, 2 and 3. 130
6.16 Mean electrical power ($A1$ map & gearbox) vs. rated torque and speed for sea states 1 to 6, contour lines for the rated power [kW]. 133

6.17 Scatter of the operating points for SS4 (left) and SS6 (right) on a merged efficiency map of $A1$ machine and gearbox for a $T6$-1500 rpm (upper) and a $T6$-1200 rpm (bottom) rated machine. . . 134
6.18 Normalised values in relation to the constraint limits for sinkage, lift, RMS torque and speed, for an $A1$ machine and gearbox. . . . 135
6.19 The yearly yield [MWh] vs. the rated torque and speed (left column), and the yearly yield per installed power [kWh/kW], or equivalent full load hours [h] vs. the rated torque and speed (right column), for the three locations, with an $A1$ efficiency map and gearbox. 136
6.20 The yearly yield [MWh] vs. the rated torque and speed (left column), and the yearly yield per installed power [kWh/kW], or equivalent full load hours [h] vs. the rated torque and speed (right column), for the three locations, with a $B3$ efficiency map and gearbox. 138
6.21 Scatter of the operating points for SS4 (left) and SS6 (right) on a merged efficiency map of $B3$ machine and gearbox for a $T6$-1500 rpm (upper) and a $T6$-1200 rpm (bottom) rated machine. . . 139
6.22 Supplementary mass m_{sup} [kg] vs. rotor inertia [kgm^2] for an $A1$ $T4$-$n5$ machine. 142
6.23 Mean electrical power vs. PTO inertia for the six sea states with purely positive m_{sup} values. Note the dropping performance for SS6 from 10 kgm^2 onwards. 144
6.24 Supplementary mass m_{sup} [kg] vs. rotor inertia [kgm^2] for an $A1$ $T4$-$n5$ machine, also allowing negative m_{sup} values for SS6. . . . 145
6.25 Mean electrical power vs. PTO inertia for the six sea states allowing also negative m_{sup} values for SS6. Note the improved performance for SS6 from 10 kgm^2 onwards compared to Fig. 6.23. . . 145

7.1 Schematic illustration of the PST together with the shafts to the rack and pinion system, auxiliary machine and flywheel plus main generator. The rack and pinion is connected to the carrier, the auxiliary to the sun and the flywheel and main generator to the ring. 152
7.2 Block diagram of the PST PTO model. 156
7.3 Rotational speeds in rpm of carrier, sun and main generator for a SS4 simulation 160
7.4 Scatter of the operating points of the auxiliary machine with preliminary control for a SS4 above the efficiency maps of an $A1$ machine (left) and a $B3$ machine (right). 161
7.5 Scatter of the operating points of the main generator with preliminary control for a SS4 above the efficiency maps of an $A1$ machine (left) and a $B3$ machine (right). 161
7.6 Absorbed power for SS4 vs. the auxiliary machine damping $K_{\mathrm{p,aux}}$ [Nms/rad] and the corresponding peak sinkage and peak lift. . . . 163
7.7 Mean electrical power [kW] for SS4 vs. the auxiliary machine damping $K_{\mathrm{p,aux}}$ [Nms/rad] for the auxiliary machine (upper) and main generator (bottom) ($A1$ map). 163

7.8 Absorbed power for SS4 vs. the main generator damping $K_{\mathrm{p,main}}$ [Nms/rad] and the corresponding peak sinkage and peak lift. . . . 164
7.9 Mean electrical power for SS4 vs. the main generator damping $K_{\mathrm{p,main}}$ [Nms/rad] for the auxiliary machine (upper) and main generator (bottom) ($A1$ map). 164
7.10 Absorbed power for SS4 vs. the auxiliary inertia J_{aux} and the corresponding peak sinkage and peak lift. 166
7.11 Mean electrical power for SS4 vs. the auxiliary inertia J_{aux} for the auxiliary machine (upper) and main generator (bottom) ($A1$ map). 166
7.12 Absorbed power [kW] in fuction of the auxiliary inertia J_{aux} and auxiliary damping factor $K_{\mathrm{p,aux}}$ [Nms/rad], contours of peak sinkage (black) and peak lift (blue). 167
7.13 Operating points of a lowly damped auxiliary machine in SS4, with negative speeds exceeding the maximum operating limit. . . 170
7.14 Operating points of a lowly damped auxiliary machine in SS6, with negative speeds exceeding the maximum operating limit. . . 170
7.15 Operating points of a lowly damped and tuned auxiliary machine in SS4, with negative speeds exceeding the maximum operating limit. 170
7.16 Electrical power vs. time for the auxiliary machine, main generator and total electrical power for the case of a highly damped auxiliary machine in SS4. 172
7.17 Electrical power vs. time for the auxiliary machine, main generator and total electrical power for the case of a low damped auxiliary machine in SS4. 172
7.18 Electrical power vs. time for the auxiliary machine, main generator and total power for the case of a tuned and low damped auxiliary machine in SS4. 172
7.19 Mean power [kW] vs. control parameters J_{sup} [kgm^2] and $K_{\mathrm{p,aux}}$ [Nms/rad] for the 6 steps of PTO power with $A1$ machine efficiency map without accounting for PST efficiency, contours for maximum sinkage (black), speed (yellow), RMS torque (magenta) and lift (blue). 175
7.20 Mean power [kW] per sea state vs. installed power [kW] with normalised values in relation to the constraint limits for sinkage, lift, RMS torque and rpm, for an $A1$ machine without accounting for the PST efficiency. 176
7.21 Optimal values of the control parameters J_{sup} [kgm^2] and $K_{\mathrm{p,aux}}$ [Nms/rad] vs. sea state for the case $P6$. 178
7.22 Optimal values of the control parameters J_{sup} [kgm^2] and $K_{\mathrm{p,aux}}$ [Nms/rad] vs. sea state for the case $P3$. 178
7.23 Yearly energy yield vs. the installed power [kW] for the 3 locations together with the energy fractions per sea state for the $A1$ efficiency map and estimated PST efficiency. 180

7.24 The yearly yield per installed power [kWh/kW], or full load hours [h] on the left y-axis, and the capacity factor [%] on the right y-axis vs. the installed power [kW] for the three locations, with an $A1$ efficiency map and estimated PST efficiency. 180
7.25 Mean power [kW] (only accounting for machine and drive losses) per sea state as a function of the 30 simulated rated torque and speed combinations. 182
7.26 Scatter of the SS4 auxiliary machine operating points above an $A1$ (left) and $B3$ (right) efficiency map for a $T6$-$n5$ case (upper) and $T6$-$n2$ case (bottom). 184
7.27 Scatter of the SS6 auxiliary machine operating points above an $A1$ (left) and $B3$ (right) efficiency map for a $T6$-$n5$ case (upper) and $T6$-$n2$ case (bottom). 185
7.28 Scatter of the main generator operating points above an $A1$ (left) and $B3$ (right) efficiency map for SS4 (upper) and SS6 (bottom). . 185
7.29 Scatter of the SS4 auxiliary machine operating points above an $A1$ (left) and $B3$ (right) efficiency map for a $T4$-$n3$ case, as an example of higher auxiliary machine damping, combined with (positive) reactive control. 186
7.30 Normalised values in relation to the constraint limits for sinkage, lift, RMS torque and speed, for an $A1$ machine and gearbox. . . . 187
7.31 Average annual yield [MWh] (left) and yield per installed power [kWh/kW] or equivalent full load hours [h] (right) for each location as a function of rated torque and rated speed. $A1$ map, drive efficiency and estimated average PST efficiency taken into account. 188

List of Tables

2.1 Significant wave height H_{s} [m] and mean wave period T_{m} [s] of the six used sea states in this work. 12

3.1 Measured and calculated energy after a +/- 30 minute run of SS3 . 30
3.2 The four steps in maximum (nominal) efficiency for the A and B variants. 32

4.1 Froude Scaling Factors for Different Quantities and the Compensated Froude scale factors after speed compensation (cfr. Section 4.4.2) 45
4.2 Overview of the setup's main specifications 52

5.1 Difference in mean electrical power between the 4 A efficiency map variants 74
5.2 Difference in mean electrical power between the 4 B efficiency map variants 74
5.3 Comparison of the electrical power P_{el} and absorbed power P_{abs} between $A1$ and $B3$ efficiency maps with equal nominal efficiency but different shape, and the resulting average PTO efficiency $P_{\mathrm{el}}/P_{\mathrm{abs}}$, for a 280 kW PTO with gearbox 76
5.4 The six power steps [kW] for the sensitivity analysis on rated power. 77
5.5 Occurence frequency (O.F.) of the sea states together with the corresponding available annual energy (A.E.) for the three locations . 83
5.6 Difference in yearly energy yield (YY) between the 4 A efficiency map variants for the three locations, for installed power $P5$ and $P3$. For $A1$ the absolute value is given in MWh, for the other variants the ratio vs. $A1$ is given in % 87
5.7 Difference in yearly energy yield (YY) between the 4 B efficiency map variants for the three locations, for installed power $P5$ and $P3$. For $B1$ the absolute value is given in MWh, for the other variants the ratio vs. $B1$ is given in % 87
5.8 Comparison of the yearly energy yield between $A1$ and $B3$ efficiency maps with equal nominal efficiency but different shape, for a $P5$ and $P3$ PTO with gearbox 88

5.9 The five steps in rotational speed $n1$ to $n5$ in [rpm] and the six steps in torque $T1$ to $T6$ in [Nm]. 93
5.10 The ratio in [%] relative to the maximum yield at Location 1, 2 and 3 respectively for every rated torque and speed combination for a $A1$ map. 99
5.11 The ratio in [%] relative to the maximum yield at Location 1, 2 and 3 respectively for every rated torque and speed combination for a $B3$ map. 101
5.12 Comparison of the yearly yield of the $B3$ cases with the $A1$ cases as YY($B3$)/YY($A1$) in [%]. 103
5.13 Comparison of the yearly yield of the $B3$ direct drive (DD) cases with the $B3$ gearbox cases as YY(DD)/YY(GB) in [%]. 104
5.14 Comparison of the yearly yield in relation to the maximum [%] vs the machine's rotor inertia for Location 1, 2 and 3. 105

6.1 Difference in mean electrical power between the 4 A efficiency map variants 122
6.2 Difference in mean electrical power between the 4 B efficiency map variants 122
6.3 Comparison of the electrical power P_{el} and absorbed power P_{abs} between $A1$ and $B3$ efficiency maps with equal nominal efficiency but different shape, and the resulting average PTO efficiency $P_{\mathrm{el}}/P_{\mathrm{abs}}$, for a 200 kW PTO with gearbox 123
6.4 The six power steps [kW] for the sensitivity analysis on rated power. 124
6.5 Difference in yearly energy yield (YY) between the 4 A efficiency map variants for the three locations, for installed power $P5$ and $P3$. For $A1$ the absolute value is given in MWh, for the other variants the ratio vs. $A1$ is given in % 129
6.6 Difference in yearly energy yield (YY) between the 4 B efficiency map variants for the three locations, for installed power $P5$ and $P3$. For $B1$ the absolute value is given in MWh, for the other variants the ratio vs. $B1$ is given in % 131
6.7 Comparison of the yearly energy yield between $A1$ and $B3$ efficiency maps with equal nominal efficiency but different shape, for a $P5$ and $P3$ PTO with gearbox 131
6.8 The five steps in rotational speed $n1$ to $n5$ in [rpm] and the six steps in torque $T1$ to $T6$ in [Nm]. 132
6.9 The ratio in [%] relative to the maximum yield at Location 1, 2 and 3 respectively for every rated torque and speed combination for an $A1$ map. 137
6.10 The ratio in [%] relative to the maximum yield at Location 1, 2 and 3 respectively for every rated torque and speed combination for a $B3$ map. 139
6.11 Comparison of the yearly yield of the $B3$ cases with the $A1$ cases as YY($B3$)/YY($A1$) in [%]. 140

6.12 Comparison of the yearly yield of the $B3$ direct drive (DD) cases with the $B3$ gearbox cases as YY(DD)/YY(GB) in [%]. 141
6.13 Comparison of the yearly yield in relation to the maximum [%] vs the PTO inertia for Location 1, 2 and 3. 143
6.14 Comparison of the yearly yield with a control allowing negative tuning in relation to the maximum [%] vs. the PTO inertia for Location 1, 2 and 3. 146

7.1 Average gearbox efficiency for every step of installed machine torque. 158
7.2 The control and mechanical parameters for a first conceptual simulation of the PST in a WEC. 159
7.3 Absorbed power per sea state for a fixed inertia limited to 0.6 kgm^2 (column 2), a variable inertia (column 3) and a fixed inertia complemented with reactive control (column 3). 168
7.4 The six power steps [kW] for the sensitivity analysis on rated power. The value represents the total installed power from auxiliary machine and main generator together. The main generator contributes in all cases for 12.5 kW. 174
7.5 The ratio in [%] of the mean electrical power of the machines over the mean electromagnetic power for each sea state, for the rack & pinion PTO (second column), the PST PTO (third column), and the difference between the two systems (fourth column). 179
7.6 The five steps in rotational speed $n1$ to $n5$ in [rpm] and the six steps in torque $T1$ to $T6$ in [Nm] of the auxiliary machine. 181
7.7 The ratio in [%] relative to the maximum yield at Location 1, 2 and 3 respectively for every rated torque and speed combination for an $A1$ map. 186
7.8 Comparison of the yearly yield of the $B3$ cases with the $A1$ cases as YY($B3$)/YY($A1$) in [%]. 189

Abbreviations

AC	alternating current
CF	capacity factor
DC	direct current
DD	direct drive
GB	gearbox
IM	induction machine
OWC	oscillating water column
PMSM	permanent magnet synchronous machine
PST	power split transmission
PTO	power take-off
rpm	revolutions per minute
SS	sea state
WEC	wave energy converter
YY	yearly yield

Most used symbols

$A1$-$A4$	four A efficiency map variants - based on an IM [-]
$B1$-$B4$	four B efficiency map variants - based on a PMSM [-]
b_{ext}	PTO damping coefficient [kg/s]
F_{damp}	damping force [N]
F_{em}	electromagnetic force - force equivalent of T_{em} [N]
F_{ex}	exciting force [N]
F_{hyd}	hydrodynamic force [N]
$F_{\mathrm{hyd,calc}}$	calculated fraction of the hydrodynamic force [N]
F_{PTO}	PTO force [N]
F_{rad}	radiation force [N]
$F_{\mathrm{rad,1}}$	linear added mass term of the radiation force [N]
$F_{\mathrm{rad,2}}$	convolution product term of the radiation force [N]
F_{res}	restoring force [N]
F_{tun}	tuning force [N]
H_{s}	significant wave height [m]
J_{aux}	inertia of auxiliary machine [kgm^2]
J_{fly}	inertia of flywheel plus main generator [kgm^2]
J_{full}	equivalent inertia at the full scale machine shaft [kgm^2]
J_{mod}	Froude scaled inertia for the model PTO [kgm^2]
J_{sup}	supplementary inertia [kgm^2]
$K_{\mathrm{p,aux}}$	proportional gain factor for the damping of the auxiliary machine [Nms/rad]
$K_{\mathrm{p,main}}$	proportional gain factor for the damping of the main generator [Nms/rad]
k	hydrostatic restoring coefficient or stiffness [kg/s^2]
m	buoy mass [kg]
$m_{\mathrm{a},\infty}$	high frequency limit of the added mass (for heave motion) [kg]
m_{a}	added mass (heave mode) [kg]
m_{eq}	equivalent mass for the rotary PTO inertia [m]
m_{sup}	supplementary mass [m]
n	rotational speed [rpm]
$P1$-$P6$	six power steps [kW]
P_{abs}	mean absorbed power [kW]

P_{el}	mean electrical power [kW]
P_{em}	mean electromagnetic power [kW]
P_{m}	electrical machine power [kW]
$P_{\mathrm{m,calc}}$	calculated electrical machine power [kW]
$P_{\mathrm{m,meas}}$	measured electrical machine power [kW]
R_{g}	gearbox ratio [-]
r	radius of drum - radius of pinion [m]
T	torque [Nm]
T_{aux}	electromagnetic torque of the auxiliary machine [Nm]
T_{c}	torque on the shaft of the carrier [Nm]
T_{em}	electromagnetic torque [Nm]
T_{J}	inertial torque [Nm]
T_{m}	mean wave period [s]
T_{main}	electromagnetic torque of the main generator [Nm]
T_{nomF}	nominal torque of the full scale [Nm]
T_{nomM}	nominal torque of the model [Nm]
T_{r}	torque on the shaft of the ring wheel [Nm]
T_{rms}	RMS torque [Nm]
T_{s}	torque on the shaft of the sun wheel [Nm]
T_{shaft}	shaft torque [Nm]
z	vertical buoy position [m]
z_{r}	number of teeth of the ring wheel [-]
z_{s}	number of teeth of the sun wheel [-]
η	efficiency [-]
μ	Froude scale factor [-]
Ω	angular shaft speed [rad/s]
Ω_{c}	angular speed of the carrier [rad/s]
Ω_{r}	angular speed of the ring wheel [rad/s]
Ω_{s}	angular speed of the sun wheel [rad/s]
Ω_{main}	angular speed of the main generator [rad/s]
ω	angular frequency [rad/s]
ω_{n}	natural angular frequency [rad/s]

Nederlandse samenvatting –Summary in Dutch–

Golfenergie kan in de toekomst een relevante bijdrage leveren aan de groeiende mondiale vraag naar energie, maar zit vooralsnog in een relatief jonge onderzoeksfase. Onderzoek dat bijdraagt om de rendabiliteit van golfenergieconvertoren (EN: wave energy converter of WECs) te verbeteren, is nodig om de technologie competitief te maken met andere (hernieuwbare) energiebronnen. Het uitgevoerde onderzoek in dit werk streeft ernaar hieraan bij te dragen door voor verschillende groottes van elektrische machines en verscheidene configuraties de energieopbrengst te begroten om het geïnstalleerd vermogen te reduceren waar mogelijk.

Een op- en neergaande point-absorber kan gemodelleerd worden als een massa-veer systeem dat geëxciteerd wordt door de golfkrachten. Via de beweging van de vlotter wordt vermogen geabsorbeerd uit de golven door het 'power take-off' (PTO) systeem dat het vervolgens omzet in elektriciteit. De vermogensabsorptie door de PTO is maximaal als het systeem in resonantie is met de inkomende golffrequentie en de PTO demping gelijk is aan de interne demping. De eigenfrequentie waarbij het massa-veersysteem resoneert, is afhankelijk van de veerconstante en de massa. Omdat de inkomende golffrequentie verandert met de weersomstandigheden, bevat de PTO controle een term die de massa van het systeem virtueel wijzigt om de eigenfrequentie te beïnvloeden in de richting van de golffrequentie en zo de vermogensabsorptie te optimaliseren. Dit wordt 'reactive control' of 'tuning' genoemd.

Een gedetailleerd simulatiemodel van een roterende elektromechanische PTO werd ontwikkeld - en dit voor drie verschillende PTO-topologieën - dat interageert met een bestaand hydrodynamisch simulatiemodel van een op- en neergaande point-absorber. De gemodelleerde PTO-karakteristieken omvatten het werkingsbereik van de elektrische machine voor zowel het koppel als toerental, de dynamica van de rotorinertie en gedetailleerde efficiëntiegegevens in functie van het actuele koppel en toerental.

Door een weloverwogen keuze te maken voor het werkingsbereik, kan het geïnstalleerd vermogen reeds gedeeld worden door twee door de machine te gebruiken tot 200% van het nominaal koppel en een volgende aanzienlijke reductie van het geïnstalleerd vermogen door gebruik van super-nominaal toerental, terwijl de maximum beschikbare PTO-kracht gelijk blijft. Het gebruik van de machine boven het nominale koppel wordt vaak toegepast bij variabele last, zolang het ermee gepaard gaande RMS koppel gemonitord wordt en onder het nominaal koppel

blijft, en/of de temperatuur van de machine gemeten wordt om te voorkomen dat de maximale temperatuur overschreden wordt. Boven het nominale toerental wordt de machine gebruikt in veldverzwakking en het maximaal koppel is dan gelimiteerd tot de curve van maximum vermogen.

Drie verschillende PTO topologieën zijn gemodelleerd en bestudeerd, alle bestaande uit een roterende elektromechanische PTO. Het eerste systeem bestaat uit een kabel die met de zeebodem verbonden is. In de boei is de kabel rond een trommel (EN: drum) gewikkeld die begint te draaien van zodra de boei omhoog gestuwd wordt door de golven. De trommel is verbonden met een elektrische machine die de mechanische energie omzet naar elektriciteit. Een tweede PTO principe is een paal met een tandheugel (tandlat) en tandwiel (EN: rack and pinion) dat de elektrische machine in beweging brengt. Het derde systeem betreft een vermogenssplit transmissie (EN: power split transmission of PST) die een extra vrijheidsgraad met zich meebrengt en bestaat daarnaast uit twee elektrische machines waarvan de koppels en toerentallen met elkaar verbonden zijn via de PST.

Voor elk van de drie PTO topologieën zijn meerdere iteraties van de PTO-configuratie gesimuleerd om gevoeligheden en trends bloot te leggen. Voor elke iteratie werden de controleparameters geselecteerd om de vermogensoutput te maximaliseren met inachtneming van de boei en PTO limieten. De boeilimieten zijn de maximale slag in zowel opwaartse als neerwaartse richting, en de PTO limieten omvatten de maximale thermische capaciteit (RMS koppel) en het maximale toerental.

Om de simulatieduur te beperken, werd de efficiëntie van de machine geïntegreerd in het model als een opzoektabel in functie van het actuele elektromagnetische koppel en de actuele snelheid in plaats van met een elektrische-machinemodel. Een machinemodel zou een hogere rekenfrequentie nodig hebben en dus een langere simulatieduur. Dit quasi-statisch efficiëntiemodel werd geverifieerd aan de hand van labotesten en een goeie correlatie werd waargenomen tussen de metingen en het quasi-statisch model. Het blijkt dus dat de vereiste dynamica van de machine nog relatief traag is ten opzichte van het elektromagnetisch gedrag in de machine.

De efficiëntie van de machine werd bestudeerd met betrekking tot de hoogte van de nominale efficiëntie, maar ook met betrekking tot de vorm van de 3D efficiëntiecurve over het werkingsbereik van koppel en toerental. Afhankelijk van de machine-topologie kan deze 3D curve relatief spitsvormig zijn met grote verschillen in efficiëntiewaarden over het werkingsbereik. Door de heel variabele belasting, inherent aan golfenergie, heeft de vorm van de efficiëntie over het werkingsbereik een aanzienlijke invloed op de jaarlijkse energieopbrengst. De analyses daarvan hebben aangetoond dat de keuze van een PTO - of zijn componenten - op basis van de nominale efficiëntiewaarde zeer misleidend kan zijn, aangezien de resultaten weergaven dat een machine met identieke nominale efficiëntie, maar een vlakkere vorm, 30% meer energieopbrengst met zich mee kan brengen dan een andere machinetopologie met een meer uitgesproken piekvorm van de 3D efficiëntiecurve.

Een andere optimalisatie werd uitgevoerd met betrekking tot de roterende inertie van de PTO. De inertie kan gezien worden als een toename van de boeimassa en beïnvloedt daardoor de hydrodynamische respons door de eigenfrequentie af te stemmen in de richting van de inkomende golffrequentie, hetgeen resulteert in een hogere absorptie van golfenergie en bijhorende elektrische output. Vooral de performantie van een rack & pinion WEC wordt daardoor verbeterd doordat PTO-krachten in twee richtingen kunnen overgebracht worden, in tegenstelling tot het drum & cable systeem.

Een update in de toepassing van de reactive control werd voorgesteld tijdens de evaluatie van de inertie-optimalisatie. Een zekere PTO inertie maximaliseerde de totale jaarlijkse opbrengst, maar de performantie in de hoogste golfconditie verminderde. De inertie bleek te groot voor die golven, en door negatieve tuning coëfficiënten toe te laten om de systeemmassa virtueel te verlagen, steeg het gemiddelde vermogen in die golfconditie opnieuw met 30% en de jaarlijkse energieopbrengst met 2% tot 5%, afhankelijk van de locatie.

In plaats van een PTO te dimensioneren om de vermogensabsorptie te maximaliseren voor elke golfconditie, wordt er aangenomen dat een economisch optimum kan gevonden worden door de gemiddelde jaarlijkse energieopbrengst op de beoogde locatie te evalueren voor verschillende geïnstalleerde vermogens. Het lokale golfklimaat kan doorslaggevend zijn bij de selectie van het geïnstalleerde vermogen. Drie (virtuele) locaties werden gedefinieerd waarvoor de opbrengst gesimuleerd kan worden. Dertig combinaties van nominaal koppel en nominale snelheid zijn gesimuleerd voor elk van de PTO topologieën om de corresponderende jaarlijkse opbrengst te begroten. Voor de machinetopologie met een relatief piekvormig efficiëntieverloop, bleek zelfs dat een kleiner machinevermogen kan leiden tot een verhoogde energieopbrengst omdat de machine dan in betere efficiëntiezones wordt gebruikt. Voor de andere bestudeerde machinetopologie, die een vlakker efficiëntieverloop heeft, leiden veel cases relatief gezien tot een significant hogere vermindering van geïnstalleerd vermogen dan de overeenkomstige relatieve daling in opbrengst.

Om de verliezen die gepaard gaan met een reductiekast te vermijden, zijn de drum & cable en rack & pinion PTO's gesimuleerd met een direct drive configuratie en vergeleken met de redutiekastopstelling. De direct drive presteert beter in de drum & cable topologie in alle dertig cases van geïnstalleerd vermogen, terwijl de prestaties van de rack & pinion direct drive PTO lijdt onder de verkleinde equivalente PTO-inertie die ermee gepaard gaat.

De derde PTO-topologie die gemodelleerd en gesimuleerd werd, is een nieuw uitgevonden systeem van patent [3], bestaande uit een power split transmissie (PST), gericht op een betere gemiddelde machine-efficiëntie en een bi- naar unidirectionele omzetting van de rotatie. De PST heeft drie assen waarvan de snelheden en koppels onderling met elkaar verbonden zijn. Door middel van het controleren van een controlemachine (auxiliary machine) op één van de drie assen kan de golfenergie worden geabsorbeerd, en verdeeld over de controlemachine en een hoofdgenerator met vliegwiel op de tweede as die in een enkele richting draait. De onderlinge relatie tussen snelheden en koppels is gemodelleerd samen met de

dynamica van de twee machines en vervolgens gecombineerd met het hydrodynamisch simulatiemodel. Een succesvolle proof-of-concept werd bereikt met een eerste reeks simulaties met een basis controlestrategie.

Een reeks gevoeligheidsanalyses met de PST PTO gaf de aanzet om een geoptimaliseerde controlestrategie te definiëren door meer vermogensabsorptie toe te laten met de controlemachine en een 'reactive control' term toe te voegen. De jaarlijkse opbrengst in functie van nominaal koppel en toerental legt de mogelijkheden bloot om het geïnstalleerd vermogen te verminderen op basis van een techno-economische optimalisatie.

Naast het onderzoek betreffende de optimalisatie van de PTO, werd een 'wave emulator' lab setup ontwikkeld en gebouwd om PTO's te testen in een controleerbare en toegankelijke omgeving die dezelfde belasting oplegt aan de PTO alsof die geïnstalleerd zou zijn in een WEC op zee. De wave emulator reageert op de PTO-acties door middel van een real-time controle op basis van het hydrodynamische boeimodel. De boeimassa en de massatermen van het hydrodynamische model worden vertegenwoordigd door de fysieke inertie van de wave emulator, om berekeningen te vermijden met versnellingsmetingen waarop veel ruis zit. Indien het gewenst is om te testen op schaal, kan de WEC worden geschaald met Froude-verschaling terwijl een identieke genormaliseerde belasting wordt behouden. Dit wordt bereikt met een compensatiemethode waarbij extra inertie aan de opstelling toegewezen wordt.

English summary

Wave energy can deliver a relevant contribution to the growing global energy demand in the future, but is for the time being still in a relatively young research stage. Research that helps to increase the profitability of wave energy converters (WECs) is necessary to make them competitive with other (renewable) energy sources. The research performed in this work aims at adding to this effort by quantifying the yield for different machine sizes and configurations to reduce the installed power where possible.

A heaving point absorber can be modelled as a spring-mass system that is excited by the wave forces. Power is absorbed from the waves through the movement of the floater by a power take-off (PTO) system that subsequently converts it to electricity. The power absorption by the PTO is maximised when the system is in resonance with the incoming wave frequency and when the PTO damping is equal to the internal damping. The natural frequency at which a spring-mass system resonates, depends on the spring constant and the mass of the system. Because the incoming wave frequency changes with the weather conditions, the PTO control includes a term that virtually changes the buoy mass to adapt the natural frequency towards the wave frequency and thus optimising the power absorption. This is called 'reactive control' or 'tuning'.

A detailed simulation model of a rotational electromechanical PTO has been developed - and this for three different PTO topologies - to interact with the existing hydrodynamic simulation model of a heaving point absorber. The modelled PTO characteristics encompass the operational range of the electrical machine in terms of available torque and speed, the dynamics of the rotor inertia and not at least precise efficiency information as a function of the actual torque and speed.

By choosing the operational range wisely, the installed power can already be divided by two by allowing the machine to operate at up to 200% of its rated torque and another significant reduction in installed power by using super-rated speeds, while maintaining the same maximum available PTO force. The super-rated torque use is known as good engineering practice with variable loads as long as the corresponding RMS torque is monitored and kept below the rated torque, and/or by measuring the temperature of the machine to prevent exceedance of the maximum temperature. At super-rated speeds, the machine is operated in field-weakening mode, the maximum torque is then reduced to a maximum power curve.

Three different PTO topologies have been modelled and studied, all consisting of a rotary electromechanical PTO. The first system consists of a cable connected with the seabed. Inside the buoy, the cable is wound onto a drum which starts to

rotate when the buoy is pushed upwards by the waves. The drum is connected to an electrical machine that converts the mechanical energy to electricity. A second PTO principle is a pile with a rack and pinion system that forces an electrical machine to rotate. The third system comprises a power split transmission bringing an extra degree of freedom and consists of two machines of which the torques and speeds are interrelated through the PST.

For each of the three PTO topologies, multiple iterations in the PTO configuration have been simulated to reveal sensitivities and trends. For every iteration, the control parameters have been selected to maximise the power output while respecting the floater and PTO constraints. The floater constraints are the maximum stroke in terms of maximum sinkage and maximum lift, and the PTO constraints comprise the maximum thermal capacity (RMS torque) and the maximum peak speed.

To decrease simulation time, the efficiency of the machine has been entered as a lookup table as a function of the actual electromagnetic torque and actual speed of the machine rather than including a machine model. A machine model needs a higher calculation frequency and thus longer simulation time. This quasi static efficiency model has been verified by experimental tests and a good correlation was observed between measurements and the quasi static efficiency model. Apparently, the required dynamics of the machine are relatively slow compared to the electromagnetic behaviour in the machine.

The efficiency of the machine was studied with regard to the magnitude of the nominal efficiency but also with regard to the shape of the efficiency map along the operational torque and speed range. Depending on the machine topology, this shape can be relatively peaky with large differences in efficiency of the machine across the operation range. Because of the very variable loads inherent to wave energy, the efficiency across the working range of the machine has a substantial influence on the annual energy yield. The analyses thereof have shown that the selection of a PTO - or its components - based on the nominal efficiency value can be very misleading as it was observed that a machine with equal nominal efficiency but flatter shape of the efficiency map can yield 30% more than a different machine topology with a more peaky shape of the efficiency map.

Another optimisation was performed regarding the rotational inertia of the PTO. The inertia can be seen as an increase of the floater mass, thus influencing the hydrodynamic response by tuning its natural frequency towards the incoming wave frequency and resulting in a higher wave energy absorption and corresponding electrical output. Especially the performance of a rack and pinion WEC can be improved due to the bidirectional transmission of PTO forces, in contrast to the unidirectional transmission of the drum and cable.

An update of the application of the reactive control was proposed in the aftermath of the inertia optimisation. It appeared that a certain PTO inertia maximised the overall yearly yield, but decreased the performance in the highest sea state. The inertia turned out to be too large for that wave condition, and by allowing negative tuning coefficients to virtually decrease the system's mass, the mean power in that sea state rose again with 30% and the yearly yield with 2% to 5% depending on

the location.

Rather than dimensioning a PTO to maximise the power absorption in every sea state, it is believed that an economic optimum can be found by evaluating the average annual yield at a targeted location for different magnitudes of installed power. The local wave climate can be decisive in the selection of installed power. Three (virtual) locations have been defined at which the yield can be simulated. Thirty combinations of rated torque and rated speed have been simulated for each of the PTO topologies to quantify the corresponding yearly yield. For the machine topology with relatively peaky efficiency map, it even appeared that a smaller machine size can result in an increased output because the machine was then used in better efficiency operating zones. For the other studied machine topology, which has a flatter efficiency map, many cases result in a significantly higher relative reduction of installed power than the corresponding relative drop in yield.

To avoid the losses associated with a gearbox, the drum & cable and rack & pinion PTOs have been simulated with a direct drive configuration to compare with the geared option. The direct drive performs better in the drum and cable topology in all of the thirty machine sizes, while the performance of the rack and pinion direct driven system suffers from the corresponding lower equivalent PTO inertia.

The third modelled and simulated PTO topology is a novel system from patent [3] consisting of a power split transmission (PST) aiming at a better average machine efficiency and a bidirectional to unidirectional conversion of the rotation. The PST has three shafts of which the speeds and torques are interrelated. By means of controlling an auxiliary machine on one of the three shafts, wave power can be absorbed and is split towards both the auxiliary machine and a main generator with flywheel on the second shaft rotating in a single direction. The interrelationship of speeds and torques have been modelled together with the dynamics of the two machines and subsequently combined with the hydrodynamic simulation model. A successful proof-of-concept was achieved with a first set of simulations with a basic control strategy.

A series of sensitivity analyses with the PST PTO gave the input to define an optimised control strategy by allowing more power absorption by the auxiliary machine and including a reactive term. The yearly yield versus rated torque and rated speed reveals possibilities to reduce the installed power in a techno-economic optimisation.

Next to the work on PTO optimisation, a wave emulator lab setup has been developed and built to test PTOs in a controllable and accessible environment applying identical normalised loads to the PTO as if it were installed in a WEC at sea. The wave emulator responds to PTO actions due to a real-time control by the hydrodynamic floater model. The buoy mass and the mass terms of the hydrodynamic model are represented in the physical inertia of the wave emulator to avoid calculations with noisy acceleration signals. If tests at scale are desired, the WEC can be scaled with Froude scaling while the identical normalised load conditions are maintained. This is accomplished by introducing a compensation method which appoints extra inertia to the setup.

1 Introduction

The conversion of ocean wave energy to electricity can offer a contribution to the supply of renewable energy in the future. Accounting for wave climate regions in the power range of 10-30kW/m wave front, the global technical resources are estimated to 200-1000TWh/year [4], compared to a global electricity consumption of 16 429 TWh in 2007 [5].

Various Wave Energy Converters (WECs) are being researched, designed, built and tested all over the world. The WECs can be divided into three main classes: oscillating water columns, oscillating bodies, and overtopping devices [6]. The Power Take-Off (PTO) systems researched in this work have been tested in simulations of an oscillating body WEC. It is a buoy of which the diameter is relatively small compared to the incident wavelength and is therefore referred to as a point absorber. The floating buoy is moved by the exciting wave forces and will consequently move in an oscillatory way according to six degrees of freedom. The only motion considered in this work is the up and down movement, referred to as heave. Inside the buoy, a PTO system extracts energy from the movement of the buoy relative to the seabed, and converts the absorbed energy into electrical energy.

The PTO systems modelled, described and used in the simulations of this work are all based on the conversion of the absorbed wave energy to electricity by means of a rotary electrical machine, in a pure electromechanical PTO. Point absorbers can also consist of a hydraulic PTO such as in [7, 8], or a linear generator such as in [9] with the additional difference that the generator unit is located on the seabed. The relative movement between two floating bodies can also act as energy source,

which is illustrated by the motion between a deep-draught spar and a buoy with a linear generator between the two in [10]. Other point absorbers with a rotary generator can be found in amongst others [11, 12].

In a point absorber moving relative to the seabed, one way of converting the vertical motion to a rotation, is by using a cable connected to the seabed and wind it onto a drum inside the buoy. Alternatively, a vertical pile could be constructed, allowing the buoy to move alongside the pile. Both principles are studied in this research and described in the corresponding chapters. One main difference between the two variants is that the drum and cable system can only absorb wave energy in one direction of the movement, while a system alongside a pile, such as a rack and pinion, can act in both directions.

Part of the work presented in this PhD was performed during the FlanSea project [13] during which a test buoy was developed and built. This test buoy - the Wave Pioneer - is a point-absorber type consisting of a buoy connected with the seabed by a cable.

After the project, further research was performed on the topic of PTO dimensioning to get better insight in the potential reduction of installed power. Additionally to the drum and cable topology, two other systems were modelled and studied in simulations: a rack and pinion system, and a power split transmission PTO. These topologies can apply PTO forces in both directions, unlike the drum & cable PTO. Although the infrastructure works might be more cost intensive, the required torque for a bidirectional PTO is found to be lower (halved in [14, 15]) to achieve similar power production as with a unidirectional system.

Next to the simulation work on PTO optimisation, a wave emulator lab steup has been further elaborated. The lab setup provides an accessible and controllable test bench for PTOs. Once a selection of a PTO has been done by using the simulation results, it is advisable to check its suitability and durability in demanding wave energy conditions by tests in a protected laboratory environment instead of directly in a WEC at sea. The lab setup provides a fully interactive wave emulator where the PTO experiences the same (normalised) torques and speeds as it would in a WEC at sea. Experimental tests of the wave emulator motion showed good correlation with the motion of the WEC in simulations using equal power take-off forces, and is thus validated as a valuable tool in future PTO development. For example, the setup has been used to confirm the assumption of the quasi static efficiency model in the framework of this work.

The hydrodynamic part of the simulation model originates from earlier research at Ghent University [16, 17], but was translated to the Simulink® environment to decrease the calculation time and facilitate the implementation of different PTO models.

Objectives and approach

The conversion of wave energy to electricity can be split in two main processes: the absorption of the wave energy, and the conversion of the absorbed energy towards electrical energy. The performance of the first part is determined by the hydrodynamic response of the floater, which is logically influenced by the wave conditions but also by the magnitude of the PTO force at each moment. The effectiveness of the second process is dependent on the efficiency of the PTO. To quantify the electrical yield, the performance of each process must be considered because both of them influence the magnitude of the electrical output. Previously, most research focussed on optimising the absorbed power without accounting for the characteristics of the PTO, or with important simplification with respect to the PTO characteristics. However, it is of the utmost importance to consider the total process in an integrated approach because the two parts are inextricably linked with each other.

Therefore a *realistic PTO model* was developed to interact with the existing hydrodynamic model of the point absorber. In this simulation model the main PTO characteristics are included: the operational range of torque and speed (i.e. installed power), dynamic behaviour (inertia), transmission ratios and not at least *the efficiencies of the drive train components*.

The integrated approach also means that the *control parameters* are adapted not only to the changing wave conditions, but that they *are optimised for every change in PTO configuration* to maximise the WEC performance. Furthermore, the selection of control parameters must account for both floater and PTO constraints. The use of reactive control to improve the performance of a WEC has already been studied in the 1970s [18, 19] and its importance has more recently been pointed out in [20–22] for a similar PTO as studied in this work. It is also found in literature that respecting the constraints of the WEC may not be underestimated and that the choice of the control parameters thus needs to incorporate this [23, 24].

The presented argumentation can be summarised as the need of a holistic view in wave energy research and is seen as a great challenge for this relatively new technology. [25] states that ”no single component should be optimised without considering the others” while wave energy is ”still in the early stages of research and development”. This is confirmed by [26] requiring a highly integrated approach and is called ”a significant problem” by [27]. A holistic performance analysis has been performed for an oscillating water column (OWC) system in [28] which starts by stating that selecting the optimum turbine remains a current research topic although the fact that OWC systems are one of the most studied WEC systems.

In this work, the holistic approach is performed on the technical side of the PTO, its characteristics and performance, and its interactions with the floater, thus also accounting for the floater constraints.

The final objective of this work is to facilitate the dimensioning of the PTO for a chosen location. Indeed, rather than optimising the power production in each sea state, the yearly yield at the location should be quantified based on the occurrence of each sea state [29]. Evaluating the yield as a function of the PTO configuration enables a PTO dimensioning in the most profitable way to achieve the project requirements. These requirements can differ, sometimes a project aims at maximum profitability, while other projects might demand a certain annual energy yield. Although the study of this work is delineated at determining the average yearly yield as a function of changing configuration characteristics, the methods used are proposed as a tool for a techno-economic analysis for the selection of the best PTO configuration for a defined location.

The intermediate objectives are to map the influence of the main characteristics of the PTO configuration on the energy yield. The installed power determines the magnitude of the available PTO force and influences substantially the degree to which a WEC can absorb power from the waves. However, the installed power is determined by the rated torque and rated speed, and therefore the operational speed range has to be considered as well. By starting to choose the operational range of torque and speed wisely, and using the machine up to its limits (i.e. super-rated usage), a significant reduction in installed power can be achieved without sacrificing substantially in power output. Additionally, the power absorption can be improved by optimising the rotary inertia of the PTO as it influences the hydrodynamic response. Finally the magnitude of the nominal efficiency of the components obviously affects the electrical power output, but also the shape of the efficiency along the operation range in torque and speed substantially influences the yield.

Essential for the economic viability is the reduction of the installed power to minimise its cost. Although the PTO contributes for only a part of the manufacturing cost (approximately 20% - 30% of the total manufacturing cost [30–32]), and logically also the installation and infrastructure works should be considered, it is clear that a cost reduction is beneficial to achieve a successful market penetration. The energy yield will determine the revenue, and thus by presenting the yield for different combinations of installed power, a subsequent cost-benefit analysis can point out the most profitable option. In reality it is not always the most performing machine that wins, and certainly in an early market introduction with low sales volumes, the ready available off-the-shelf machine is probably much cheaper than a custom made design and can therefore be more profitable, even if its efficiency is lower.

In a comparison of PTO systems, the operational costs should not be neglected.

And to honour the holistic view, an environmental impact assessment [33] and a life cycle assessment is at its place to design a WEC in a sustainable way and/or to choose for the options with the smallest impact towards the environment and future generations.

The proof of the pudding is in the eating... Once a system has been defined and designed, it will have to demonstrate its suitability in action. Inherent to a WEC at sea is that the remote location and variable weather conditions complicate the accessibility. Consequently it is advised that PTO systems - or their separate components - are tested before they are subjected to the harsh load conditions in a WEC. To provide a tool for this, a lab setup consisting of a wave emulator has been developed and built in the framework of this work. The wave emulator is controlled by an interactive hydrodynamic model and thus providing identical load conditions to the PTO (component) under test in the setup. If tests at scale are preferred, the design includes a method to maintain equal normalised load conditions after Froude scaling.

Outline of this work

The second Chapter of this work describes the hydrodynamic model calculating the response of the floater under influence of the PTO force and exciting wave force. It is meant to give the essential background information of the model based on linear theory. The basic principles are explained on which the reactive control is inspired and the constraints of the floater motion are discussed.

In the third Chapter the core elements of the electromechanical PTO are modelled: the electrical machine that converts the mechanical power to electrical power and the variable frequency drive. For the machine, the dynamic behaviour is considered as well as the efficiency as a function of the actual operating point, within a predefined working range of torque and rotational speed. A quasi static model concerning the efficiency as a function of the actual torque and actual speed is assumed and validated with experimental tests. The variable frequency drive is entered in the model with a fixed efficiency value over its operational range.

Chapter 4 describes the concept and development of a lab setup consisting of a wave emulator controlled by an interactive hydrodynamic model. After emphasising the importance of a real-time emulation of the hydrodynamic force, the representation of the floater and sea in the setup is explained. Next, Froude scaling is carried out and the undesired consequence of increased rotational speed is compensated by appointing extra inertia to the setup. Subsequently, the proposed concept is used to dimension the setup. As a last step, the adequacy of the wave emulator has been validated by comparing the motion of the setup with simulation.

The fifth Chapter is the first of three chapters in which a PTO topology is modelled and studied. This first PTO system consists of a drum and a cable to con-

vert the heaving buoy motion to a rotation. After describing the PTO model and sketching the system's specific control, a set of sensitivity analyses were carried out, as part of a process to optimise the PTO both in performance as in reduction of installed power. The efficiency has been analysed both in terms of nominal magnitude as in terms of shape along the operational range. The impact of the location and corresponding wave climate has been studied and yields are quantified for a variety of system configurations, varying in efficiency, installed power, inertia, and rated torque and rated speed. The distinction between a geared and direct drive transmission has also been mapped.

The outline of Chapter 6 is mainly analogue to the previous chapter but deals with a bidirectional PTO system comprising a rack and pinion. This PTO topology can exert PTO forces in the two directions, which also means that the equivalent PTO mass of the rotational inertia incorporates an increase of the total system mass of the spring-mass system.

Chapter 7 introduces a novel PTO system consisting of a power split transmission (PST) of the patent [3]. The PST under study is a planetary gear system of which all three shafts are able to rotate. The system aims at a conversion of the bidirectional motion inherent to a heaving buoy to a unidirectional rotation of a main generator equipped with a flywheel by controlling an auxiliary machine on the third shaft. This additional degree of freedom brings extra complexity towards the PTO model and the control. After composing the PST model, a proof of concept has been established by including the PST model in the hydrodynamic simulation environment. Subsequently a series of sensitivity studies is performed to explore the potential of the topology and to optimise the absorption performance. A control strategy is proposed including a reactive component to increase the power absorption. Next, the chapter focusses on the electrical power output to optimise the PTO configuration with the methods also used for the previous two topologies.

The last chapter, Chapter 8, contains the main conclusions of this work and suggestions for future research.

2 Hydrodynamic Model

In this chapter the hydrodynamic part of the used simulation model will be described. It is meant to give the essential information to understand the executed simulations and interpret the results, without going into all details. More in depth information can be found in [16, 17, 34]. Some parts of this chapter were used to clarify the hydrodynamic model in the publication of the wave emulator lab setup [35].

2.1 Working principle of a heaving point absorber

All simulations in this work have been done assuming a heaving buoy point absorber for which the time domain simulation model was available from earlier research at Ghent University [16, 17, 34]. The point absorber is used as an example of a wave energy converter with an oscillatory power input, the methods presented in this work might as well be applicable to other oscillatory (renewable) energy converters. One of the main characteristics of a point absorber concern the horizontal dimensions, which are relatively small compared to the incident wave length. The horizontal dimension in case of a body of revolution is the diameter.

A freely floating buoy is subjected to the wave induced forces and moments and will start to oscillate in six degrees of freedom as a result. The only mode considered in this work is the heaving motion, which is understood as the vertical relative motion between the buoy and the sea bottom. Due to this motion, the power take-off (PTO) in the wave energy converter (WEC) can subsequently

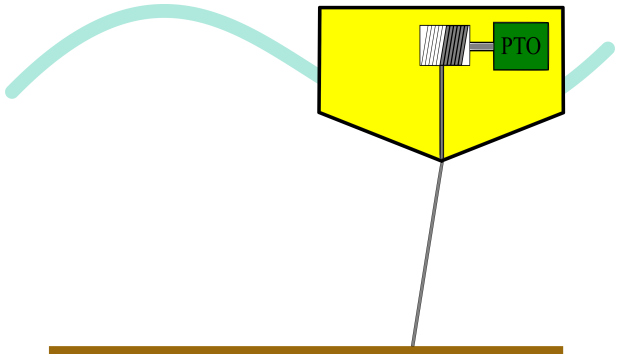

Figure 2.1: Point absorber buoy with a drum and cable PTO

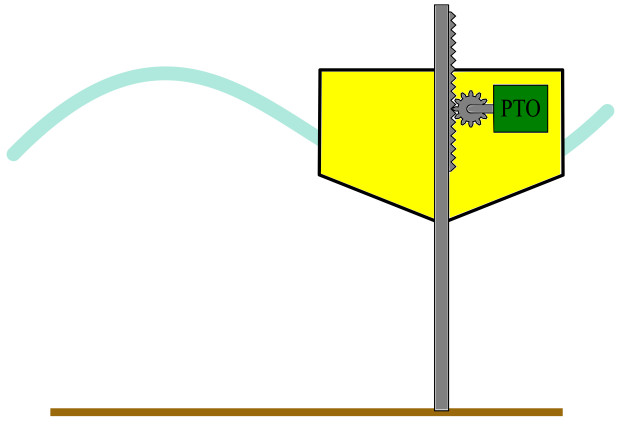

Figure 2.2: Point absorber buoy around a pile with a rack and pinion PTO

absorb the wave energy and convert it into electricity.

The detailed working principle of the different studied PTOs is given in the respective chapters. The following explanation aims at giving an overall view on the working principle of the complete WEC and the conversion of the linear heave motion towards a rotation. For this conversion, two variant systems will be discussed. In the first variant, illustrated in Fig. 2.1, the buoy is connected to the seabed by a cable. In the buoy, the cable is wound onto a drum. Assuming that the cable is always kept under sufficient tension, the drum will start to rotate when the buoy is pushed upwards by the incident wave. In our examples, the drum-PTO is located inside the buoy, but the same principle is valid for a drum-PTO on the seabed and the cable fixed to the buoy. Having a cable between the seabed and the WEC, leads to the fact that power can only be absorbed in one direction, during the upwards movement for the example in Fig. 2.1, and to the necessity of a PTO being able to keep the cable taut in the other direction.

The second variant, depicted in Fig. 2.2, consists of a rack and pinion com-

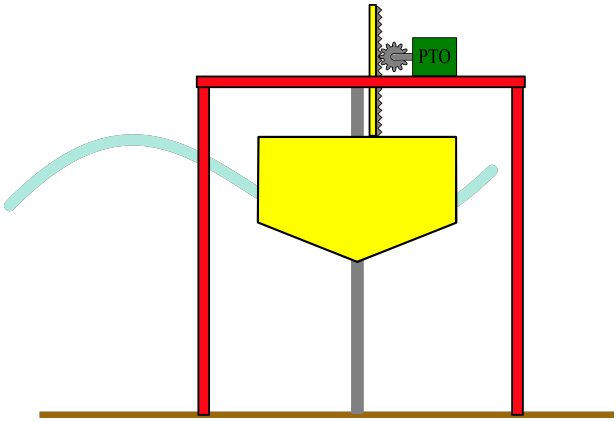

Figure 2.3: Point absorber buoy around a pile with a rack and pinion PTO based on a platform

bination and has the big advantage of being able to extract energy in both the upwards and the downwards movement. In the studied examples, the floater is assumed to be mounted around a vertical pile fixed in the seabed with a rack mounted alongside the pile (or equivalent, as long as the PTO forces can be applied in both directions towards the floater). The pinion, running on the rack and thus driving the rest of the PTO, is located in the floater. The same working principle is valid if the PTO was to be put on top of the pile or on a platform as sketched in Fig. 2.3, and a separate rod with a rack attached to the buoy would drive the pinion and subsequently the complete PTO. The latter configuration can have advantages in accessibility of the PTO and easier cable connection towards the grid as the PTO itself does not move, only the buoy. Thus, a fixed cable can be used for the grid connection in contrast to a PTO in the floater, where the cable will be subjected to heavy motions.

2.2 Terminology

While this work has a strong electromechanical focus, wave energy needs a holistic approach. The PTO cannot work without a hydrodynamic actuator, and vice versa is a floater unable to generate electricity without a PTO. It is also important to understand some basic marine terms and account for related physical boundaries to ensure realistic simulations. This section provides a short overview of important terms illustrated by Figures 2.4, 2.5 and 2.6.

WEC The Wave Energy Converter is the device that converts wave energy into electricity. It is the whole of the floater and PTO.

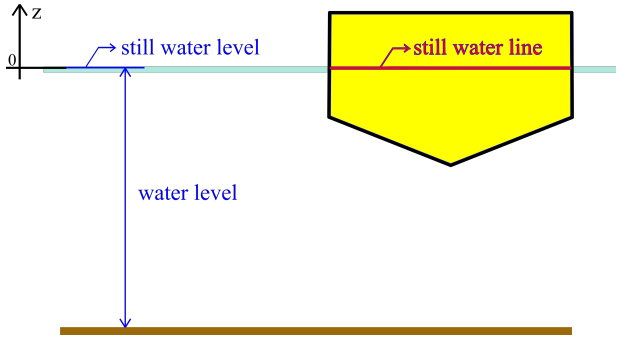

Figure 2.4: A buoy in still water

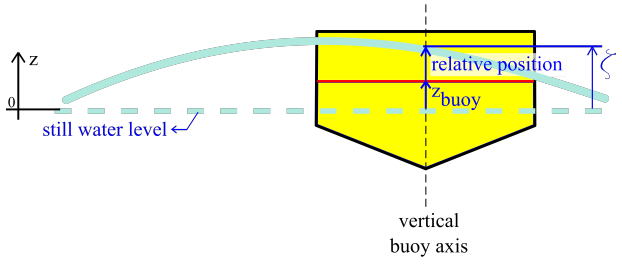

Figure 2.5: Buoy position z, relative position and actual wave elevation ζ

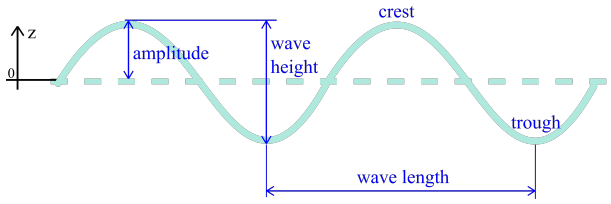

Figure 2.6: Wave amplitude, height, crest and trough

PTO The Power Take-Off system converts the motion energy coming from the waves into electrical energy. In this work the PTO is defined as the complete electromechanical drive train from the components that convert the translational motion to a rotation up to the variable frequency drive that controls the machine. The drive can either output a DC current to inject on a common DC bus of an array of WECs, or directly output an AC current.

Still water level The water level in absence of waves. It is often used as a reference for displacements, and therefore $z = 0$ at the still water level.

Still water line The still water line of a floating device is the line made by the water around the body in water without waves. It is the reference point to define the vertical displacement z of the floater relative to the still water line.

Buoy position z The buoy position is the vertical position measured between the buoy's still water line and the still water level at the vertical axis of the buoy.

Wave elevation ζ The actual wave height relative to the still water level at the vertical axis of the buoy.

Relative position The relative position of the buoy is the distance between the actual water surface and the still water line at the vertical axis of the buoy:

$$\text{relative position} = z - \zeta. \tag{2.1}$$

Sinkage The sinkage is the distance between the actual water surface and the still water line when the still water line is below the water surface, i.e. when the buoy immerses in the water. It is thus the absolute value of the relative position when it is negative:

$$\text{sinkage} = \text{abs}(\text{relative position})|_{\text{relative position}<0} \tag{2.2}$$

Lift The lift is the distance between the actual water surface and the still water line when the still water line is above the water surface, i.e. when the buoy emerges from the water. It is thus the relative position of the buoy when it is positive:

$$\text{lift} = \text{relative position}|_{\text{relative position}>0} \tag{2.3}$$

Crest The highest point within one wave length above the still water level.

Table 2.1: Significant wave height H_{s} [m] and mean wave period T_{m} [s] of the six used sea states in this work.

	SS1	**SS2**	**SS3**	**SS4**	**SS5**	**SS6**
H_{s}	0.25	0.75	1.25	1.75	2.25	2.75
T_{m}	4.15	4.67	5.53	5.95	6.21	6.59

Trough The lowest point within one wave length below the still water level.

Wave height The vertical distance between crest and trough.

Amplitude Half of the wave height of a regular wave.

Wave length The horizontal distance between two successive troughs or crests of a regular wave.

Wave period The time it takes for one complete wave length of a regular wave to pass a certain point.

Sea state (SS) In real seas, the waveform can be considered as the sum of a large number of regular components of different amplitudes, periods and directions. Various wave spectra can be measured at different times and can be identified by their significant wave height H_{s} and mean period T_{m}. They can be divided in ranges of significant wave height, called sea states (SS). In this work, six sea states have been defined based on a moderate wave climate as a base for the calculation of the exciting wave force with WAMIT® per sea state (SS) for the given WEC using a JONSWAP spectrum [36] and for infinite water depth. The six sea states have significant wave heights from 0.25 m to 2.75 m and mean periods of 4.15 s to 6.59 s as listed in Table 2.1.

2.3 Hydrodynamic simulation model

The hydrodynamic time domain model which is used, and the explanation thereof, is based on the model described in the PhD of Griet De Backer [17], and is based on linear potential theory. The model has been validated in a wave flume for a heaving buoy moving around a pole in [34]. For a buoy which is cylindrical at the water line and has a cone shape at the bottom, a difference was found of less than 10% between the average absorbed power of the wave flume experiments and simulations.

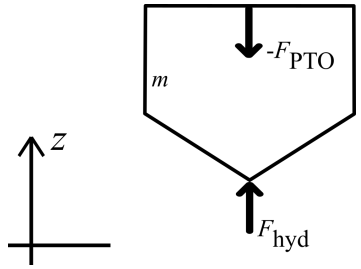

Figure 2.7: A partially decomposed representation of a buoy with the hydrodynamic force F_{hyd} and the PTO force F_{PTO}

The hydrodynamic model is the basis to calculate the position, speed and acceleration of the heaving buoy at every instance. Therefore an equation of motion taking account for all forces acting on the buoy needs to be developed. It was previously implemented in Matlab® code, and has been translated to Matlab-Simulink® for this work, with a significant gain in simulation time.

Principally the floater is a mass m with two forces working on it, the hydrodynamic force F_{hyd} and PTO force F_{PTO}. Only the vertical force component of these forces is considered in this work, as illustrated in Fig. 2.7. The equation of motion, with z the vertical displacement of the buoy, is thus:

$$m\frac{d^2z}{dt^2} = F_{\mathrm{hyd}} + F_{\mathrm{PTO}} \tag{2.4}$$

2.3.1 Hydrodynamic force

The resulting force of the water acting on the WEC is defined as the hydrodynamic force F_{hyd}. It can be described as the sum of the exciting wave force F_{ex}, the restoring force F_{res}, and the radiation force F_{rad}:

$$F_{\mathrm{hyd}} = F_{\mathrm{ex}} + F_{\mathrm{res}} + F_{\mathrm{rad}} \tag{2.5}$$

Before the terms of this equation are explained in detail, it is interesting and almost necessary to know that a floating buoy on the water acts as a mass-spring-damper system. The spring is the restoring force F_{res}. The more a floating device is pushed in the water, the higher the so-called Archimedes or buoyancy force becomes, just as with a spring. Together with the gravitation force and when the floater is cylindrical around the water line, the water acts as a linear spring with restoring force F_{res}. The system also has an internal damper: the hydrodynamic reaction force will damp the motion due to the generation of radiation waves, this is included in the radiation force F_{rad}. One of the functions of the PTO is to act as the external damper. When the waves act on the buoy, the mass-spring-damper system

is excited by an external force: the exciting wave force or shortly the exciting force F_{ex}.

The model assumes a buoy in pure heave motion, in a single degree of freedom. The following subsections describe the different terms of Equation (2.5).

2.3.1.1 Exciting wave force

The exciting wave force is based on calculations with WAMIT® and is the force that a body would experience if kept still in a passing wave, with the still water line at the still water level. This term of the hydrodynamic force is movement independent and is thus read from a time series of processed WAMIT® calculations per sea state (SS) for the given WEC using a JONSWAP spectrum [36]. Six sea states were generated for significant wave heights from 0.25 m to 2.75 m and mean periods of 4.15 s to 6.59 s.

2.3.1.2 Hydrostatic restoring force

The hydrostatic restoring force includes the Archimedes force F_{arch} and the gravity force F_{g}. It can also be expressed as the spring force in the mass-spring-damper analogy for a WEC that is cylindrical around the waterline:

$$F_{\mathrm{res}} = F_{\mathrm{arch}} - F_{\mathrm{g}} = \rho g \left[V(t) - V_0 \right] = -kz \tag{2.6}$$

The spring constant k is therefore called the hydrostatic restoring coefficient and is expressed as $k = \rho g A_{\mathrm{w}}$, where A_{w} is the waterline area, g the gravity constant, ρ the density of the water, z is the vertical position of the buoy relative to the still water line, $V(t)$ the instantaneous, submerged buoy volume and V_0 being the displacement volume at rest.

2.3.1.3 Radiation force

The radiation force F_{rad} is defined as the hydrodynamic reaction force due to the motions of the floating body in still water. The radiation force can be formulated as

$$F_{\mathrm{rad}} = -m_{\mathrm{a}}(\omega)\frac{d^2 z}{dt^2} - b_{\mathrm{hyd}}(\omega)\frac{dz}{dt} \tag{2.7}$$

in the frequency domain with ω the angular frequency of the wave and b_{hyd} the hydrodynamic damping coefficient, and m_{a} the added mass. However, a time domain approach is required due to the necessity of considering irregular seas and due to the nonlinearities induced by the cable and the control strategy. In the time

domain, the radiation force F_{rad} can be decomposed in a linear added mass term and a convolution product [34, 37]:

$$F_{\mathrm{rad}} = F_{\mathrm{rad},1} + F_{\mathrm{rad},2} \tag{2.8}$$

$$F_{\mathrm{rad},1} = -m_{\mathrm{a},\infty}\frac{d^2z}{dt^2} \tag{2.9}$$

$$F_{\mathrm{rad},2} = -\int_0^t K_r(t-\tau)\frac{dz(\tau)}{dt}d\tau \tag{2.10}$$

where $m_{\mathrm{a},\infty}$ is the infinite frequency limit of the added mass, it is defined as the factor by which the buoy's vertical acceleration has to be multiplied to obtain the acceleration dependent component of the hydrodynamic reaction force, and can therefore be interpreted as the mass of the water surrounding the buoy and moving along with it. K_r is the radiation impulse response function obtained by Fourier transformation of the frequency domain hydrodynamic parameters of added mass and damping, which can be computed with frequency domain Boundary Element Method codes like WAMIT®. K_r is obtained from [37]:

$$K_r(t) = \frac{2}{\pi}\int_0^\infty b_{\mathrm{hyd}}(\omega)\ \cos(\omega t)\ d\omega \tag{2.11}$$

The frequency to time domain utility provided by WAMIT® has been used to determine K_r. Duclos and Clément et al. [38] developed a method to obtain a system of ordinary differential equations which are implemented in the calculation of this component of the hydrodynamic force.

2.4 PTO Control

2.4.1 Spring-mass-damper principle

A heaving buoy on the water acts as a spring-mass system. Moreover, due to the incident wave forces, it can be seen as an excited spring-mass system on which an external damping force is applied by the PTO. Indeed, by damping the buoy's motion, the PTO can extract energy from the waves. From such a system it is known that the maximum of energy can be extracted from the exciting force when the system is in resonance and by applying external (PTO) damping equal to the internal hydrodynamic damping. To reach resonance, the natural frequency ω_{n} of the spring-mass system has to be equal to the frequency ω of the wave, assuming a regular wave. The natural frequency is expressed by:

$$\omega_{\mathrm{n}} = \sqrt{\frac{k}{(m + m_{\mathrm{a}}(\omega_{\mathrm{n}}))}} \tag{2.12}$$

with m the mass of the buoy, $m_{\mathrm{a}}(\omega_{\mathrm{n}})$ the added mass for the natural frequency, k the spring constant or hydrostatic restoring coefficient as in Equation (2.6). As the incoming waves on a WEC cannot be controlled, two possible interventions to tune the natural frequency would be to change either the mass of the system, or the diameter of the buoy to influence the spring constant. However, these two interventions are physically difficult to accomplish, certainly when aiming at controlling the natural frequency to react on variable incoming waves. Nonetheless, a control strategy could consist of adding a supplementary mass m_{sup} [16]. To overcome the difficulty of adding a physical mass, the supplementary mass is virtualized by applying a PTO force which is proportional with the buoy's vertical acceleration (here along the z-axis). As this force tunes the natural frequency of the system towards the frequency of the waves, it is called the tuning force F_{tun}:

$$F_{\mathrm{tun}} = -m_{\mathrm{sup}} \frac{d^2 z}{dt^2} \tag{2.13}$$

This results in an adaption of the natural frequency of (2.12) to

$$\omega_{\mathrm{n}} = \sqrt{\frac{k}{(m + m_{\mathrm{a}}(\omega_{\mathrm{n}}) + m_{\mathrm{sup}})}} \tag{2.14}$$

When neglecting all other modes of motion except the vertical translation, a damping force F_{damp} proportional with the vertical velocity of the buoy can be applied by the PTO with external damping coefficient b_{ext}:

$$F_{\mathrm{damp}} = -b_{\mathrm{ext}} \frac{dz}{dt} \tag{2.15}$$

Hence the theoretical PTO force consists of the damping and tuning forces. This force is a consequence of the electromagnetic torque T_{em} of the machine, and is therefore defined as the electromagnetic force F_{em}:

$$F_{\mathrm{em}} = F_{\mathrm{damp}} + F_{\mathrm{tun}}. \tag{2.16}$$

In reality, the PTO force will differ slightly depending on the PTO topology which might have additional requirements, such as winding up of the operational cable. The specific requirements are explained in the respective chapters.

To prevent jitter in the simulation, the acceleration signal coming from the hydrodynamic model needs to be averaged out sufficiently to calculate the tuning force F_{tun} of Equation (2.13). In the simulations for this work, a moving average of 150 ms was used, which is 15 calculation cycles.

2.4.2 Reactive control

Applying a tuning force by adding a (virtual) supplementary mass as in Equation (2.13), is an application of reactive control. The use of reactive control to improve

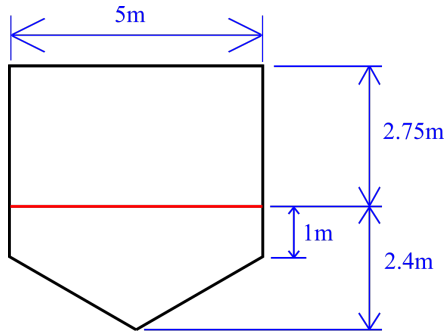

Figure 2.8: Dimensions of the WEC used in the simulations

the performance of a WEC has already been studied in 1970s [18, 19] and its importance has more recently been pointed out in [20–22]. The reactive control implies a bidirectional power flow, and the analogy with the electrical reactive power explains the origin of the term. During a part of the wave cycle, energy will flow from the PTO towards the hydrodynamic system which can be seen as an energy investment to improve the energy harvesting in the next part of the wave cycle and is therefore also called 'motor tuning'. This calls attention to the PTO efficiency, as this invested energy is influenced two times by the PTO losses before it is generated back to electricity.

2.5 Shape and dimensions of used WEC

For the simulations of the different PTOs in this work, a WEC with a diameter of 5 m is chosen. It is a cylindrical buoy around the waterline with a cone shape at the bottom. The cone apex angle is 120°. The mass of the complete WEC is 29 135 kg.

Fig. 2.8 shows the buoy's main dimensions: a freeboard of 2.75 m, a draft of 2.4 m with a cilindrical part of 1 m below the still water line.

2.6 Constraints of the buoy dimensions and simulation model

When the buoy is excited by the waves close to resonance, the movement reaches high amplitudes. This has consequences towards the hydrodynamic behaviour which are undesired as explained in the next subsections.

2.6.1 Sinkage constraint

When the downwards movement is such that the sinkage is more than the freeboard value, the buoy gets submerged and the water on top of the buoy will influence the hydrodynamic behaviour. It can be assumed that the upwards force will decrease. This behaviour is not included in the model, thus the hydrodynamic model is not valid for moments where the sinkage is more than the 2.75 m, which is the height of the freeboard of the simulated WEC.

2.6.2 Lift or slamming constraint

If the upwards movement exceeds the draft of the buoy, the body will experience high impact forces when landing again on the water surface. This phenomenon is called slamming. The slamming forces can cause fatigue on the WEC structure as well as on the PTO and should therefore be avoided. Additionally, the model is not valid when the floater leaves the water.

For the floater used in this work, the slamming constraint is reached when the lift is higher than 2.4m, which is the draft of the used WEC.

As mentioned in Section 2.3, the model is only valid for floaters which are cylindrical around the water line, acting as a linear spring. It is clear that our floater is not cylindrical around the waterline once the lift surpasses 1m, but as this is also the case for the full scale equivalent of the scaled buoy used in the model validation of [34], this inconsistency is assumed to be included in the 10% deviation.

2.6.3 Consequences towards power production

To secure the operation within the constraints of the WEC and the hydrodynamic model, the control parameters of every PTO concept will have to take account for these constraints which will influence the resulting energy yield.

Without going into detail on the PTO control in this chapter, we shortly illustrate the consequences. In the example of Fig. 2.9 a rack and pinion PTO is analysed in sea state 4. The chosen parameters taking account for all constraints (of which the lift constraint is the most stringent in this case) are m_{sup} = 150 000 kg and b_{ext} = 80 000 kg/s, as marked with a blue circle, resulting in a mean electrical power of 18.7 kW. The results of the linear theory model in the colour plot suggests that the optimum lies at m_{sup} = 150 000 kg and b_{ext} = 60 000 kg/s with a corresponding mean power of 21.4 kW. However, these parameters result in at least one exceedance of the lift constraint where the model is actually not valid and the calculated hydrodynamic force would differ from the real force. Moreover, the buoy risks slamming when the lift limit is crossed. As slamming needs to be avoided at all times due to the high corresponding impact forces, the control

parameters were chosen not to cross the limit at any instance as a safety measure. In further analyses, the results are therefore not presented beyond the validity of the model.

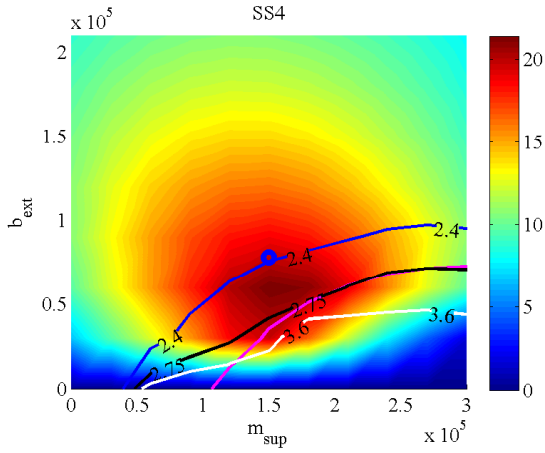

Figure 2.9: Colorplot of produced electrical power as a function of the control parameters m_{sup} and b_{ext} and contours of WEC contraints lift (blue), sinkage (black) and PTO constraints RMS torque (magenta), speed (white)

Therefore it could be considered as suboptimal control. Consider that the 'optimal' parameters for Fig. 2.9 result in only one exceedance of the lift constraint. The simulation run of approximately 8 minutes concerns a sea state 4 with a mean wave period of 5.95 s. Thus approximately 80 waves in the simulation run with on average 1.25% of the produced energy per wave, while the difference between the 'optimal' and 'suboptimal' parameters is 12.6%. Even though realising that this one wave inducing a very large amplitude will produce significantly more than average, it is very likely that the WEC will be controlled suboptimally during the other 79 waves.

This work concentrates on the dimensioning and corresponding electromechanical optimisation and does not aim at improving the control algorithms, however future research on it is suggested in the concluding chapter of this work.

2.7 Conclusion

The hydrodynamic model covered in this chapter is based on linear theory. It assumes a purely heaving buoy and can be influenced by a PTO force from which the absorbed wave power can be quantified. The model also outputs the buoys acceleration from which the speed and position are calculated. The floater has some hydrodynamic constraints which are not intrinsically implemented in the model, but are considered in the post-processing by determining the PTO control

parameters as such that the limits are not exceeded. This hydrodynamic model can be connected to a detailed PTO model to assess the interaction between the two. The floater's position, speed and acceleration are inputs for the PTO model as the base to calculated the appropriate PTO force. This PTO force on its turn is then an input for the hydrodynamic model.

To the extent of the possibilities of the PTO, the composition of the PTO force is based on the maximisation of the power extraction from an excited spring-mass system (which the floater in the waves is). Therefore, the PTO force is a combination of a damping force and a tuning force. The latter is an application of optimised control or reactive control which implies a power flow from the PTO to the hydrodynamic system during a part of the wave cycle.

3

Modelling of electrical machine and drive characteristics

While the WEC body converts the wave energy into kinetic energy, the PTO absorbs and converts it into electrical energy, and is therefore the core of the WEC. The PTO - and its control - are decisive on the ability of the WEC to produce electrical energy.

When simulating the behaviour of a WEC from a hydrodynamic point of view, initial feasibility assessments are mostly executed using assumed PTO forces without taking into account any PTO constraints nor other PTO characteristics. In a further WEC design stage, more profound study of the PTO characteristics and behaviour is indispensable to define and design an appropriate PTO and appraise the yielded energy [20, 21, 24, 39, 40]. Therefore realistic simulation models of electromechanical PTOs are developed to interact with the hydrodynamic model of the floater. The core of the PTO is always a rotary electrical machine connected to a variable frequency motor drive. The mechanical conversion of the linear buoy movement to a rotation is considered a part of the PTO train, as well as any speed and torque conversion such as a gearbox.

In this chapter the focus lies on the modelling of the machine and drive, which are distilled into relatively simple black-box models considering torques, speed, inertias and efficiencies. The efficiency is read from a lookup table as a function of the actual torque and actual speed. This approach results in a shorter simulation time than the implementation of a complete simulation model of the electrical machine model.

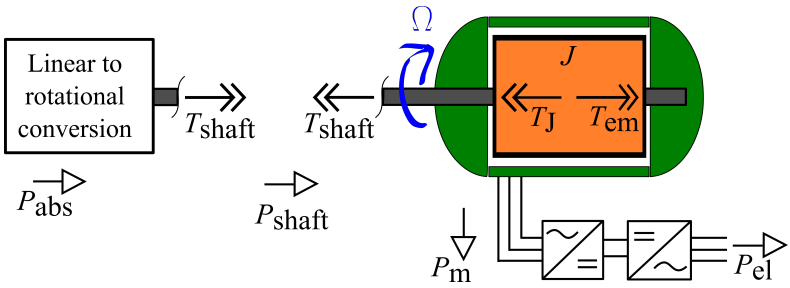

Figure 3.1: Schematic of the PTO drive train with electrical machine and variable frequency drive

In the next chapters different variants of PTO drive trains will be discussed, which include the machine and drive model described in this chapter.

3.1 Machine dynamics

In all studied PTO variants, the wave power is converted to mechanical power and eventually presented to a rotary shaft of an electrical machine as depicted in Fig. 3.1. At every calculation cycle of the simulation, a torque set-point will be calculated which the electrical machine needs to apply. It is assumed that this torque is also actually and immediately applied as an electromagnetic torque in the machine (within the working range). This assumption is verified on the wave emulator lab setup in Chapter 4 Section 4.6 as suitably accurate.

As the goal is to generate electricity, the machine is studied from a generator point of view, although the electrical machine can act both as motor and generator. In this reference system, the electrical power is positive when the machine is generating. According to the schematic of Fig. 3.1, the shaft torque is expressed as

$$T_{\text{shaft}} = T_{\text{em}} - T_{\text{J}} \tag{3.1}$$

where T_{shaft} is the torque on the machine shaft, $T_{\text{J}} = -J\ d\Omega/dt$ the inertial torque of the rotor inertia, and T_{em} the electromagnetic torque applied by the machine on the rotor. Internal friction in the machine, such as from the bearings, is not yet taken into account here, but is considered as a part of the losses comprised in the machine efficiency accounted for in Equation (3.2).

It is clear that the torque on the shaft, passed through to the WEC, is not solely dependent on the applied electromagnetic torque, but is influenced by the actual rotational acceleration $d\Omega/dt$. The machine will have to change direction every few seconds as the WEC moves up and down, accompanied by relatively high rotational accelerations with accordingly high inertial torques. Assume an upwards

moving WEC, with a positive rotary acceleration of the shaft, the counter torque T_{em} has a positive value (cfr. Fig. 3.1) and as a result of $T_{\mathrm{em}} + J\ d\Omega/dt$ (3.1), the shaft torque reaches values higher than the electromechanical torque T_{em}. Hence the inertia has a significant influence on the maximum torque on the shaft and should therefore be taken into account in the simulation and in the dimensioning of the parts of the PTO drive train: couplings, transmission systems, etc.

3.2 Machine working region

Because of the variable nature of wave energy, it was proposed to use the machines up to 200% of their nominal torque value, which is a general used practice with intermittent or variable loads. This use of super-rated torque halves the required rated torque to maintain an equal maximum PTO force. Additionally, the machines were allowed to operate in super-rated speed range to 200% of the rated speed. In that region the machine is used in field-weakening and thus the torque is limited to respect the maximum power curve at every instance. A method that showed to have only little impact on the power output for low over-speed ratios [12]. The super-rated use of the machine has - for the operational range of up to 200% of the rated values used in this work - as a consequence that the *necessary installed power can be reduced significantly*.

3.2.1 Super-rated torque usage

Super-rated torque usage for variable load is known as good engineering practice as long as the RMS torque is kept below the rated value, which needs to be monitored, and/or by measuring the temperature of the machine and preventing exceedance of the maximum temperature. The mean wave period in the used sea state ranges between 4 and 7 seconds, and temporary overload duration will not exceed half of the wave period. The RMS torque is calculated over the simulation time of approximately 8 minutes and the selection of the control parameters is done such that the RMS torque remains below the nominal torque value.

The maximum allowed torque in this work is taken at 200% of the nominal value. Depending on the machine type and design, higher values can be possible.

An overload factor of 200% results in a reduction of the installed power of 50% as the required nominal torque can be halved while maintaining the same maximum PTO force towards the WEC. It could otherwise also double the available PTO force when keeping the same installed power.

The rules of thumb of good engineering practice used here are a first step to dimension the machine of a PTO for wave energy. In the process of choosing a type, one should consult the manufacturer on the overload capabilities.

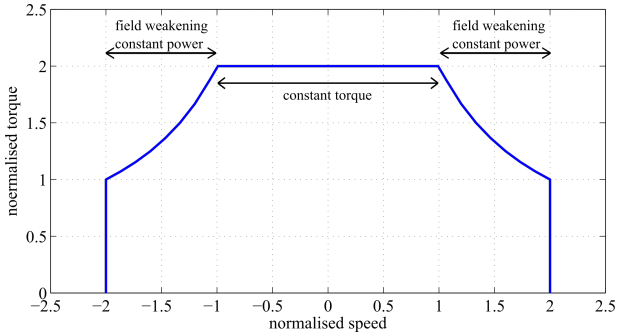

Figure 3.2: Limitation of torque in the super-rated speed region due to field weakening

3.2.2 Super-rated speed usage

The maximum allowed speed used in this work is 200% of the rated speed. Above rated speed, the electrical machine is controlled in field weakening mode, resulting in a constant power limit above rated speed instead of a constant torque limit in the rated speed range, as shown in Fig. 3.2. Hence, the model was fitted with a torque limitation based on the actual speed where the maximum allowed torque is reduced above the rated speed.

Compared to a machine used up to rated speed, super-rated speed usage provides a significant reduction in required installed power by subsequently changing the transmission ratio of the PTO drive train, or changing the number of poles of the machine, while maintaining the same maximum available PTO force over a large range of the working region.

3.2.3 Practical implementation

The limits of the operational range of the machine are implemented in the simulation model by limiting the set point torque by the maximum available torque at the actual speed. The maximum available torque is read from a look-up table of the curve of Fig. 3.2.

3.3 Machine efficiency

The implementation of the machine efficiency is an indispensable step in the evaluation of the energy yield of a WEC concept [20, 21, 24, 41]. A first step often taken, is the implementation of a fixed efficiency value for the complete PTO [41], or for the components of the drive train. For some of the parts this could be an accurate representation of their performance, however in most cases the conversion efficiency is heavily dependent on the operating point, i.e. the combination of the applied torque and actual speed.

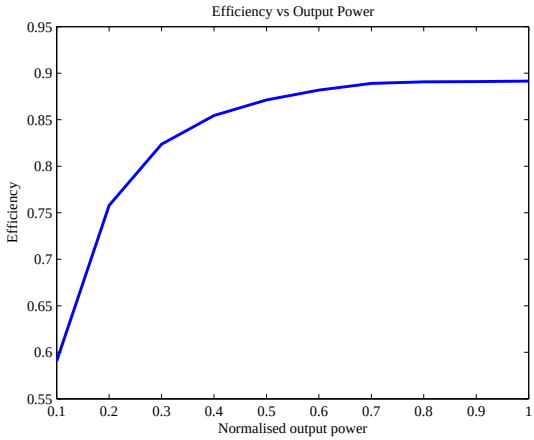

Figure 3.3: Machine motoring efficiency vs. normalised power output

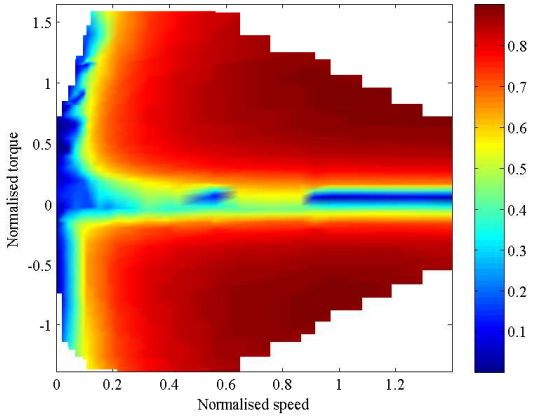

Figure 3.4: Efficiency map as a function of normalised speed and torque

For electrical machines, efficiency graphs as a function of the output power such as Fig. 3.3 are easily available in datasheets. Yet, it is measured at nominal speed and thus does not provide any detail about the efficiency corresponding to a combination of an applied torque and actual speed other than at nominal speed. Efficiency maps [1, 42, 43] where the machine efficiency is given as a function of both torque and speed as shown in Fig. 3.4 offer this detail, but are more difficult to lay hand on. In such a map, a more precise value is given for an operating point of the machine. As can be seen from the figure, there is also a difference between the motoring ($T < 0$) and the generating ($T \geq 0$) efficiency of a certain machine.

To illustrate the difference in values between a simple graph as a function of

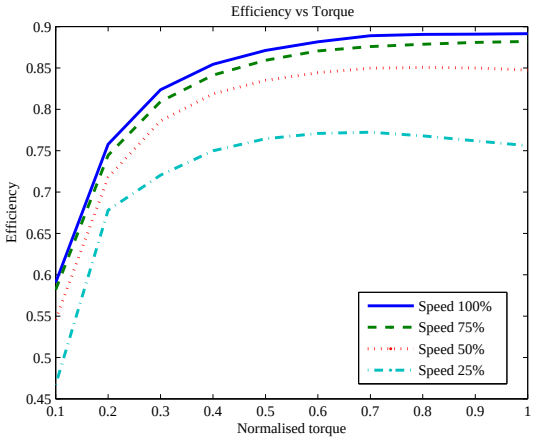

Figure 3.5: Machine motoring efficiency vs normalised torque at 100%, 75%, 50% and 25% of nominal speed

output power and a map as a function of both speed and torque, some graphs have been distilled from Fig. 3.4. In Fig. 3.5 the efficiency is plotted vs. normalised torque, and this for 4 different speeds. The plots illustrate that both the operated torque and speed are sensitive parameters for the machine efficiency. It is clear from the graphs that, next to the fact that the efficiency is highly sensitive to the applied torque, the efficiency vs. torque drops significantly with decreasing speeds.

Fig. 3.6 shows the risk of using a graph as function of output power at nominal speed for different operating speeds: the curve of efficiency vs. output power is clearly not valid for the complete speed range.

The broad operation range of Fig. 3.7 confirms the need to implement the torque and speed based efficiency map in the model.

3.3.1 Implementation of an efficiency map in the simulation

Because of the above discussed reasons, an efficiency map of the electrical machine has been implemented in the simulation model to calculate the actual electrical power at every time step based on the actual torque and speed. In the Simulink model, the actual values of electromagnetic torque T_{em} and speed Ω are the input of a lookup table to find the according efficiency for the operating point. Next, the efficiency extracted from the map is used to determine the calculated electrical

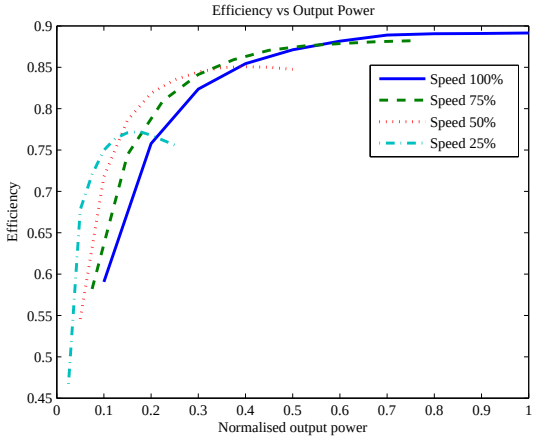

Figure 3.6: Machine motoring efficiency vs normalised power output at 100%, 75%, 50% and 25% of nominal speed

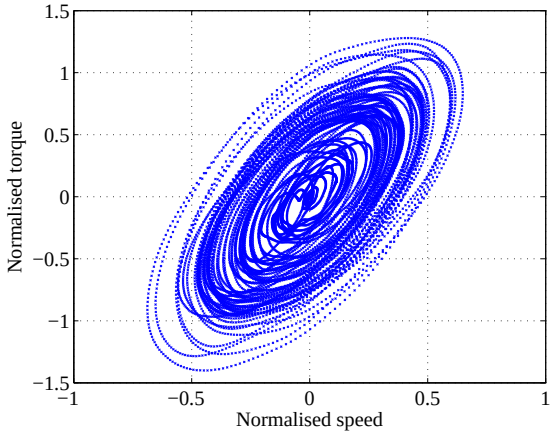

Figure 3.7: Scatter of the operating points of the first 5 minutes of the 30 minutes test.

machine power $P_{\mathrm{m,calc}}$ at every simulation cycle as follows:

$$P_{\mathrm{m,calc}} = \begin{cases} P_{\mathrm{em}} \cdot \eta & \text{for } P_{\mathrm{em}} \geq 0: \text{ generating} \\ \dfrac{P_{\mathrm{em}}}{\eta} & \text{for } P_{\mathrm{em}} < 0: \text{ motoring} \end{cases} \tag{3.2}$$

with $P_{\mathrm{em}} = T_{\mathrm{em}} \cdot \Omega$ the electromagnetic power.

3.3.2 Static efficiency map validation for dynamic operation

Efficiency maps are recorded at steady state. To build this map, the machine is sequentially loaded at steady state for a grid of operation points in the torque and speed working region. Subsequently the efficiency is calculated for each point to generate the static map. In our application, the machine is subject to a dynamic loading and the question is raised whether the appraisal of the electrical power calculated by means of the static efficiency map is ample accurate, in other words, can we use a quasi static model concerning the machine efficiency. In [44] the consumption of energy in motor mode is estimated by processing the operating points trough the static efficiency map for six motoring trajectories of sinusoidal torque and speed changes with frequencies from 0.002Hz to 0.1Hz. The paper concludes that for all six trajectories there is a maximum divergence of 2.6% between the predicted and measured energy. Also [1] makes use of quasi static models in simulating machines in studying hybrid working machines.

The use of a quasi static efficiency model to appraise the energy consumption is validated by [44] on relatively slow changes in torque and speed (maximum frequency of 0.1Hz), however in wave energy frequencies of 0.4Hz are not exceptional. Higher dynamics might cause a lower correspondence with steady state efficiency measurements. Moreover, the tests from [44] have been executed with a periodical signal in motor mode only while the irregular waves of real sea conditions envelop a broader operating spectrum and includes both motor as generator actions. Therefore, the benchmark has been repeated on the wave emulator PTO test setup described in Chapter 4 with real wave conditions and corresponding operation points and dynamics.

3.3.2.1 Using the setup as benchmark

The wave emulator PTO test setup of Chapter 4 has been extended with electrical measurements of voltage and current between the drive and machine to measure the electrical machine power P_{m} during a masters thesis [45] in the framework of this PhD. Earlier available measurements include a torque transducer providing T_{shaft} and an encoder providing the rotational speed Ω. Fig. 3.8 depicts the different power flows and torques in the setup.

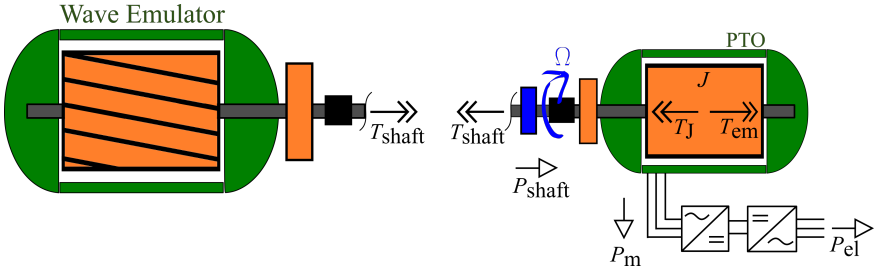

Figure 3.8: Power flows in the wave emulator PTO test setup

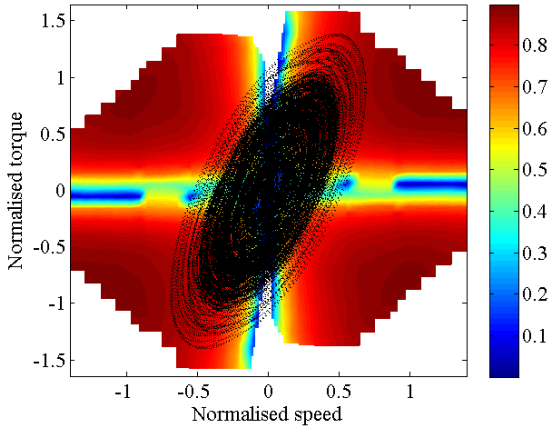

Figure 3.9: Scatter of operation points of a +/- 30 minute SS3 run on the setup above the efficiency map

The setup is run with SS3 wave conditions and reactive control (which includes instances where the machine acts as motor to increase final energy yield, cfr. Chapter 2 Section 2.4) to ensure both operation as generator and motor. The torque, speed and electrical power measurements are acquired at 50 Hz. For every torque-speed combination the according efficiency is extracted from the static efficiency map as illustrated in Fig. 3.9 using linear interpolation. Subsequently the calculated electrical machine power $P_{\mathrm{m,calc}}$ of Equation (3.2) is obtained for each sample using the corresponding efficiency. Finally this calculated power will be compared to the measured electrical machine power $P_{\mathrm{m,meas}}$.

Defining the correct torque value

In steady state, the shaft torque T_{shaft} equals the electromagnetic torque T_{em} as the inertial torque T_{J} is then zero. In dynamic operation however, the inertial torque influences the resulting shaft torque significantly due to the acceleration of

Table 3.1: Measured and calculated energy after a +/- 30 minute run of SS3

	Wh
Measured energy	285.6
Calculated energy	279.1
Ratio calc/meas	97.7%

the rotor inertia. Because the torque on the Y-axis of the efficiency map is the electromagnetic torque, this value is to be used to look up the efficiency. In theory, T_{em} is known, as it should follow the torque setpoint commanded by the control. In practice however, tests have shown it is more precise to deduce the value from the measured shaft torque. The electromagnetic torque can easily be found rewriting the relationship of (3.1) (again neglecting friction):

$$T_{\mathrm{em}} = T_{\mathrm{shaft}} + T_{\mathrm{J}} \tag{3.3}$$

Subsequently, Equation (3.2) results in the calculated electrical machine power $P_{\mathrm{m,calc}}$.

3.3.2.2 Comparison of net energy

A first evaluation has been done by comparing the net produced energy for both cases: measured and calculated. About 30 minutes of measurements of the SS3 on the wave emulator lab setup have been processed. The results in Table 3.1 show a close correspondence and are a first step in validating the use of static efficiency maps in wave energy yield assessment by simulations. Nonetheless the small difference, this end result might be favourable due to dents compensating for the bumps. Therefore, as a second evaluation, the cumulative sum of the energy has been plotted in time in Fig. 3.10 showing two lines diverging only slightly to the end without large discrepancies during the complete test. There is no clear difference to be seen in periods with high absorbed wave power - when the slope is higher - or periods with lower absorbed power.

To check the relative error, the ratio between the calculated and measured cumulative sum of energy is given in Fig. 3.11. Already after a short time period the variation between the measured and calculated energy converges to a difference of approximately 2%. A slight declining trend can be observed, which is not a problem for our application because simulation runs of approximately 8 minutes are performed for the PTO assessments in this work.

Measurement accuracy

The relative error of the electrical and mechanical power (at torque transducer)

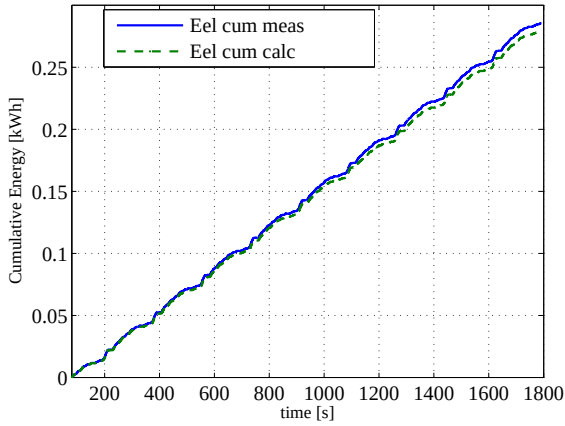

Figure 3.10: Cumulative energy for measured and calculated cases

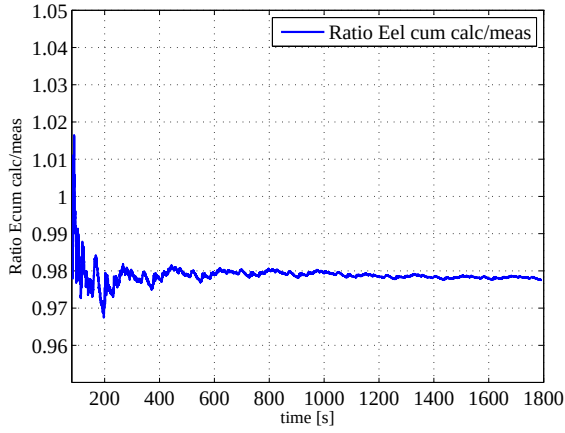

Figure 3.11: Ratio of calculated over measured cumulative sum of energy

Table 3.2: The four steps in maximum (nominal) efficiency for the A and B variants.

	$A1$	$A2$	$A3$	$A4$
Max. efficiency [%]	95.7	94.7	93.7	92.7

	$B1$	$B2$	$B3$	$B4$
Max. efficiency [%]	98.1	97.0	95.7	94.5

measurements have been estimated around 8% and 4% respectively in [45]. The used value for the inertia can also differ from the exact value, as datasheet values are used for all separate components, and at least a deviation of the rotor inertia can be expected after replacement of the shaft-fixed fan by a separately powered cooling fan.

3.3.3 Efficiency maps used in the simulations of this work

For the simulations described in the next chapters of this work, two efficiency maps have been distilled from the same source [1]. The first map is based on an induction machine (IM) rated 37 kW 1480 rpm and is further referred to as the A map variant. The second map, the B map variant, is taken from a 200 kW 1500 rpm rated permanent magnet synchronous machine (PMSM). From these maps, 4 sub variants are made of which the maximum efficiency has been rescaled in four steps of approximately 1%, to analyse the influence of the maximum (nominal) efficiency's magnitude towards the energy output. For the PMSM machine the best efficiency is 98.1%, and for the IM 95.7%. The nominal values for all variants are presented in Table 3.2. To be able to analyse the sensitivity of the shape of the efficiency map, the map sub variants have been chosen such that the maximum efficiency of the $A1$ variant is equal to the $B3$ variant. The $A1$ and $B3$ maps have been plotted in Fig. 3.12 and Fig. 3.13 respectively.

As can be seen from the $A1$ map in Fig. 3.12 and the $B3$ map in Fig. 3.13, the shape of the efficiency map changes significantly: the IM machine has a relatively pointed shape, while the PMSM machine shows a much flatter region where the efficiency is close to the maximum. Another difference is the poorer efficiency at high torques and low speed with the IM.

3.4 Variable frequency drive efficiency

In [1] an efficiency map of an inverter is given with a very flat efficiency, ranging from 97% up to 98.5%. Moreover, the lower efficiency zones are located at the lower power zones. Therefore it is chosen to introduce the efficiency of the vari-

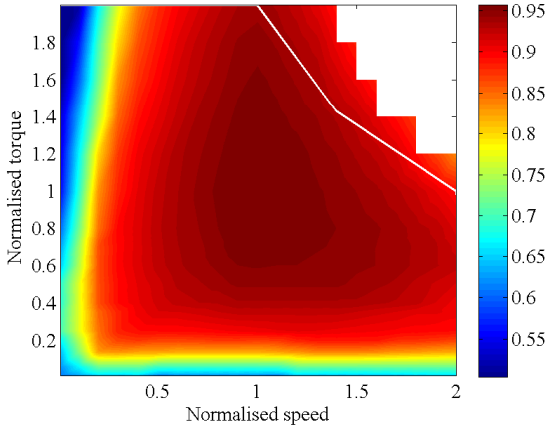

Figure 3.12: Efficiency map for the $A1$ map variant vs. normalised speed and torque. The white line represents the 200% maximum power limit in the field-weakening region. (Based on [1])

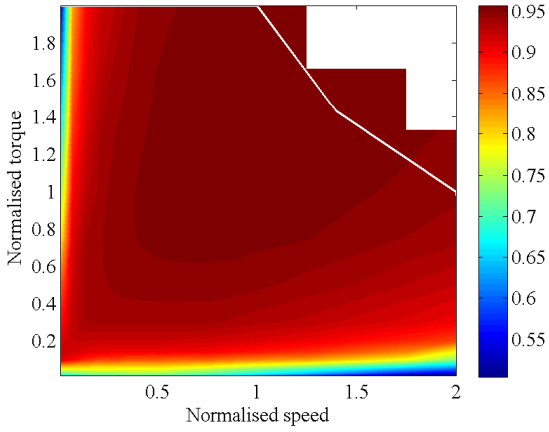

Figure 3.13: Efficiency map for the $B3$ map variant vs. normalised speed and torque. The white line represents the 200% maximum power limit in the field-weakening region. (Based on [1])

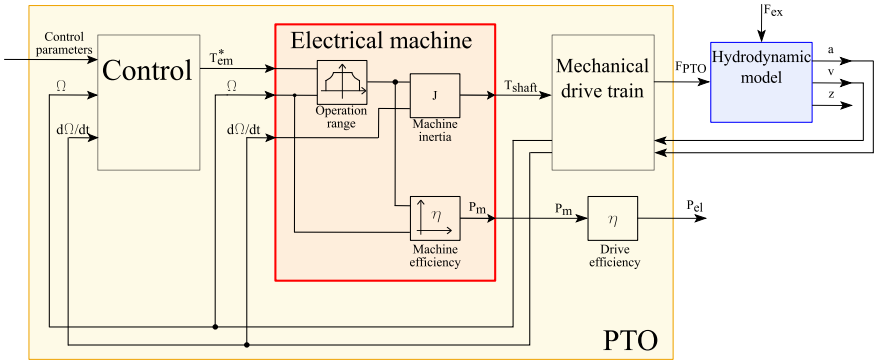

Figure 3.14: Simplified block diagram of the machine submodel in the PTO model with the connection with the hydrodynamic sub model

able frequency drive as a fixed value of 98% instead of a separate map to prevent unessential calculation time in the model. As an alternative, a map including both machine and drive efficiency can be used if this would be available from measurements.

3.5 Resulting machine and drive model

The resulting machine and drive model are visualised in the block diagram of Fig. 3.14 as a part of the complete simulation model. The 'Control' and 'Mechanical drive train' blocks are PTO specific and therefore described in each PTO chapter. The content of the 'Hydrodynamic model' block is explained in Chapter 2.

The control parameters are an input to determine the PTO action which is based on the actual PTO and/or WEC speed and acceleration. Subsequently a desired value for the electromagnetic torque T_{em} is transferred to the electrical machine model where it undergoes the described characteristics of operation range, machine efficiency and inertia to output the shaft torque to the mechanical drive train and the electrical machine power to the drive which results in the electrical output power P_{el}. The PTO force F_{PTO} is the input to the hydrodynamic submodel together with the exciting wave force F_{ex}.

A simulation run of the complete WEC model, with a time series of the exciting wave force of approximately 8 minutes, takes around 8 seconds for the drum and cable model, 7 seconds for the rack and pinion model, and 24 seconds for the PST model on a standard PC (i7) in the Matlab-Simulink environment.

3.6 Conclusion

In addition to the previously existing model a detailed PTO model is developed, adding the machine dynamics and operating constraints to increase the similitude of the simulation results with reality and to facilitate dimensioning of the electrical machine for real life tests. Next to the implementation of the machine inertia, a working region has been defined taking into account the variable character of the wave energy application resulting in an installed power that can be reduced significantly, with interesting consequences towards the cost of the machine and drive. With this intervention the same maximum available PTO force towards the WEC is maintained along a large part of the working range. This is effectuated by operating the machine above rated torque and speed while monitoring that the RMS torque remains below the nominal value to keep the machine from overloading. An alternative is measuring the temperature of the machine and preventing exceedance of the maximum temperature.

To increase the accuracy of the electrical energy yield estimation of the simulated WEC and PTO concept, the machine and drive efficiency have been included in the model. For the machine, efficiency maps have been implemented which provide a value as a function of both the actual torque and speed at every calculation cycle of the simulation. In this pursuit to reach close similarity with reality, steady state efficiency maps have been used. This approach permits to focus on the total WEC system without having to worry about the accuracy of an implemented electrical machine model. Moreover, the simulation time is shorter than with a detailed machine model. Furthermore, a lookup table can be included for all PTO components separately, or one for the global efficiency. After all, the method is not limited to a purely electrical PTO, but can also be used for hydraulic PTO systems.

To validate the quasi static assumption for the machine efficiency, a benchmark has been executed on the wave emulator lab setup of Chapter 4. The experimental measured electrical energy and the electrical energy obtained by processing the sampled operation points through a steady state efficiency map have been compared and showed very good correlation. After a run of approximately 30 minutes a discrepancy of only 2.3% was observed. Even shorter runs result in reliable results with also only a few percent of variation. Therefore we can assume that the use of a static efficiency map in wave energy simulations provides an ample correspondence with reality to assess the electrical output of the electrical machine.

Simulation runs of approximately 500 seconds are often used for first estimations of the potential of a WEC, PTO system or subsystems. The obtained results also support this method regarding the machine efficiency.

For both an induction machine and a permanent magnet synchronous machine, four variant efficiency maps have been defined to study their sensitivity in the next chapters of this work.

The variable frequency drive efficiency has been included in the model as a fixed value for the entire working range as its performance is relatively flat over this range.

4

A Wave Emulator for Ocean Wave Energy, A Froude-scaled Dry Power Take-Off Test Setup

4.1 Introduction

Before testing a selected PTO technology in a wave energy converter at sea, a setup in a protected and controllable environment is advisable, as interventions at a remote location can be very expensive and impractical due to weather conditions. An intermediate step may consist of tests in a wave flume or tank. However, the (large) scale factor to be selected for such tests in general does not allow to investigate the behaviour of the electrical machines of which the PTO is composed. For example, in [46–48] wave basin experiments have been performed, for which the smallest length scale factor used was approximately 24 [49]. Using Froude similarity [50, 51] this results in a scale factor of approximately 70 000 for the power. Therefore, one might consider to reserve these tests for the study of the hydrodynamic behaviour of the floater and opt for a dry test bench for the PTO. A protected laboratory environment facilitates the feasibility study of a chosen PTO topology to meet the requirements of the highly dynamic movements.

The setup's design is primordial to obtain a realistic emulation and accurate testing and assessment of the energy conversion by acquiring the PTO's dynamic response to varying incoming waves. Moreover, control algorithms and the power take-off technology have a drastic influence on the energy conversion of the WEC

[52]. For both hardware testing and control algorithm examination purposes, the design described in this chapter aims at (a) maximum resemblance with a full scale wave energy converter, (b) performing tests in a dry setup and (c) testing at equal normalised load conditions as the full scale PTO in the buoy, even when scaled.

The resemblance should encompass the main factors of the floater's movement: it moves due to the resulting force of hydrodynamic forces and the PTO force acting on the mass of the buoy. As a result of the motion, the buoy experiences hydrodynamic reaction forces. Hence, emulating the floater motion needs to consist of reproducing the relevant forces and masses. As described in [53], the reproduction of the WEC's inertia and hydrostatic restoring force are two key elements for a realistic lab setup. Herein, the focus lies on linear actuators and the inertia and restoring force are reproduced by means of the body of water in a U-tube. Other linear test rigs were described in [54, 55]. For the Pelamis, a scaled hydraulic PTO was introduced in [56]. A rotary shaft-to-shaft connected setup was presented in [57]. In [58] tests were performed on a rotary setup for an oscillating-water-column wave energy converter. This setup was reused to test latching control on an oscillating-water-column device in [59], and for testing speed control strategies for an oil-hydraulic PTO in [8].

In contrast to [53], the present concept describes a dry setup where the physical behaviour of floater body and waves is represented by rotary inertias and an electromechanical torque. Compared to the linear PTO in [54, 55] and the hydraulic one in [56], a rotary electrical PTO is implemented. In [57], time series of torques are used, in contrast, in this work the hydrodynamic forces are calculated interactively in the emulation. Thus the applied torque of the emulator corresponds to the actual force acting on the body in irregular waves based on the actual floater motion also accounting for changing PTO actions. This is accomplished by real-time calculation of the restoring force and the non-linear term of the radiation force and has the advantage that the PTO action can be varied during the tests.

For the setup presented in this chapter, a shaft-to-shaft assembly of two electrical machines is proposed, they can act both as generator and as motor and are therefore further referred to as (electrical) machine. One machine acts as a Wave Emulator that applies a hydrodynamic force equivalent torque. Subsequently the (scaled) PTO machine, the shaft of which is connected directly to the emulator's shaft, can be controlled as if it were installed in a buoy at sea. To reduce the power of the setup, a scaling is implemented. Froude scaling [50, 51] is proposed as it enables transformation of the entire wave energy converter and accompanying hydrodynamic environment towards a scale model.

Parts of this chapter have earlier been published in [35, 60].

4.2 Importance of real-time emulation of the hydrodynamic force

When hydrodynamic and PTO forces interact with a floating buoy, the buoy's movement depends on the magnitude of these forces and the mass of the buoy and rotary inertia of the PTO. To enhance the resemblance of the setup with reality, not only the forces but also the mass and rotary inertia should be reproduced. The rotary inertia of the PTO influences the motion of the floater as it contributes to the PTO force as an inertial force due to its acceleration. Especially when the PTO drive train contains a gearbox, because the equivalent inertia at the slow side of the gearbox is proportional to the square of the gear ratio.

To represent the floater and the PTO in the lab setup, the interaction between both needs to be respected, as well as the hydrodynamic forces. The hydrodynamic forces are described in Chapter 2 Section 2.3 and the PTO topology and its model upon which the setup was done (drum & cable) is described in Chapter 5 Section 5.1.1. The use of the setup is however not limited to this topology.

The movement of a floating body is initially induced by the exciting wave force, but its inertia and the PTO force acting on the body influence the magnitude of the hydrodynamic force significantly, mainly due to the increasing restoring force as a result of the movement. To illustrate the influence of the movement on the total hydrodynamic force, the different calculated hydrodynamic force components have been extracted from simulations and are plotted in Fig. 4.1. From this graph it can be noticed that the total hydrodynamic force peaks at three times the peak value of the exciting force. It emphasises the importance of including the different force components of Equation (2.5) in the control of the Wave Emulator, and not only the exciting wave force. The resulting movement of a body exposed to only the exciting wave force would differ greatly from the movement of a body subjected to all resulting hydrodynamic forces.

Additionally, the magnitude of the PTO action has a significant influence on the resulting hydrodynamic force. As an example, a second simulation has been done with different control parameters than the first simulation of Fig. 4.1. Following the control algorithm [16] described in Chapter 2 Section 2.4, the first simulation uses reactive control, the second simulation is done without reactive control. The results of the latter are plotted in Fig. 4.2. The effect of the changing PTO action is illustrated by the difference between the total hydrodynamic force F_{hyd} of Fig. 4.1 and Fig. 4.2. While both simulations used the same exciting wave force F_{ex} (dashed blue line), it is clearly visible that the total hydrodynamic force F_{hyd} (solid cyan line) is much lower for the second case.

It is concluded that, to have a setup that represents reality and that can react on changing PTO actions (and can thus handle different PTO control strategies), a real-time calculated hydrodynamic force is crucial to control the wave emulator.

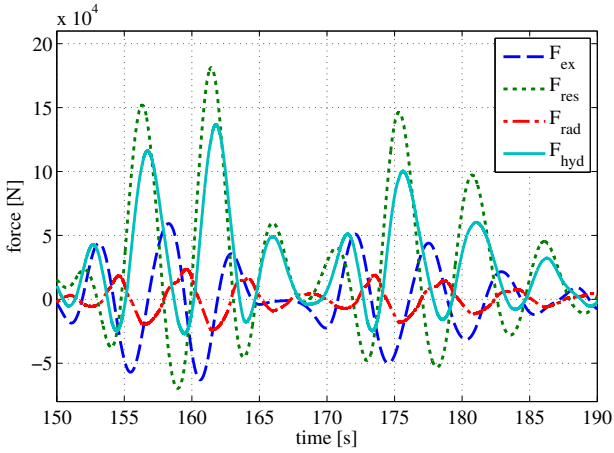

Figure 4.1: Plot of the total hydrodynamic force and its components for a control consisting of reactive control (m_{sup} = 60 000 kg, b_{ext} = 80 000 kg/s) in a SS3 with a 4.4m diameter buoy with a drum & cable PTO.

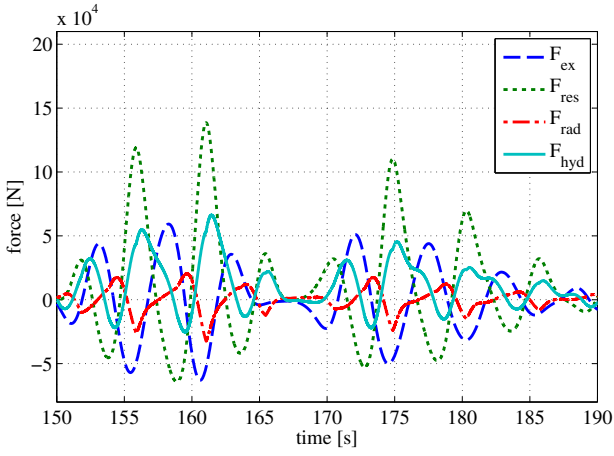

Figure 4.2: Plot of the total hydrodynamic force and its components for a control without reactive control, i.e. pure damping (m_{sup} = 0 kg, b_{ext} = 80 000 kg/s) in a SS3 with a 4.4m diameter buoy with a drum & cable PTO.

4.3 Lab setup

4.3.1 Representation of the floater and sea in the setup

As the intended layout of the setup is a shaft-to-shaft connection of two electrical machines, the wave emulator machine needs to provide the identical torque to the shaft of the PTO machine as in a real wave energy converter. Thus the floater and the sea need to have an equivalent representation at the PTO machine shaft.

4.3.1.1 Hydrodynamic force and mass

The floater in the water can be seen as an inertial mass with two forces acting on it, the hydrodynamic force and the PTO force. The wave emulator machine has a rotary inertia where two torques act upon, the electromagnetic torque and the torque from the shaft. Therefore it is proposed that the hydrodynamic force is converted to a torque, implemented by the electromagnetic torque, and the mass is converted to a rotary inertia to be represented by the rotor inertia of the machine adjusted with a flywheel if necessary.

Next to the buoy mass, a part of the hydrodynamic force can also be inserted physically in the setup. The linear added mass term of the radiation force, $F_{\mathrm{rad},1}$ of Equation (2.9), is proportional with the buoy acceleration and is therefore referred to as the hydrodynamic inertia term. It can be seen as the inertia force due to a mass of water $m_{\mathrm{a},\infty}$ surrounding the buoy moving along with the buoy mass. When this force was to be calculated based on the derivative of a speed measurement in the setup, this would result in a noisy outcome. Therefore it is proposed to combine the added mass $m_{\mathrm{a},\infty}$ together with the buoy mass m to be physically represented in the inertia of the wave emulator. Therefore the hydrodynamic force is split up in a part that is calculated, $F_{\mathrm{hyd,calc}}$, and the linear added mass term of the radiation force $F_{\mathrm{rad},1}$ which is physically represented. $F_{\mathrm{hyd,calc}}$ is thus defined as

$$F_{\mathrm{hyd,calc}} = F_{\mathrm{hyd}} - F_{\mathrm{rad},1} = F_{\mathrm{ex}} + F_{\mathrm{res}} + F_{\mathrm{rad},2}. \tag{4.1}$$

Consequently the equation of motion can be written as

$$(m + m_{\mathrm{a},\infty}) \frac{d^2 z}{dt^2} = F_{\mathrm{hyd,calc}} + F_{\mathrm{PTO}}. \tag{4.2}$$

Fig. 4.3 schematically illustrates the representation of the floater and sea in the lab setup. In contrast with the cable that can only transfer forces in one direction, there is a fixed coupling between the PTO machine and the emulator machine. This is tackled by a torque transducer (HBM T22) in between the two shafts. The torque between the shafts is a measure for the cable force and is used to monitoring the cable force, and thus assess the ability of the PTO control to keep the cable under tension at all times.

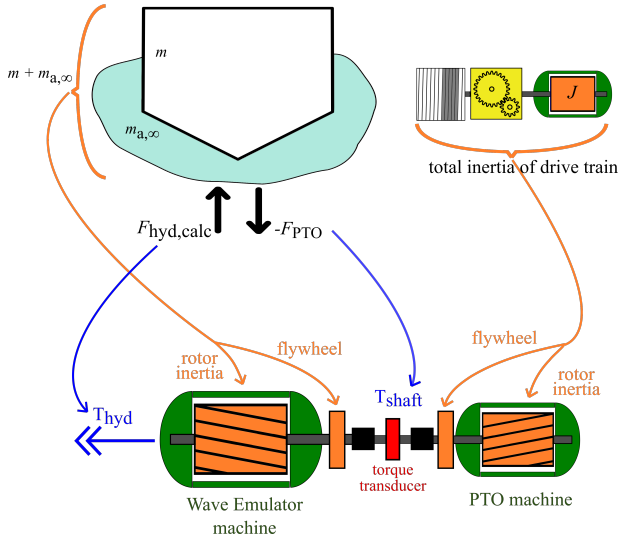

Figure 4.3: Schematic presentation of the correspondence between the floater at sea and PTO drive train with the setup

4.3.1.2 Emulator torque and inertia

The equivalent torque T_{hyd} of the calculated hydrodynamic force is found using the same relationship between the PTO force and the shaft torque as in Equation (5.1):

$$T_{\mathrm{hyd}} = \frac{r}{R_{\mathrm{g}}} F_{\mathrm{hyd,calc}} \tag{4.3}$$

The equivalent rotary inertia for the buoy mass and added mass can be expressed as

$$J_{\mathrm{eq}} = \frac{(m + m_{\mathrm{a},\infty})r^2}{R_{\mathrm{g}}^2}, \tag{4.4}$$

considering that the masses can be seen as moving along the drum with radius r and a gearbox with gear ratio R_{g} between the drum and machine shaft. Note that Equations (4.3) and (4.4) do not include any scaling, but only provide a rotary equivalent.

4.3.2 Configuration

The configuration of the setup is illustrated in Fig. 4.4. Each machine is connected by a frequency controlled motor drive and is provided with a forced cooling fan to assure ventilation at lower speeds. To optimise the resemblance with full scale,

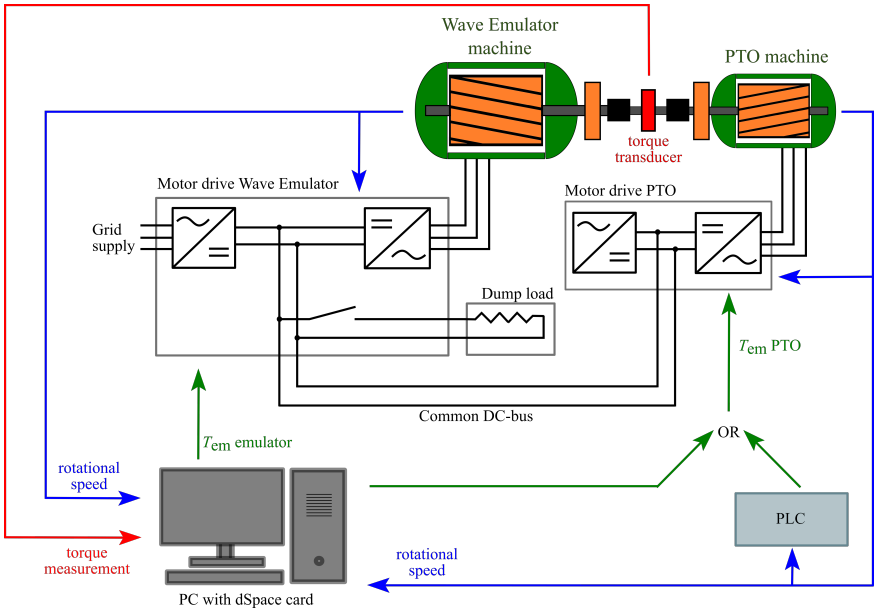

Figure 4.4: Schematic of the configuration of the setup

it is advised that the (scaled) PTO machine is of the same product line as in the full-scale PTO. Next to the electrical machine, also the drive and other components need to be selected to have a close match. This has as additional advantage that drive settings can be tested and set in the lab environment and can afterwards easily be transferred to the real system.

4.3.2.1 Control

The calculation of Equation (4.1) is programmed in Matlab-Simulink®, subsequently compiled to a dSPACE® rapid control prototyping card. The card has an embedded processor where the code is run to read inputs and control outputs. The program runs at 100Hz, which is based on the time-step chosen by the variable time-step solver of Matlab-Simulink. As the model supposes that the floater moves in a pure heave motion and the cable is always kept taut, the drum speed and the length of the unwound cable is directly linked to the vertical speed and position of the floater. Thus the actual encoder position of the setup is read and used to calculate the buoy position and velocity. In this way, the measured signals are used to calculate the torque setpoint of the emulator in real-time which is sent to the drive by means of an analogue signal.

The implementation of the rapid control prototyping card provides great flexibility for extensive testing of the PTO and control algorithms. This type of card was chosen as it includes software enabling easy compilation of Matlab-Simulink®

code to the embedded processor of the card.

Also the PTO can be controlled by the dSPACE® environment, or as an alternative, by a programmable logic controller (PLC) identical to the one used in the WEC at sea, to test this part of the drive train.

4.3.2.2 Grid connection of the setup

As an energy saving measure, the two drives are connected on a common DC-bus, and only the wave emulator drive is supplied from the grid as shown in Fig. 4.4. At most of the instances in time when one of the machines acts as a motor, the other machine is acting as a generator. Nevertheless, this behaviour is not always synchronous and depends on the applied PTO-control. Consequently, moments occur where one of the machines is generating at higher power than the other is consuming as motor. However, the rectifier of the drive is not regenerative, and a significant amount of energy is available in the rotary inertias, which the capacitors in the drives can not store. Therefore a dump load is necessary to dissipate excessive energy on the DC-bus when the actual generating power exceeds the actual consumed motor power.

The dimensioning of the dump load is WEC-device specific and can be calculated in simulation by summing the instantaneous powers of the PTO and emulator so that it can dump the peak generated resulting power.

By interconnecting the two drives on the DC-bus level, the consumed energy of the setup is reduced significantly: only the drive-train losses plus the dumped energy are taken from the grid.

4.4 Scaling

4.4.1 Froude scaling

To keep the installed power of the setup within the range of tens of kilowatts, a downscaling is necessary. The scaling proposed in this work consists of downscaling the complete wave energy converter and wave conditions, and subsequently represent this (virtual) scale model and scaled waves in the setup. Physical quantities of moving marine constructions can be scaled using Froude's Law [50, 51]. This is a common method for physical scale model tests in wave flumes [34,61,62], and is also proposed for this dry lab setup because it enables easy transformation of data and parameters from the full scale design to the scale model, and backwards.

Next to the power, all hydrodynamic parameters to obtain the calculated hydrodynamic force need to be scaled as well. Including the timeseries of the exciting wave force, where not only the force is scaled, but also the time. Alternatively, timeseries of exciting wave force and hydrodynamic parameters can be generated based on the dimensions of the scaled floater. Both methods are equivalent.

Table 4.1: Froude Scaling Factors for Different Quantities and the Compensated Froude scale factors after speed compensation (cfr. Section 4.4.2)

Quantity	**Unit**	**Froude scale factor**	**Compensated Froude scale factor**
Length/distance	m	μ	μ
Mass	kg	μ^3	μ^3
Force	N	μ^3	μ^3
Torque	Nm	μ^4	μ^4
Time	s	$\mu^{0.5}$	$\mu^{0.5}$
Velocity	m/s	$\mu^{0.5}$	$\mu^{0.5}$
Acceleration	m/s^2	$\mu^0 = 1$	$\mu^0 = 1$
Linear damping	kg/s	$\mu^{2.5}$	$\mu^{2.5}$
Power	W	$\mu^{3.5}$	$\boldsymbol{\mu^4}$
Rotational speed	rpm	$\mu^{-0.5}$	$\mathbf{1}$
Mass moment of inertia	kg.m^2	μ^5	$\boldsymbol{\mu^{4.5}}$

The Froude scaling factor μ is the ratio between a length measurement (for example the diameter) of the full scale design L_F and the model scale L_M.

$$\mu = \frac{L_F}{L_M} \tag{4.5}$$

The scale factors for other quantities according to Froude's Law can be found in Table 4.1. To dimension the setup, the relationships for torque and inertia are necessary:

$$T_{\text{model}} = \frac{T_{\text{fullscale}}}{\mu^4} \tag{4.6}$$

$$J_{\text{model}} = \frac{J_{\text{fullscale}}}{\mu^5} \tag{4.7}$$

The consequence of Froude scaling is that the rotational speed of the machine in the scaled model is greater than in the full scale since

$$n_{\text{model}} = n_{\text{fullscale}}\sqrt{\mu}. \tag{4.8}$$

This is undesirable because the setup aimed at testing the PTO at equal normalised load conditions as at full scale. Fig. 4.5 displays that the load conditions change significantly due to the Froude scaling: the scaling increases the normalised speed at every instant. Two load profiles - normalised torque vs. rotational speed - are plotted. The upper plot shows the load profile at full scale, the lower profile shows the load profile of the machine in a Froude scaled model where it is

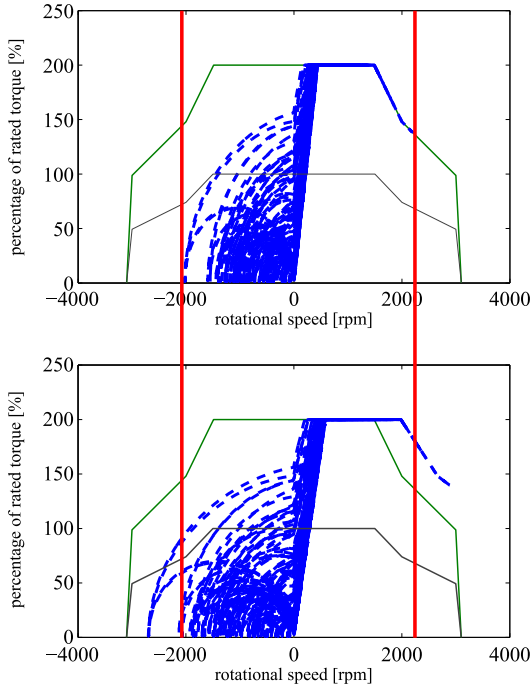

Figure 4.5: Applied torque-speed path (blue dashed) for the full scale (upper figure) and for the Froude scale model (lower figure) with the nominal (black) and 200% of nominal working range (green)

clear that the speed of all working points is increased significantly. To tackle this, a compensation method is proposed.

4.4.2 Compensation by inertia to adapt speed after Froude scaling

As a solution to the increase in rotational speed due to the Froude scaling, it is proposed to add inertia to the Froude scaled value of inertia of both the PTO side and the emulator side of the lab setup. By doing so, the speed decreases when applying an identical sequence of torque set-points to the setup. By using the right value of this additional inertia, the load curve corresponds to the full scale.

To appraise this value, J_{model} and Ω_{model} are defined as the Froude scaled inertia and angular velocity, and J_{comp} and Ω_{comp} as the speed-compensated inertia and angular velocity. The intention is to reduce the speed back to the values of the full scale, hence

$$\Omega_{\text{comp}} = \frac{\Omega_{\text{model}}}{\sqrt{\mu}} \tag{4.9}$$

As the torque sequence is kept equal in both situations, the following expression

is valid:

$$T = J_{\text{model}} \frac{d\Omega_{\text{model}}}{dt} = J_{\text{comp}} \frac{d\Omega_{\text{comp}}}{dt} \tag{4.10}$$

and by inserting Equation (4.9) in Equation (4.10), the speed-compensated inertia is found:

$$J_{\text{comp}} = J_{\text{model}} \sqrt{\mu} \tag{4.11}$$

The compensated inertia should thus be $\sqrt{\mu}$ times larger than the Froude scaled value so that the normalised load curve of the setup corresponds with the normalised load curve of the full scale. This can be implemented by adding a flywheel to the inertia of the machine rotor to reach the compensated value, for both PTO machine and wave emulator machine.

The Compensated Froude scaling factor for the inertia is thus:

$$\frac{\mu^5}{\sqrt{\mu}} = \mu^{4.5}. \tag{4.12}$$

4.4.2.1 Consequences of the compensation towards the emulator control

The calculation of the hydrodynamic torque for the emulator setpoint is based on the buoy position and speed. The computation of the buoy position and speed in the emulator control is based on the encoder data of the machine shaft and therefore needs to account for this compensation factor $\sqrt{\mu}$ too. The linear velocity of the Froude scale model for the case of the Wave Pioneer, consisting of a cable on a drum connected with a gearbox to the PTO machine, can then be expressed as:

$$v_{\text{model}} = \frac{2\pi \, r_{\text{mod}} \, n_{\text{comp}}}{60 R_{\text{g}}} \sqrt{\mu} \tag{4.13}$$

where n_{comp} is the actual rotational speed in rpm of the compensated setup, R_{g} the gear ratio and r_{mod} the radius of the drum in the scale model. Note that the gearbox ratio is not affected in the scaling.

4.4.2.2 Consequences of the compensation towards interpreting the results

Another implication is that the actual power P_{comp} of the PTO machine no longer corresponds with the Froude scaled power P_{model}. If the power of the scale model is to be evaluated, it can be found as follows:

$$P_{\text{model}} = P_{\text{comp}} \sqrt{\mu}. \tag{4.14}$$

And the Compensated Froude scaling factor for the power is:

$$\mu^{3.5} \cdot \sqrt{\mu} = \mu^4. \tag{4.15}$$

4.5 Sizing the Setup

4.5.1 PTO torque

The nominal power of the scaled PTO is chosen to be large enough to maintain close correspondence with the dynamic behaviour of the full scale PTO. A machine of 11 kW was chosen for this setup. The nominal torque of this machine is chosen as the starting point for the calculation of the Froude scale factor. This is justified by the fact that one of the main purposes of the setup is the assessment of the dynamic response of the PTO by keeping its relative load equal to the relative load of the full scale. However, other starting points for the scaling are possible. Thus, the scale factor is assigned as the ratio of the nominal torque of the full scale PTO T_{nomF} and the nominal torque of the scaled model T_{nomM}:

$$\mu = \sqrt[4]{\frac{T_{\mathrm{nomF}}}{T_{\mathrm{nomM}}}} \tag{4.16}$$

Based on this Froude scale factor, the dimensions of the virtual scaled buoy can be calculated using the factors in Table 4.1. This scaled WEC is further referred to as 'scale model' or 'the model'. For the scale model the hydrodynamic parameters are calculated and time series for exciting wave forces are generated using WAMIT®. These time series and scale model are the input for computer simulations for further dimensioning of the setup, and are used in the control of the setup.

4.5.2 PTO inertia

The complete mechanical drive train of a PTO in a real buoy contains more components (such as gearbox, drum) than the PTO side of the setup. Still, the inertia of all components needs to be represented in the setup. Therefore the inertia of the full scale drive train is to be converted to an equivalent inertia at the machine shaft before a scaling can be performed. In Equation (4.17) J_{full} is the equivalent inertia at the full scale machine shaft and J_{mod} is the Froude scaled inertia for the model PTO:

$$J_{\mathrm{mod}} = \frac{J_{\mathrm{full}}}{\mu^5}. \tag{4.17}$$

To find the required value for a setup running at equal speed as the full scale, the compensation of Equation (4.11) needs to be added:

$$J_{\mathrm{compPTO}} = \frac{J_{\mathrm{full}}}{\mu^{4.5}} \tag{4.18}$$

The resulting inertia value J_{compPTO} can be realised by adding a flywheel on the shaft of the PTO machine so that the sum of the rotor inertia and flywheel equals J_{compPTO}, as illustrated in Fig. 4.3.

4.5.3 Wave Emulator torque

In most of the WEC designs the hydrodynamic forces exceed the maximum available PTO force at many instances, consequently the installed power of the emulator machine needs to be higher than the PTO machine.

The hydrodynamic force is reproduced by the electromechanical torque of the emulator machine. To appoint the required emulator machine, computer simulations [34] of the hydrodynamic movement of the virtual WEC are performed. The total hydrodynamic force $F_{\mathrm{hyd,calc}}$ that the scale model would encounter is calculated in time domain simulations for the six sea states. The force is thereafter translated to the torque of the emulator machine using Equation (4.3) which accounts for all PTO drive train transmission ratios until the shaft of the PTO machine, such as drum and gearbox. Note that the scaled drum radius must be used. Next, the torque (T) is plotted versus the rotational speed (n) at each moment to define the needed working region for the Wave Emulator electrical machine.

These torque-speed ($T - n$) plots permit a graphical determination of the required power for the emulator machine. The choice of the appropriate machine can then be done by fitting the working region across the most demanding load curve. As new control strategies might be more demanding and arouse higher hydrodynamic forces or higher speeds, it is advised to take sufficient margin during the sizing.

As the movement in our case is intermittent, good engineering practice allows to use a machine up to the maximum allowed torque of the machine specifications, as long as the RMS torque remains below the rated torque. This practice reduces the necessary rated power by 50% when the maximum allowed torque is 200% of the nominal. Moreover, as the plots in Fig. 4.6 do not show high torque needs at higher speeds, usage of super-rated speed region seems appropriate to realise a second reduction of installed power. Thus a machine with a rated speed of 1500 rpm is chosen and used up to 3000 rpm. The machine is used up to 200% of its rated torque. The same measures have earlier been adopted in the dimensioning of the (full scale) Wave Pioneer's PTO [63].

In Fig. 4.6 the selected working region of 200% of rated torque and speed for three different machine sizes (18.5 kW, 22 kW and 30 kW) have been fitted above

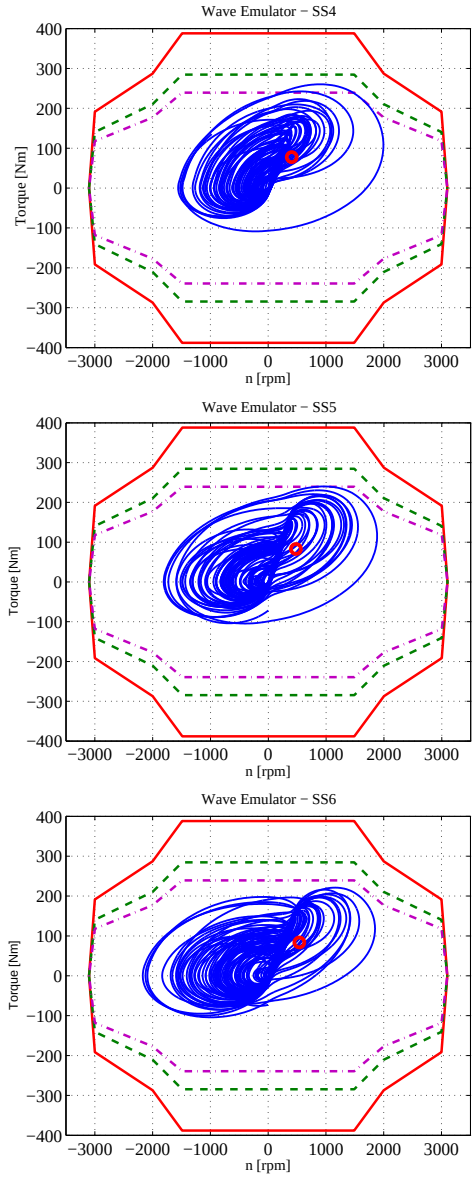

Figure 4.6: Torque-speed 200% working regions for three different machine sizes fitted above the most demanding load plots. Machine sizes of 18.5 kW (purple -.), 22 kW (green –) and 30 kW (red solid line). Load curves in blue solid line.

the load plots of the three most demanding sea states.

To provide ample margin in higher loads and increase experimental potential towards the future, for our setup a 30 kW 1500 rpm rated induction machine was

chosen. The red circle in Fig. 4.6 points at the RMS torque, which is in all cases lower than the nominal torque.

The inertia of the rotor can be decisive in the machine choice, as it should not exceed the value of the compensated reproduced inertia corresponding with the buoy mass and added mass. The calculation of this scaling is found in the next paragraph.

4.5.4 Wave Emulator inertia

As introduced earlier, a scaling similarity is achieved by including the buoy's mass m and added mass $m_{\mathrm{a},\infty}$ in the rotational inertia of the emulator machine. This avoids inertia compensation calculations with noisy acceleration signals.

In order to do so, the sum of the floater's mass and added mass must be converted to an equivalent inertia J_{eq} at the shaft of the PTO. In case of the Wave Pioneer, consisting of a cable on a drum connected with a gearbox to the PTO machine, this is done using the expression of Equation (4.4). Assuming this is done for the full scale floater, the inertia for the emulator side of the setup is scaled analogous to the calculation of the PTO inertia. Hence, the emulator's rotary inertia for a setup running at equal speed as the full scale is:

$$J_{\mathrm{comp\ emu}} = \frac{J_{\mathrm{eq}}}{\mu^{4.5}} \tag{4.19}$$

As for the PTO part, this equivalent inertia $J_{\mathrm{comp\ emu}}$ can be established with the total rotational inertia on the emulator side of the setup, i.e. machine rotor, coupling and half of the torque transducer's inertia, expanded with a flywheel to match the calculated value.

4.5.5 Overview of lab setup electrical machines and drives

Table 4.2 collects the specifications of the main components of the setup following the design concept described here. The electrical machines are intermittently used up to 200% of their nominal power. To ensure this super-rated operation, the drives are dimensioned to a rated power of at least 200% of the rated machine power since the overloading ability of the drives is much smaller than machines due to the limited thermal inertia of the power electronics. The final attained power for the drives was the first available power rating matching or exceeding the maximum used motor power.

4.6 Validation of the Emulator

To verify the accuracy of the wave emulator control and to validate the setup's design concept, experimental results of the lab setup have been compared with

Table 4.2: Overview of the setup's main specifications

	PTO	**Wave Emulator**
Electrical machine		
Rated power	11 kW	30 kW
Maximum power	22 kW	60 kW
Rated torque	71.5 Nm	194 Nm
Maximum torque	143 Nm	388 Nm
Rated speed	1500 rpm	1500 rpm
Maximum speed	3000 rpm	3000 rpm
Variable frequency drive		
Rated power	22 kW	75 kW

simulation results. The simulation model itself has earlier been validated by scaled wave flume tests by De Backer et al. [34], and this same hydrodynamic model is used to control the wave emulator (cfr. Equations (4.3) and (4.1)). By comparing the setup's motion with the computer simulation results, the validity of the design concept can be checked. The design concept includes the implementation of the masses as rotary inertias and the speed scaling compensation in the wave emulator. But also the practical implementation by means of the rapid control prototyping card, variable frequency drive and electrical machine are under evaluation in these tests at the same time. It is considered that the emulation of the WEC motion can be approved if the resulting speed curves of the setup and simulation correlate well when run with the same wave excitation force time series and same PTO force.

The PTO force is calculated following the control method of [16] described in Section 2.4, and is thus proportional to the actual speed and acceleration. This control method has been used in the setup as well. To focus on the accuracy of the emulator, the calculation of the PTO force has not been repeated in the simulations for this validation. Instead, a time series of the measured cable force of the setup (represented by the torque measurement) is used as input for the calculation of the equation of movement of the WEC. The time series of the wave exciting force for the simulation is equal as in the setup to use as a simulation input. Using this method, the virtual WEC in the simulation experiences the same forces as in the setup.

The analysis is done with the actual rotational speed of the setup, meaning that the speed of the simulation is recalculated to the corresponding compensated speed as defined in Equation (4.9).

The comparison has been carried out for all six sea states for a time window of approximately 8 minutes. For each sea state the WEC speed has been processed and examined by means of the PTO rpm. The rotational speeds of setup and sim-

ulation together with the rpm error from Equation (4.20) have been plotted in Fig. 4.7.

$$\mathrm{error}_{\mathrm{rpm}} = \mathrm{rpm}_{\mathrm{setup}} - \mathrm{rpm}_{\mathrm{sim\_comp}} \tag{4.20}$$

Subsequently histograms of the relative error show the distribution of the relative error magnitudes in Fig. 4.8.

$$\mathrm{Rel\_error}_{\mathrm{rpm}} = \frac{\mathrm{rpm}_{\mathrm{setup}} - \mathrm{rpm}_{\mathrm{sim\_comp}}}{\mathrm{rpm}_{\mathrm{sim\_comp}}} \tag{4.21}$$

Fig. 4.7 zooms in on 100s of the results. It indicates that the rpm error is relatively high in the lowest sea state, SS1. Once the load increases at higher sea states, the rpm error decreases resulting in a setup speed curve that approximates the simulated one. The absorbed power in SS1 is too low to have a net electrical energy production, consequently the difference in speed curve for this sea state can be ignored, because the sea state is irrelevant to draw any conclusions about the PTO. From SS2 on, the rpm error reduces significantly and the speed curves show a satisfying match.

The accuracy of the emulator depends on a number of factors. Firstly, the control is an open loop torque control and any deviation influences the setup's speed. When comparing against the simulations, it should be kept in mind that the friction of the bearings is not taken into account because measurements of the friction with peaks of 2Nm were categorised as negligible compared to peak set-point torques of up to 300Nm. Another potential cause of deviation is the possible difference between the final rotational inertia in the setup and the value from the datasheets due to minor modifications to the motor shaft (removal of fans and adding encoders) and couplings. This discrepancy in inertia is rather small and a more precise value could not be determined experimentally.

The convergence in the correlation can be seen in the histograms of the relative error from Equation (4.21) in Fig. 4.8.

4.7 Conclusions

In this chapter, a wave emulator PTO test setup is presented. A lab setup should be a tool for performing dynamic response tests and long duration tests for a power take-off system as if it was in a wave energy converter at sea.

The presented setup succeeds in providing an environment with equal normalised load conditions using a Froude scale model. This has been realised by implementing the hydrodynamic model of the floater in the setup to control the wave emulator in real-time and thus responding to the PTO actions. To avoid calculations with noisy acceleration signals, all mass terms of the hydrodynamic model have been represented physically as rotary inertias in the wave emulator.

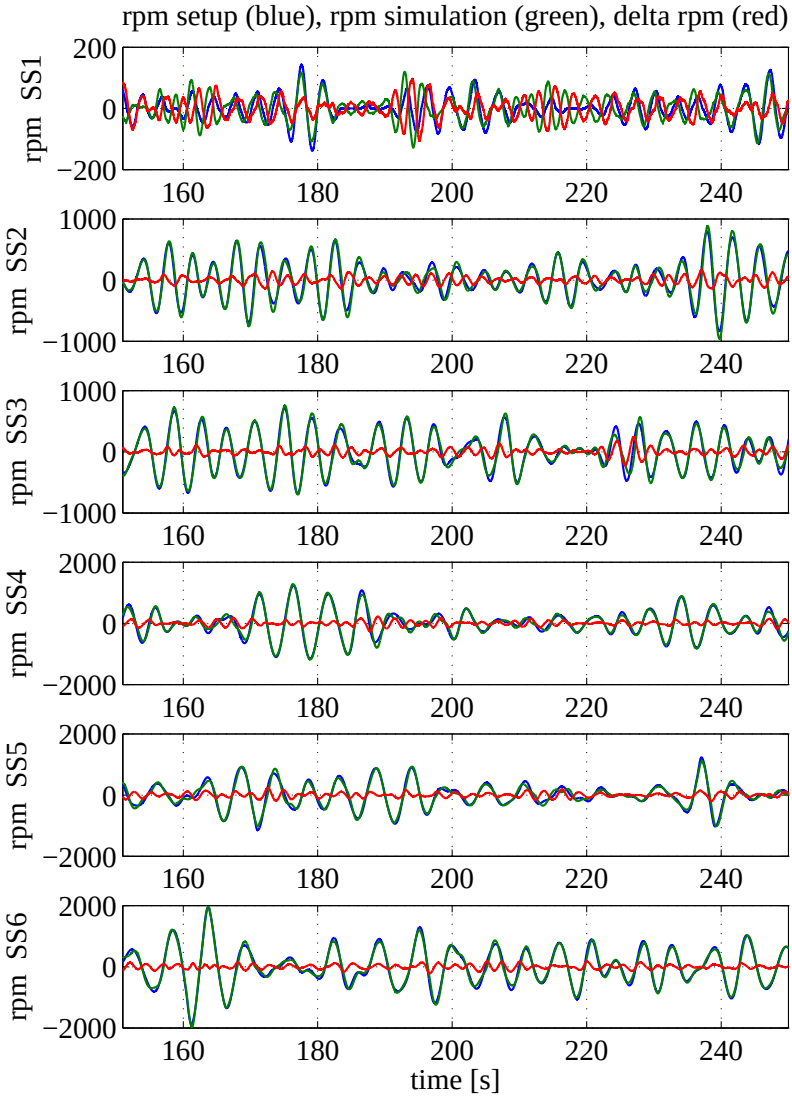

Figure 4.7: Plots of 100s of the rotational speed of setup (blue), simulation (green) and the speed error (red) for sea state 1 up to 6

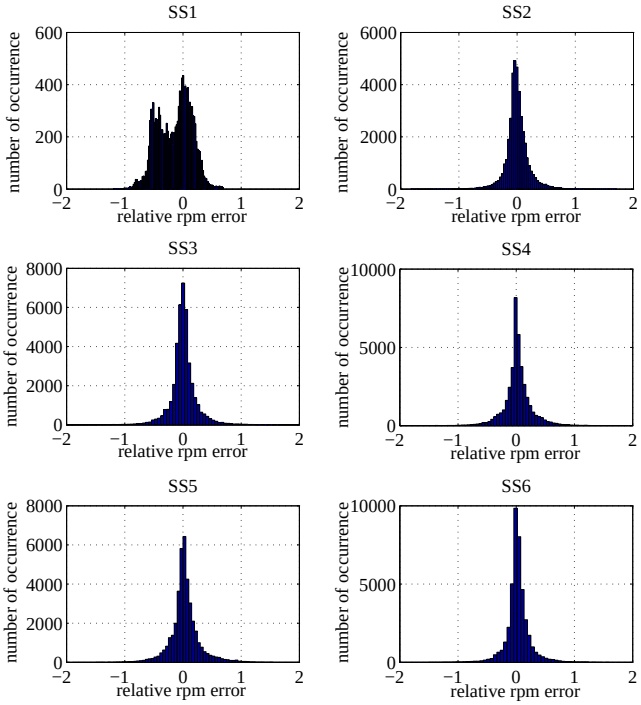

Figure 4.8: Histograms number of occurrence vs. relative rpm error per sea state

The undesired consequence of the increased rotational speed after Froude scaling has been dealt with by appointing extra inertia to the setup.

The experimental results of the wave emulator setup have been compared to simulation using equal power take-off forces on the scaled model. The control of the emulator uses the same hydrodynamic model as the computer simulations, so the comparison aims at validating the design concept of the wave emulator. The comparison showed good correlation for the shaft speed of the PTO for the significant sea states. This makes the proposed Wave Emulator a valuable tool in the development of power take-off systems for wave energy converters.

The intermittent and reciprocating motion accompanied with wave energy, is a considerable challenge for PTO designs. This setup provides an accessible environment to test a PTO with realistic loads before employing it for (expensive and less accessible) tests at sea.

Because the wave emulator is controlled in real-time by a hydrodynamic model, the actual PTO actions are considered. This enables the control parameters to be altered while the setup is running, but moreover that the wave emulator can be used with different PTO control strategies, without the need to change the emula-

tor's control. In fact, the setup is ideally suited to test a new - or changed - control strategy and evaluate the response of a real electromechanical drive train.

Next to suitability and durability tests, the setup can also be used to appraise the efficiency of a PTO. For example, the setup has been successfully used to confirm the quasi static efficiency model assumption of the electrical machine in Section 3.3.2.

5
A drum and cable based PTO

The work described in this chapter is a continuation and expansion of the research during FlanSea. Parts of the text have earlier been published in [63] and [35]. First, the mechanical layout of the drum and cable PTO is presented which is the basis for the simulation model subsequently explained. Next, several sensitivity analyses are discussed and processed, evaluating the resulting power and the energy yield for three (virtual) locations. Subsequently some optimisations are proposed to maximise the energy yield, or to minimise the installed power. A definite choice of PTO size will not be made. The methods proposed in this work can be the base for a techno-economic analysis to determine a viable PTO considering all corresponding costs (the PTO contributes for approximately 20% - 30% to the total manufacturing cost [30–32]) and revenues. The described analyses and optimisations offer a means to bring forth the sensitivities of a proposed PTO topology. The result is then a yearly energy yield curve - or map - for which every data-point corresponds to a PTO size which (or a relevant selection) can subsequently be provided with its according cost and revenue. The outcome will reveal the economic performance of every PTO size and might show a difference in optimum installed power depending on the location.

Although based on values of produced power, the presented analyses are not meant as an assessment of the exact amount of power (or energy) a certain PTO in the WEC can produce, but as a means to show the sensitivity of the studied control and hardware parameters, and to propose a method to design a PTO based on all boundary conditions such as PTO configuration, local wave climate and energy economics. The PTO sizing can subsequently be performed based on a techno-

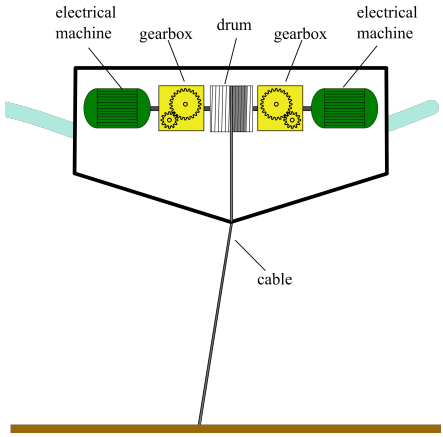

Figure 5.1: Schematic overview of the Wave Pioneer and the drum and cable PTO system: two electrical machines are connected to a drum by means of a gearbox.

economic optimum rather than on a energy maximisation at any cost.

5.1 Working principle and mathematical model

The principle is here explained based on the layout of the Wave Pioneer of the FlanSea project, where the PTO power was split up between two machines for practical reasons. The drum and cable PTO consists of a cable connected with the seabed. In the buoy, the cable is wound onto a drum and connected with two electrical machines through a gearbox as depicted in Fig. 5.1. The gearbox increases the working torque towards the drum, while decreasing the speed. The machines are connected to two variable frequency drives. The machine is subsequently connected to a variable frequency drive injecting the produced power either on a common DC-bus, or convert it to the frequency of the AC grid. This assembly of drum, gearbox, electrical machines and drives is referred to as the PTO system, and converts the power absorbed from the waves to electrical energy. When the buoy is pushed upwards by the wave motion, the cable is wound off and electricity is generated by applying a braking torque by the electrical machines. During the downward movement, the electrical machines act as motor to wind up the cable and keep it under tension, and apply reactive control to optimise the power absorption from the waves.

A purely heaving motion is assumed in the model, although this is not the case in reality for a buoy attached with a cable to the seabed.

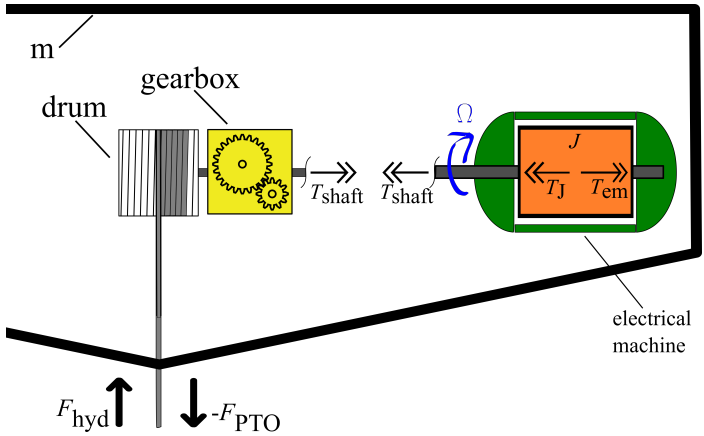

Figure 5.2: Schematic overview of the drum and cable PTO in the floater and the resulting PTO force together with the hydrodynamic force on the buoy

5.1.1 PTO model

In Fig. 5.2, a schematic overview of the PTO in the floater is given. In the Wave Pioneer two machines were installed, though this was mainly for practical reasons of fitting the PTO into the floater's diameter, therefore all further explanation is done in the assumption of one machine. (Still, the underlying simulation model assumes two machines, e.g. if said that the simulation is done with a machine of 280 kW, this is in fact split up in two machines of 140 kW in the simulation.) The electrical machine is connected through a gearbox to a drum. On the drum a cable is wound which is connected to the sea bottom. The torque on the shaft of the electrical machine is increased by the gearbox and subsequently translated to a force on the cable by the drum. The force on the cable is defined as the PTO force F_{PTO} and in the case of an ideal gearbox (or a direct drive concept without gearbox), it can be expressed as

$$F_{\mathrm{PTO}} = -\frac{R_{\mathrm{g}}}{r}\, T_{\mathrm{shaft}} \tag{5.1}$$

with R_{g} the gearbox ratio, r the radius of the drum and T_{shaft} the torque on the machine shaft. The minus sign in the expression originates from the fact that all forces are positive in upwards direction, as in [17], and the convention of having a positive electrical power when the machine generates electricity. And by maintaining the sign between the vertical buoy speed and the rotational speed, this implies a sign reversion between the torque and PTO force. The relation between the vertical floater speed dz/dt and the rotational speed is given by

$$\frac{dz}{dt} = \frac{n}{R_{\mathrm{g}}}\,\frac{2\pi r}{60}, \tag{5.2}$$

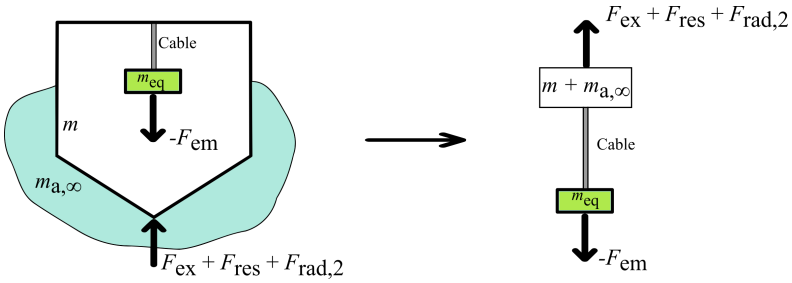

Figure 5.3: Linear representation of the PTO inertia and electromagnetic force.

with n the rotational speed of the machine in revolutions per minute (rpm), or expressed in radians per second as angular velocity $\Omega = n\ 2\pi/60$.

Taking the rotor inertia of the machine into account (and by extension the equivalent intertia of the entire mechanical drive train), the force can be expressed in relation to the electromagnetic torque T_{em} as

$$F_{\mathrm{PTO}} = -\frac{R_{\mathrm{g}}}{r}\left(T_{\mathrm{em}} - T_{\mathrm{J}}\right) \tag{5.3}$$

with $T_{\mathrm{J}} = -J\ d\Omega/dt$ the inertial torque of the rotor inertia. The electromagnetic torque is the torque controlled by the variable frequency drive and acts upon the machine rotor. As the dynamics in the wave application are relatively slow compared to the electrical dynamics, the requested electromagnetic torque is assumed to be immediately present. Internal friction in the machine, such as from the bearings, is neglected.

5.1.1.1 Equivalent linear PTO model

Because the hydrodynamic model is an equation of motion consisting of forces and linear movement, the PTO model has been translated to a linear equivalent to avoid unnecessary back and forth conversions between forces and torques and linear and rotational speeds during the simulation. The simulation time is important as the upcoming analyses and optimisations are done by iterative simulations.

Fig. 5.3 represents the linear equivalent of the rotary PTO comprising an electromagnetic force and mass inertia corresponding to the electromagnetic torque and rotary inertia respectively. In the linear equivalent model, the equivalent PTO mass is connected to the buoy mass through the main cable because it is only through this cable that the PTO can apply a force on the floater. The PTO force F_{PTO} is then

$$F_{\mathrm{PTO}} = F_{\mathrm{em}} - m_{\mathrm{eq}}\frac{d^2 z}{dt^2} \tag{5.4}$$

The electromagnetic force F_{em} is related to its torque equivalent through the gearbox ratio and drum radius:

$$F_{\mathrm{em}} = -\frac{R_{\mathrm{g}}}{r}\, T_{\mathrm{em}}. \tag{5.5}$$

m_{eq} is the equivalent mass for the rotary PTO inertia. For a PTO consisting of a drum with radius r and gearbox ratio R_{g} the equivalent mass is expressed as

$$m_{\mathrm{eq}} = J_{\mathrm{PTO}} \frac{R_{\mathrm{g}}^2}{r^2} \tag{5.6}$$

J_{PTO} is the total PTO inertia at the machine shaft, and comprises the complete drive train from machine up to gearbox and drum. It can be noticed that the influence of the gearbox ratio is significant towards the equivalent PTO mass as it is proportional with its square.

5.1.1.2 Gearbox efficiency

Taking the efficiency of the gearbox into account, the PTO force is expressed as

$$F_{\mathrm{PTO}} = \begin{cases} (F_{\mathrm{em}} - m_{\mathrm{eq}} \dfrac{d^2 z}{dt^2}) \cdot \dfrac{1}{\eta_{\mathrm{g}}} & \text{for } P_{\mathrm{em}} \geq 0: \text{ generating} \\ \\ (F_{\mathrm{em}} - m_{\mathrm{eq}} \dfrac{d^2 z}{dt^2}) \cdot \eta_{\mathrm{g}} & \text{for } P_{\mathrm{em}} < 0: \text{ motoring} \end{cases} \tag{5.7}$$

With $\eta_{\mathrm{g}} < 1$ the gearbox efficiency. From Equation 5.7 can be understood that the torque at the drum side is increased by the gearbox losses with respect to the torque on the machine shaft in case power flows towards the machine, i.e. it will be generating, and if power flows from the machine (as motor) towards the drum, the drum torque is decreased by the gearbox losses.

The gearbox efficiency value is read from a lookup table for each actual operation point during the simulation. The efficiency map is based on a measured map for a 2 stage helical bevel transmission presented in [2]. The efficiency map is not a representation of the most fit gearbox for a wave energy converter (in fact the nominal efficiency might be rather low for the highest installed powers simulated in this work), but it is a step towards realistic simulation of an electromechanical PTO drive train, to demonstrate the influence on the net generated energy. The map displayed in Fig. 5.4 shows a significant dependency on the torque. Even though the efficiency is relatively flat above 20% of the rated torque, it illustrates the importance of the use of a map rather than a fixed efficiency value for a transmission stage in the PTO.

Because the maximum shaft torque of the machine can be approximately 1.5 times higher than the maximum electromagnetic torque due to the inertia torque

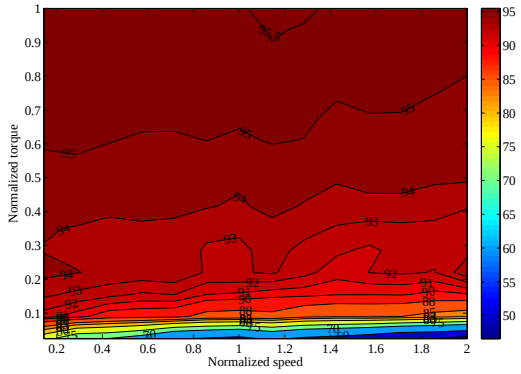

Figure 5.4: Efficiency map of a 2 stage helical bevel transmission as a function of normalised speed and normalised torque (Source: [2])

T_{J}, a normalised torque of 1 for the gearbox corresponds to 3 times the rated machine torque, as the machine is used up to 200% of its rated torque.

5.2 PTO control

The general PTO control based on the mass-spring-damper system is explained in Chapter 2 Section 2.4. Each PTO topology might have specific requirements or variations on the theoretical external PTO force, with characteristic consequences. For the drum and cable PTO this is described in the following sections.

5.2.1 Specific control for a drum and cable PTO

5.2.1.1 Unidirectional forces due to cable

With this type of PTO composed of a drum and cable, the only way to exert a PTO force on the WEC is through the cable providing only downward forces on the buoy. Consequently the tuning force can be applied only when the acceleration is positive (i.e. directed upwards) and the damping force only when the velocity is positive. Additionally, an extra force F_{tense} should ensure that the cable remains under tension at all times. The total required electromagnetic force can thus be expressed as:

$$F_{\text{em}} = F_{\text{damp}}\big|_{\frac{dz}{dt}>0} + F_{\text{tun}}\big|_{\frac{d^2z}{dt^2}>0} + F_{\text{tense}}\big|_{\frac{d^2z}{dt^2}<0} \tag{5.8}$$

F_{tense} is the force required to keep the cable under tension when this is not accomplished by the hydrodynamic force. It is reminded that at some instances of the

wave cycle, the tuning action of F_{tun} will result in a power flow from the PTO towards the hydrodynamic system, thus the electrical machine will act as a motor.

5.2.1.2 Keeping the cable under tension

Assuming initially a taut cable, buoy at standstill and starting an upwards acceleration, i.e. $d^2z/dt^2 > 0$, then the PTO inertia will be accelerated by the force on the cable, and the cable will be unwound from the drum. When the buoy starts to decelerate, the only way to decelerate the PTO inertia is by an electromagnetic torque of the machine, as the cable can only transfer force in one direction. If an adequate PTO torque is not applied, the cable will continue to wind off as the PTO will not be decelerated sufficiently.

Decelerating the PTO inertia

This control consists of a pragmatic solution to induce the same deceleration of the PTO inertia as the buoy when the buoy acceleration is negative, supplemented with an extra force:

$$F_{\text{tense}} = m_{\text{eq}} \frac{d^2z}{dt^2} - F_{\text{windup}}. \tag{5.9}$$

The term $m_{\text{eq}}\ d^2z/dt^2$ of Equation (5.9) can also be seen as a compensation to eliminate the inertial force of Equation (5.4). F_{windup} is a constant value that should at least encompass the weight of the cable pulling on the drum.

The acceleration d^2z/dt^2 used in this model is technically the buoy acceleration, and not really the acceleration of the PTO, as this model does not include a separate equation of motion for the PTO dynamics. By applying the above force F_{tense} of Equation (5.9), the PTO is assumed to follow the buoy's motion, and therefore the model *assumes* that the cable is kept under tension at all times. Technically this model can still result in a negative cable force. Nevertheless it is an acceptable first approach for this PTO topology to assess its potential energy production and dimensions of the PTO.

5.2.2 Influence of control parameters on power absorption

Even though the philosophy of the described control strategy is based on the response of the system excited by regular waves, and irregular waves occurring in real seas cannot bring the WEC in resonance, an optimum combination of the parameters b_{ext} and m_{sup} can also be found for irregular waves by running iterative simulations. To maximise the power absorption in every sea state, an adequate control with carefully chosen control parameters are indispensable [16, 20, 21, 64].

In a first assessment of the system, the maximum power that can be absorbed by the PTO from the waves has been evaluated. This is the mean mechanical power

absorbed by the PTO from the waves, thus the PTO efficiency is not yet taken into account. It is calculated by multiplying the PTO force F_{PTO} from Equation (5.4), i.e. the force on the cable, with the buoy speed dz/dt.

To illustrate the influence of the control parameters on the absorbed power P_{abs}, time simulations using the described model were run to estimate the absorbed power per sea state by calculating the hydrodynamic response of the WEC. A first simulation set has been performed under the assumptions that an unlimited PTO force is available, hence the desired force of Equation (5.8) can always be applied and the PTO inertia is set to zero. For each sea state a multitude of combinations of values for b_{ext} and m_{sup} are simulated by iteratively changing them within a predefined range. The results are visualised in the colour plots of Fig. 5.5 where the absorbed power versus the control parameters b_{ext} and m_{sup} is plotted per sea state, a presentation method also used in [65]. Every colour plot consists of approximately 100 simulations, depending on the resolution and range. Next to the power, other important system parameters are analysed for every combination: in addition to the floater's boundaries and PTO force constraint already analysed in [65] and [17], the PTO constraints have been extended in the examinations of this work and are taken into account from Section 5.3 onwards.

Evaluating the power

The maximum absorbed power that can be reached is marked with a blue circle in each of the plots. The coordinates of the blue circle correspond with the optimal values for m_{sup} and b_{ext}. From the figure can be seen that the quantity of absorbed power is heavily dependent on the control parameters. If not carefully set, the absorbed power drops significantly. The minimum scale of the colour bar is set at 0 to optimise the contrast, but negative values occur at very low values for b_{ext}.

Taking account for the floater constraints

The buoy has a freeboard of 2.75 meter above the still water line (see drawing of Fig. 2.8). During operation, the buoy may not be overtopped by the water, i.e. a sinkage of more than 2.75 m, as this will heavily affect the subsequent upwards movement of the buoy and is not desirable from operational point of view. Therefore a black contour plot indicates from where on the sinkage limit is reached. Moreover, the simulation model does not account for the hydrodynamic behaviour beyond the maximum sinkage, hence results from simulations that exceed the sinkage limit are of no physical significance and are therefore omitted and left blank in Fig. 5.5. The limit is set such that not a single exceedance of the sinkage in the complete simulation of irregular waves is allowed.

The first part of the tuning action occurs during the second half of the downwards movement ($dz/dt < 0$ and $d^2z/dt^2 > 0$), and hence increases the sinkage of the buoy as the force is directed downwards. Fig. 5.5 indeed shows that the

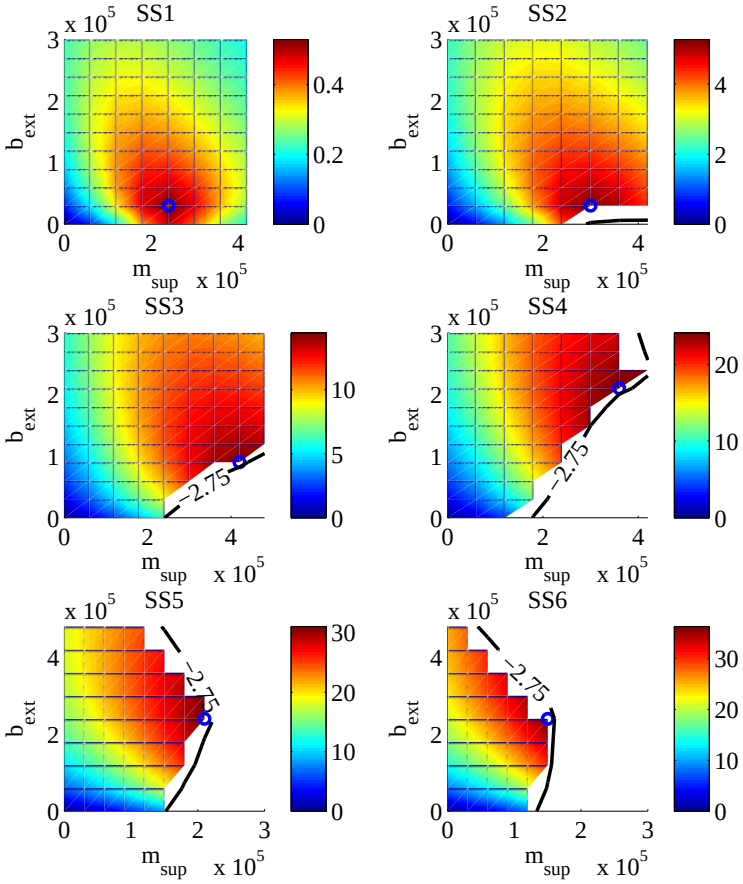

Figure 5.5: Absorbed power [kW] vs. control parameters m_{sup} and b_{ext} for an unlimited available PTO force, contours for maximum sinkage (black).
(Note the different axis scales for some of the plots.)

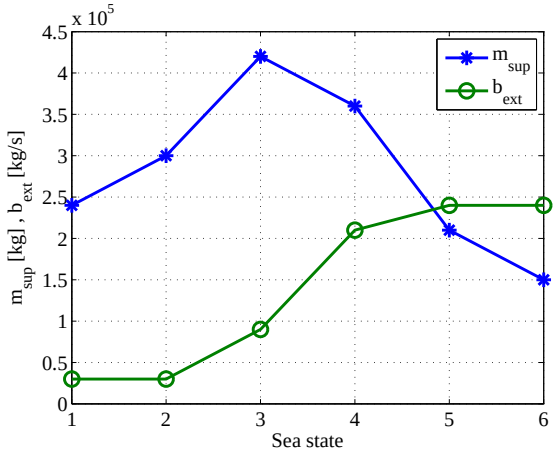

Figure 5.6: Optimal values for the control parameters m_{sup} and b_{ext} to maximise the absorbed power for the different sea states for an unlimited PTO force without inertia

sinkage limit is reached at higher values for m_{sup}, especially for the higher sea states.

Another constraint of the floater is that it might lift out of the water during the upwards movement to subsequently land in a hard manner back in the water, which is called slamming. Slamming causes unwanted high impact forces on the body and system and is thus to be avoided. The accompanying constraint is defined as the maximum *lift* and is 2.4 m for the buoy under study. Because the drum and cable PTO can only damp the floater in the upwards direction, the buoy is damped to a degree that the lift constraint is never reached for this PTO topology.

As the sea state changes, the optimal control parameters values differ, as plotted in Fig. 5.6. It shows the importance of using the appropriate parameters to prevent exceeding the maximum sinkage, and not at least to optimise the energy yield in every sea state. It can be noticed that the value of m_{sup} is affected by the reaching of the sinkage limit.

Effect of tuning

As explained in Chapter 2 Section 2.4, b_{ext} is the external damping factor that determines the amount of PTO damping and m_{sup} is the factor that determines the supplementary mass virtually added by the PTO force to tune the natural frequency of the floater towards the wave frequency. A pure damping strategy can be achieved by setting m_{sup} equal to 0. The corresponding power production can be read from the colour plots on the vertical axis, and an optimum b_{ext} can then be chosen for pure damping for each sea state. Comparing these values with the power reached with an optimal combination of m_{sup} and b_{ext} as plotted in the

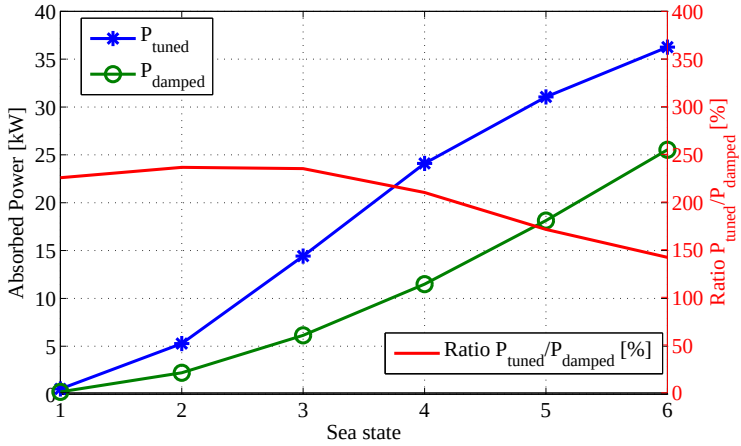

Figure 5.7: The absorbed power with a tuning strategy compared with the absorbed power with a purely damping control strategy for an unlimited PTO (left axis in [kW]), together with the ratio between the two (right axis in [%]).

power curves of Fig. 5.7, it can be concluded that the effect of the reactive control by means of a supplementary mass is significant and reaches absorbed powers of up to 230% compared to pure damping.

It should be remembered that this analysis is made on the *absorbed* power, and that PTO efficiencies are not yet taken into account. Because the reactive control implies a power flow from the PTO towards the hydrodynamic system at some instances of the wave cycle, it is to be expected that the PTO efficiency will influence the effectiveness of the tuning. This will be studied further in Section 5.3.2.

5.2.3 Time course of power and buoy movement

In Fig. 5.8 the position, speed and acceleration of the buoy are plotted together with the according PTO force and the resulting absorbed power as a function of the time. The plots illustrate the high irregularity of the wave energy system, resulting in a very variable power shape. There is a high peak-to-mean ratio of 26 for the shown sea state 3 with the unlimited PTO, there are peaks of 374 kW and a mean power of 14.4 kW. The invested (negative) power shows lower peaks, but still significantly crossing 200 kW. Characteristic for the PTO topology of drum and cable is the purely downwards directed PTO force resulting in power absorption in the upwards direction only.

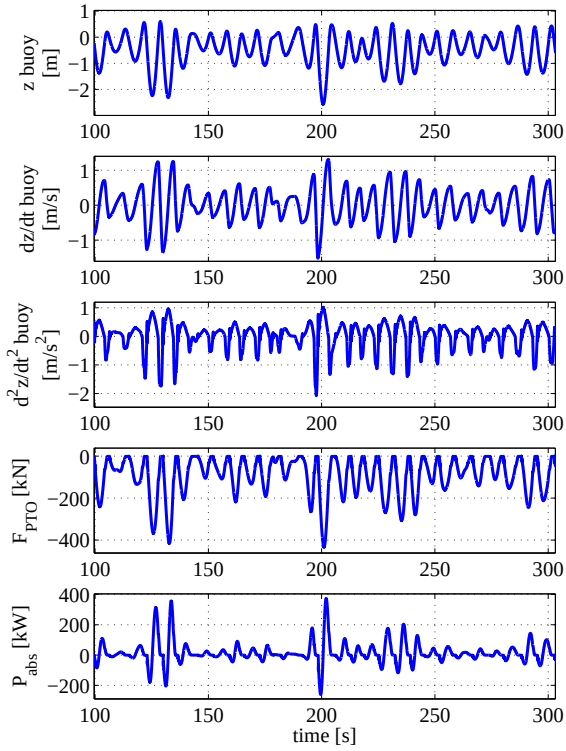

Figure 5.8: Plots of the buoy position, speed and acceleration together with the absorbed power vs. time for 200 seconds of the simulation for SS3.

5.3 Introducing PTO dynamics and efficiency

Based on the maximum required PTO force from the analysis with the unlimited PTO, a realistic PTO consisting of a machine and gearbox can be defined. The rated speed of the machine and gearbox ratio is chosen such that an ample margin in available speed is expected. As described in Section 3.2, the machine is used up to 200% of its rated torque and speed because the movement is highly variable. This results in a significant reduction of the required installed power in comparison with a machine only used up to the rated power. To have ample margin for the speed, a gearbox ratio of 37.3 and drum radius of 0.4 m is chosen with a 1500 rpm rated machine. Consequently, a machine power of 280 kW is required to apply the maximum PTO force that was necessary in the unlimited PTO analyses.

The control is such that the desired electromagnetic PTO force is calculated based on the actual speed and acceleration (Equation (5.8)), and capped by the

maximum available torque defined by the working range of Fig. 3.2 if necessary.

The rated machine powers used in this work do not necessarily correspond with existing off-the-shelf available machines, as the power values are used to demonstrate their influence rather than as a commercially available choice that can/should be made. The corresponding rotor inertias are therefore a result of interpolation of realistic datasheet values for existing power output values. The used data are taken from induction machines (IM) for 1500 rpm rated machines [66], and from permanent magnet synchronous machines (PMSM) for the studied direct drive cases with rated speed of 100 rpm or lower [67].

5.3.1 Influence of PTO dynamics

The simulation model is run with the given installed power and transmission ratio, and a rotor inertia of 6.4 kgm^2 (based on two machines of 140 kW with an inertia of 3.2 kgm^2 [66]). The colour plots of Fig. 5.9 show equal values for the mean absorbed power per sea state as for the unlimited PTO (Fig. 5.5 and Fig. 5.6). What can be observed, and separately plotted in Fig. 5.10, is that the optimal values for the PTO damping b_{ext} are higher for this realistic PTO than for the unlimited PTO. Contrarily, the optimal values for the supplementary mass m_{sup} are lower. This decrease in motor tuning can be attributed to the PTO inertia, which has an equivalent mass of 55 600 kg in the linear mass-force model. Indeed, the PTO inertia helps to tune the natural frequency of the WEC towards the frequency of the incoming waves, as it adds to the floater inertia when it is accelerated by the hydrodynamic force through the cable when the acceleration is positive. Therefore, it is interesting to study the sensitivity of the PTO inertia towards the energy output, which can be found in Section 5.6.4.

When the actual electromagnetic force is plotted next to the PTO force in Fig. 5.11, it can be noticed that the force towards the cable is indeed significantly increased due to the inertial torque of the PTO inertia when accelerating. On the other hand, when the acceleration is negative, the PTO force is lower than the electromagnetic force because a part of it is needed to decelerate the PTO inertia. At around 200 seconds, it can be noticed that the electromagnetic force F_{em} is capped, corresponding with the maximum available torque of the machine.

5.3.2 Influence of PTO efficiency

Up to this point, all analyses were done on the absorbed power, the mechanical power on the PTO shaft. However, it is clear that the electrical power that can be injected into the electrical grid is of higher concern. Therefore the simulation model has been extended with the efficiency maps of the different PTO components as described in Sections 3.3, 3.4 and 5.1.1.2 for machine, drive and gearbox respectively.

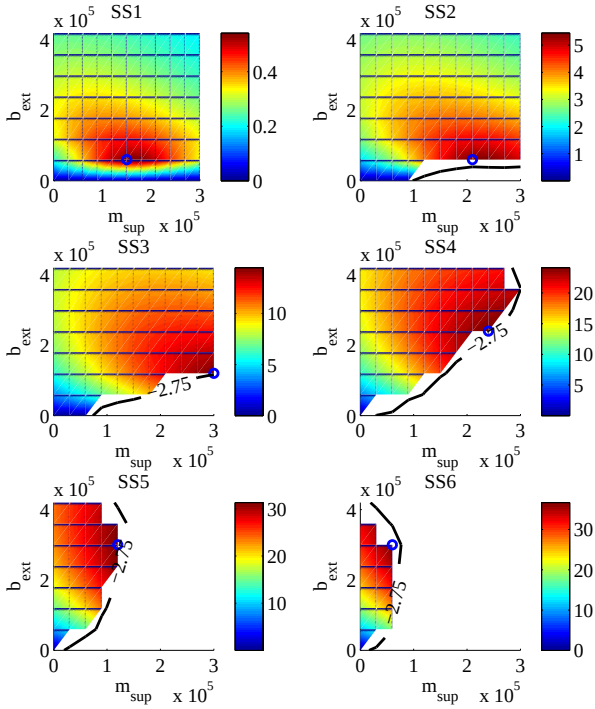

Figure 5.9: Absorbed power [kW] vs. control parameters m_{sup} and b_{ext} for a 280kW PTO, contours for maximum sinkage (black).

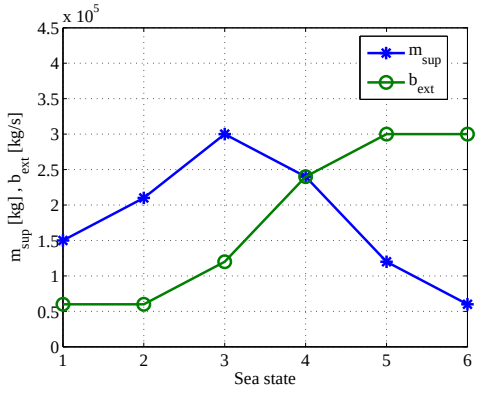

Figure 5.10: Optimal values for the control parameters m_{sup} and b_{ext} to maximise the absorbed power for the different sea states for a 280kW PTO

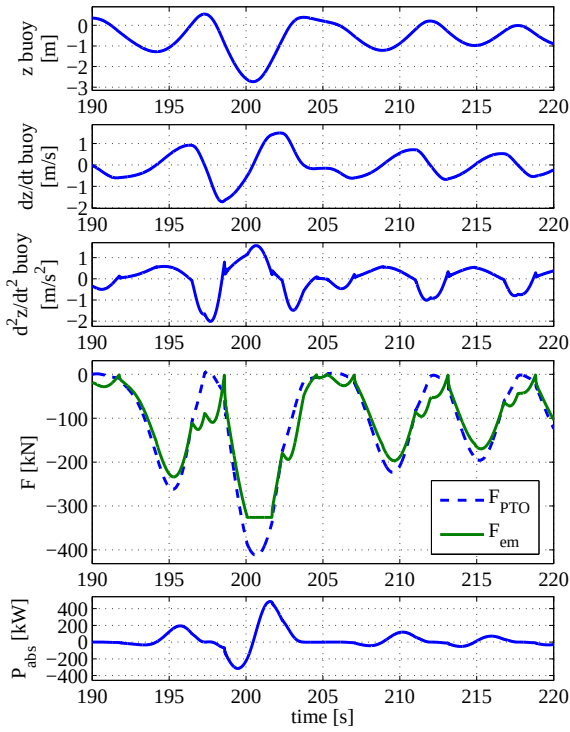

Figure 5.11: Buoy movement and PTO force together with the electromagnetic force.

For the efficiency of the electrical machine, maps are generated based on two different machine topologies, the A map variants are based on an induction machine (IM) and the B map variants are based on a permanent magnet synchronous machine (PMSM), both from [1]. For each machine topology, the maximum efficiency of the map has been rescaled in four steps of approximately 1% to analyse the influence of the nominal efficiency's magnitude. Additionally, the shape of the efficiency maps of the two machine topologies is rather different, enabling the assessment of the sensitivity thereof on the electrical output of the WEC. The maps and their variants are discussed and displayed in Chapter 3 Section 3.3.3.

Next to the machine efficiency, the gearbox efficiency is taken into account using the map displayed in Fig. 5.4 and a fixed drive efficiency as described in Section 3.4. A machine power of 280 kW is used.

5.3.2.1 Effect on control parameters

A first simulation run analysing the electrical output has been executed for the $A1$ efficiency case, which maximum efficiency of 95.7 % corresponds with the nominal efficiency of a 1500 rpm IE4 induction machine from catalogue [66]. The resulting colour plots for the mean electrical power at the grid side of the variable frequency drive for sea states 1 to 6 are presented in Fig. 5.12.

Comparing these results with the results of Fig. 5.9, it can be noticed that, next to the fact that the maximum reachable power value is lower due to the losses in the PTO drive train, the optimum value for m_{sup} is lower for sea states 1-3 and the external PTO damping is higher. Both control parameters are plotted in Fig. 5.13 vs the sea state. Once the PTO efficiency is taken into account, it becomes clear that this has an influence on the tuning capacity, which was also observed by [41]. This is due to the electrical energy required to be invested during a part of the tuning cycle. This so called reactive power passes two times by the 'pay desk' of the losses before it is again converted to electricity. Luckily it is accompanied with a gain in net produced electrical energy which is still larger than in the pure damping case, as illustrated in the power curves of Fig. 5.14. Nevertheless, it should be noted that this gain decreases when the efficiency of the PTO drops. At very low PTO efficiencies, tuning becomes irrelevant, as it might even decrease the mean electrical power compared to pure damping.

Because the control parameters for SS4-6 are limited by the sinkage constraint, the influence is in these sea states not visible in the parameter values plotted in Fig. 5.13. For SS1-3, the optimum is found in the middle of the domain, hence there is no constraint with regard to sinkage.

5.3.2.2 Effect on produced power

Nominal efficiency

The same analysis has been executed for the other 7 efficiency map variants described in Chapter 3 Section 3.3.3. The results are plotted in Fig. 5.15 and the values are collected in Tables 5.1 and 5.2. The mean electrical power for the A map variants decreases with approximately 3.5% per 1% lower nominal efficiency in SS3 and with 2.5% in SS5. For the B variants, the difference in SS3 is even slightly more pronounced, and similar in SS5. It is clear that a step of 'only' 1% in the nominal efficiency has an amplified repercussion on the power output of the system.

The electrical power of SS1 is much too low to deliver a contribution towards the grid. Considering all possible uncertainties of the model, and taking into account that the model does not include any base load losses e.g. for auxiliaries, the results for SS1 are not always shown in further analyses.

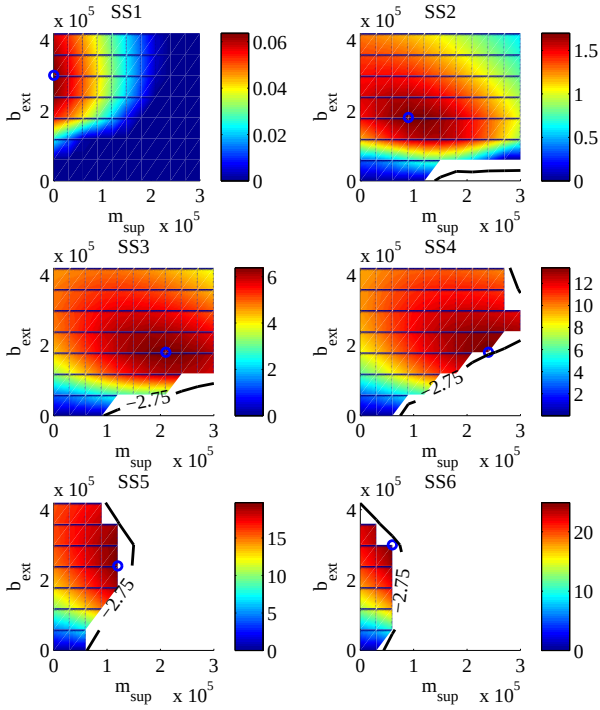

Figure 5.12: Electrical power [kW] vs. control parameters m_{sup} and b_{ext} for a 280kW PTO with gearbox and $A1$ machine efficiency map, contours for maximum sinkage (black).

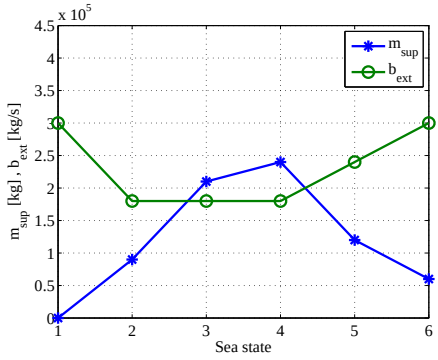

Figure 5.13: Optimal values for the control parameters m_{sup} and b_{ext} to maximise the electrical power for the different sea states for a 280kW PTO with gearbox and $A1$ machine efficiency map

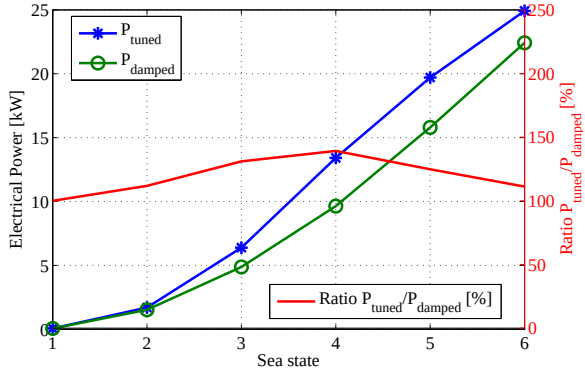

Figure 5.14: The electrical power with a tuning strategy compared with the electrical power with a purely damping control strategy, together with the ratio between the two, both for an $A1$ machine.

Table 5.1: Difference in mean electrical power between the 4 A efficiency map variants

SS	$A1$ P_{el} [kW]	$A2$ % of $A1$	$A3$ % of $A1$	$A4$ % of $A1$
1	0.1	95.4	90.7	86.0
2	1.7	96.6	93.3	89.8
3	6.4	96.5	93.0	89.4
4	13.4	96.6	93.2	89.8
5	19.7	97.5	95.0	92.5
6	24.9	97.9	95.8	93.7

Table 5.2: Difference in mean electrical power between the 4 B efficiency map variants

SS	$B1$ P_{el} [kW]	$B2$ % of $B1$	$B3$ % of $B1$	$B4$ % of $B1$
1	0.2	96.4	92.0	88.2
2	2.8	96.4	92.2	88.2
3	9.3	96.1	92.0	88.7
4	17.9	97.2	94.0	90.9
5	24.3	97.8	95.3	92.9
6	29.6	98.0	95.6	93.4

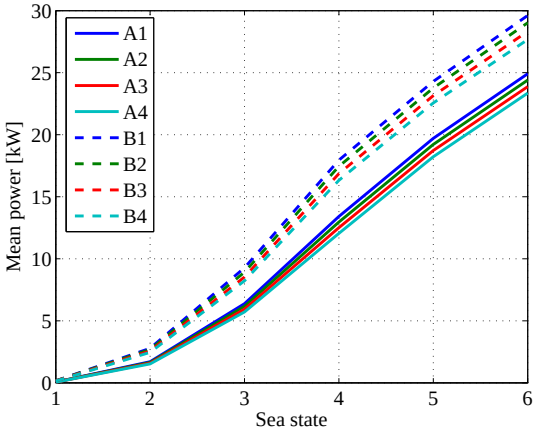

Figure 5.15: Mean electrical power vs. sea state for the 8 efficiency map variants for a 280kW PTO with gearbox

Shape of the efficiency map

The shape of the efficiency map, i.e. the flatness, has undoubtedly a huge influence on the resulting electrical power. In Fig. 5.15 all B variants show a significant higher mean power in all sea states, despite the fact that the nominal efficiency of $A1$ is equal to $B3$ and even 1% higher than $B4$. Still, the mean electrical power of both the $B3$ and $B4$ variants is considerably higher than for $A1$. Table 5.3 compares the electrical power P_{el} of the $A1$ and $B3$ maps: the electrical power of $B3$ ranges from 114% up to 151% of the values of $A1$ for SS6 and SS2 respectively. This is mainly due to a better conversion of mechanical towards electrical energy, but the higher efficiency is also beneficial for the tuning capability allowing more power to be absorbed from the waves in SS2 and SS3 in the case of a $B3$ machine. Indeed, Fig. 5.16 shows higher values for the optimum m_{sup} than for the $A1$ case plotted in Fig. 5.13. Still, the main reason can be found in the conversion from mechanical towards electrical energy as the values in column 8 and 9 indicate. The ratio of the mean elecrical power over the mean absorbed power $P_{\mathrm{el}}/P_{\mathrm{abs}}$ indicates the average PTO efficiency. For the $B3$ case, the average efficiency is approximately 9% to 15% higher than for the $A1$ case. It may be clear that the choice of a PTO and/or its components must not be done based on the efficiency at nominal operating conditions for an application such as wave energy with highly intermittent operation of which the usage range in terms of torque and speed is relatively large.

The average efficiency values between 46% and 68% for the $A1$ case, and between 58% and 77% for the $B3$ case should help to realise that feasibility assessments of a WEC based on absorbed power are highly overrated.

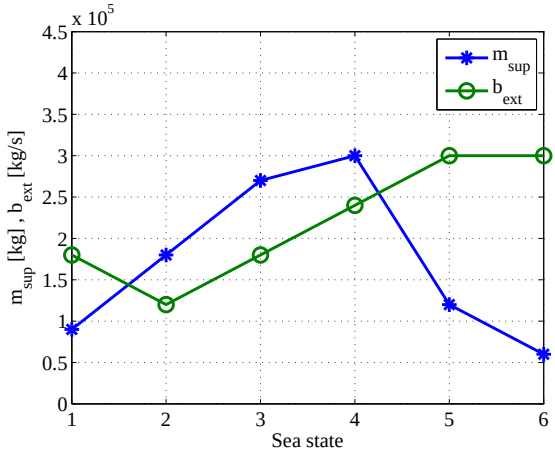

Figure 5.16: Optimal values for the control parameters m_{sup} and b_{ext} to maximise the electrical power for the different sea states for a 280 kW PTO with gearbox and $B3$ machine efficiency map

Table 5.3: Comparison of the electrical power P_{el} and absorbed power P_{abs} between $A1$ and $B3$ efficiency maps with equal nominal efficiency but different shape, and the resulting average PTO efficiency $P_{\mathrm{el}}/P_{\mathrm{abs}}$, for a 280 kW PTO with gearbox

	P_{el} [kW]		$B3$	P_{abs} [kW]		$B3$	P_{el} / P_{abs} [%]	
SS	$A1$	$B3$	% of $A1$	$A1$	$B3$	% of $A1$	$A1$	$B3$
2	1.7	2.6	151	3.7	4.4	120	46.3	58.3
3	6.4	8.5	134	12.2	12.7	104	52.3	67.3
4	13.4	16.9	126	23.9	23.9	100	56.2	70.7
5	19.7	23.1	117	30.6	30.6	100	64.4	75.6
6	24.9	28.3	114	36.7	36.7	100	67.8	77.1

5.4 Influence of PTO installed power

All simulations so far have been performed with a PTO where the absorbed power was not limited by the available PTO force. The 280 kW machine was chosen based on the maximum required PTO force resulting from the simulations with an unlimited PTO force. The floater constraint of sinkage was the only limit encountered until now.

Although this installed power of 280 kW might be the largest required to absorb the maximum with this floater geometry and the used control strategy, it might not be the techno-economic optimum. Therefore, a sensitivity analysis on the installed power is performed to assess its influence on the power production. For each installed power and every sea state, the control parameters m_{sup} and b_{ext}

Table 5.4: The six power steps [kW] for the sensitivity analysis on rated power.

	$P1$	$P2$	$P3$	$P4$	$P5$	$P6$
Rated power [kW]	46	94	140	188	234	280

have been chosen to maximise the electrical power output P_{el}, accounting for the floater and PTO constraints. A comparable analysis at smaller scale has been done by [39] for 4 power steps, but only 3 sets of control parameters and in only one sea state.

It should be noted that in fact the analysis of this section comes down to a sensitivity on the available electromagnetic force (F_{em}) because the rated speed is kept fixed, but the installed power is taken as criterion because it has a direct link to the cost of the PTO. Anyhow, the installed power is in direct relation to the force through the transmission ratio and rated speed of the machine.

Power steps

The analysis has been done for 6 steps in power for 1500 rpm machines, a gearbox ratio of 37.3 and a drum radius of 0.4 m. The resulting powers $P1$ to $P6$ range from 46 kW to 280 kW as listed in Table 5.4. The results using the $A1$ map are illustrated in the colour plots of Fig. 5.17. In addition to the mean electrical power as colour plot, the system constraints are plotted as contours. The black contours delineate the validity range of the model by the sinkage limit and impose a restriction on the control parameters. Another hydrodynamic constraint is the lift (blue), which prevents the buoy from jumping out of the water followed by slamming back accompanied with high impact forces on the buoy shell which should be avoided. Because this PTO topology of cable and drum applies only a damping force in the upwards movement, the upwards movement is damped in such a way that the lift constraint is not reached in the valid region of the model.

PTO constraints

More importantly for this analysis, contour lines have been added corresponding with the PTO constraints. An important machine constraint is its thermal limit. The machine is used up to 200% of its rated torque, which can be done by monitoring the resulting RMS torque over a moving (machine-specific) time window, or by measuring the temperature of the machine to prevent exceedance of the maximum temperature.. To avoid the machine from overheating in this work, the RMS torque must stay below the rated torque. Therefore the boundary is indicated in magenta where the RMS torque T_{rms} of the simulation run exceeds the nominal torque of the corresponding machine. The other machine limit is the maximum speed, the crossing of 200 % of the rated speed is marked here in white (the value

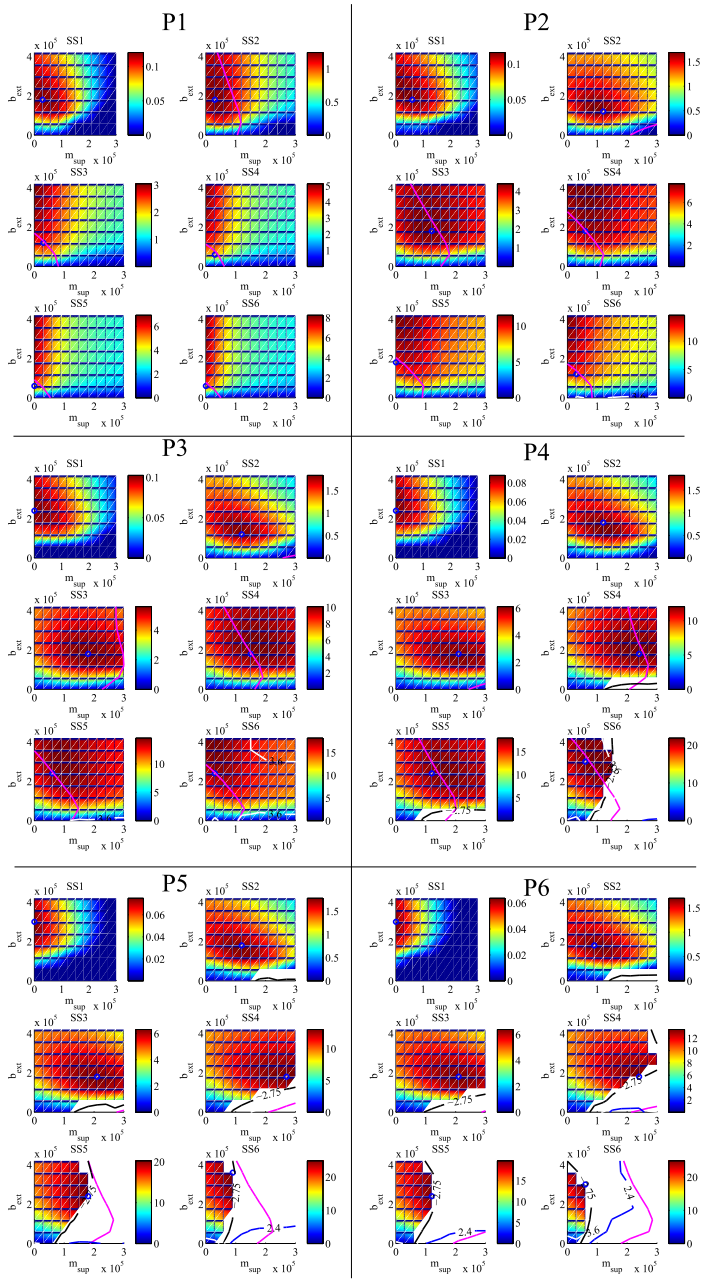

Figure 5.17: Electrical power [kW] vs. control parameters m_{sup} and b_{ext} for the 6 steps of PTO power with gearbox and $A1$ machine efficiency map, contours for maximum sinkage (black), maximum speed (white), maximum RMS torque (magenta) and lift (blue).

of 3.6 on the figure, is the related buoy speed of 3.6 m/s).

It is not necessary to choose the control parameters to limit the maximum electromagnetic torque, as the operational working range of the machine is implemented in the simulation model.

Effect on the control parameters

When the installed power is high, $P5$ and $P6$, the only reached limit is the sinkage constraint, as visible in Fig. 5.17. When the installed power drops, the RMS torque constraint takes over to decide on the control parameters. Consequently it can be understood that the mean power is not only influenced by the lower available force, but also by this suboptimal control to prevent the machine from overheating.

Overview of the results

Although the plots of Fig. 5.17 show the mean electrical power per installed power for all sea states, and show where the constraints are reached, an overview such as plotted in Fig. 5.18 gives more insight in the relation between installed power, mean output power and constraints.

The first figure shows the relation between the installed power and the mean electrical output power per sea state. The plots below show the different constraints of the system as the normalised value, i.e. the ratio relative to the limit.

The mean electrical power increases strongly with higher installed power. For SS5 and SS6 the rise is capped due to the reaching of the sinkage constraint as can be seen in the plots of the sinkage. The slope is less steep for SS3 and SS4. For SS3, the $P6$ outputs a power that is 5 % higher than with a $P4$, while the installed power is one and a half times larger.

From the constraint plots can be derived that the sinkage constraint is only reached in the higher sea states from SS4 onwards and from $P5$ and higher. The lift constraint is never an issue for this PTO topology. The machine constraints of RMS torque and maximum rotational speed give an interesting view on the used capacity of the machine power. From $P5$ on, the margin towards the RMS torque starts to grow even for SS4, SS5 and SS6. Hence, above $P5$ the machine is never used at its maximum thermal capacity.

5.5 Influence of location

The power curve per sea state of a WEC shows the conversion performance in relation to the sea states. Although this is an essential step in the assessment of the technology, it is the produced (yearly) energy that is of concern to make a WEC viable. Dimensioning the PTO to maximise the power conversion in the highest sea states because they provide the highest power, might not be the way to go, as a low yearly occurrence frequency might reduce the importance of these

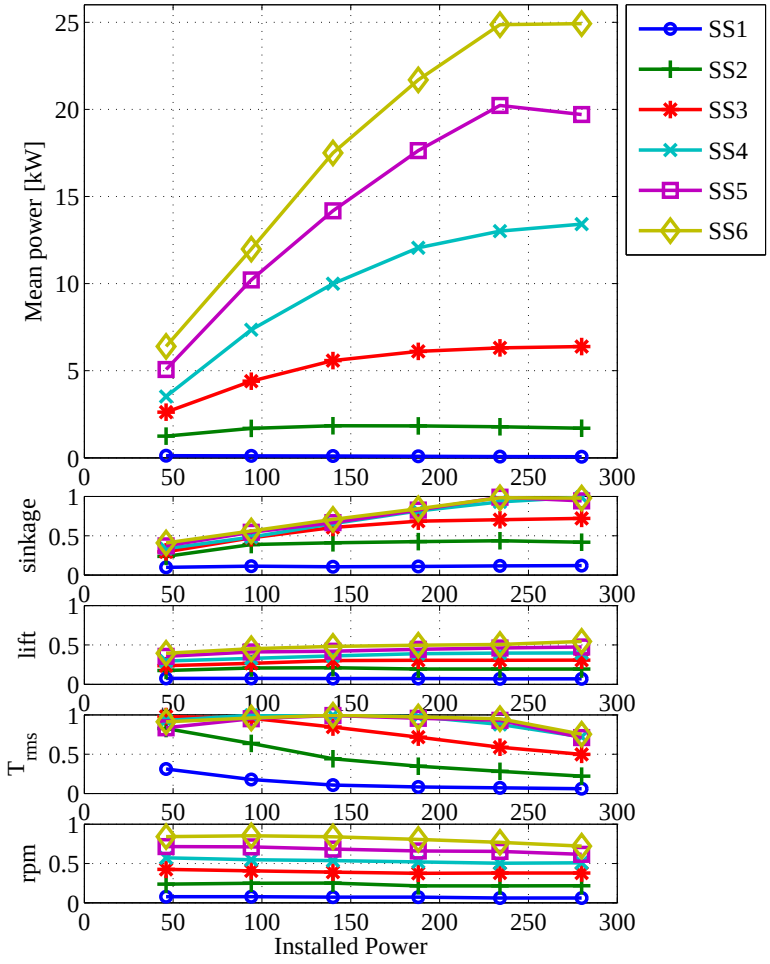

Figure 5.18: Mean electrical power per sea state vs. installed power with normalised values in relation to the constraint limits for sinkage, lift, RMS torque and rpm, for an $A1$ machine and gearbox.

sea states from an energy point of view. Therefore it is better to design the PTO taking the envisioned location in mind [29]. Looking at the mean available power at a location, however, can be misleading, especially when there are large seasonal differences in wave climate [68]. And [69] states that WECs should be designed with adjustable power matrices to fit the location where they will be installed.

Consequently, calculating the yearly produced energy of a PTO under study is an indispensable step in the designing process. To do so, the occurrence frequency of each sea state at the intended location is a required input.

To appraise the influence of the location on the sensitivity of the PTO power, three wave energy locations have been chosen from [70] as a base to define three virtual possible locations: (i) Westhinder on the Belgian Continental Shelf with an average annual wave power of 4.6 kW/m, (ii) Fino-Borkumriff on the German Continental Shelf which has an annual average of 11.6 kW/m, and (iii) Utsira with 23.1 kW/m, located on the Norwegian Continental Shelf. These values however differ for the used derived virtual locations.

From the above locations, three virtual locations are derived: Location 1, 2 and 3. These virtual locations are based on the occurrence frequencies of the real locations (i), (ii), (iii) for the six sea states with characteristic wave heights from 0.25 m up to 2.75 m as detailed in Table 5.5. If any higher waves occur at the real locations, the buoy is assumed to be in survival mode and will not convert any energy. Zero production due to too low or too high waves happens for 1%, 7% and 19% of the time of the year for the three locations respectively. Therefore the available annual averages for the derived Locations 1 to 3 are reduced to 4 kW/m, 6.3 kW/m and 7.6 kW/m respectively. The difference is also for a smaller part due to the fact that equal mean periods per sea state are supposed for all three virtual locations, which in fact is not the case. Nevertheless, this way of working provides a realistic distribution of the occurrence frequencies, which are displayed in Fig. 5.19.

The bars for the occurrence frequency of Fig. 5.19 clearly show that the occurrence of Location 1 is concentrated in the lower sea states while this shifts towards the medium sea states for Location 2 and even more to the higher states for Location 3. Furthermore, calculating the yearly available energy per meter wave crest as plotted in Fig. 5.20, the emphasis gets a new shift to the right for all three locations. Besides the low capture ratio of the WEC at SS1, it is clear that also the available energy of SS1 is negligible.

For Location 1, the available energy of SS2 is relatively large compared to the other sea states at this location, making it not negligible for the power contribution in the conversion process.

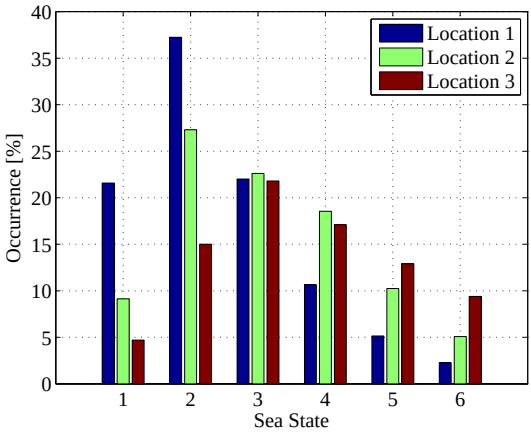

Figure 5.19: Occurence frequencies for SS1 to SS6 for locations Location 1, 2 and 3.

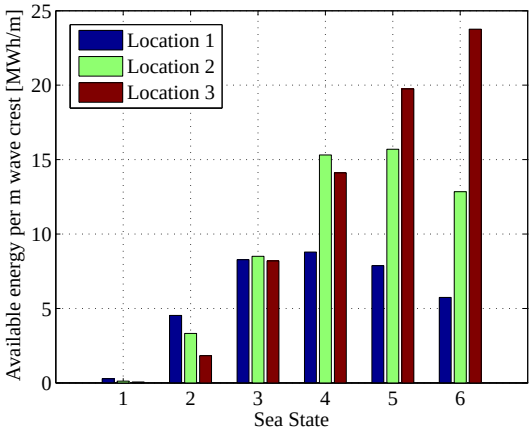

Figure 5.20: Yearly available energy per meter wave crest in MWh per sea state for the 3 locations

Table 5.5: Occurence frequency (O.F.) of the sea states together with the corresponding available annual energy (A.E.) for the three locations

SS	1	2	3	4	5	6
Hs [m]	0.25	0.75	1.25	1.75	2.25	2.75
Tm [s]	4.15	4.67	5.53	5.95	6.21	6.59
Avg annual available wave power [kW/m]	0.13	1.35	4.5	9.57	16.77	27.73
O.F. [%] Location 1	21.58	37.25	22.02	10.65	5.14	2.27
O.F. [%] Location 2	9.14	27.31	22.62	18.55	10.25	5.08
O.F. [%] Location 3	4.7	15	21.8	17.1	12.9	9.4
A.E. [MWh] Location 1	0.3	4.5	8.3	8.8	7.9	5.7
A.E. [MWh] Location 2	0.1	3.3	8.5	15.3	15.7	12.8
A.E. [MWh] Location 3	0.1	1.8	8.2	14.1	19.8	23.8

5.5.1 Yearly energy yield vs. installed power per location

By including the occurrence frequency of the sea state for each location, the yearly energy yield can be calculated as a function of the installed power. In a project assessment, it will be the amount of energy that can be injected into the electricity grid that makes an income. For each of the defined locations, the yearly energy yield has been determined and collected in Fig. 5.21 for the $A1$ machine efficiency map and a gearbox.

It is obvious from the above given occurrence frequencies, that the yearly yield is hugely dependent on the location. In addition, the figure gives insight to which degree the installed power influences the produced energy per location. One can see that the gradient of the yearly yield vs. installed power is slightly lower for Location 1 than for the more energetic Locations 2 and 3. The ratio between $P5$ and $P1$ is 2.7 for Location 1, while this is 3.1 and 3.4 for Location 2 and 3 respectively. From both the power and yield curves can be concluded that an installed power higher than $P5$ is useless, as there is no increase in yearly energy production. Also, the fractions per sea states can be distinguished, which are slightly different compared to the contribution of available wave energy of Fig. 5.20.

5.5.1.1 Capacity factor

The price of the PTO is often referred to as Euro per kW installed. Then it is of interest to know the *produced energy* per kW *installed*. As this is expressed as kWh/kW, it can be simplified to h (hour). Indeed, it is the equivalent number of hours the PTO would have to operate at its nominal capacity (= full load) to generate the same amount of energy, hence called the *equivalent full load hours*. If the number of full load hours is subsequently divided by the total numbers of hours

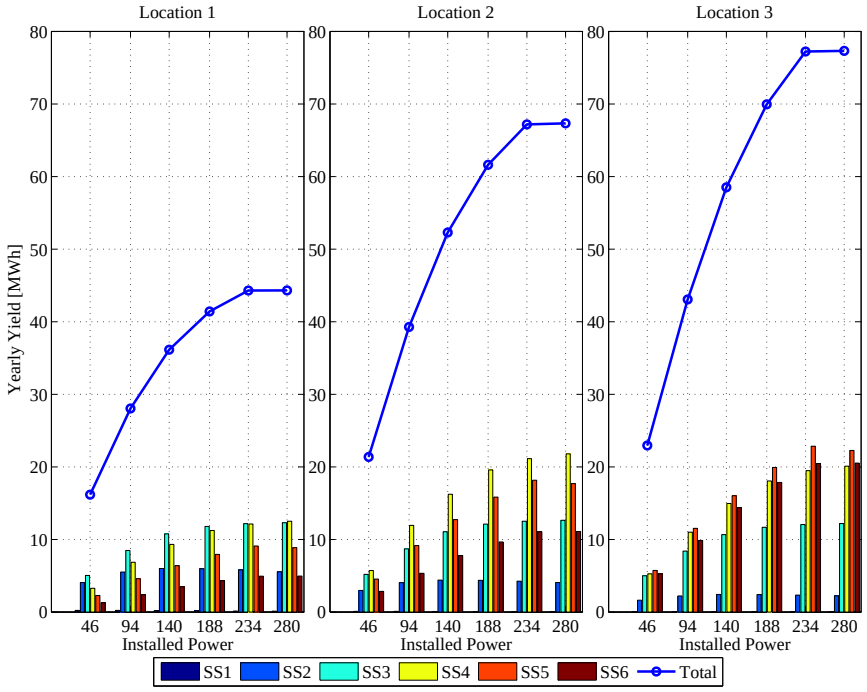

Figure 5.21: Yearly energy yield vs. the installed power for the 3 locations together with the energy fractions per sea state for the $A1$ efficiency map and gearbox.

in one year, a value is obtained expressing in which amount the full capacity of the PTO is utilised over the duration of one year. This value is called the *capacity factor*.

The three possible expressions (kWh/kW installed, equivalent full load hours and capacity factor) have been plotted in Fig. 5.22 for the three locations vs. to the installed power. Analysing this figure one could conclude that the $P1$ case of 46 kW is the most interesting PTO power because it has the highest outcome per installed kW. Assuming a linear price per kW, and assuming that there is enough room in the sea, 5 WECs with a $P1$ PTO would indeed produce more energy than a single WEC with a $P5$ PTO, and this with the same installed PTO power. However, this reasoning is of course too simplistic as it does not account for the total cost of the WEC, including the floater, installation and other corresponding costs. Still, the graph is an interesting tool for a cost optimisation when all costs - manufacturing, installation and operations & maintenance - and revenue per MWh are known.

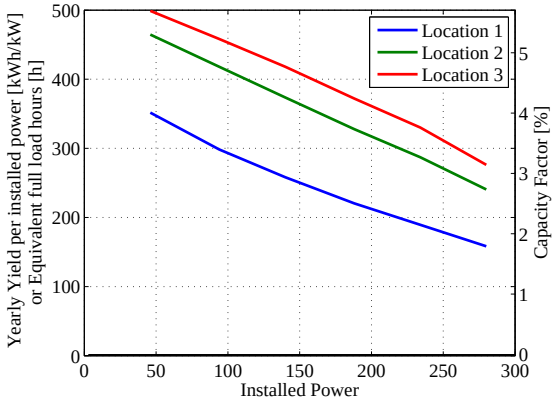

Figure 5.22: The yearly yield per installed power [kWh/kW], or full load hours [h] on the left y-axis, and the capacity factor [%] on the right y-axis vs. the installed power for the three locations, with an $A1$ efficiency map and gearbox.

5.5.1.2 Influence of the PTO efficiency on the yearly yield per location

The analyses of Section 5.3.2 focussed on the influence of the PTO efficiency on the mean power per sea state, of which the results were collected in Fig. 5.15. A step further is to assess the impact towards the yearly yield on the three studied locations. The results are gathered in Fig. 5.23 where per location the yearly electrical energy production for all efficiency map variants are plotted.

The yield curves in Fig. 5.23 demonstrate that the energy yield varies significantly with changing PTO efficiency, as could already be expected from the power curves of Fig. 5.15.

Within the map variants

The diverging output between the A variants is still noticeable, as summarised in Table 5.6. For a $P5$ PTO (see Table 5.4), a drop of 1% in maximum efficiency has a decrease of more than 3% as a consequence at Location 1 and 2. At Location 3 this is slightly more modest, approximately 2.8% per percent of maximum efficiency. With a smaller installed power of $P3$, this reduction is less, but still significant between 2.4% and 2.7% per percent drop in maximum efficiency. This lower sensitivity with a lower installed power can be attributed to the fact that the PTO operates more often at more efficient regions.

For the B efficiency maps, the difference in between its variants is slightly more pronounced, as demonstrated in Table 5.7. An identical trend is observed as within the A variants, both for a $P5$ and $P3$ PTO.

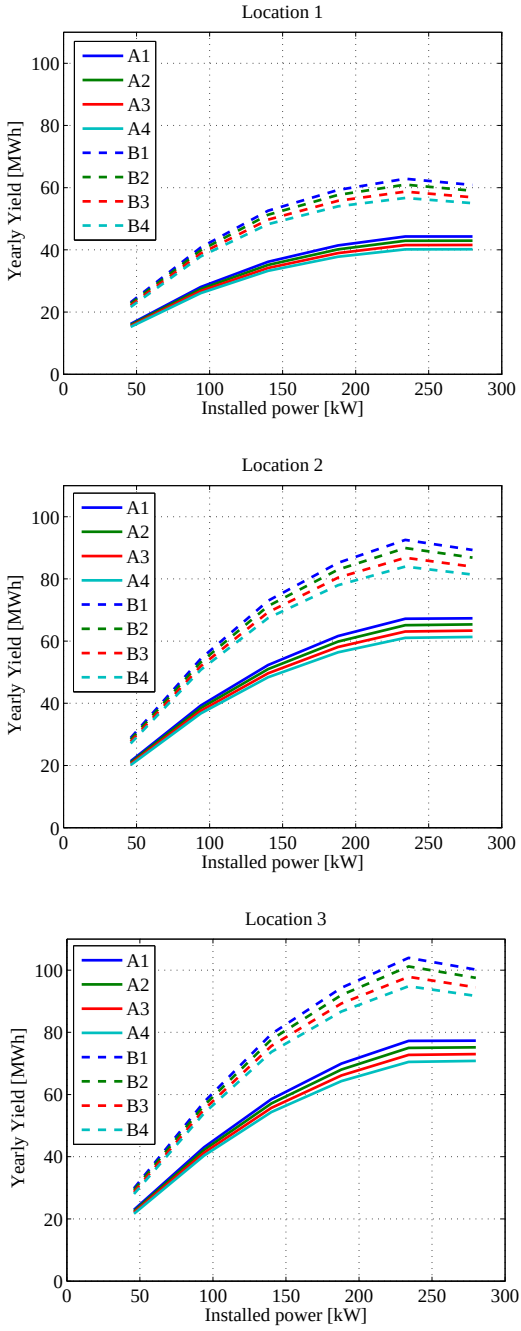

Figure 5.23: Yearly energy yield vs. the installed power for the A and B variants efficiency map also including a gearbox map for Location 1, 2 and 3.

Table 5.6: Difference in yearly energy yield (YY) between the 4 A efficiency map variants for the three locations, for installed power $P5$ and $P3$. For $A1$ the absolute value is given in MWh, for the other variants the ratio vs. $A1$ is given in %

Installed power	Location	$A1$ YY [MWh]	$A2$ % of $A1$	$A3$ % of $A1$	$A4$ % of $A1$
$P5$	Location 1	44.3	96.8	93.7	90.6
	Location 2	67.2	96.9	93.9	90.9
	Location 3	77.2	97.1	94.2	91.3
$P3$	Location 1	36.2	97.3	94.5	92.0
	Location 2	52.3	97.5	94.9	92.5
	Location 3	58.5	97.6	95.2	92.9

Table 5.7: Difference in yearly energy yield (YY) between the 4 B efficiency map variants for the three locations, for installed power $P5$ and $P3$. For $B1$ the absolute value is given in MWh, for the other variants the ratio vs. $B1$ is given in %

Installed power	Location	$B1$ YY [MWh]	$B2$ % of $B1$	$B3$ % of $B1$	$B4$ % of $B1$
$P5$	Location 1	62.9	97.0	93.4	90.2
	Location 2	92.5	97.2	93.8	90.7
	Location 3	104.0	97.3	94.1	91.2
$P3$	Location 1	52.6	97.5	94.5	91.8
	Location 2	72.9	97.7	94.9	92.4
	Location 3	79.5	97.8	95.2	92.8

Between the A and B map variants

Table 5.8 compares the yield of the $A1$ and $B3$ maps, which have an equal maximum efficiency. However, due to its much flatter shape, the $B3$ map benefits from a higher efficiency over a larger operation range of the machine. This has a substantial effect on the yearly electrical energy yield: a machine with a $B3$ shaped efficiency map outputs up to 133% of a $A1$ shaped map for a $P5$ installed power (see Table 5.4), and up to 138% for a $P3$ PTO.

The better performance logically results in a better capacity factor as plotted in Fig. 5.24, the capacity factor for a $P5$-$B3$ is 4.8% at Location 3, compared to 3.8% for a $P5$-$A1$ machine.

From the table (and the plots of Fig. 5.23) can also be noted that a $P3$-$B3$ PTO outputs more than a $P5$-$A1$ at Location 1 and 2, and almost as much at Location 3. This is an important finding: a $P3$-$B3$ machine produces the same amount of energy as the $P5$-$A1$ machine, with only 60% of the installed power.

It is consequently a matter of economics and/or life-cycle analysis (a.o. rare resources and other environment concerns) to decide on the most interesting PTO

at a proposed location.

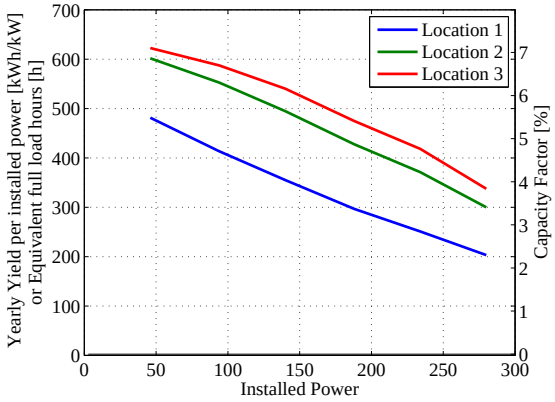

Figure 5.24: The yearly yield per installed power [kWh/kW], or full load hours [h] on the left y-axis, and the capacity factor [%] on the right y-axis vs. the installed power for the three locations, with a $B3$ efficiency map and gearbox

Table 5.8: Comparison of the yearly energy yield between $A1$ and $B3$ efficiency maps with equal nominal efficiency but different shape, for a $P5$ and $P3$ PTO with gearbox

Installed power	Location	$A1$ [MWh]	$B3$ [MWh]	$B3$ % of $A1$
$P5$	Location 1	44.3	58.7	133
	Location 2	67.2	86.8	129
	Location 3	77.2	97.9	127
$P3$	Location 1	36.2	49.7	138
	Location 2	52.3	69.3	132
	Location 3	58.5	75.6	129

5.6 Electromechanical optimisation of PTO sizing

5.6.1 Optimising the available speed

The sensitivity analysis on the installed power of Section 5.4 mainly comes down to a sensitivity on the available force, i.e. the electromagnetic torque of the machine because the rated speed was fixed. However, the maximum available torque is not just taken into account as a fixed maximum, because the inclusion of the operation range (with field weakening) forces the maximum available torque to drop above the rated speed.

The optimisation of the speed is an interesting next step to further minimise the installed power for a certain yearly yield, or increase the amount of energy for a certain installed power. This essentially results in a higher capacity factor, or more energy per PTO cost for a fixed technology.

To optimise the rated speed of the PTO, the bottom plot of Fig. 5.18 is a good indicator: it shows the degree to which the available speed is used. The y-axis represents the normalised speed relative to the maximum speed of 200% of the nominal speed (1500 rpm in that case). The highest speeds occur in sea state 6, the maximum occupation ratio of the available speed is 85% for $P2$, and 77% for a $P5$ installed power. Consequently, when focussing on the $P5$ case, a theoretical power reduction of 20% could be carried out by lowering the available speed. This could be effectuated by using a machine with a lower rated speed, and/or by changing the transmission ratio between the machine and the drum. To avoid too many sidetracks in this study, the transmission ratio is kept fixed (and thus also the gearbox efficiency map), and the rated speed of the machine is varied, possibly leading to virtual machine sizes, which in practice can be tackled an adjustment of the gear ratio with an existing machine size. (Please keep in mind that a different gear ratio can change the gearbox efficiency and will affect the equivalent linear mass of the PTO).

To evaluate if the reduction in rated speed of 20% is indeed possible, a simulation is run for the $P5$ case using the same control parameters but with a rated speed of 1200 rpm. The scatter of the operation points for the 1500 rpm reference case is shown in the upper figure of Fig. 5.25 and the lower figure presents the operation points of the reduced nominal speed of 1200 rpm. The figure makes clear that the actual maximum speed of the PTO even increases. This can be explained by the earlier manifestation of the field weakening. Therefore the buoy is less damped and reaches a higher peak speed. Thus this intervention is not advantageous as it exceeds the predefined PTO constraints. Additionally, the resulting absorbed power drops with almost 5%, and the electrical power with almost 2.5%. The smaller drop in electrical power than in absorbed power can be explained by the relative relocation of the operation points on the efficiency map, here apparently with a beneficial effect.

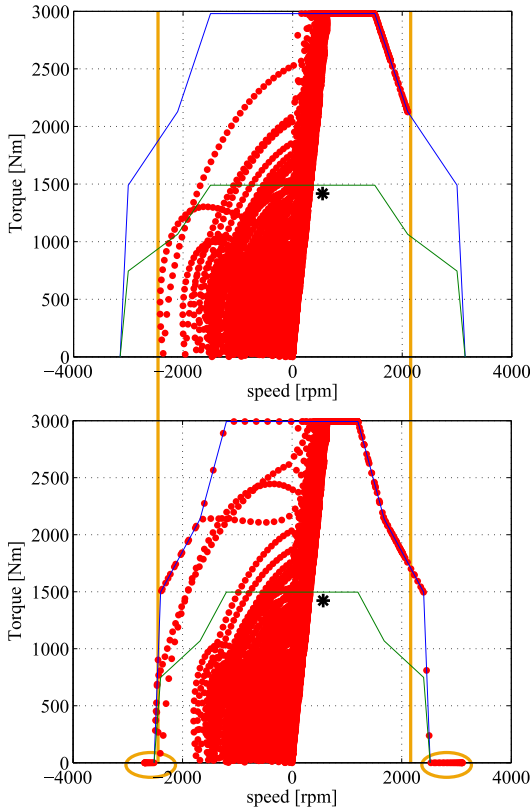

Figure 5.25: Scatter of the operating points for a SS6 simulation for a 1500 rpm rated machine (top), and a 1200 rpm rated machine (bottom), showing the increase of speed due to the lack of damping at field weakening.

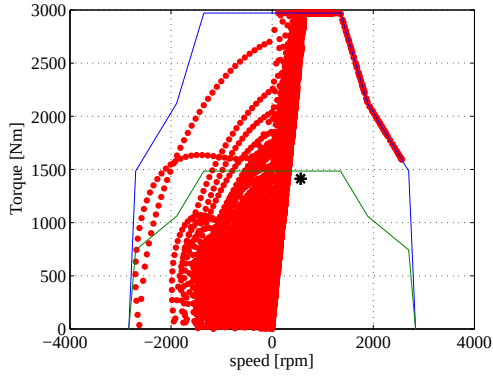

Figure 5.26: Scatter of the operating points for a SS6 simulation for a 1350rpm rated machine.

By giving the installed power minimisation a second try with a rated speed of 1350 rpm, i.e. 90% of 1500 rpm, the resulting absorbed power drops only with 1%, and more importantly the electrical power is the same. A drawback is the very small margin in available speed as can be seen in Fig. 5.26. A compromise could be made by increasing the margin while remaining some percent of power reduction.

Adapting control parameters to reduce the installed power

In the above reduction of the rated speed, the control parameters were not optimised for the 1350 rpm rated machine, but the optimal parameters for a 1500 rpm machine were maintained. Optimising the control parameters for the 1350 rpm machine might already lower the peak speed, but even suboptimal control for SS6 could be performed as this sea state contributes only for a limited part to the yearly yield.

Thus it is proposed to examine the effect of the control parameters on the PTO peak speed. Accordingly, new simulations have been run with a higher iteration resolution and a larger range for the control parameter b_{ext} for the $P5$ machine. Fig. 5.27 shows the colour plot of 108 simulations of different parameter combinations. The figure shows by means of the yellow contour lines of peak buoy speed that the control parameters can be adapted to diminish it. The blue dot on the y-axis indicates the parameter combination where the lowest maximum speed is reached, a buoy speed of 2.55 m/s corresponding with approximately 2230 rpm at the machine shaft, hence a required rated rotational speed of 1115 rpm.

Even though this is significantly lower compared to the 2420 rpm of the initial $P5$ situation (top plot of Fig. 5.25), the speed might again rise when simulating with a 1115 rpm rated machine due to the lower available torque at field weakening, as illustrated in the bottom plot of that same figure.

Therefore a sensitivity investigation of the influence of both the rated torque and speed on the mean power per sea state - and thus the yearly yield - seems necessary for a clear view on the possibility to reduce the installed machine power.

5.6.2 Optimizing rated torque and speed

While the pragmatic power reduction of 10% described above is already meaningful, the conclusion suggests a stepwise analysis of the available speed in combination with the available torque to have a well-founded outcome. It was also questioned if maximising the power conversion at SS6 is necessary. And, is it justified or necessary to dimension the PTO for power maximisation at a sea state contributing for 11%, 16% and 27% (for Location 1, 2 and 3 respectively) of the yearly yield? The sensitivity analysis of the installed power already showed that the gain in energy is less than linear proportional with the torque. Hence a subopti-

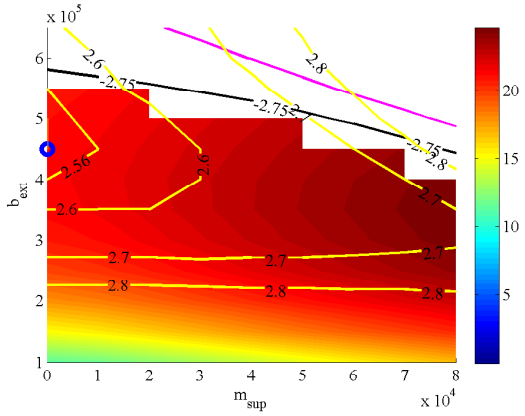

Figure 5.27: Mean electrical power [kW] for SS6 with a $P5$-$A1$ machine, contour lines for the buoy speed [m/s] in yellow, for the sinkage in black, and RMS torque in cyan.

mal dimensioning of the PTO can be interesting as a slight loss in mean power for the higher sea states due to of a smaller speed range will have an attenuated effect on the yearly yield, certainly for Location 1 and 2 where its occurrence frequency is relatively low.

The previous analyses revealed that not the installed power as a single parameter influences the power output of the PTO, but that it is the available force (torque) together with the speed range that determine the maximum ability to absorb the wave power. New simulations have been set up to vary both the available torque and the available speed iteratively. The results of these simulations can no longer be plotted in a two axis plot, but are represented as colour plots as a function of rated torque and speed of the machine used. To help to distinguish these plots from the efficiency maps and T-n plots of operation points, the torque has been put on the x-axis and the speed on the y-axis. This way of representing is also the closest to the previous representation of P_{el} vs. the installed power. There, the rated speed was fixed, thus the installed power of the x-axis was directly proportional to the rated torque.

For the rotational speed fives steps have been taken $n1$ to $n5$, and six steps as for the installed power have been maintained for the torque: $T1$ to $T6$. The corresponding values are displayed in Table 5.9. The values are not set at ratings of available machines, but as a tool to illustrate the influence of the available torque and speed. The change in available speed can be effectuated by changing the transmission ratio of the drive train. A $n4$ machine, for example, can be realised with a 1500 rpm machine and a gearbox ratio that is 1500/1400 higher than the $n5$ case. When both have a $T6$ rated torque, the rated torque of the $n4$ machine will in reality be lower than the 1788 Nm, to be exact: 1400/1500*1788 = 1669 Nm.

Table 5.9: The five steps in rotational speed $n1$ to $n5$ in [rpm] and the six steps in torque $T1$ to $T6$ in [Nm].

	$n1$	$n2$	$n3$	$n4$	$n5$
[rpm]	1100	1200	1300	1400	1500

	$T1$	$T2$	$T3$	$T4$	$T5$	$T6$
[Nm]	298	596	894	1192	1490	1788

The $T6$-$n5$ case has the same power as the $P6$ case, i.e. 280 kW. To concentrate on the influence of torque and speed, the PTO inertia has been fixed for all cases at the value from the $P5$ case, i.e. a rotor inertia value of 5.3 kgm^2, consisting of two times 2.65 kgm^2 based on a split PTO analogous to the Wave Pioneer.

5.6.2.1 Mean electrical power - $A1$ map

For every of the 30 combinations of torque and speed, the control parameters are optimised accounting for the PTO and hydrodynamic constraints by iterative simulations such as in the previous simulations, and this for every sea state (with approximately 90 simulations per case on average, this makes 30*90*6=16200 simulations). The resulting mean electrical power for an $A1$ machine with gearbox has consequently been plotted in the colour plots of Fig. 5.28 vs. rated torque and speed, for each sea state. The corresponding rated power has been added as contour lines to enhance the interpretation towards the performance in relation to the installed power.

Sea state 1 is included for completeness, but it is clear again that the power is too low. From SS2 on, it emerges that a lower rated speed increases the mean output power. Even though the rise is moderate, the fact that the corresponding installed power drops (and as assumed, the price) makes it interesting.

From SS4 on, the $T1$ simulations did not give any useful results, as well as some of the $T2$ points for SS5 and SS6. The power value is hence set to zero. This is probably due to the fixed rotor inertia which could be relatively too high for the lower rated torques. In the simulations for the power steps the rotor inertia was a function of the installed power. This is nevertheless not seen as an issue as it is very unlikely to equip a WEC with such a low powered PTO.

For SS6, none of the $n1$ simulations gave a workable control parameter set, the power value is hence also set to zero. Which assumes the buoy to go in survival mode at that time.

The rise in mean electrical output power is not (necessarily) because the lower speed rated machines can absorb more power from the waves. Sometimes they do, but sometimes on the contrary the absorbed power drops or remains status quo.

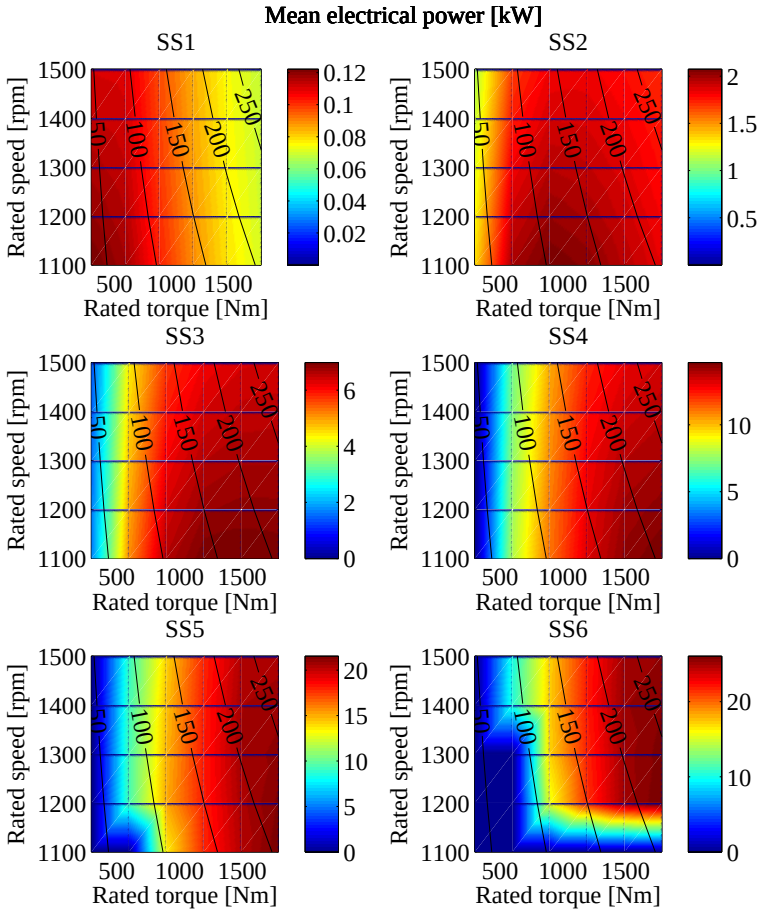

Figure 5.28: Mean electrical power ($A1$ map & gearbox) vs. rated torque and speed for sea states 1 to 6, contour lines for the rated power [kW].

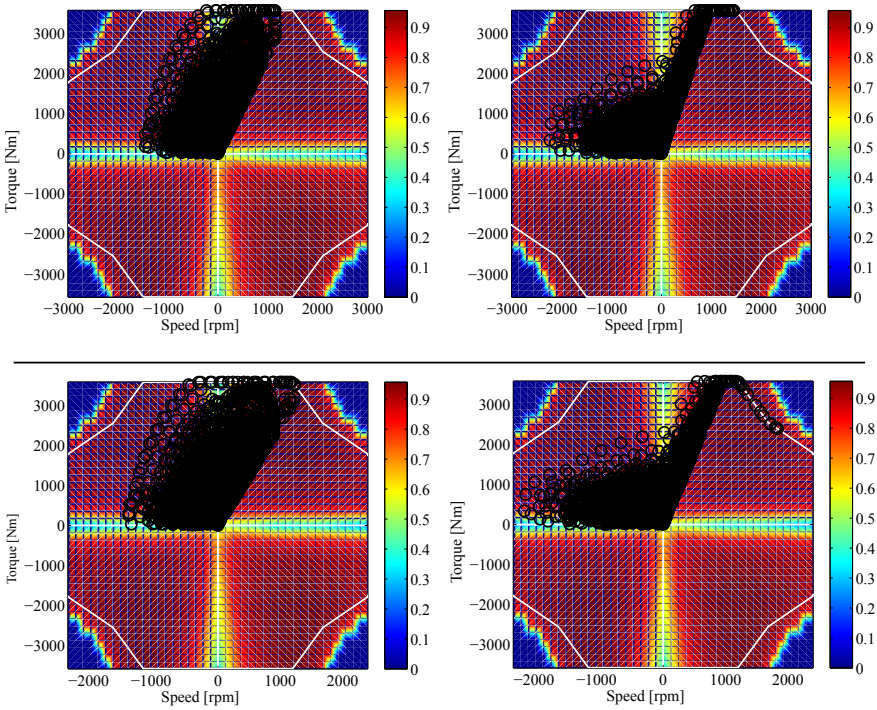

Figure 5.29: Scatter of the operating points for SS4 (left) and SS6 (right) on a merged efficiency map of $A1$ machine and gearbox for a $T6$-1500 rpm (upper) and a $T6$-1200 rpm (bottom) rated machine.

The power rise with lower rated speed can be explained by the fact that the PTO operates at more efficient operation points more often as the operation is shifted toward the optimum efficiency.

In Fig. 5.29 the operation points are scattered on a merged efficiency map of the $A1$ machine and the gearbox efficiency map. In the left column two cases have been presented for SS4, and in the right column for SS6. The upper figures depict a $T6$-1500 rpm rated machine, and the lower figure a $T6$-1200 rpm machine. The figures illustrate the shift of the operating points towards the better efficiency zones.

The resulting average PTO efficiency, i.e. the ratio of the mean electrical power to the absorbed power $P_{\mathrm{el}}/P_{\mathrm{abs}}$, confirms this: 58.7% for the 1200 rpm case vs. 55.8% for 1500 rpm in SS4, and 70.4% vs. 67.8% in SS6.

5.6.2.2 Constraints - $A1$ map

As for the earlier analyses, the hydrodynamic constraints of sinkage and lift, and the PTO constraints of RMS torque and maximum speed have been accounted

for. The normalised values in relation to the constraint limits have been plotted in Fig. 5.30. The maximum sinkage is reached at the highest rated torques from SS4 on. The lift limit does not pose any problem for the drum and cable PTO topology. The thermal capacity of the machines is well occupied for the higher sea states, only $T6$ offers some margin for the RMS torque. In SS5 some margin in RMS torque can be detected as well for the 1100 rpm machines, but this is due to the fact that the control parameters are determined by the speed limit as can be seen in the corresponding plot for the speed limit: it is coloured dark red around $T3$-$n1$ and $T4$-$n1$. The speed is also the limiting factor for most of the machines in SS6 as indicated by the large dark red spot.

In the simulations, the hydrodynamic and PTO constraints are considered as such that a combination of control parameters is chosen where the limits were not exceeded during the hydrodynamic simulation using a defined timeseries of exciting wave forces per sea state. In real life however, waves might occur during a certain sea state that do exhibit a risk towards the constraints. It should be noted that if an economic analysis is in favour of a certain PTO size, further research should investigate if the margin towards the PTO constraints is sufficient. Additionally, an advanced control algorithm could be developed to monitor the PTO constraints in real-time during operation and adjust the control action to respect the limits.

5.6.2.3 Yearly yield - $A1$ map

The trends of the power maps of Fig. 5.28 are in favour of the lower rated speed machines for most of the sea states, but the occurrence frequency of the sea states at the three test locations is decisive for the yearly energy production. The plots of the yearly electrical energy yield are collected in the left column of Fig. 5.31 for all three locations, and $T6$-$n2$ appears to be the most favourable option in terms of energy production. In contrast to the $n5$ cases, the energy still increases between $T5$ and $T6$, and might even further increase as can be assumed from the graphs. However, with an energy rise of approximately 1%, 2% and 3% for the three locations respectively, it will be quite uneconomically to do this as this needs a 20% higher torque. Numerical values of all cases have been gathered in Table 5.10. For each case the ratio relative to the maximum case has been displayed in percent. The n cases have been ordered in descending order to correspond to the order in the colour plots.

Another observation that can be made is the influence of the zero production at SS6 for the $n1$ cases. As the occurrence frequency of SS6 at Location 1 is very low, the influence thereof towards the yearly yield is much more moderate compared to Location 2 and certainly Location 3 where SS6 occurs 2 to 3 times as much.

The right column of Fig. 5.31 depicts the amount of energy per rated power

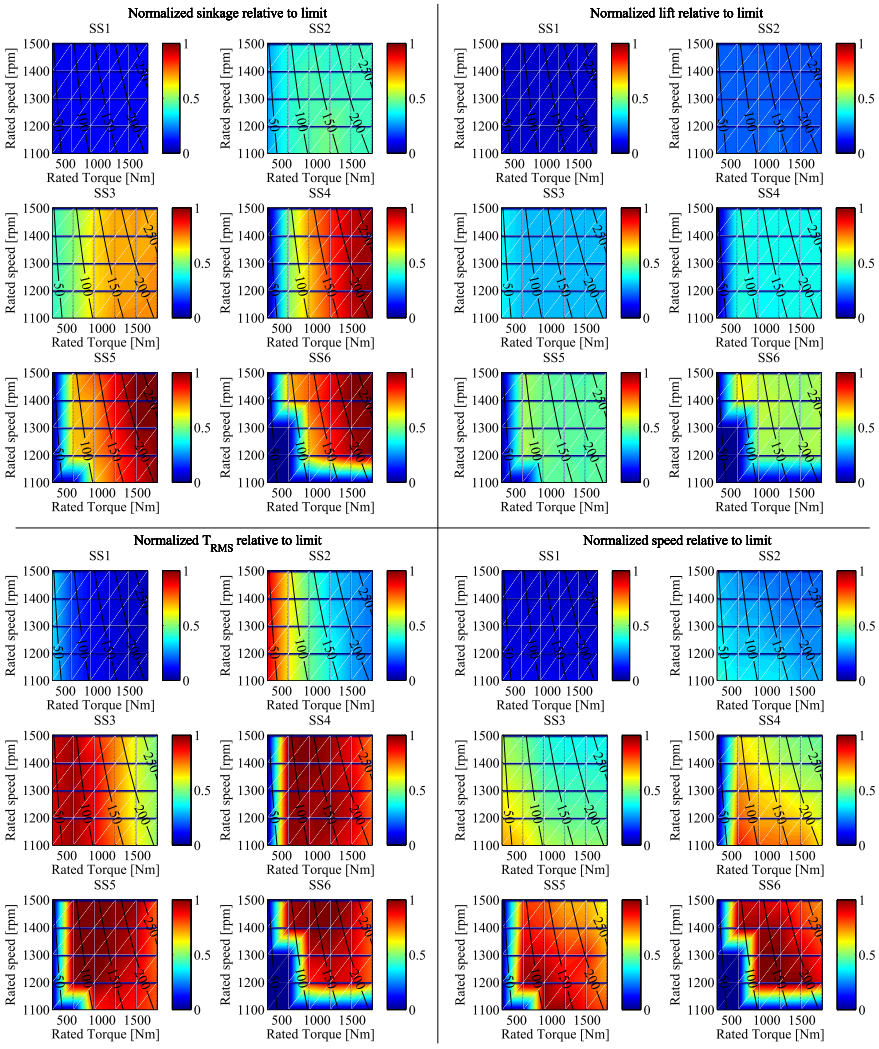

Figure 5.30: Normalised values in relation to the constraint limits for sinkage, lift, RMS torque and speed, for an $A1$ machine and gearbox.

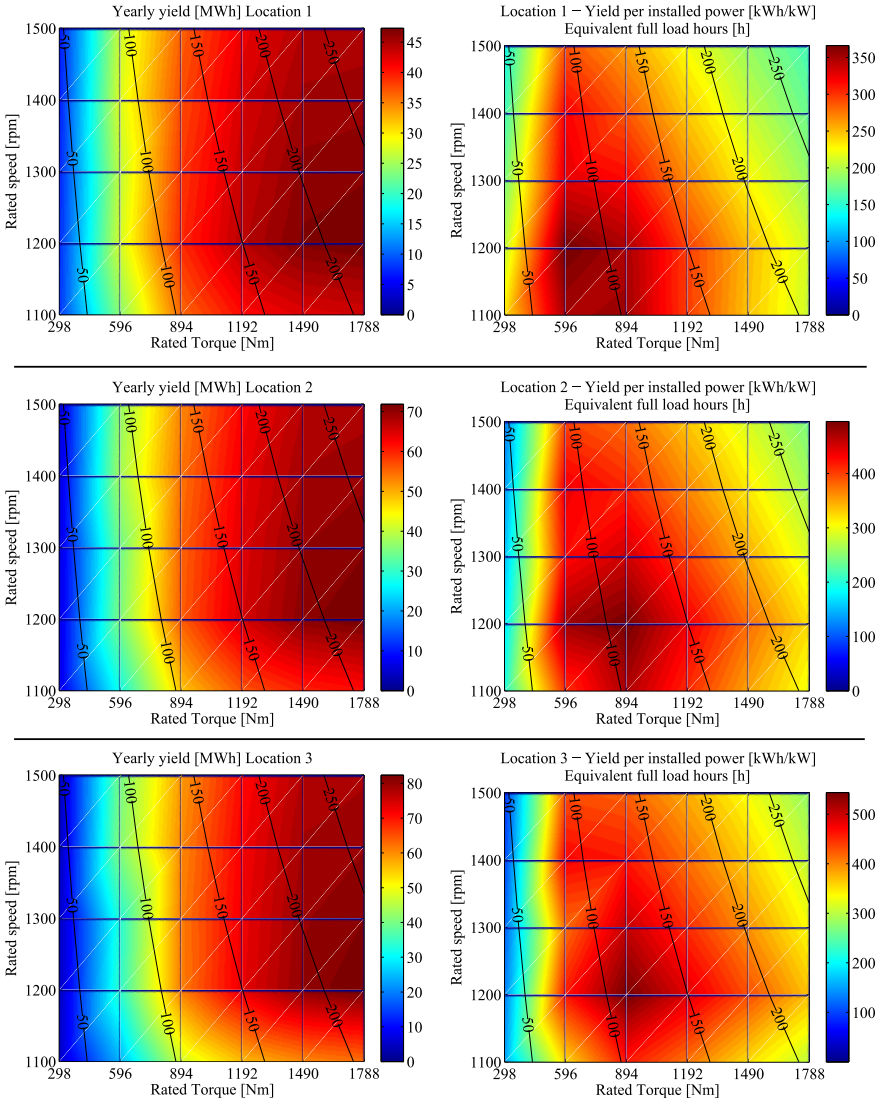

Figure 5.31: The yearly yield [MWh] vs. the rated torque and speed (left column), and the yearly yield per installed power [kWh/kW], or equivalent full load hours [h] vs. the rated torque and speed (right column), for the three locations, with an $A1$ efficiency map and gearbox.

Table 5.10: The ratio in [%] relative to the maximum yield at Location 1, 2 and 3 respectively for every rated torque and speed combination for a $A1$ map.

Location 1	$T1$	$T2$	$T3$	$T4$	$T5$	$T6$
$n5$	14.0	57.0	77.0	88.3	93.8	94.3
$n4$	14.7	58.8	79.2	90.3	95.8	96.2
$n3$	15.5	56.2	81.2	92.0	97.5	98.2
$n2$	16.2	58.0	82.6	93.4	98.9	100.0
$n1$	17.0	50.6	76.2	85.8	89.6	90.8
Location 2	$T1$	$T2$	$T3$	$T4$	$T5$	$T6$
$n5$	7.8	51.7	73.3	86.6	93.7	94.6
$n4$	8.2	53.2	75.3	88.4	95.5	96.4
$n3$	8.6	48.1	76.8	89.7	96.9	98.3
$n2$	9.1	49.4	77.5	90.5	98.0	100.0
$n1$	9.5	38.7	67.0	78.2	83.3	85.5
Location 3	$T1$	$T2$	$T3$	$T4$	$T5$	$T6$
$n5$	5.1	48.7	71.3	85.8	94.1	95.0
$n4$	5.4	50.0	73.1	87.3	95.6	96.7
$n3$	5.7	40.6	74.2	88.2	96.7	98.5
$n2$	6.0	41.7	74.1	88.7	97.4	100.0
$n1$	6.3	29.5	57.2	67.9	73.0	75.3

of the simulated machines. As already explained, this can be seen as the amount to which a machine is used in relation to its maximum capacity. By dividing the number of equivalent full load hours by the number of hours per year, the capacity factor is found. The corresponding maximum capacity factor for Locations 1, 2 and 3 is 4.2%, 5.7% and 6.2% respectively.

5.6.2.4 Yearly yield - $B3$

The efficiency map shape of the B variants is flatter than the A variants, therefore it is interesting to repeat the rated torque and speed sensitivity analysis for the $B3$ map to evaluate the resulting yearly yield. The $B3$ map has been chosen as its maximum efficiency is equal to the $A1$ map.

The plotted results of the yearly yield for the three locations in the left column of Fig. 5.32 already show that the trend is different as for the $A1$ results. The smaller rated speed machines are now not the right choice for yield maximisation, as also illustrated by the numbers of Table 5.11. In all of the three locations the $T5$-$n5$ outputs the highest yield on an annual basis.

As for the $A1$ analysis, the $T1$ cases and some of the $T2$ cases do not give useful results from SS4 onwards, and none of the $n1$ cases for SS6.

The flatter efficiency map of the $B3$ machine, even when merged with the gear-

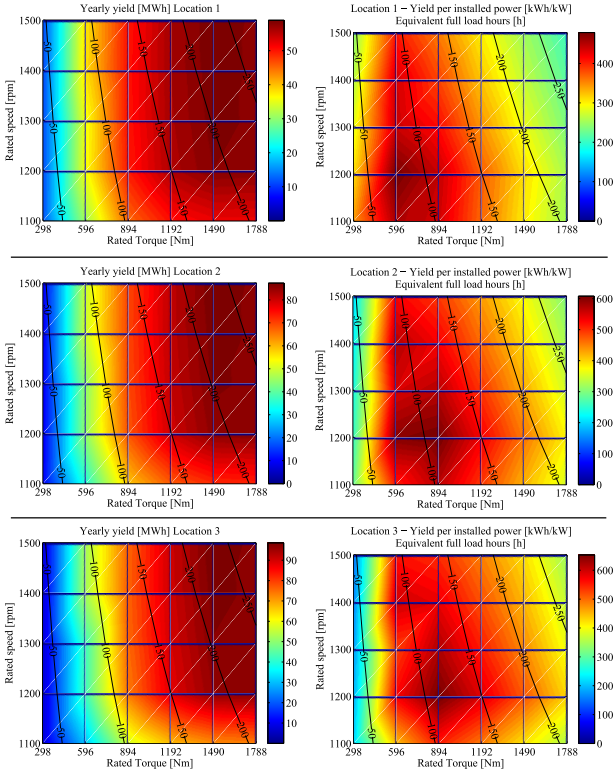

Figure 5.32: The yearly yield [MWh] vs. the rated torque and speed (left column), and the yearly yield per installed power [kWh/kW], or equivalent full load hours [h] vs. the rated torque and speed (right column), for the three locations, with a $B3$ efficiency map and gearbox.

box efficiency map as displayed in Fig. 5.33, apparently results in an slightly opposite effect as seen with the $A1$ map. It can be noticed that the $A1$ map (Fig. 5.29) has rather low efficiencies around zero-speed, while this band is much smaller for the $B3$ map (Fig. 5.33). On the other hand, some of the motoring points will end up at lower efficiency zones as can be spotted in the upper left quadrant of the SS6 1200 rpm case of Fig. 5.33.

Nevertheless, the yield does not drop substantially for decreasing rated speeds, and the choice for a smaller rated speed machine can thus be a more economic option as demonstrated by the fact that the relative drop in installed power for the $T5$-$n2$ (and even the $T5$-$n1$) case is larger than the relative difference in yield compared to the $T5$-$n5$ case. The figures on the right of Fig. 5.32 represents this in terms of energy per installed power (or equivalent full load hours) which is directly proportional with the capacity factor.

If the choice was to be made between a $A1$ or a $B3$ machine, the numbers of

Table 5.11: The ratio in [%] relative to the maximum yield at Location 1, 2 and 3 respectively for every rated torque and speed combination for a $B3$ map.

Location 1	$T1$	$T2$	$T3$	$T4$	$T5$	$T6$
$n5$	19.3	64.2	84.7	95.3	100.0	97.8
$n4$	19.5	64.4	85.1	95.3	99.7	97.9
$n3$	19.6	60.6	84.9	95.0	99.2	98.0
$n2$	19.8	60.8	84.1	94.3	98.4	97.9
$n1$	19.9	52.6	76.1	85.1	88.2	88.2
Location 2	$T1$	$T2$	$T3$	$T4$	$T5$	$T6$
$n5$	10.9	56.9	79.5	93.0	100.0	97.9
$n4$	11.0	57.1	79.9	92.9	99.5	98.0
$n3$	11.0	51.1	79.4	92.3	98.8	98.0
$n2$	11.1	51.2	78.3	91.3	97.6	98.0
$n1$	11.2	40.1	66.7	77.6	82.4	83.3
Location 3	$T1$	$T2$	$T3$	$T4$	$T5$	$T6$
$n5$	7.2	52.9	76.7	91.6	100.0	97.7
$n4$	7.2	53.0	77.0	91.3	99.2	97.8
$n3$	7.3	43.0	76.3	90.5	98.2	97.8
$n2$	7.3	43.1	74.4	89.1	96.8	97.7
$n1$	7.4	30.7	57.1	67.7	72.5	73.8

Table 5.12 demonstrate that a $B3$ machine can output importantly more energy than the the $A1$ machine. Up to 30% more yield for the $T4, 5, 6$ cases. A $B3$ machine consequently has a significant margin to be more expensive, or can be dimensioned much smaller to output an equal yearly yield. Again, all costs, from manufacturing over installation to operational and yearly expected revenues must be taken into account to make a justified choice.

5.6.3 Direct drive machine

All previous simulations assumed a PTO including a gearbox, with accompanying losses. A gearbox enables the use of fast turning, widely available machines, which are mostly less expensive than slow turning direct drive (DD) rotational machines, but a gearbox brings friction losses. Furthermore, it is a component which might need maintenance with associated costs and mechanical transmission systems are believed to be challenged by the reciprocating motion accompanied with WECs [24].

Here again, it is the cost together with the revenues of the yearly yield that will decide on the economic end-total, therefore a thorough study of the effect of the gearbox, or better the effect of omitting it, is necessary.

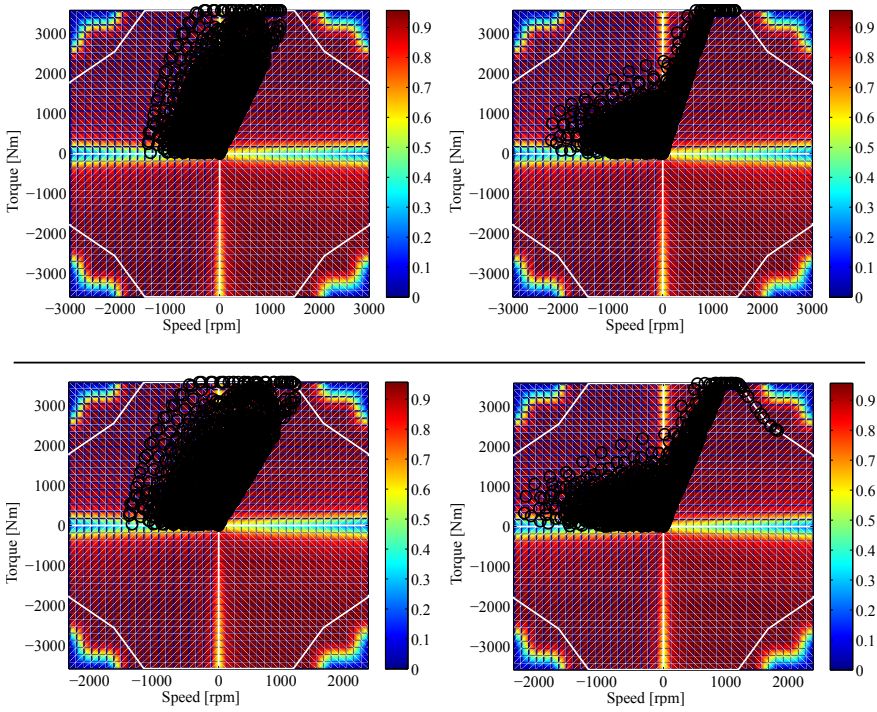

Figure 5.33: Scatter of the operating points for SS4 (left) and SS6 (right) on a merged efficiency map of $B3$ machine and gearbox for a $T6$-1500 rpm (upper) and a $T6$-1200 rpm (bottom) rated machine.

In the results that follow, the gearbox has been removed from the drive train and the machine is assumed to be a high pole machine connected directly to and thus running at the same speed of the drum. Depending on the minimum bending radius of the cable, the drum diameter can be adapted to adjust the rotational speed in relation to the floater speed to fit to the speed range of a machine, hence the best techno-economic option can be chosen.

As the A efficiency map variants are from an induction machine, and low speed induction machines are considered to have rather poor efficiencies, the analysis has been done for the $B3$ map only.

Table 5.13 collects the comparison between the direct drive and the gearbox results as the ratio of the yearly yield (YY) of the DD case relative to the yield of the gearbox (GB) case in percentage: YY(DD)/YY(GB) in [%]. The effect is larger for the lower energy locations than for higher energy locations. It is supposed that this is due to the fact that the PTO uses more often higher torques in higher sea states, at which point the gearbox efficiency is higher. In lower sea states, the PTO operates more frequently at the lower efficiency zone of the gearbox, thus removing it has a greater effect on the resulting mean power in lower sea states.

Table 5.12: Comparison of the yearly yield of the $B3$ cases with the $A1$ cases as YY($B3$)/YY($A1$) in [%].

Location 1	$T1$	$T2$	$T3$	$T4$	$T5$	$T6$
$n5$	172	140	137	135	133	129
$n4$	165	137	134	132	130	127
$n3$	158	135	130	129	127	124
$n2$	152	131	127	126	124	122
$n1$	146	130	125	124	123	121
Location 2	$T1$	$T2$	$T3$	$T4$	$T5$	$T6$
$n5$	170	134	132	130	130	126
$n4$	163	130	129	128	127	123
$n3$	156	129	126	125	124	121
$n2$	149	126	123	122	121	119
$n1$	143	126	121	121	120	118
Location 3	$T1$	$T2$	$T3$	$T4$	$T5$	$T6$
$n5$	167	130	129	128	127	123
$n4$	160	127	126	125	124	121
$n3$	153	127	123	123	122	119
$n2$	146	124	120	120	119	117
$n1$	140	124	119	119	119	117

The yield increase of the DD vs. the gearbox PTO varies between 9% and 15% for the $T5$-$n2$-5 cases, while the nominal efficiency of the gearbox is 95%. These results emphasise again the importance of using efficiency maps instead of the nominal value for wave energy yield estimations, although it should be kept in mind that the equivalent PTO mass of a DD is much lower than for a geared PTO. And the magnitude of the equivalent mass affects the WEC performance, which is studied in detail in the next subsection.

Although the absolute inertia for the direct drive machines is much larger (two times 48.5kgm^2), the influence is almost not noticeable under the low rotational speed and according low rotational acceleration. The corresponding equivalent PTO mass in the linear analogy is consequently very moderate: 1 ton compared to the buoy mass of 29 ton and certainly compared to the equivalent PTO mass of the gearbox cases of 47 ton (with two times 2.65 kgm^2).

What can be noticed also is that the ratio for the $T1$ cases is very high. In the gearbox cases, the performance of the $T1$ cases is very low due to the relatively high inertia for this rated torque, and its low ability to deal with its acceleration.

In general, there is a clear margin to take a more expensive direct drive solution over a geared fast turning machine. Additionally a direct drive PTO could offer higher reliability as there are less mechanical components, and might need less

Table 5.13: Comparison of the yearly yield of the $B3$ direct drive (DD) cases with the $B3$ gearbox cases as YY(DD)/YY(GB) in [%].

Location 1	$T1$	$T2$	$T3$	$T4$	$T5$	$T6$
$n5$	211	109	108	111	114	120
$n4$	210	109	108	111	115	120
$n3$	210	116	109	112	115	118
$n2$	209	116	110	112	114	117
$n1$	194	125	112	113	124	129
Location 2	$T1$	$T2$	$T3$	$T4$	$T5$	$T6$
$n5$	319	110	106	108	111	118
$n4$	318	110	106	108	111	117
$n3$	316	123	106	109	111	115
$n2$	314	123	108	109	111	113
$n1$	286	138	110	111	125	131
Location 3	$T1$	$T2$	$T3$	$T4$	$T5$	$T6$
$n5$	434	112	105	107	109	118
$n4$	432	112	105	107	110	117
$n3$	430	138	106	108	109	113
$n2$	427	138	109	108	109	111
$n1$	362	153	110	110	137	144

maintenance. This should be kept in mind while budgeting the operational costs.

5.6.4 Optimizing the PTO inertia

The machine's rotor inertia contributes to the total (linear) inertia of the hydrodynamic system. An equivalent linear mass can be calculated taking into account the transmission ratios, see equation (5.6). The relation shows the high influence of the gearbox ratio R_g as the equivalent mass is proportional to its square. Thus the influence is substantially lower (even almost not noticeable) in direct drive systems. In the drum and cable system, the rotary PTO inertia only influences the hydrodynamic system when the acceleration is positive as only pull forces can be exerted by the cable. On the other hand, the magnitude of the inertia has an effect on the required torque to accelerate it to keep the cable taut.

A certain amount of rotor inertia is expected to be beneficial, since motor tuning already showed to increase the yearly yield by mimicking the behaviour of a physical inertia. Optimizing the rotational PTO inertia is also called *inertia tuning*, it will tune the natural frequency of the WEC towards the wave frequency by adapting the inertia.

By increasing the physical inertia, it is expected that the virtual supplementary

Table 5.14: Comparison of the yearly yield in relation to the maximum [%] vs the machine's rotor inertia for Location 1, 2 and 3.

Inertia [kgm^2]	Location 1	Location 2	Location 3
2	96.8	96.6	96.7
3	98.1	98.0	98.2
4	99.1	99.2	99.4
5	99.3	99.2	99.2
6	100.0	100.0	100.0
7	99.9	99.7	99.5
8	99.7	99.5	99.5
9	99.6	99.3	99.0

mass applied by the PTO can be decreased, with a corresponding improvement of the WEC's performance.

A sensitivity analysis has been performed on a 1500 rpm machine to allow for some speed margin. It is known that the inertia increases the shaft torque in relation to the electromagnetic torque due to its acceleration torque, therefore a torque size of $T4$ has been chosen, as the effect might be less visible at higher torques due to the fact that the yield stops rising from a certain torque level (cfr. Fig. 5.21). In this analysis the gearbox efficiency is not taken into account, because the implementation needs the maximum occurring shaft torque which is not known in advance. From the results, the effect on the supplementary mass is evaluated, as well as the effect on the yearly yield.

The decrease in motor tuning need by means of the supplementary mass m_{sup} is illustrated by the plots in Fig. 5.34, where a descending trend in all sea states confirms the expectation (the stepped curve is due to the resolution of m_{sup} used in the simulations). The other control parameter b_{ext}, determining the PTO damping, remains nearly unaffected.

The influence of the inertia's magnitude on the yearly yield is collected in Table 5.14 and shows an increase of more than 3% between the lowest and the optimum inertia for all three locations. Above 6 kgm^2 the system performance drops slightly.

The simulations for the torque-speed optimisation used a rotor inertia value of 5.3 kgm^2, consisting of two times 2.65 kgm^2 based on a split PTO analogous to the Wave Pioneer. The value of 5.3 kgm^2 is coincidentally close to the optimum. Splitting of the PTO power might have had an advantageous effect on the yield, as larger machines might have a larger inertia density per kW installed power.

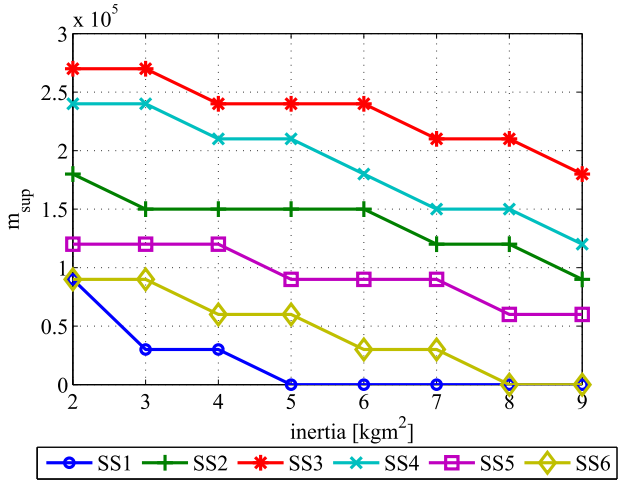

Figure 5.34: Supplementary mass m_{sup} [kg] vs. rotor inertia [kgm^2] for an $A1$ $T4$-$n5$ machine.

5.7 Conclusion

As an extension to the hydrodynamic model of the floater, a detailed PTO model has been developed, in this chapter for the drum and cable topology. The model consists of the dynamics and the operational limits of the electrical machine, and accounts for the efficiency of the most relevant parts of the drive train. The efficiency has been included as maps as a function of the actual torque and speed from which the actual efficiency value for that specific load condition is read at every simulation cycle. The latter is done for the machine and the gearbox, and a fixed value is used for the variable frequency drive. In this way the electrical output of the PTO can be estimated more realistically. This is especially important given the highly variable nature of wave energy where the PTO operates at a very broad working range. The use of only the nominal efficiency value is therefore not appropriate.

After explaining the drum & cable simulation model, the specific PTO control is described considering the unidirectional nature of the cable and comprising of a term to keep the cable tense at all times. The importance of the control parameters is pointed out by means of an unlimited PTO: on the one hand to maximise the power absorption, and on the other hand to respect the floater constraints. The amount of tuning should be restricted to prevent the buoy from being overflooded by the water. Notwithstanding the need to limit the magnitude of the tuning, the effect of the reactive control is still significant and increases the power absorption up to 230% compared to a simple damping control. The control parameters are sea state dependent and should thus be selected appropriately.

Analysing the electrical output instead of only the absorbed power, the studies performed in this chapter with the drum & cable PTO showed that the PTO efficiency has a major influence on the electrical outcome. Due to the bidirectional power flow inherent to the reactive control, the effect thereof diminishes, but is still substantial: a reactively controlled WEC reaches up to 140% in electrical power compared to a WEC that is only damped.

The level of the efficiency is logically not to be underestimated. In first instance the magnitude of the nominal efficiency of the PTO is evaluated. A difference of 1% results in a change of approximately 3% in yearly yield for the simulated locations (Tables 5.6 and 5.7). Secondly, and not at least, the shape of the PTO efficiency map has a substantial effect. The shape is mainly dependent on the machine topology (e.g. induction machine or permanent magnet synchronous machine) and design. The performed analysis revealed a significant influence of the shape of the efficiency map as a function of actual torque and speed. Two electrical machines with equal maximum efficiency were compared. The first - $A1$ - has a relatively pointed shape, while the other - $B3$ - has a flatter shape and hence higher efficiency along a larger operation range. The difference in yearly yield was approximately 30% for a high installed power at all locations, and even up to 40% for a moderate installed power at a low energetic location (Table 5.8 and Table 5.12). This creates an important potentiality for the use of high performance machines: a more efficient machine has an ample margin to be more expensive and still reach equal or better profitability.

The average PTO efficiency depends on the wave conditions because the PTO operates more often in lower efficiency zones at lower sea states. The values vary between 46% and 68% for the $A1$ case for SS1 and SS6 respectively, and between 58% and 77% for the $B3$ map, for a drum and cable PTO of 280kW 1500 rpm with gearbox. These values should help to realise that feasibility assessments of a WEC based on absorbed power are highly overrated.

Several sensitivity studies have been performed as guidelines to the dimensioning of the PTO. Power maximisation for all sea states for a certain floater shape is not necessarily the economic optimum as this requires a relatively high installed PTO power. Better is to dimension the PTO with the envisioned exploitation site in mind. The local wave climate, i.e. the occurrence of each sea state, has a non-negligible influence on the relation between the installed power and the average yield. The more energetic a location is, the higher the gradient of the yield vs. the installed power (Fig 5.21). By using these yield values and the associated revenue per MWh, an economic assessment can be executed accounting for all costs from manufacturing over installation up to operational and end-of-life costs to decide on the optimal PTO power. Considering that the PTO cost is estimated at 20% - 30%

of the total manufacturing cost of the WEC [30–32], a significant contribution can be made to the total cost by reducing the PTO cost.

It should be noted that the optimal diameter might also be location dependent. This is out of scope of this study, but the presented methodology can be used to find the most profitable PTO for each floater diameter to subsequently choose the optimal WEC out of the studied diameters.

To determine the effect of the installed power on the electrical power, six power steps based on the available torque have been evaluated. The mean electrical power achieved per sea state rises with the installed power until capped due to reaching of the sinkage constraint. Because the wave climate of the location where the WEC will be deployed will determine the potential wave energy conversion, the average annual yield for three different locations has been quantified based on the occurrence frequency of each sea state. Revealing a substantial different yield curve for each location.

The iterations in available torque showed an ample margin in speed range, and moreover, the control parameters can be selected to diminish the peak speed with only a moderate loss in output power. Consequently, in a following stage, this chapter presented a decomposition of the rated PTO power in the rated torque and rated speed to study the influence of these design parameters separately. The starting point was to minimise the installed power by reducing the available required speed margin with a certain rated torque. The outcome was slightly different for the $A1$ and $B3$ map, but permitted a substantial power reduction for both. For the $A1$ map, the yearly yield even increases with decreasing available speed because the operating points shift to better efficiency zones in the operational range. For example, the installed power can be reduced by 20% accompanied by a yield increase of approximately 5% for $T5$ ($n5$ to $n2$), or a power reduction of 35% can be effectuated from $T5$-$n5$ to $T4$-$n2$ while maintaining an equal yield (Table 5.10). For the $B3$ map, the influence of the shift of the operational points is slightly opposite. The maximum yield is achieved at the largest available speed, but the loss in yield is maximum 3.2% for a 20% drop in installed power for the $T5$ cases ($n5$ to $n2$).

Another electromechanical optimisation investigated is the use of a direct drive rotational machine. The gearbox losses are then omitted with a corresponding yield gain of 9% to 15% for the $T5$ cases (Table 5.13). This can however not be seen as the losses over the gearbox, because the yield is also affected by the change in hydrodynamic response due to the smaller equivalent PTO mass of the DD. A direct drive option possibly also reduces the maintenance cost due to the absence of a gearbox transmission.

Finally, the sensitivity of the PTO inertia is examined as it can increase the power absorption by tuning the natural frequency of the system towards the incoming wave frequency. The results showed that the motor tuning can be diminished by adding PTO inertia. A gain of more than 3% in average yearly yield has been observed for all test locations between the lowest simulated inertia and the optimal value (Table 5.14). Adding inertia to a PTO drive train consisting of a gearbox is considered a relatively cheap intervention. However, the machine's own inertia could quickly reach or exceed the optimal inertia. Splitting up the PTO power in two electrical machines might then have a beneficial effect because the inertia per installed kW appears to be lower for smaller machine sizes. Nevertheless, the decrease in yield beyond the optimal inertia is moderate.

Splitting the PTO power might also have opportunities towards PTO performance optimisation. Further research on the control could investigate the effect of using only one of the machines at lower torques, or uneven division of the torque load to end up with a higher average efficiency.

It should be noted that if a certain torque-speed combination would be chosen, the workability should be further examined, amongst others towards the margin in speed range and the reaction of the control to prevent crossing of the constraints. Future research could also study the further increase of super-rated speed usage. The mechanical design of the drive train is affected by both the choice of machine size as the additional inertia, as the latter adds a substantial inertial torque to the electromagnetic torque.

The performed analyses can be the starting point for an techno-economic optimisation. For each (relevant) point of the yield map as a function of rated torque and speed a cost and revenue estimation can be performed to assess the profitability of every case. Next to the costs of manufacturing, installation and operation, it is encouraged to perform a life-cycle assessment to ensure the best option for now and future generations. The use of rare resources or pollutant materials (or manufacturing processes) is for example a factor that can have large consequences. Additionally, the question is in place if machines containing rare resources should be employed in this application with a low capacity factor, instead of in an application where they offer a larger yield gain.

A drawback of the drum and cable PTO is that the motion is not purely heaving in reality, although as such assumed in the simulation model. This might include a considerable inaccuracy of the model. Moreover, the technology allows energy to be absorbed from the waves in the upwards direction only, leaving a share of the floater's potential untapped. Furthermore the cable needs to be kept tense at all times to be able to absorb in the next upwards movement. Moreover, high impact forces can occur in the cable after getting slack.

As general conclusions of this chapter, firstly it can be stated that it is important to use the efficiency at the actual operation points when estimating the electrical output. The magnitude at the nominal load can be misleading because the shape (flatness) of the efficiency map is of much higher importance. Secondly it can be conlcuded that a PTO should be sized keeping the targeted location in mind, certainly when the share of the PTO cost in the total WEC cost is considerable. The local wave climate can determine the degree to which it is interesting to increase the installed power.

6
Rack and Pinion PTO

The previous chapter concerns a PTO where the PTO forces are transferred by a cable to the seabed. Consequently PTO forces can only be applied in the downwards direction and wave power can only be absorbed in upwards direction and potentially leaving a share of the available wave energy untapped. Furthermore the cable must be kept tensioned at all times.

When a buoy is mounted around a vertical pile, a rack and pinion system can transfer the PTO forces to the seabed in both directions and there is no cable to be kept tensioned. Moreover, the required PTO torque appears to be lower than for a unidirectional PTO. In [14, 15] a simplified control strategy is considered using a constant torque reference to compare a unidirectional with a bidirectional PTO, and it was found that for the bidirectional PTO the required torque could be halved to achieve a similar power production in comparison with the unidirectional operation.

Principles of this PTO system are illustrated in Fig. 2.2 and Fig. 2.3 of Chapter 2. The latter shows the PTO on a platform which facilitates the accessibility of the PTO and grid connection. Multiple WEC's of an array could make use of a common platform. An additional advantage the rack and pinion system could offer, is the possibility to hoist up the floater to protect it from storm conditions. However, the technical feasibility thereof is not part of the studies performed in this work, but are mentioned to show this potential next to the expected increased energy yield. Neither is the mechanical design of the rack and pinion transmission system part of the research.

This chapter focusses on the power absorption potential of the rack and pinion

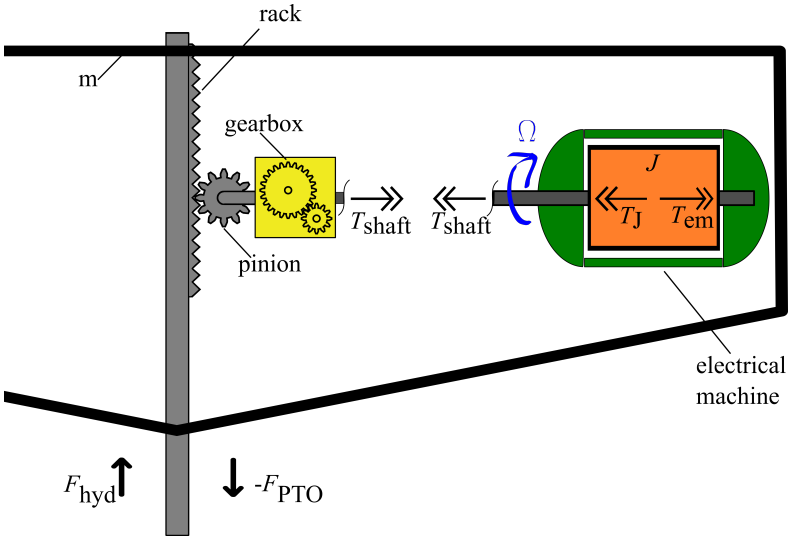

Figure 6.1: Schematic overview of the rack and pinion PTO in the floater and the resulting PTO force together with the hydrodynamic force on the buoy

PTO and studies subsequently the sensitivity of the control and design parameters analogously as for the drum and cable PTO of Chapter 5. Based on the mechanical layout, the PTO model has been built to replace the drum and cable model in the overall simulation model including the hydrodynamic model. Subsequent to the sensitivity analyses, the optimisation method from the previous chapter has also been adopted on the rack and pinion PTO to be an input for a techno-economic assessment.

Similar as in the previous chapter, the results are not meant as an absolute determination of the performance of the rack and pinion WEC, but as illustration of the presented methods a tool to compare PTO sizes and to reveal sensitivities for the dimensioning of the system.

The structure of this chapter is based on the previous, and to avoid unnecessary repetition, the reader is kindly referred to the corresponding sections for background information.

6.1 Working principle and mathematical model

The heaving buoy under the influence of the incoming waves can be damped by the PTO system in both the upwards as downwards movement with the rack and pinion system (remember that the gravity force is part of the total hydrodynamic force). The movement is - as with the drum and cable - relative to the sea bottom, the PTO force is transmitted through the rack and pile to the seabed as depicted in

Fig. 6.1. An electrical machine is connected through a gearbox to the pinion, or alternatively a direct drive rotary machine could be installed to eliminate the use of the gearbox. The machine is subsequently connected to a variable frequency drive injecting the produced power either on a common DC-bus, or convert it directly to the frequency of the AC grid.

The combination of rack, pinion, possible gearbox, electrical machine and drive is referred to as the PTO system. The PTO system absorbs (a part of) the wave energy to convert it to usable electrical energy.

The buoy can be damped in the two directions, and also enables tuning (i.e. reactive control, cfr. Section 2.4) in both directions to optimise the power absorption from the waves.

6.1.1 PTO model

Fig. 6.1 shows a rack and pinion PTO inside a floater. The shaft torque T_{shaft} is increased by the gearbox with gear ratio R_{g} and converted to the PTO force F_{PTO} by the pinion with radius r on the rack, which gives an expression analogue to Equation (5.1), where r is now the pinion radius.

As a matter of fact, the rest of the mathematical model of the rack and pinion is also analogue to the drum and cable model, with the difference that the rack and pinion can transfer PTO forces in both directions, while the cable in only one. Hence the model description of Section 5.1.1 and the Equations (5.1) to (5.7) are also valid for the rack and pinion PTO, with r the pinion radius. In Fig. 5.3 the cable should be replaced by a stiff connection, being able to transfer both pull and push forces.

6.2 PTO control

The general PTO control based on the mass-spring-damper system is explained in Chapter 2 Section 2.4. Each PTO topology might have specific requirements or variations on the theoretical external PTO force, with characteristic consequences. For the rack and pinion PTO this is described in the following sections.

6.2.1 Specific control for a rack and pinion PTO

The rack and pinion topology allows a force to be exerted on the floater in both directions, thus there is no sign condition to be met for the speed or acceleration to calculate the damping and tuning force, which was the case for the drum and cable PTO. There is also no need to have a constant force nor inertia compensation force to keep the cable tense. Hence the required electromagnetic force F_{em} for

the PTO control is expressed as:

$$F_{\mathrm{em}} = F_{\mathrm{damp}} + F_{\mathrm{tun}} \tag{6.1}$$

F_{damp} and F_{tun} are expressed in Equations (2.15) and (2.13).The damping coefficient b_{ext} and tuning coefficient m_{sup}, are respectively taken equal for both the upwards as downwards motion. Future research on the control could examine if this is the right choice, or whether they should be determined independently from each other to increase the yield, or to reduce the required speed range.

6.2.2 Influence of control parameters on power absorption

To maximise the power absorption from the waves, the PTO action should be adapted depending on the incoming wave conditions to change the PTO damping and tuning action. To find the optimal combination of parameters, iterative simulations are performed for a range of the control parameters b_{ext} and m_{sup}, i.e. 121 simulation runs per sea state. In this first assessment an unlimited PTO in both torque (force) and speed range has been assumed and the PTO inertia has been set to zero to estimate the maximum potential of the used floater with a rack and pinion PTO. From these simulations, the absorbed power has been calculated and plotted in Fig. 6.2. To recapitulate, the absorbed power is the mean mechanical power absorbed by the PTO and does not incorporate the PTO efficiency. It is calculated by multiplying the buoy speed and the PTO force F_{PTO}.

Fig. 6.2 shows that the maximum absorbed power (marked with a blue circle) is limited by the floater constraint of lift from SS3 on. Hence the control parameters need to be chosen to avoid that the floater lifts out of the water and causes consequent slamming on the water surface with corresponding high forces on the body [17].

Effect of tuning

The colour plots show a strong influence of the control parameters towards the absorbed power, if not appropriate set, the power drops significantly. The optimal parameters are sea state dependent as also illustrated by the plots of m_{sup} and b_{ext} vs. the sea state in Fig. 6.3.

The effect of tuning is emphasised by Fig. 6.4, where both the mean power using a purely damping control and the mean power using tuning are plotted together with the ratio between the two. This ratio reaches 300% in SS3 and does not drop under 150% in higher sea states.

It is reminded that the PTO efficiency will influence the tuning capacity as the reactive control requires a power investment with according PTO losses in both ways.

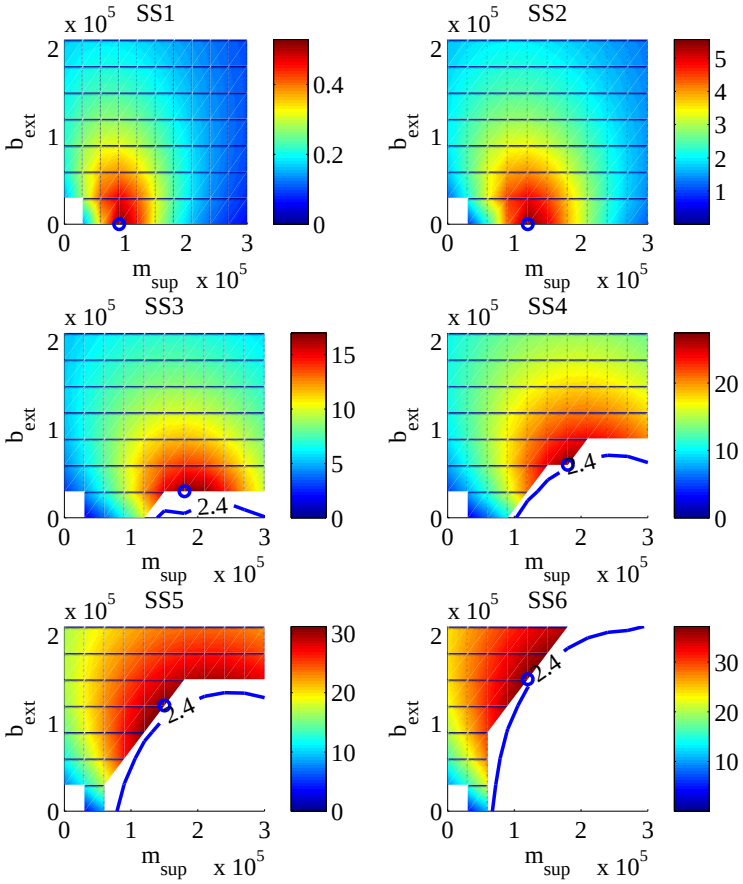

Figure 6.2: Absorbed power [kW] for SS1-6 vs. control parameters m_{sup} and b_{ext} for an unlimited available PTO force, contours for maximum lift (blue) and sinkage (black).

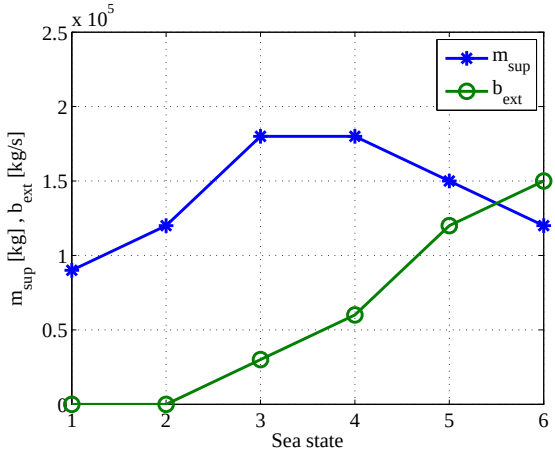

Figure 6.3: Optimal values for the control parameters m_{sup} and b_{ext} to maximise the absorbed power for the different sea states for an unlimited PTO force without inertia.

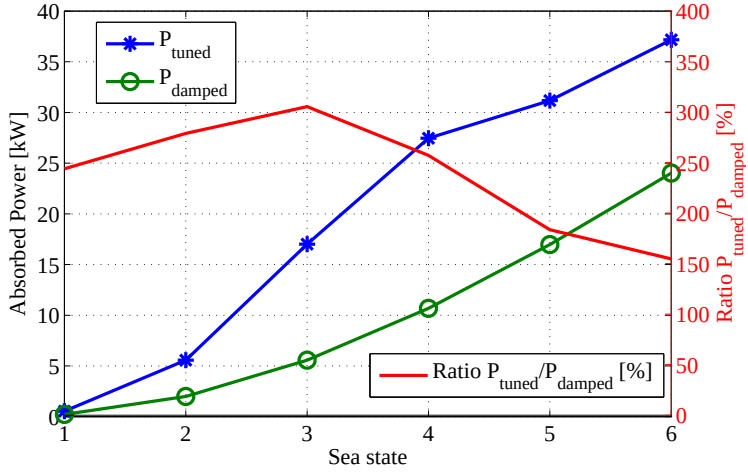

Figure 6.4: The absorbed power with a tuning strategy compared with the absorbed power with a purely damping control strategy for an unlimited PTO (left axis in [kW]), together with the ratio between the two (right axis in [%]).

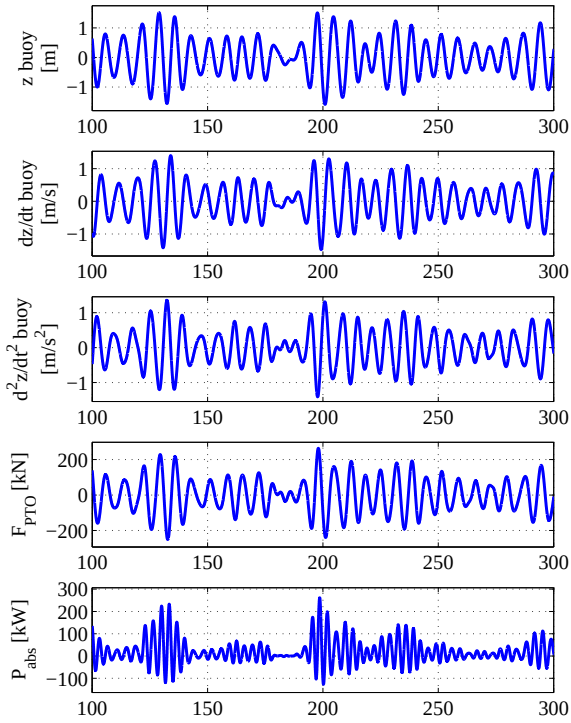

Figure 6.5: Plots of the buoy position, speed and acceleration together with the absorbed power vs. time for 200 seconds of the simulation for SS3.

6.2.3 Time course of power and buoy movement

In Fig. 6.5 the position, speed and acceleration of the buoy are plotted together with the according PTO force and the resulting absorbed power as a function of the time. The variable nature of the waves induces a peak-to-mean ratio of 15.4 for the shown SS3, peaks of 262 kW against 17 kW mean absorbed power. The peak invested (reactive) power reaches 127 kW.

There is no substantial difference noticeable between the upwards and downwards peaks of acceleration, speed or position, consequently neither in the actual absorbed power of the two directions.

6.3 Introducing PTO dynamics and efficiency

From the results of the previous analysis of the unlimited PTO, and more specifically the maximum required force, a realistic PTO can be defined being able to provide equal PTO forces. A gear ratio of 37.3 and pinion radius of 0.4 m has been taken, identical as the gear ratio and drum radius of the drum and cable PTO of Chapter 5. The dimensioning of the overall transmission stage (rack & pinion and gearbox) should optimise the total efficiency by aligning the pinion diameter, gearbox ratio and rated machine speed. The dimensioning of the rack and pinion is out of scope for this work, but the discussed methodology can be used to assess the influence of this part of the drive train as well when more information on the efficiency is at hand. In this work, the rack & pinion losses are assumed to be included in the gearbox efficiency map.

Considering the above transmission and a 1500 rpm rated machine, a power of 200 kW rated is required to apply an equal maximum PTO force as with the unlimited PTO. As explained in Chapter 5, in the simulation model the PTO technically consists of two machines, in this case two of 100 kW.

6.3.1 Influence of PTO dynamics

The absorbed power with the realistic PTO is shown for every sea state in Fig. 6.6. The maximum values are similar as for the unlimited PTO from Fig. 6.2, but a shift in optimal m_{sup} can be detected.

A 1500 rpm 200 kW rated PTO has a total machine rotor inertia of 4.53 kgm^2 (two times 2.265 kgm^2 [66]). Together with the rest of the drive train inertia, this represents an equivalent linear PTO mass m_{eq} of 40 ton (cfr. Equation (5.6)). The rack and pinion transfers PTO forces in two directions, hence the equivalent PTO mass can be seen as an increase of the floater mass and influences the natural frequency of the system. This effect is visible in the drop in optimal m_{sup} for all sea states. The control parameters are plotted in Fig 6.7, showing lower m_{sup} values for every sea state than for the unlimited PTO as plotted in Fig. 6.3. A separate sensitivity analysis on the PTO inertia is performed in Section 6.6.4.

The influence of the PTO inertia can also be noticed in the difference between the PTO force (at the rack and pinion) and the electromagnetic force. Both are plotted in the fourth graph of Fig. 6.8 accompanied with the buoy motion and corresponding actual absorbed power for SS4. The electromagnetic force F_{em} is complemented with the inertial force to form the PTO force F_{PTO}. In the same graph the capping of the electromagnetic force (i.e.machine torque) is noticeable between 195 s and 200 s, this force corresponds to a torque of 200% of the rated torque.

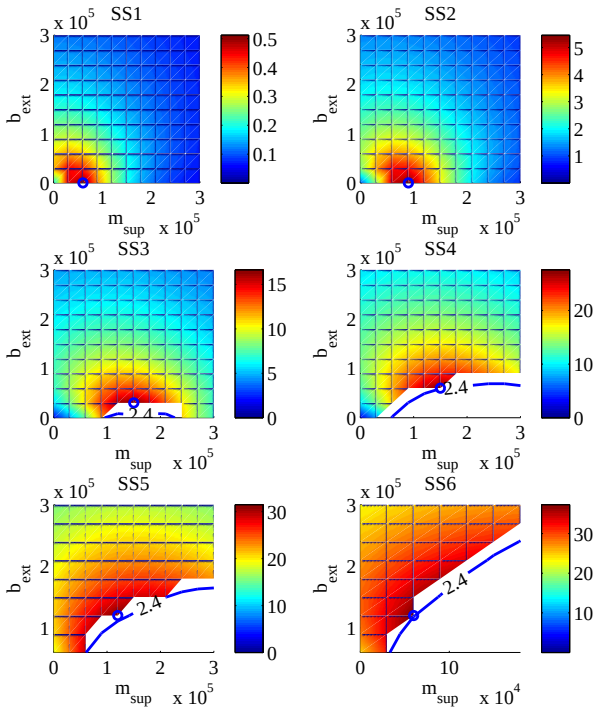

Figure 6.6: Absorbed power [kW] vs. control parameters m_{sup} and b_{ext} for a 200 kW 1500 rpm PTO, contours for maximum lift (blue).
(Please note the different range for the x axis of SS6)

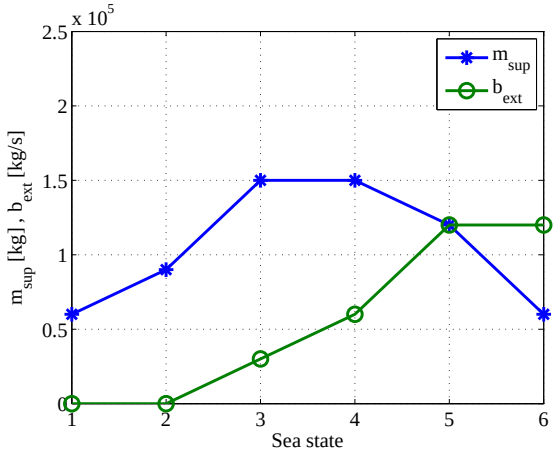

Figure 6.7: Optimal values for the control parameters m_{sup} and b_{ext} to maximise the absorbed power for the different sea states for a 200 kW PTO.

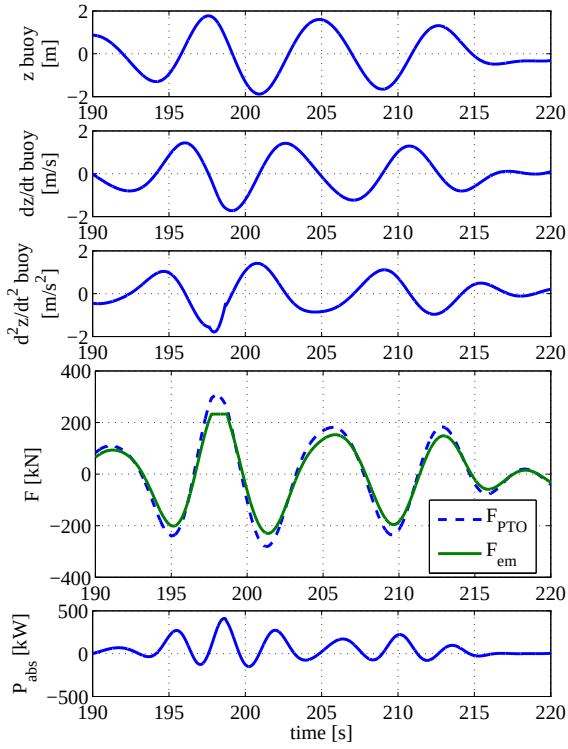

Figure 6.8: Buoy movement and PTO force together with the electromagnetic force for SS4 with a 200 kW 1500 rpm machine.

6.3.2 Influence of PTO efficiency

Analysing the absorbed power can be a first step in assessing the potential of a floater-PTO combination. However, the performance of the PTO to convert this absorbed mechanical power to electricity will decide on the profitability of the WEC, the electrical energy will after all provide the revenues.

Analogous as for the drum and cable PTO, analyses have been done using the efficiency maps of the two different machine topologies A and B with each four steps of maximum (nominal) efficiency. The details of which can be found in Chapter 3 Section 3.3.3. Next to the machine, an efficiency map for the gearbox has been included and a fixed efficiency value for the variable frequency drive, as described in Chapter 3. For the upcoming examinations a PTO of 200 kW 1500 rpm rated has been used.

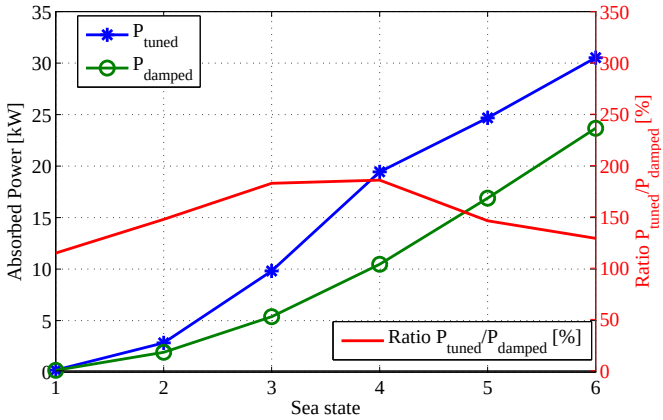

Figure 6.9: The electrical power with a tuning strategy compared with the electrical power with a purely damping control strategy, together with the ratio between the two, both for an $A1$ machine with gearbox.

6.3.2.1 Effect on control parameters

The PTO efficiency influences the control parameters to reach the maximum electrical power. The optimal tuning parameter m_{sup} to maximise the electrical power is generally lower than for the maximum absorbed power, and the damping coefficient b_{ext} is in most sea states higher. This is explained by the nature of the reactive control, a substantial amount of energy needs to be invested in the system. This energy is skimmed two times by the PTO losses before it is again converted to electricity. Hence it is not the goal to first maximise the absorbed power and subsequently convert it to electricity, because this might result in a lower electrical output than directly defining the best control parameters to maximise the electrical output. This might include less absorbed power, but more electrical.

The reactive control by adding a supplementary mass m_{sup} - or tuning - bears fruit: the mean electrical power reached with tuning is up to 185% of the electrical power reached with a purely damping strategy in SS4. This ratio is in all relevant sea states (SS2 to SS6) more than 129%, as plotted in Fig. 6.9 for a 200 kW $A1$ machine with gearbox.

6.3.2.2 Effect on produced power

Nominal efficiency

The magnitude of the nominal efficiency logically has an influence on the electrical outcome. A lower maximum efficiency is however less magnified towards the mean electrical power than with the drum and cable PTO. For a drop of 1% in maximum efficiency, a decrease in mean electrical power between 1.1% and 2.3%

Table 6.1: Difference in mean electrical power between the 4 A efficiency map variants

SS	$A1$ P_{el} [kW]	$A2$ % of $A1$	$A3$ % of $A1$	$A4$ % of $A1$
1	0.2	98.6	97.2	95.8
2	2.8	98.3	96.6	94.9
3	9.8	97.7	95.4	93.1
4	19.4	98.3	96.6	95.0
5	24.7	98.8	97.7	96.5
6	30.5	98.9	97.9	96.8

Table 6.2: Difference in mean electrical power between the 4 B efficiency map variants

SS	$B1$ P_{el} [kW]	$B2$ % of $B1$	$B3$ % of $B1$	$B4$ % of $B1$
1	0.2	98.6	97.0	95.6
2	3.4	98.4	96.5	94.8
3	12.2	97.6	94.8	92.2
4	22.4	98.4	96.4	94.6
5	27.3	98.8	97.4	96.0
6	32.8	98.9	97.5	96.3

can be observed for the A map variants, and between 1.1% and 2.8% for the B variants. The values are collected in Table 6.1 and Table 6.2 for the A and B maps respectively, and plotted in Fig. 6.10.

The electrical output in SS1 is too low to deliver any usable energy to the electricity grid, considering uncertainties in the model and the fact that auxiliaries are not taken into account in the model. Therefore the results for SS1 might be omitted in further results to concentrate on the relevant sea states.

Shape of the efficiency map

The shape of the efficiency map has a substantial effect on the average performance of a PTO. Fig. 6.10 illustrates this by the fact that all four B variants show higher electrical powers than the A variants while $A1$ and $A2$ have a higher maximum efficiency than $B4$.

To investigate the influence of the shape of the efficiency map more closely, the $A1$ and $B3$ variants are compared because they have an equal maximum efficiency. The numbers are put side by side in Table 6.3 and demonstrate a significant higher performance of the $B3$ map. Next to the electrical power, also the absorbed power has been displayed in columns 5 to 7. In column 7 the absorbed power of the two cases is compared and except for SS3 the absorbed power is identical. (In

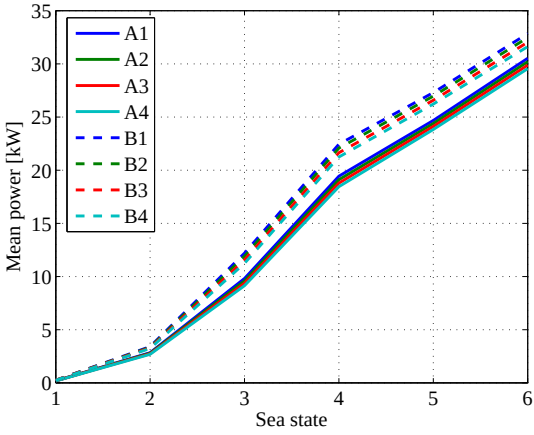

Figure 6.10: Mean electrical power vs. sea state for the 8 efficiency map variants for a 200 kW PTO with gearbox.

Table 6.3: Comparison of the electrical power P_{el} and absorbed power P_{abs} between $A1$ and $B3$ efficiency maps with equal nominal efficiency but different shape, and the resulting average PTO efficiency $P_{\mathrm{el}}/P_{\mathrm{abs}}$, for a 200 kW PTO with gearbox

		P_{el} [kW]	$B3$		P_{abs} [kW]	$B3$	P_{el} / P_{abs} [%]	
SS	$A1$	$B3$	% of $A1$	$A1$	$B3$	% of $A1$	$A1$	$B3$
2	2.8	3.3	116	4.8	4.8	100	59.6	69.2
3	9.8	11.6	118	16.0	16.6	104	61.4	69.5
4	19.4	21.6	111	27.6	27.6	100	70.5	78.5
5	24.7	26.6	108	31.5	31.5	100	78.4	84.4
6	30.5	32.0	105	37.3	37.3	100	81.8	85.8

SS3 the absorbed power is higher for the $B3$ case because the optimal parameters resulted in a higher tuning value (150 000 kg instead of 120 000 kg). The higher efficiency of the machine allows here to to use more reactive power to increase the net absorbed power.) Hence the higher electrical output of 5% to 16% is almost solely due to the better average conversion ability from mechanical to electrical power of the $B3$ machine as shown in the last two columns. The use of a $B3$ map results in an average efficiency ($P_{\mathrm{el}}/P_{\mathrm{abs}}$) that is 4% to 9.6% more than with the $A1$ map. Nonetheless, the difference is less pronounced than with the drum and cable PTO topology.

The values of the average efficiency in column 8 and 9 show that the use of efficiency maps is justified and even necessary as upgrade to the use of a fixed efficiency value, because the values differ significantly depending on the sea state. It also makes clear that a WEC should not be appraised by its absorbed power, but

Table 6.4: The six power steps [kW] for the sensitivity analysis on rated power.

	$P1$	$P2$	$P3$	$P4$	$P5$	$P6$
Rated power [kW]	34	66	100	134	166	200

by its electrical output.

6.4 Influence of PTO installed power

As for the drum and cable PTO, a sensitivity study on the installed power has been performed for the rack and pinion PTO as well. Six power steps between 34 kW and 200 kW have been defined as listed in Table 6.4. The values do not necessarily correspond to available machine ratings, but are used here to illustrate the influence of the installed power. The rated speed is fixed on 1500 rpm and the rotor inertia is in relation to the installed power, i.e. torque, ranging from 0.76 kgm^2 to 4.53 kgm^2 based on interpolated data from [66].

For each power step, the optimal control parameters have been defined for every sea state accounting for the floater and PTO constraints, depicted by the colour plots of Fig. 6.11 as a result of approximately 4000 simulation runs.

PTO constraints

The graphs of Fig. 6.11 demonstrate that the thermal capacity, i.e. the condition that the RMS torque needs to stay below the rated torque of the machine, is the limiting factor for the lower installed powers up to $P3$. From $P4$ on, the lift constraint takes over to determine the control parameters m_{sup} and b_{ext}. Apparently the RMS torque and lift constraints are the only limits reached. This is also illustrated by the plots of the normalised limits of Fig. 6.12. As the sinkage limit is higher than the lift constraint, and due to the damping in both directions, the sinkage limit is never reached. The normalised speed peaks of the bottom graph show that there is margin in the speed operation range of the PTO to reduce its installed power. As already mentioned, the RMS torque constraint is the limiting factor for the lower installed powers, and has some margin from $P5$ on, thus the machine is then never used at its maximum thermal capacity which could be interpreted as over-dimensioned. It is doubtable that $P5$ or $P6$ would be more profitable than $P4$ or lower because the gradient of the power curves drop strongly from $P4$.

By choosing the control parameters to respect these constraints, it is assumed that they are respected. Nevertheless, a final design will have to encompass for example a mechanical damped end-stop for the floater stroke. The stroke length is to be determined based on the maximum stroke during operation and accounting for the tidal range.

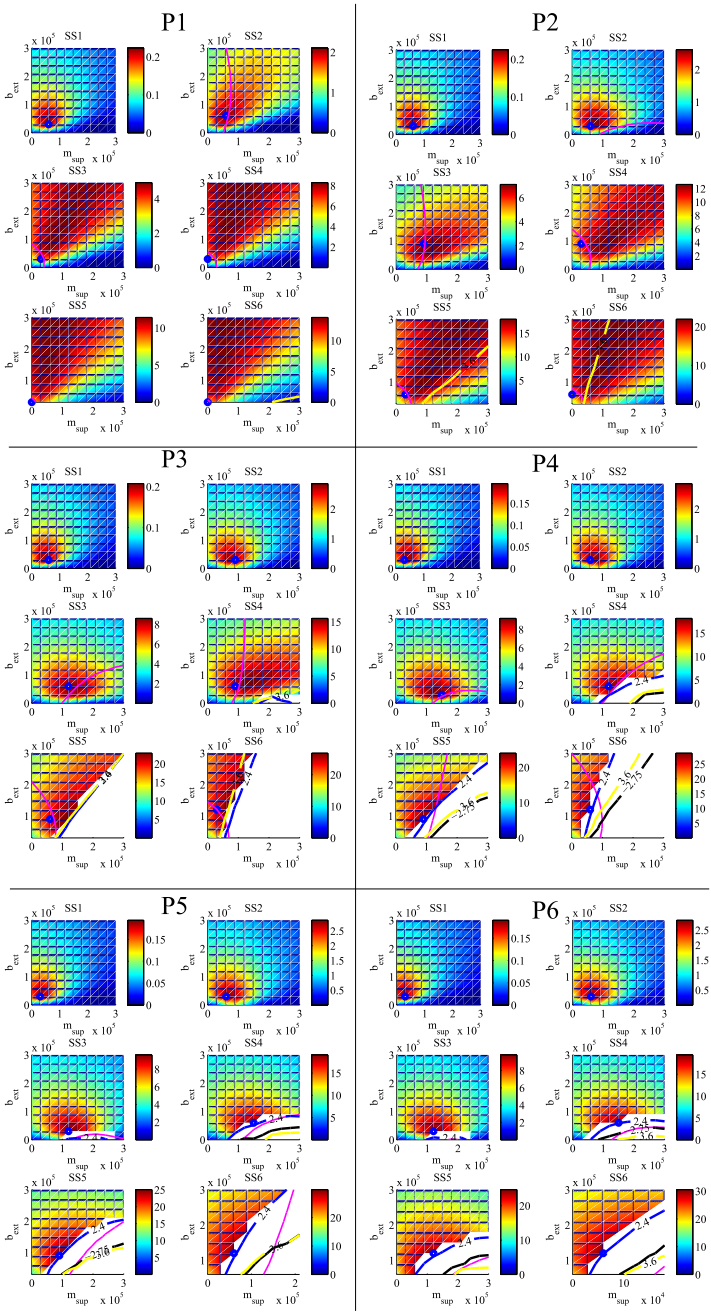

Figure 6.11: Electrical power [kW] vs. control parameters m_{sup} and b_{ext} for the 6 steps of PTO power with gearbox and $A1$ machine efficiency map, contours for maximum sinkage (black), speed (yellow), RMS torque (magenta) and lift (blue).

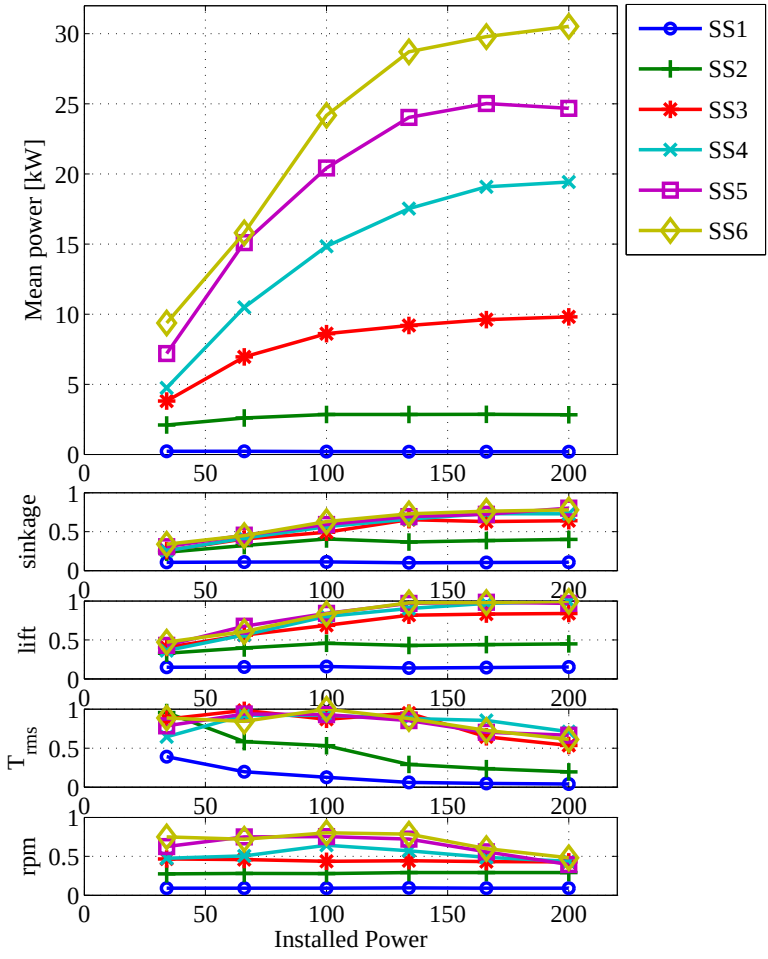

Figure 6.12: Mean electrical power per sea state vs. installed power with normalised values in relation to the constraint limits for sinkage, lift, RMS torque and rpm, for an $A1$ machine and gearbox.

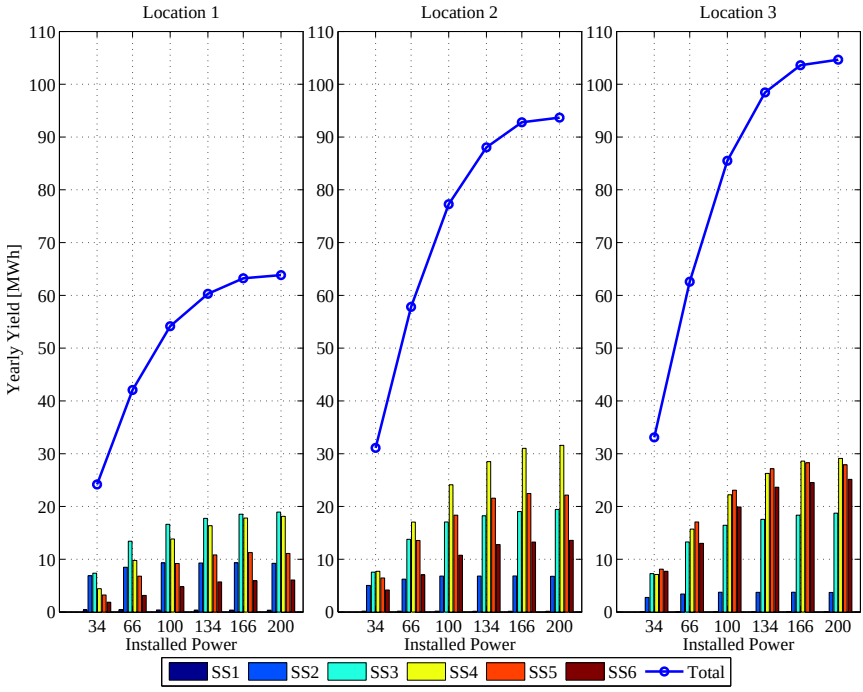

Figure 6.13: Yearly energy yield vs. the installed power for the 3 locations together with the energy fractions per sea state for the $A1$ efficiency map and gearbox.

Overview of the results

The upper plot of Fig. 6.12 depicts the mean electrical power for every sea state in relation to the installed power. The gradient is higher as the wave condition gets more energetic and diminishes as the installed power increases. This behaviour is attributed to the reaching of the lift limit: the power is capped to respect the constraints.

6.5 Influence of location

While a power curve is interesting to estimate the potential of a PTO in a certain floater, the location and its wave climate will determine to which degree this potential is useful towards the yearly electrical energy yield. The optimal dimensioning might be location dependent, hence an analogous calculation as in Chapter 5 Section 5.5 for the same three locations is analysed and described there.

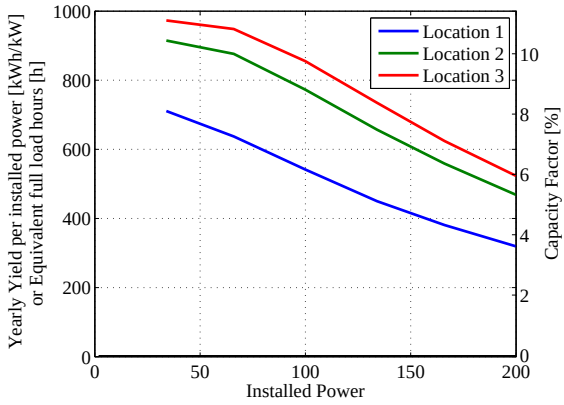

Figure 6.14: The yearly yield per installed power [kWh/kW], or full load hours [h] on the left y-axis, and the capacity factor [%] on the right y-axis vs. the installed power for the three locations, with an $A1$ efficiency map and gearbox.

6.5.1 Yearly energy yield vs. installed power per location

Given the occurrence frequency of each sea state for Location 1 to 3, and the power curves of Fig. 6.12, the yearly electrical energy yield can be quantified. The yields are plotted in relation to the installed power in Fig. 6.13. The significant difference in magnitude and gradient between the three locations indicates clearly that the location is not only of substantial importance for the magnitude of potential energy, but that the decision of the installed power of the PTO should account for the local wave climate. Indeed, the gradient of the yield vs. installed power is higher for a high energy location than for a low energy location, which might determine the economic incentive for a high installed power. The incentive also depends on the ratio of PTO cost vs. total cost (the share of the PTO cost is estimated at 20% - 30% of the total manufacturing cost of the WEC [30–32]).

Next to the total yield, the fractions per sea state are plotted as bars to show the contribution of each sea state in the three locations.

6.5.1.1 Capacity factor

The amount of energy per kW installed power, or full load hours, is an interesting measure to know the degree to which a machine is used in relation to its full capacity. It is thus also expressed as the capacity factor in [%] by dividing the full load hours by the hours in one year.

The three expressions are plotted in Fig. 6.14 for the three locations. The capacity factor is almost halved between $P1$ and $P6$, but here again the total cost of the WEC and operational costs should be considered to make an informed decision of installed power.

Table 6.5: Difference in yearly energy yield (YY) between the 4 A efficiency map variants for the three locations, for installed power $P5$ and $P3$. For $A1$ the absolute value is given in MWh, for the other variants the ratio vs. $A1$ is given in %

Installed power	Location	$A1$ YY [MWh]	$A2$ % of $A1$	$A3$ % of $A1$	$A4$ % of $A1$
$P5$	Location 1	63.2	98.3	96.6	94.8
	Location 2	92.8	98.4	96.8	95.2
	Location 3	103.6	98.5	97.0	95.4
$P3$	Location 1	54.2	98.5	97.0	95.5
	Location 2	77.3	98.6	97.2	95.8
	Location 3	85.5	98.7	97.4	96.1

6.5.1.2 Influence of the PTO efficiency on the yearly yield per location

Next to the influence of the PTO efficiency on the power discussed in Section 6.3.2, the effect on the yearly yield is assessed. Fig. 6.15 collects the graphs for the three locations which plot the yield as a function of the installed power for all eight efficiency map variants.

Within the map variants

The difference within the A and B maps respectively is visible in Fig. 6.15 and quantified in Table 6.5 and Table 6.6. The effect of the nominal efficiency is more pronounced for the B maps than for the A maps, but is for both in the order of magnitude of 1.5% - 2% yield drop per percent in nominal efficiency for a $P5$ PTO, and approximately 1.5% yield drop per percent for a $P3$ PTO. The influence is smaller if the location is more energetic.

Between the A and B map variants

The difference between the B and A variants is significant. From Fig. 6.15 can be noticed that a $P4$-$B3$ PTO produces 117% of a $P4$-$A1$ PTO for an equal installed power and identical nominal efficiency at Location 1. Alternatively, to reach an equal yield of 60 MWh, a $B3$ machine needs only 70% of the installed power of a $P4$-$A1$.

For $P5$ and $P3$, the average annual yields of an $A1$ machine and a $B3$ machine are compared with each other for the three locations in Table 6.7. The ratio of yield of $B3$ over $A1$ lies between 111% and 115%.

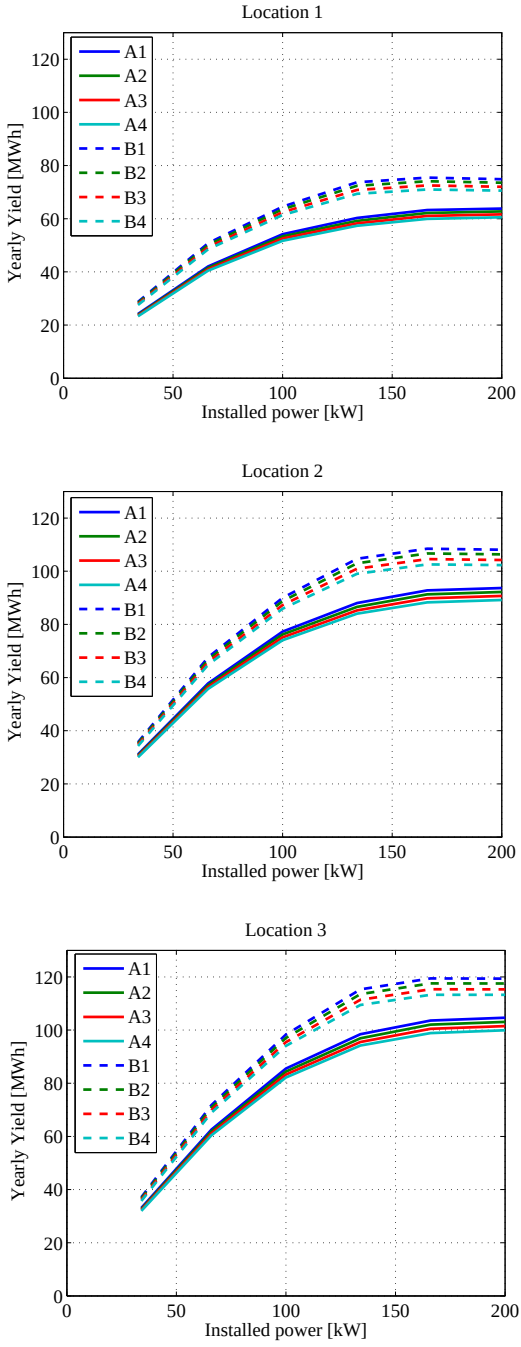

Figure 6.15: Yearly energy yield vs. the installed power for the A and B variants efficiency map also including a gearbox map for Location 1, 2 and 3.

Table 6.6: Difference in yearly energy yield (YY) between the 4 B efficiency map variants for the three locations, for installed power $P5$ and $P3$. For $B1$ the absolute value is given in MWh, for the other variants the ratio vs. $B1$ is given in %

Installed power	Location	$B1$ YY [MWh]	$B2$ % of $B1$	$B3$ % of $B1$	$B4$ % of $B1$
$P5$	Location 1	75.5	98.2	96.1	94.1
	Location 2	108.5	98.3	96.4	94.5
	Location 3	119.5	98.4	96.6	94.8
$P3$	Location 1	64.5	98.5	96.8	95.2
	Location 2	90.0	98.6	97.0	95.5
	Location 3	98.3	98.7	97.1	95.7

Table 6.7: Comparison of the yearly energy yield between $A1$ and $B3$ efficiency maps with equal nominal efficiency but different shape, for a $P5$ and $P3$ PTO with gearbox

Installed power	Location	$A1$ [MWh]	$B3$ [MWh]	$B3$ % of $A1$
$P5$	Location 1	63.2	72.5	115
	Location 2	92.8	104.6	113
	Location 3	103.6	115.4	111
$P3$	Location 1	54.2	62.4	115
	Location 2	77.3	87.3	113
	Location 3	85.5	95.5	112

6.6 Electromechanical optimisation of PTO sizing

6.6.1 Optimising the available speed

The pragmatic reduction of the rated speed done for the drum and cable PTO in Chapter 5 learned that an integrated approach of the speed reduction in the simulation is necessary to achieve solid results. Therefore the methodology of varying both the torque and speed of the PTO machine is immediately applied on the rack and pinion topology as a second case study.

6.6.2 Optimizing rated torque and speed

Fig. 6.12 showed a margin towards the maximum speed limit of the machine. Up to $P4$ there is a margin of 20%, and this margin even increases for $P5$ and $P6$ to up to 50% because a higher available machine torque can damp the floater more. Hence a significant potential for power reduction arises.

Table 6.8: The five steps in rotational speed $n1$ to $n5$ in [rpm] and the six steps in torque $T1$ to $T6$ in [Nm].

	$n1$	$n2$	$n3$	$n4$	$n5$
[rpm]	1100	1200	1300	1400	1500

	$T1$	$T2$	$T3$	$T4$	$T5$	$T6$
[Nm]	212	424	637	849	1061	1273

Analogous as for the drum and cable PTO, a thorough study of 30 rated powers has been performed with torque and rated speed combinations as given in Table 6.8. The values are not set at ratings of available machines, but as a tool to illustrate the influence of the available torque and speed. The change in available speed can be effectuated by changing the transmission ratio of the drive train. A $n4$ machine, for example, can be realised with a 1500 rpm machine and a gearbox ratio that is 1500/1400 higher than the $n5$ case. When both have a $T6$ rated torque, the rated torque of the $n4$ machine will in reality be lower than the 1273 Nm, to be exact: 1400/1500*1273 = 1188 Nm.

The values for the rated speed are to be seen as virtual, and the speed

For each of the 30 combinations all six sea states are simulated with on average 100 sets of m_{sup} and b_{ext}, counting for approximately 18 000 simulation runs. By optimising the control parameters for each case, not only the power is optimised, but automatically the corresponding PTO constraints of speed and RMS torque are respected.

The $T6$-$n5$ case has the same power as the $P6$ case, i.e. 200 kW. To concentrate on the influence of torque and speed, the PTO inertia has been fixed for all cases at the value from the $P5$ case, i.e. a rotor inertia value of 3.8 kgm^2, consisting of two times 1.9 kgm^2 based on a PTO split up in two machines analogous to the Wave Pioneer.

With the described methodology, the PTO will no longer be dimensioned for maximised power output in the most demanding sea state, but the yearly performance as a function of rated torque and speed will be quantified to provide a starting point for a techno-economic optimisation. A logical design choice is not to maximise the power output, but will be a well-thought-out cost-benefit analysis.

6.6.2.1 Mean electrical power - $A1$ map

The mean electrical power as a function of the rated torque and speed has been displayed in the colour plots of Fig. 6.16. The plots reveal that a higher mean power can be reached with a lower rated speed. This is similar as with the drum and cable topology, and the scatter of operation points above the merged efficiency map of

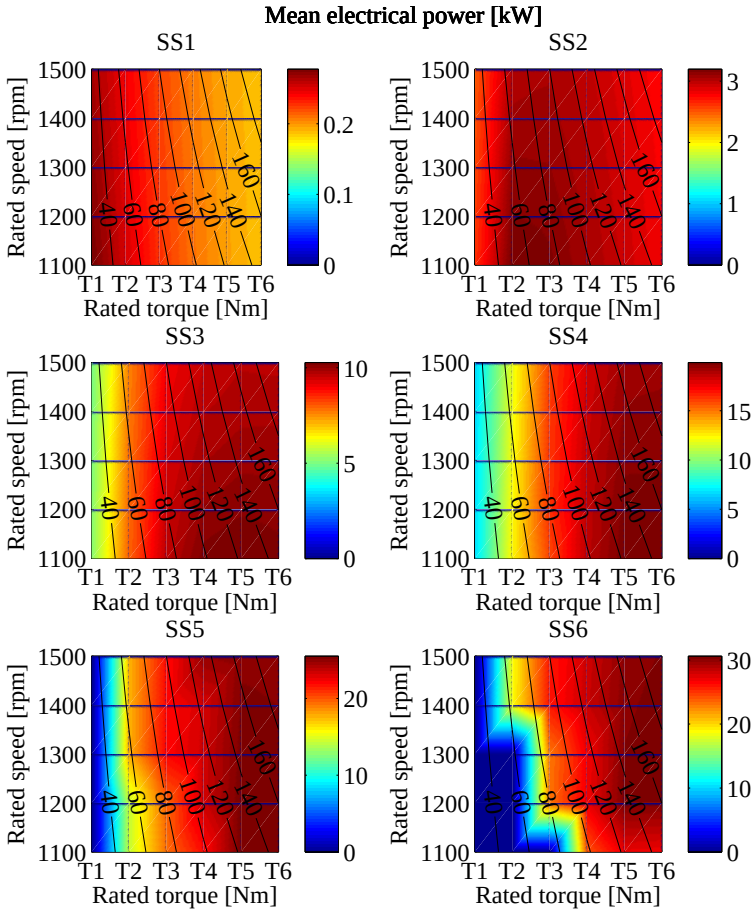

Figure 6.16: Mean electrical power ($A1$ map & gearbox) vs. rated torque and speed for sea states 1 to 6, contour lines for the rated power [kW].

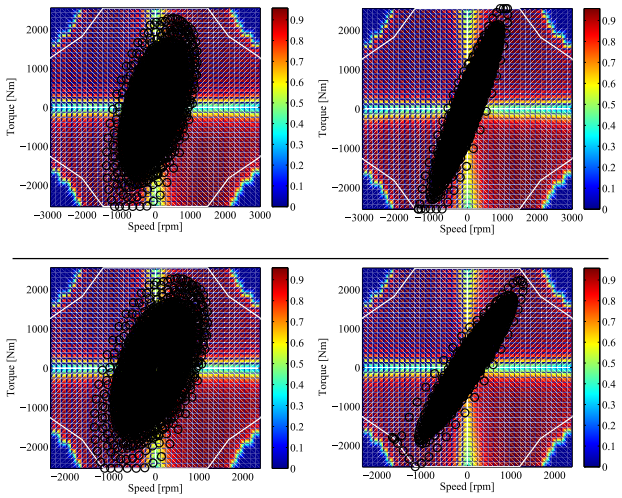

Figure 6.17: Scatter of the operating points for SS4 (left) and SS6 (right) on a merged efficiency map of $A1$ machine and gearbox for a $T6$-1500 rpm (upper) and a $T6$-1200 rpm (bottom) rated machine.

machine and gearbox of Fig. 6.17 indeed shows an equal behaviour: the operation points are shifted to better efficiency zones when the rated speed is reduced. The two left figures correspond with a SS4 wave condition and the right figures with a SS6. The upper plots display the operation range of a 1500 rpm rated machine, the lower a 1200 rpm.

It appears that it might be interesting to use the machine up to more than 200% of its rated speed. In [12] it is found that a so called overspeed factor of five can be reached without significant loss in annual energy, and only 10% drop for an overspeed factor of 10.

6.6.2.2 Constraints - $A1$ map

The normalized values for the floater and PTO parameters that are subjected to a constraint are now also plotted as colour plots as a function of rated torque and speed in Fig. 6.18. The reaching of the limits does not show large dissimilarities with the sensitivity study on installed power, except the logical effect of a dropping speed margin with decreasing rated speed.

6.6.2.3 Yearly yield - $A1$ map

By combining the mean electrical power for every sea state with the occurrence for the three locations, and this for all 30 torque-speed combinations, the average annual yield plots of Fig. 6.19 are composed. The left column of this figure shows

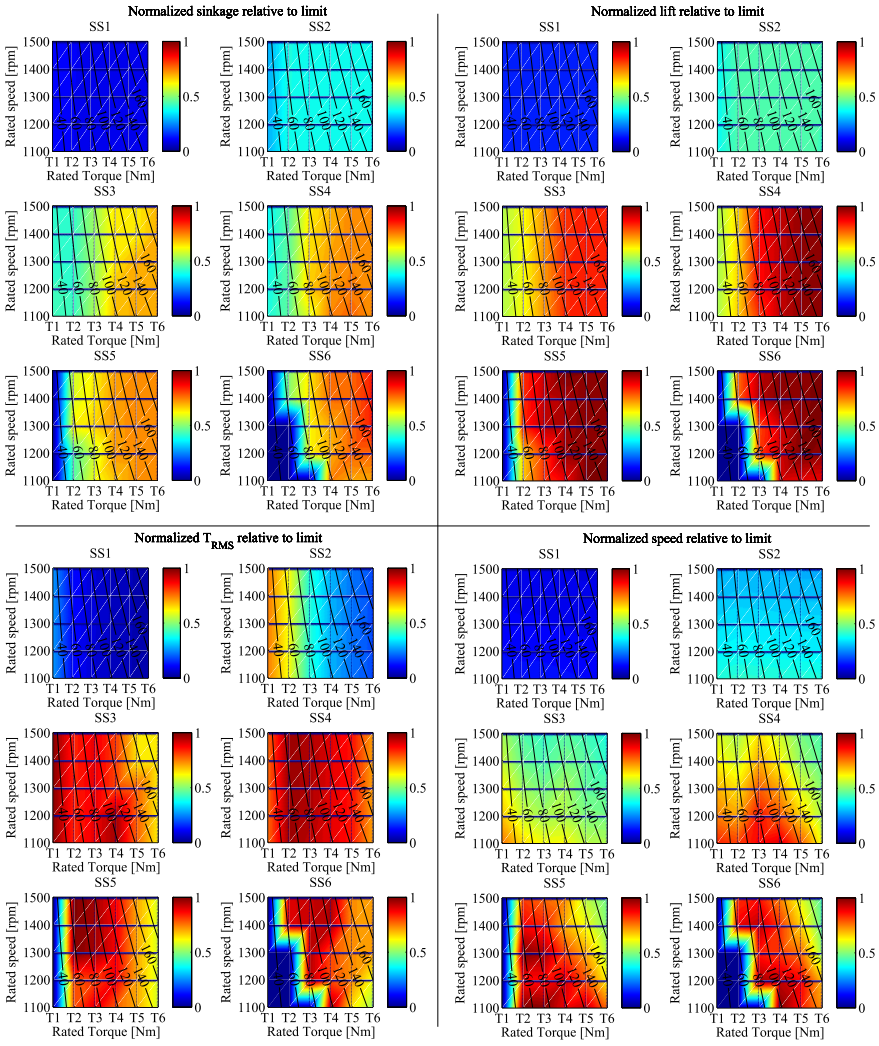

Figure 6.18: Normalised values in relation to the constraint limits for sinkage, lift, RMS torque and speed, for an $A1$ machine and gearbox.

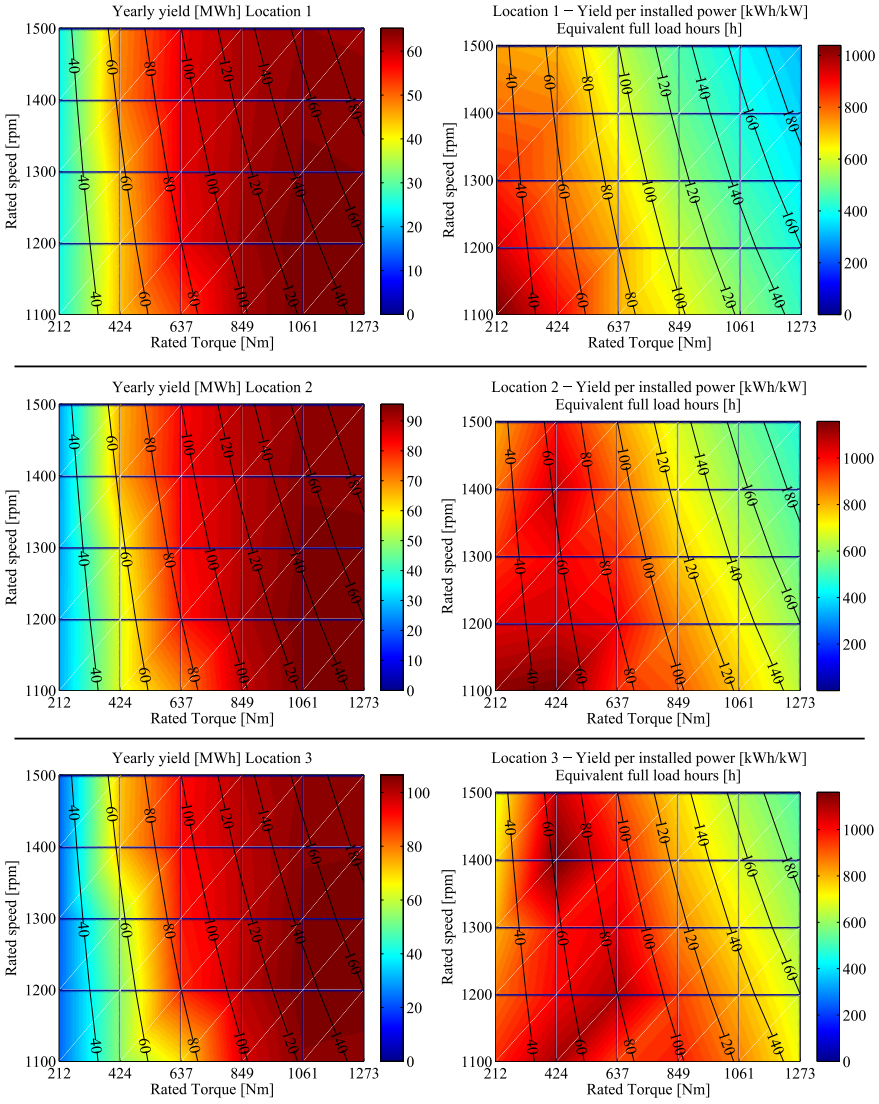

Figure 6.19: The yearly yield [MWh] vs. the rated torque and speed (left column), and the yearly yield per installed power [kWh/kW], or equivalent full load hours [h] vs. the rated torque and speed (right column), for the three locations, with an $A1$ efficiency map and gearbox.

Table 6.9: The ratio in [%] relative to the maximum yield at Location 1, 2 and 3 respectively for every rated torque and speed combination for an $A1$ map.

Location 1	$T1$	$T2$	$T3$	$T4$	$T5$	$T6$
$n5$	37.4	73.0	88.3	94.7	96.9	96.5
$n4$	37.8	73.8	89.1	94.5	97.9	97.4
$n3$	38.2	68.8	89.0	95.0	98.9	98.4
$n2$	38.6	67.1	88.0	95.9	100.0	99.1
$n1$	38.9	67.8	80.8	94.9	99.9	98.9
Location 2	$T1$	$T2$	$T3$	$T4$	$T5$	$T6$
$n5$	28.0	69.0	86.2	94.1	97.1	97.1
$n4$	28.3	69.6	86.9	93.4	98.0	98.0
$n3$	28.6	61.4	86.2	93.6	99.0	98.8
$n2$	28.8	58.8	84.5	94.3	100.0	99.4
$n1$	29.0	59.2	73.1	92.2	99.2	98.6
Location 3	$T1$	$T2$	$T3$	$T4$	$T5$	$T6$
$n5$	21.4	67.3	85.6	93.8	97.3	97.5
$n4$	21.6	67.8	86.2	92.9	98.2	98.3
$n3$	21.8	53.7	84.5	92.6	99.1	99.2
$n2$	22.0	50.6	82.4	93.2	100.0	99.5
$n1$	22.1	50.9	64.0	89.9	98.1	97.6

the yearly yield values in MWh and the right column displays the yield per installed power in kWh/kW, or in equivalent full load hours. The resulting yields from this analysis demonstrate that a reduction of installed power can be achieved by lowering the rated speed with even an rising energy production.

In Table 6.9 the ratio of power relative to the maximum at each location is gathered. At Location 1, for example, a $T5$-$n2$ machine produces in an average year 3% more energy with a PTO that has 20% less installed power than a $T5$-$n5$. Otherwise, a $T3$-$n2$ produces only 9% less than the $T5$-$n5$ case with only half of the installed power. The same exercise can be made for other cases and at the other locations. The right choice of PTO size can be made considering the total manufacturing cost of both floater and PTO, together with installation and operational costs (and ideally a life-cycle assessment including end-of-life costs and impact). By consequently quantifying the revenues using the obtained yields with the described methods, the most profitable WEC can be dimensioned.

It should be noted that the relevant machines of the torque-speed combinations should be subjected to an extra thorough technical assessment. This should include amongst others a check-up if ample margin is available towards the speed operation range, and the eventual consequences if the limit is crossed. Most machines have a larger mechanical speed limit than electrical, hence this offers a buffer. Ei-

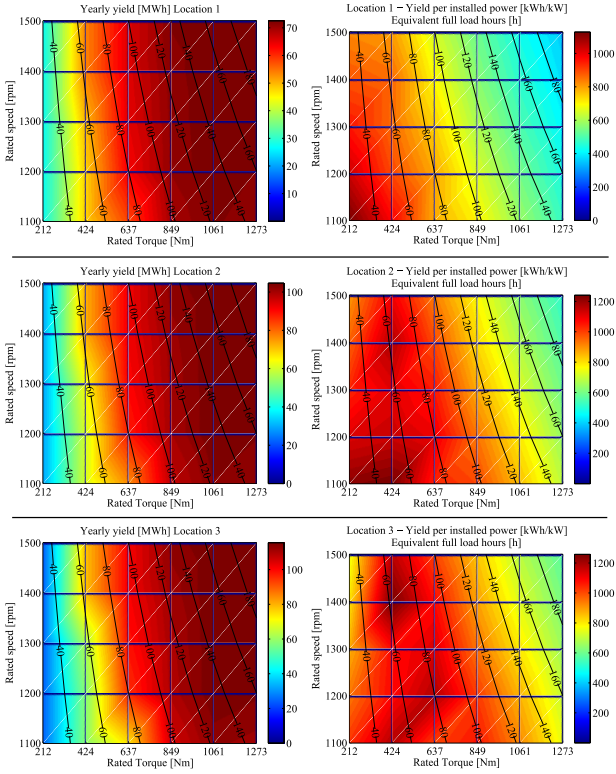

Figure 6.20: The yearly yield [MWh] vs. the rated torque and speed (left column), and the yearly yield per installed power [kWh/kW], or equivalent full load hours [h] vs. the rated torque and speed (right column), for the three locations, with a $B3$ efficiency map and gearbox.

ther way, an advanced control should monitor this in real-time and adapt the PTO action to avoid crossing the limits. This also counts for RMS torque and the floater constraints of lift and sinkage as well.

6.6.2.4 Yearly yield - $B3$

The $B3$ efficiency map has a relatively flatter shape than the $A1$ map, but has an equal maximum efficiency. By comparing these two maps, the influence of this shape of the efficiency map is appraised. With the $B3$ map, the average yearly yield barely changes with changing rated speed as illustrated in Fig. 6.10 and represented as the ratio with respect to the maximum in Table 6.10. This is a consequence of the flatter shape of the $B3$ map (even when merged with the gearbox efficiency). For a PTO with a $T5$ rated torque, a reduction of 20% in installed power can be effectuated without yield loss from $n5$ to $n2$.

Table 6.10: The ratio in [%] relative to the maximum yield at Location 1, 2 and 3 respectively for every rated torque and speed combination for a $B3$ map.

Location 1	$T1$	$T2$	$T3$	$T4$	$T5$	$T6$
$n5$	37.9	73.7	90.0	98.6	99.9	98.7
$n4$	38.0	73.8	89.9	97.7	100.0	98.7
$n3$	38.0	68.4	89.1	97.3	100.0	98.7
$n2$	38.0	66.1	87.2	97.0	100.0	98.3
$n1$	38.0	66.1	79.8	95.0	98.8	97.2
Location 2	$T1$	$T2$	$T3$	$T4$	$T5$	$T6$
$n5$	28.4	69.6	87.9	97.7	99.9	99.1
$n4$	28.5	69.6	87.8	96.3	100.0	99.1
$n3$	28.5	61.2	86.5	95.7	100.0	99.1
$n2$	28.5	58.1	83.9	95.2	100.0	98.6
$n1$	28.4	58.0	72.6	92.4	98.2	97.0
Location 3	$T1$	$T2$	$T3$	$T4$	$T5$	$T6$
$n5$	21.8	67.8	87.3	97.5	99.9	99.5
$n4$	21.8	67.8	87.2	95.9	100.0	99.5
$n3$	21.8	53.8	85.1	94.8	100.0	99.5
$n2$	21.8	50.1	82.0	94.2	100.0	98.8
$n1$	21.8	50.1	63.9	90.5	97.2	96.2

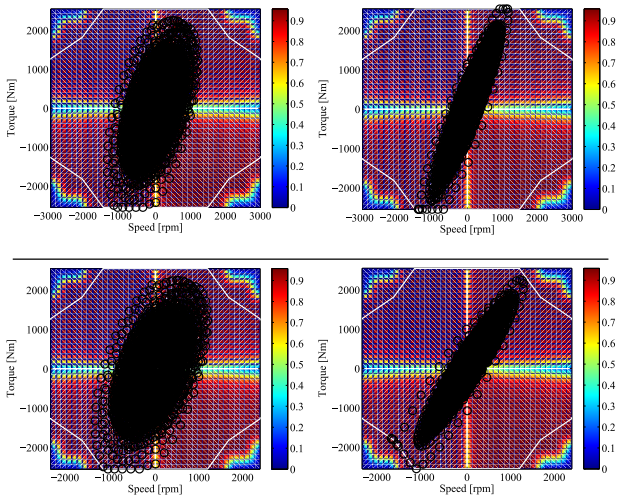

Figure 6.21: Scatter of the operating points for SS4 (left) and SS6 (right) on a merged efficiency map of $B3$ machine and gearbox for a $T6$-1500 rpm (upper) and a $T6$-1200 rpm (bottom) rated machine.

Table 6.11: Comparison of the yearly yield of the $B3$ cases with the $A1$ cases as YY($B3$)/YY($A1$) in [%].

Location 1	$T1$	$T2$	$T3$	$T4$	$T5$	$T6$
$n5$	113	112	113	116	115	114
$n4$	112	111	112	115	114	113
$n3$	111	111	111	114	112	111
$n2$	110	109	110	112	111	110
$n1$	109	108	110	111	110	109
Location 2	$T1$	$T2$	$T3$	$T4$	$T5$	$T6$
$n5$	111	110	112	114	113	112
$n4$	110	109	111	113	112	111
$n3$	109	109	110	112	111	110
$n2$	108	108	109	111	109	109
$n1$	107	107	109	110	108	108
Location 3	$T1$	$T2$	$T3$	$T4$	$T5$	$T6$
$n5$	110	109	111	113	111	111
$n4$	109	108	110	112	110	110
$n3$	109	108	109	111	109	109
$n2$	108	107	108	109	108	108
$n1$	107	107	108	109	107	107

The merged efficiency map of $B3$ machine and gearbox is depicted in Fig. 6.21 with the operation points scattered upon it. The two left figures originate from a SS4 simulation and the right figures form a SS6, the upper figures for a 1500 rpm rated machine, the bottom figures for a 1200 rpm device. The shift of the operation points is quasi identical as in Fig. 6.17. The change in yield was more pronounced in the study of the $A1$ map however, demonstrating the importance of considering the efficiency over the complete working region.

Replacing an $A1$ by a $B3$ machine results in a yield gain between 8% and 16%, depending on the case and location as illustrated by Table 6.11. The incentive diminishes slightly when the location is more energetic.

6.6.3 Direct drive machine

The use of a direct drive (DD) machine omits the need of a gearbox in the PTO drive train, as it runs at the speed of the pinion shaft. Seen the efficiency map of the gearbox in Fig. 5.4, it is clear that the influence on the energy yield is larger than if the losses were appraised by only considering the nominal datasheet efficiency of 95.5%. The speed of the direct drive machine can be adjusted in the design process by choosing an appropriate pinion diameter with a high transmission efficiency.

Table 6.12: Comparison of the yearly yield of the $B3$ direct drive (DD) cases with the $B3$ gearbox cases as YY(DD)/YY(GB) in [%].

Location 1	$T1$	$T2$	$T3$	$T4$	$T5$	$T6$
$n5$	103	93	101	103	111	114
$n4$	103	93	99	103	111	115
$n3$	103	100	100	102	109	115
$n2$	104	104	100	99	106	114
$n1$	104	101	106	98	103	111
Location 2	$T1$	$T2$	$T3$	$T4$	$T5$	$T6$
$n5$	116	91	99	102	109	112
$n4$	116	91	96	101	108	112
$n3$	116	103	98	99	106	112
$n2$	116	109	97	96	101	112
$n1$	116	105	108	95	99	108
Location 3	$T1$	$T2$	$T3$	$T4$	$T5$	$T6$
$n5$	141	90	98	101	108	111
$n4$	141	90	95	100	107	111
$n3$	141	113	97	98	104	111
$n2$	141	121	95	94	99	110
$n1$	141	114	118	93	97	107

Not only the assumed efficiency gain is an advantage, furthermore a direct drive PTO could involve a smaller risk of mechanical failures and reduce maintenance interventions. A drawback is an expected higher manufacturing cost.

To appraise the performance of the direct drive option, new simulation runs have been executed without a gearbox in the drive train, and control parameters have been optimised at every sea state and every rated torque and speed combination to maximise the electrical power while respecting the system constraints. The analysis has been done for a $B3$ map only, as the A maps are based on an induction machine which efficiency is assumed too low for high pole machines.

The comparison between the direct drive and geared PTO has been summarised in Table 6.12. The ratio of the yield from a direct drive relative to the yield from a fast turning machine with gearbox is given.

The numbers however are out of expectation: at some cases the yield of the direct drive is lower than the geared PTO, down to a ratio of 90%, still other cases have a ratio of up to 118% (considering the $T3$ to $T6$ cases). The lower yields are assumed to be attributed to the fact that the equivalent PTO mass is substantially lower. The absence of a significant amount of equivalent PTO mass apparently could affect the yearly yield more in some cases than a better drive train efficiency. With a geared PTO, even with a moderate available electromagnetic torque, the

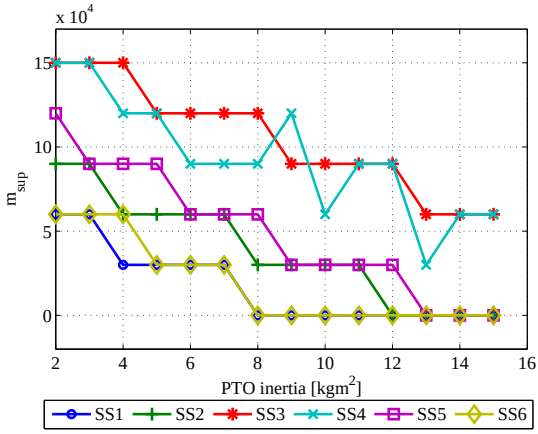

Figure 6.22: Supplementary mass m_{sup} [kg] vs. rotor inertia [kgm^2] for an $A1$ $T4$-$n5$ machine.

PTO torque can reach higher values due to the PTO inertia, and thus absorb more energy from the waves. The influence of the direct drive inertia is close to zero, the equivalent PTO mass of this simulation series is 870 kg, against 40 000 kg for a PTO with gearbox.

In the higher torque cases the performance is higher with the direct drive than with the geared PTO, which can be explained by the fact that there is enough electromagnetic torque available to tune the WEC by reactive control, and together with the better PTO efficiency this results in higher yields. Furthermore, the gearbox is more often operated at partial load with lower efficiency than with the lower torque cases. PTOs with a lower installed torque operate more often at the maximum torque where the gearbox efficiency is higher. Thus the influence of the gearbox is more pronounced with the higher installed torques.

The explanation of the higher performance for the $T1$ cases and the cases with low torque and speed, can be found in the fact that the geared PTO cannot operate in the $T1$ cases in SS5 and SS6, neither in $T2$-$n1$-3 and $T3$-$n1$ in SS6.

6.6.4 Optimizing the PTO inertia

With the rack and pinion PTO topology, the PTO inertia affects the hydrodynamic behaviour in both directions which makes its influence much larger than with the drum and cable PTO.

An increasing physical inertia reduces the need of motor tuning (reactive control), as demonstrated by the descending m_{sup} curves in Fig. 6.22 with ascending physical inertia, and this for all sea states. An increase of 1 kgm^2 corresponds to approximately 8350 kg equivalent PTO mass (cfr. Equation 5.6). Furthermore, the

Table 6.13: Comparison of the yearly yield in relation to the maximum [%] vs the PTO inertia for Location 1, 2 and 3.

Inertia [kgm^2]	Location 1	Location 2	Location 3
2	81.7	85.3	88.1
3	84.7	88.5	91.4
4	85.7	88.9	91.4
5	88.6	91.7	93.7
6	89.6	92.2	94.7
7	90.9	93.4	95.4
8	93.0	95.5	96.9
9	93.3	95.0	96.9
10	96.3	97.5	98.8
11	99.2	99.5	100.0
12	100.0	100.0	99.6
13	98.4	97.9	96.9
14	98.1	97.7	96.7
15	98.8	98.6	97.5

motor tuning is limited to the maximum torque capacity of the machine, a problem that is overcome by the physical inertia.

Table 6.13 collects the ratio to the maximum average annual yield for the three locations for ascending inertias. The maximum is reached at 12 kgm^2 for Location 1 and 2, and at 10 kgm^2 Location 3. The difference in yield between the lowest inertia and the optimum is significant: approximately 18%, 15% and 12% for Location 1, 2 and 3 respectively.

The inertia will add a significant inertial torque above the electromagnetic machine torque, which should be borne in mind when dimensioning the mechanical parts of the drive train.

The analyses of Section 6.6.2 of this chapter used a rotor inertia of 3.8 kgm^2, which is far from the ideal inertia of Table 6.13. A new analysis on rated torque and speed could be performed using the optimal inertia to see the corresponding yields for all 30 combinations. It might be possible that the optimal inertia is different for other torque-speed combinations.

It is interesting to note that the optimal m_{sup} parameter for SS6 reaches zero from 8 kgm^2 onwards in Fig. 6.22. Apparently at that point the system has the optimal physical inertia for SS6 because motor tuning seems no longer necessary. Still, increasing the inertia further is beneficial for the overall annual yield as the numbers of Table 6.13 demonstrate, however the performance in SS6 drops significantly from 10 kgm^2 onwards. This is illustrated by the plots of mean electrical power vs. inertia in Fig. 6.23. It appears that the inertia is too large for SS6, and

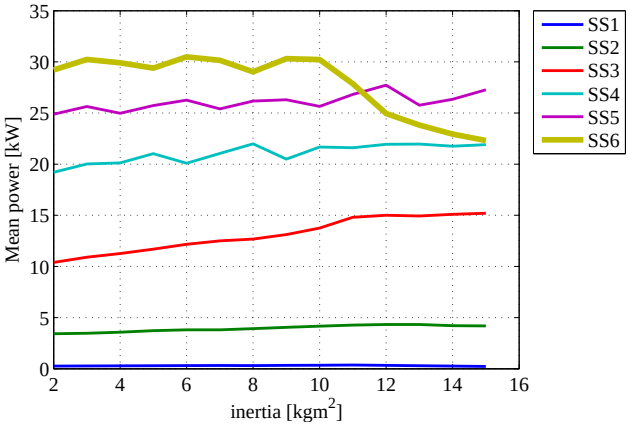

Figure 6.23: Mean electrical power vs. PTO inertia for the six sea states with purely positive m_{sup} values. Note the dropping performance for SS6 from 10 kgm^2 onwards.

the floater is pushed away from resonance. This brings forth the idea of introducing negative m_{sup} values to improve the performance by virtually decreasing the inertia of the system when relevant, which is discussed in the next section.

The zigzag in the curves of SS4, SS5 and SS6 indicate that the resolution of the m_{sup} and b_{ext} parameters is rather coarse, still the trend is clear.

A question that arises is: why not optimise the buoy mass to have the optimal hydrodynamic response? The answer lies in the required floater mass to do so: the equivalent PTO mass of the optimal inertia of 10 kgm^2 is more than 80 ton. This would result in a floater of approximately 110 ton, which is almost four times the current mass of 29 ton. With the current diameter this does not seem realistic, because the floater's draft would have to be roughly four times higher. Moreover, the higher draft would decrease the exciting force and thus the hydrodynamic response. Enlarging the diameter would need a complete new optimisation because the diameter defines the spring constant with its own optimal floater mass (cfr. Equation (2.12)).

For the direct drive option the inertia has not been optimised because this would require an immense amount at low speed. If a direct drive solution would be economically competing, the inertia optimisation could still be researched. In all cases, the gyroscopic effect should be kept in mind.

6.6.5 Introducing negative motor tuning

Optimising the physical inertia is distinctly a beneficial adjustment to the PTO. However, the optimal inertia showed a decreased performance at SS6 where the

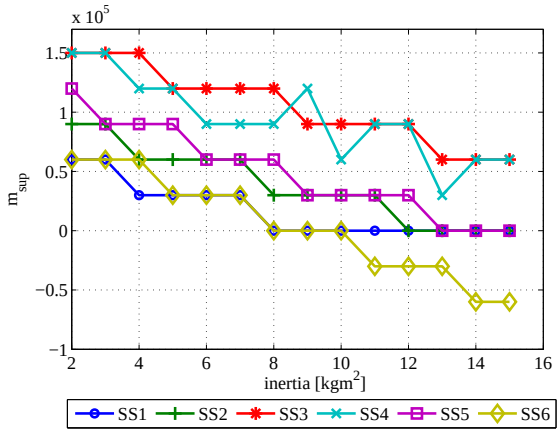

Figure 6.24: Supplementary mass m_{sup} [kg] vs. rotor inertia [kgm^2] for an $A1$ $T4$-$n5$ machine, also allowing negative m_{sup} values for SS6.

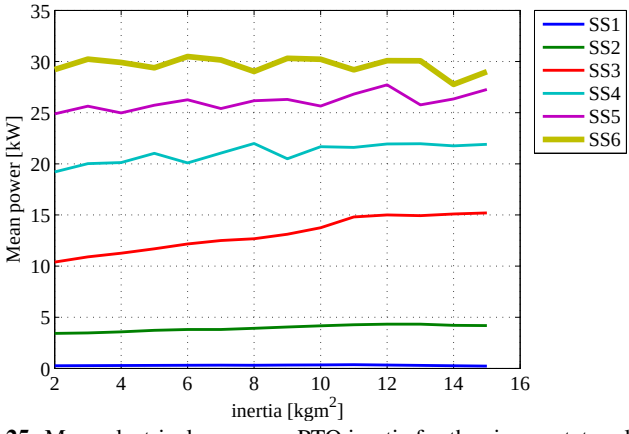

Figure 6.25: Mean electrical power vs. PTO inertia for the six sea states allowing also negative m_{sup} values for SS6. Note the improved performance for SS6 from 10 kgm^2 onwards compared to Fig. 6.23.

Table 6.14: Comparison of the yearly yield with a control allowing negative tuning in relation to the maximum [%] vs. the PTO inertia for Location 1, 2 and 3.

Inertia [kgm^2]	Location 1	Location 2	Location 3
2	80.7	83.6	85.4
3	83.6	86.8	88.6
4	84.6	87.1	88.6
5	87.5	89.8	90.8
6	88.5	90.4	91.7
7	89.8	91.5	92.4
8	91.9	93.6	93.9
9	92.1	93.1	93.9
10	95.1	95.6	95.8
11	98.3	98.0	97.8
12	100.0	100.0	100.0
13	98.7	98.3	98.1
14	98.1	97.6	97.0
15	99.2	99.2	99.0

system is assumed to be pushed further away from resonance with the incoming waves. As a solution it is proposed to introduce negative m_{sup} values to virtually reduce the buoy mass, with the aim to restore, and possibly further improve the performance of SS6 (and other sea states if necessary in other configurations). It is interesting to state that this is an intervention without extra cost. The resulting supplementary mass values are plotted in Fig. 6.24. Fig. 6.25 depicts the corresponding electrical power from which can be noticed that the mean power for SS6 from an inertia of 10 kgm^2 is significantly better compared to purely positive m_{sup} values as plotted in Fig. 6.23. The power in SS6 increases 5% for an inertia of 11 kgm^2 and up to 30% for 15 kgm^2.

The yearly yield improves with up to 2% at Location 1, and up to 5% at Location 3. The influence is larger for this last location as the occurrence of SS6 is higher. The comparison between the inertia steps with a control allowing negative tuning is given in Table 6.14. Because the total yields rose for inertias above 10 kgm^2, the difference between the maximum and minimum yields are accentuated. It is also apparent that the optimal inertia for Location 3 is now the same as for Location 1 and 2, viz 12 kgm^2.

Another option that could be studied - if technically possible - is the use of a controllable flywheel, ie. a flywheel from which the inertia can be changed during operation. Then the optimal inertia could be defined per sea state to improve the yield due to the reduction of required motor tuning.

6.7 Conclusion

A detailed PTO model has been built for the rack and pinion PTO including the dynamic effects of its inertia and the conversion efficiency towards electrical energy. The PTO efficiency is included as maps as a function of the actual torque and speed at every calculation cycle of the simulation. The model also comprises the operational limits of the electrical machine, both in torque as in speed.

The rack and pinion PTO offers, in contrast to the drum and cable, energy absorption in both directions. Moreover there is no worrying about keeping the operational cable tense at all time.

In theory, the control parameters could be chosen differently for the two directions of movement (and in an advanced control changed from wave to wave), but in this work no distinction has been made between upwards or downwards movement regarding the determination of control parameters. Further research could examine if any potential wave energy is left there, or that other beneficial effects could be achieved, such as a reduction of the required speed range.

A first analysis has been done using an unlimited PTO to assess the maximum power that can be absorbed with the used floater, regardless of any PTO efficiency. From these simulations can be concluded that reactive control increases the absorbed power significantly compared to a pure damping strategy. In SS3, the absorbed power achieved by reactively controlling the PTO is three times the power when purely damping. In SS6 this ratio is still an ample 150% (cfr. Fig. 6.4).

To reach equal power absorption as the unlimited PTO with a realistic PTO, an installed power of 200 kW is necessary for a 1500 rpm rated machine. Including a realistic PTO in the model enabled the subsequent study of the PTO dynamics and efficiency. Due to the working principle of the rack and pinion, the PTO inertia is a direct increase of the floater inertia. Thus the necessary motor tuning action can be reduced.

Looking at the influence of the installed power with a fixed speed range (what comes down to studying the influence of the available torque), it is clear that the mean power per sea state rises with higher available torque, but not infinitely. The curve starts to flatten from $P4$ on (Fig. 6.12). Considering the operational constraints, it can be concluded that the limiting factor for small installed powers is the thermal capacity of the machine, i.e. the RMS torque. When the installed power increases, the limiting factor is the peak lift. While the sinkage was the limiting floater constraint for the drum and cable PTO, the peak lift appears to be reached earlier now. This is because the motion of the floater is significantly different due to the damping in both directions.

Subsequently, the yearly yield has been calculated as a function of the installed power for three virtual locations. The gradient of the yield curve as a function of the installed power differs strongly per location. The yield has been calculated for

the different efficiency map variants and this showed that the nominal (maximum) efficiency obviously influences the electrical output, but is not heavily amplified towards the yield: a drop of 1% efficiency means a yield decrease in the order of magnitude of 1.5% - 2% for both the A and B maps. Comparing the shape of the efficiency map, it appears that a $B3$ machine performs up to 15% better than a $A1$, yet having an equal nominal efficiency. Or, a $B3$ machine with an installed power of only 60% of an $A1$ machine would produce the same amount of energy on an annual basis. This opens room towards a more profitable solution with B machines, although they are assumed to be more expensive than A machines.

In a next stage the PTO has been subjected to an electromechanical optimisation. Instead of keeping the operational speed range fixed as in the previous analyses, the speed range has been varied to examine the effect towards the performance of the PTO. Indeed, a reduced speed range means a smaller installed power and thus lower cost. The results showed a large potential to reduce the installed power of the PTO machine. With the $A1$ machine, a smaller speed range resulted even in a higher annual yield for the higher torque cases, because the machine operates in better efficiency zones due to the speed reduction. A $T5$-$n2$ machine produces in an average year 3% more energy than a $T5$-$n5$, although it has 20% less installed power. For the $B3$ machine a yield increase could not be observed because the shape of the efficiency map is relatively flat, but the yield did not drop either. Hence a significant power reduction can be achieved by reducing the speed range.

These results prove again that a WEC should not be dimensioned to maximise the *power absorption in every sea state*, but that the location and its wave climate should be taken into account to appraise the *average annual electrical yield*. Gathering the information for (a selection of) different PTO sizes can subsequently be the starting point for an economic optimisation. All costs should be accounted for, from manufacturing over installation up to operational costs. It needs to be stated that the relevant PTO sizes from that analysis need to be checked again for technical feasibility towards PTO constraints and moreover its behaviour in unexpected high waves. Additionally it is encouraged to perform a life-cycle assessment including end-of-life impact (and costs) to choose the most sustainable option.

Subsequently a direct drive option is studied. The elimination of the gearbox increases the overall PTO efficiency, but a direct drive PTO has a significantly lower equivalent PTO mass which made clear that the PTO inertia has a compelling effect on the performance of the rack and pinion WEC. For low installed torques, the direct drive PTO performed worse than the geared PTO. Still, for high installed torques, an increase in yearly yield of up to 15% is found, because the machine itself can compensate for the loss of the inertial torque compared to a geared PTO by adding virtual mass through reactive control.

Next, the influence of the PTO inertia is studied in various steps. For the rack

and pinion PTO, the rotary inertia of the PTO increases of the inertia of the mass-spring system as it can be accelerated in both directions by the hydrodynamic force. By optimising the rotary inertia, the necessary motor tuning can be reduced significantly which benefits the nett electrical outcome. Furthermore, the motor tuning is limited by the maximum torque capacity of the machine, and can thus not perfectly emulate a mass increase. Hence, a physical inertia is better to improve the hydrodynamic response of the WEC, moreover there are no electrical losses associated with it as is the case with motor tuning. With the optimal inertia, an increase between 12% and 18% could be observed compared to the lowest studied inertia, depending on the location (Table 6.13). Optimising the inertia is assumed to be relatively cheap and offers thus an huge opportunity to add substantially to the yield.

While the overall performance was enhanced by optimising the inertia, the mean power in SS6 dropped beyond a certain amount of inertia. The corresponding m_{sup} value was zero, from which can be understood that the physical inertia had become too large. As a solution, it is proposed to allow negative m_{sup} values to virtually reduce the inertia, with a mean power increase in that sea state of up to 30% and a yearly yield increase of 2% at Location 1, up to 5% at Location 3. Hence this update to the control offers a meaningful yield gain without extra investment.

A general conclusion of this chapter is that the rack and pinion PTO offers a large potential towards a reduction of the installed power compared to a PTO that maximises the absorbed power. By considering the detailed efficiency of the PTO drive train, the average annual electrical yield can be quantified for different PTO sizes at a targeted location. These yields can subsequently be used to asses the economic viability of these cases. Taking account for the wave climate of the place of exploitation is assumed to affect the optimal PTO sizes. The more energetic a location is, the higher the yield gain per extra installed kW of the PTO. Also for this PTO topology it is clear that the magnitude of the nominal efficiency of a (part of) PTO can be misleading, as the variable nature of wave energy employs a large operational range, where the efficiency might be much lower than the at nominal load.

7

Power Split Transmission PTO

The rack and pinion system converts the heave motion of the buoy to a bidirectional rotary movement. When a drive train is directly (or through a gearbox) connected to the pinion shaft such as in Chapter 6, the average efficiency of the electrical machine is influenced, as it operates at many instances in working regions with low efficiency.

The PTO studied in the current chapter tries to improve the machine efficiency by introducing a mechanical power split transmission (PST) in the drive train. The PST of patent WO2015055441 [3] takes on the challenge of transforming the bidirectional movement of the buoy into a unidirectional rotation, hence allowing the connected electrical machine to work in a region at or close to its maximum efficiency. Furthermore, a flywheel facilitates smoothing of the absorbed power towards the grid to tackle another challenge in wave energy: the high peak to average power ratio due to the oscillatory motion of the waves. Indeed, if a smooth electrical output is desired, an energy storage system at buoy level is required or an array of devices compensating each other [71].

Comparable transmissions were proposed decades ago in wind turbines to allow the turbine to operate at variable speed, optimising turbine efficiency while the generator could operate at a strictly fixed grid frequency [72–74]. Even after the introduction of power electronics, research is being done recently to increase the energy yield of a wind turbine by responding to turbulences in the wind by means of a continuously variable transmission and an advanced control [75].

The chapter first deals with the modelling of the PST and according electrical machines. The model is subsequently combined with the hydrodynamic model to

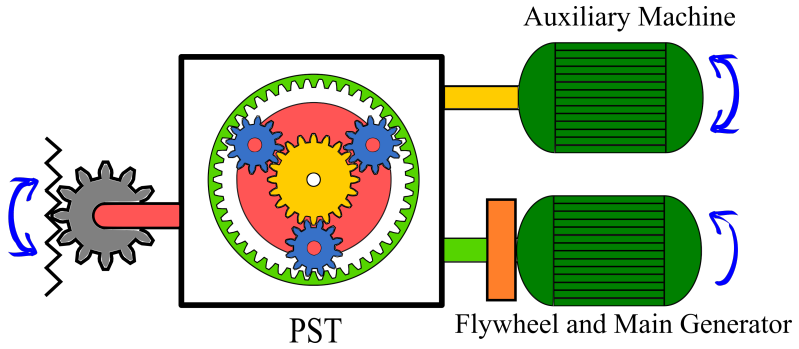

Figure 7.1: Schematic illustration of the PST together with the shafts to the rack and pinion system, auxiliary machine and flywheel plus main generator. The rack and pinion is connected to the carrier, the auxiliary to the sun and the flywheel and main generator to the ring.

estimate the power production of the PST PTO topology. Next, the sensitivity of the control and design parameters is investigated to result in a proof-of-concept system to further explore the PTO topology.

Parts of this chapter have earlier been published in [76].

7.1 Working principle

The PST discussed in this work comprises a planetary gearbox with three input/output shafts. One is connected to the planet carrier, a second to the ring wheel and the third to the sun wheel as illustrated in Fig. 7.1. In a classical application of a planetary gearbox, one of the shafts is fixed to the surrounding, resulting in a fixed transmission ratio (with loss of the desired degree of freedom studied here). When all three shafts are allowed to rotate, changing the speed of one of the shafts enables a varying speed transmission between the other two. Hence, the bidirectional rotation of the shaft connected to the pinion can be converted into a unidirectional rotation of a generator by controlling the speed of the auxiliary machine connected on the third shaft.

Another characteristic of the PST is that a torque can only be transferred between two shafts if a torque is also applied on the third, i.e. the control or auxiliary shaft. This characteristic is illustrated by the example of a car, equipped with a differential (which is a particular type of PST), the auxiliary machine and the main generator are replaced by the wheels and the engine replaces the rack and pinion shaft. The torque ratio between the two wheels equals 1 for a differential. Imagine a car of which one wheel has no grip on the ground and is slipping. Even if the other wheel would have enough grip, it would not receive a torque large enough to get the car moving. This is due to the fact that the only counter torque delivered

by the slipping wheel is the acceleration torque of its inertia (neglecting friction). Thus the same torque is applied to the other wheel, but this is too small to get the car moving.

The aim is to enable operation of the main generator equipped with a flywheel close to its optimal working range with maximum efficiency by controlling the auxiliary machine. The latter needs to make sure that power is transmitted from the buoy towards the generator. The flywheel can store temporarily excess of energy, and hence facilitates a smoother power generation of the main generator.

By applying a torque with the auxiliary machine during the upwards movement of the buoy, the PST will impose a torque on the other two shafts as well, providing a damping PTO force to the buoy on the one hand, and an acceleration torque towards the flywheel and main generator on the other hand.

During the downwards motion of the buoy, the auxiliary machine is kept idle (cfr. slipping car wheel). It can freely rotate in opposite direction enabling the main generator to maintain its unidirectional rotation. The only torque being transferred is the torque due to the acceleration of the auxiliary machine's rotor inertia. The corresponding torque transferred by the PTO will slightly decelerate the flywheel and main generator, but is not necessarily a loss: it can tune the natural frequency of the buoy towards the frequency of the incident wave initiating higher power absorption as the motion gets closer to resonance.

The working principle just explained can be seen as a controlled one-way (freewheel) clutch. However, compared to a simple mechanical clutch, the transferred torque can be ramped gradually by controlling the set point torque of the auxiliary machine. This gives the PST the major advantage of avoiding the often very high impact torques of a purely mechanical freewheel clutch. On the other hand, compared to the rack and pinion PTO of the previous chapter, the PST requires two independently working machines, and is possibly more demanding to the gearbox in terms of speeds and reciprocating behaviour.

After a first simulation run, sensitivity analyses of the mechanical and control parameters were performed. The results thereof showed a higher WEC performance when the auxiliary machine was not simply redirecting all absorbed wave power to the main generator. Consequently, the further research on the PST presented in this work left the idea of smoother power production to explore the potential of the PST with regard to the energy production.

7.2 Modelling

To insert the PST in the hydrodynamic model of the buoy, the relation between speeds and torques of the different shafts of the transmission needs to be analysed and determined which of the parameters are an input to the model, and which are an output. In this first approach, internal inertias, friction or torsions are not taken

into account. The internal relation between the rotational speeds of the shafts of a planetary gear is expressed by

$$z_{\mathrm{s}}\Omega_{\mathrm{s}} - z_{\mathrm{r}}\Omega_{\mathrm{r}} + (z_{\mathrm{r}} - z_{\mathrm{s}})\Omega_{\mathrm{c}} = 0, \tag{7.1}$$

with z_{s}, z_{r} the number of teeth for the sun wheel and ring wheel respectively ($z_{\mathrm{r}} < 0$ for internal gearing), and Ω_{s}, Ω_{r}, Ω_{c} the angular speed of sun, ring and carrier in radians per second. Hence, there are two degrees of freedom, when two angular speeds are chosen, the third is defined.

Using the method of virtual power, with $\delta\Omega$ the notation for a virtual angular velocity, two independent relations between the torques of the (frictionless) planetary gear can be written:

$$\begin{cases} T_{\mathrm{s}}\delta\Omega_{\mathrm{s}}^1 + T_{\mathrm{r}}\delta\Omega_{\mathrm{r}}^1 + T_{\mathrm{c}}\delta\Omega_{\mathrm{c}}^1 = 0 \\ T_{\mathrm{s}}\delta\Omega_{\mathrm{s}}^2 + T_{\mathrm{r}}\delta\Omega_{\mathrm{r}}^2 + T_{\mathrm{c}}\delta\Omega_{\mathrm{c}}^2 = 0, \end{cases} \tag{7.2}$$

with T_{s} ,T_{r} and T_{c} the torques on the shaft of the sun wheel, ring wheel and carrier wheel respectively, and $\delta\Omega_{\mathrm{s}}^1$, $\delta\Omega_{\mathrm{r}}^1$, $\delta\Omega_{\mathrm{c}}^1$ and $\delta\Omega_{\mathrm{s}}^2$, $\delta\Omega_{\mathrm{r}}^2$, $\delta\Omega_{\mathrm{c}}^2$ two independent virtual movements.

Given the transmission ratios of a planetary gear, and the relatively higher inertia of the ring wheel, it was proposed to connect the main generator to the ring wheel shaft, the auxiliary machine to the sun wheel and the carrier to the pinion. Nevertheless, alternative configurations might be interesting.

To be able to define which of the speeds and torques of Equation (7.1) and (7.2) will be considered as inputs of the PST model and which as outputs, the three subsystems are shortly analysed separately: (i) the shaft to the buoy, (ii) the auxiliary machine and (iii) the main generator with flywheel.

7.2.1 Shaft to the buoy

The movement of the buoy is a result of the forces acting upon it. These forces are the hydrodynamic force on the one hand, and the PTO force on the other hand. The PTO force originates from the PST, thus influencing the buoy motion. Subsequently, the resulting buoy speed imposes a rotational speed on the pinion through the rack. Consequently, the speed of the carrier Ω_{c} is an input to the PST model and the carrier torque T_{c} an output.

7.2.2 Auxiliary machine

The electromagnetic torque of the auxiliary machine is the controllable parameter that defines the PTO force to the buoy. The auxiliary machine is therefore also called the 'control' machine. The actual torque $T_{\mathrm{aux,shaft}}$ on the sun shaft

to the PST however, is not equal to the electromagnetic torque T_{aux} because the machine's rotor inertia J_{aux} should be taken into account:

$$T_{\mathrm{aux,shaft}} = T_{\mathrm{aux}} + J_{\mathrm{aux}} \frac{d\Omega_{\mathrm{s}}}{dt} \tag{7.3}$$

Hence, the torque on the sun shaft T_{s} is an input to the PST and the rotational speed of the sun is an output.

7.2.3 Main generator with flywheel

The torque on the shaft to the flywheel and main generator $T_{\mathrm{main,shaft}}$ originates from the ring wheel and is considered a result of the torque on the control shaft (T_{s}) and consequently an output of the PST. At the other shaft end of the flywheel, the main generator will apply an electromagnetic torque T_{main}. When combining the inertia of the flywheel and the machine's rotor inertia to J_{fly}, the rotational speed Ω_{main} of the shaft is the result of the two torques applied on J_{fly}:

$$\frac{d\Omega_{\mathrm{main}}}{dt} = \frac{T_{\mathrm{main,shaft}} - T_{\mathrm{main}}}{J_{\mathrm{fly}}} \tag{7.4}$$

Accordingly, the rotational speed of the main generator is an input to the PST.

7.2.4 Model of the PST

Based on the above conclusions for each of the three shafts, three inputs have been defined: the torque on the sun wheel T_{s}, the speed on the carrier Ω_{c} and the speed on the ring wheel Ω_{r}. These values will determine the magnitude of the outputs: rotational speed of the sun Ω_{s}, torque of the carrier T_{c} and torque of the ring wheel T_{r}. A block diagram of the PST model is illustrated in Fig. 7.2.

Equation (7.1) gives the relation between the rotational speeds to calculate Ω_{s}:

$$\Omega_{\mathrm{s}} = \frac{z_{\mathrm{r}}}{z_{\mathrm{s}}}\Omega_{\mathrm{r}} + \frac{(z_{\mathrm{s}} - z_{\mathrm{r}})}{z_{\mathrm{s}}}\Omega_{\mathrm{c}} = \frac{z_{\mathrm{r}}}{z_{\mathrm{s}}}\Omega_{\mathrm{r}} + (1 - \frac{z_{\mathrm{r}}}{z_{\mathrm{s}}})\Omega_{\mathrm{c}} \tag{7.5}$$

If, in a virtual movement, the carrier would be kept still, i.e. $\delta\Omega_{\mathrm{c}}^{1}$= 0, then Equation (7.1) and (7.2) can be combined to find an expression for the torque on the ring:

$$T_{\mathrm{r}} = -\frac{z_{\mathrm{r}}}{z_{\mathrm{s}}} T_{\mathrm{s}} \tag{7.6}$$

If in contrast, the ring wheel would be kept still, i.e. $\delta\Omega_{\mathrm{r}}^{2}$ = 0, than Equation (7.1) and (7.2) give an expression for the carrier torque:

$$T_{\mathrm{c}} = \frac{(z_{\mathrm{r}} - z_{\mathrm{s}})}{z_{\mathrm{s}}} T_{\mathrm{s}} \tag{7.7}$$

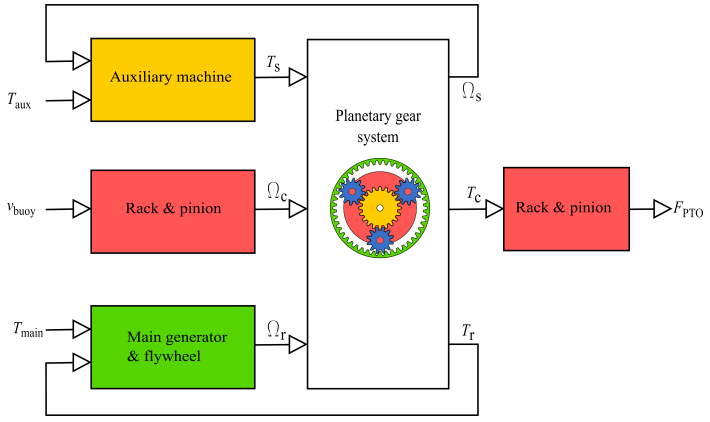

Figure 7.2: Block diagram of the PST PTO model.

Equations (7.5), (7.6) and (7.7) are the core of the PST model, and define the interaction between the three shafts.

It is interesting to mention that - even though the PST could be seen as continuously variable transmission - only the speed ratio is variable and the ratio between the torques does not change as can be derived from Equations (7.5), (7.6) and (7.7). This can be elucidated by understanding that the diameters of the gears (sun, ring, planets) do not change. In other words, the levers with which the torques are converted do not change. Though the speed relation between two shafts can be altered by changing the speed of the third shaft.

7.2.5 Additional speed conversions and transmission ratio of the planetary gear PST

The speed of the rack and pinion is very slow, in the order of magnitude of 100 rpm with a pinion radius of 15 cm. Therefore, after some initial simulations with the PST model, a transmission with a ratio of 20 was added between the rack and pinion and the PST carrier shaft. Another transmission with a ratio of 5 was added between the ring wheel and the main generator shaft to increase the speed towards the operational (200%) range of 1000 rpm machines for the main generator and 3000 rpm for the auxiliary machine.

The transmission ratio of the planetary gear PST has been set by iteratively changing the ratio z_r/z_s to keep the positive operational speed of the auxiliary machine in the range of 200% of the nominal speed of a 3000 rpm rated device. Eventually z_r/z_s was set to -62/30 (negative as $z_r < 0$). The practical feasibility has not been checked at this proof-of-concept phase, but it is reassuring that an identical transmission ratio could be achieved with a stepped planet configuration. Furthermore, the additional transmissions between rack & pinion and between PST

and main generator offer room to optimise the complete system in the future.

These ratios are considered as fixed during this study of a single PST configuration. The extra transmission between ring wheel and main generator results in the following expressions:

$$\Omega_{\mathrm{r}} = \frac{\Omega_{\mathrm{main}}}{5} \tag{7.8}$$

$$T_{\mathrm{main,shaft}} = \frac{T_{\mathrm{r}}}{5}. \tag{7.9}$$

The corresponding equations to connect the PST PTO model with the hydrodynamic model are:

$$\Omega_{\mathrm{c}} = 20 \cdot \Omega_{pinion} = \frac{20}{r}\frac{dz}{dt} \tag{7.10}$$

$$F_{\mathrm{PTO}} = \frac{20}{r} T_{\mathrm{c}}, \tag{7.11}$$

with r the pinion radius and $\frac{dz}{dt}$ the vertical buoy speed.

7.2.6 PTO efficiency

The machine and drive efficiencies are considered in the model as efficiency maps as a function of actual torque and speed as described in Chapter 3 Section 3.3.3 and Section 3.4.

The efficiency of the PST is not as straightforward as for a gearbox with only two rotating shafts. In a planetary gear system with three rotating shafts, the power of these shafts can either be positive or negative, and the torque and speed can span the whole working range, in both directions.

To explore the potential of the PST in a WEC in this proof-of-concept phase, the efficiency of the PST is not implemented in the simulation model itself. Nevertheless, an estimated average transmission efficiency is taken into account in the post-processing. To obtain an estimation of this average efficiency, the rack and pinion PTO simulation has been ran without the gearbox efficiency taken into account. Subsequently the yield results of the simulations with gearbox efficiency are divided by the yield results with ideal gearbox to obtain an average value presented in Table 7.1. The numbers in the table make us remember that the gearbox efficiency (Fig. 5.4) is heavily dependent on the actual torque which is translated to the average efficiency. A PTO with a lower available torque will be more frequently capped on the maximum torque and remain there longer during operation, where the gearbox performs better, resulting in a better average efficiency.

The estimated average PST efficiency is brought into account in the post-processing while calculating the average yearly yield. The machine efficiency is

Table 7.1: Average gearbox efficiency for every step of installed machine torque.

	$T1$	$T2$	$T3$	$T4$	$T5$	$T6$
Average Efficiency [%]	82	94	91	91	86	87

still part of the simulation model where the efficiency is calculated at every simulation cycle based on the actual torque and speed. Subsequently the drive efficiency is added as a fixed value as explained in Chapter 3.

7.3 Control

The idea of the concept was that the power from the waves is directed towards the flywheel and main generator by controlling the auxiliary machine. To respect the unidirectional rotation of the main generator, this implies that the wave energy absorption will happen during the upwards movement. A basic control for this proof of concept has been started with, inspired on the patent description [3].

The sign of the rotational speed is taken positive for the rack and pinion shaft when the buoy moves up. Taking the speed sign also positive at the desired operation speed of the main generator (ring), fixes the speed sign of the sun shaft to the auxiliary machine: when the ring would be kept still, the rotation is positive when the buoy moves up.

During the downwards motion, no torque is applied by the auxiliary machine allowing itself a free rotation in the negative direction. Once the buoy is moving up and the rotation of the auxiliary machine tends to change direction, a torque is applied by the auxiliary machine creating a braking torque for rotations in positive direction to redirect the wave power to the flywheel and main generator by accelerating them. Hence an electromagnetic torque T_{aux}, proportional with the rotational speed of the auxiliary machine is proposed, applied only when the shaft speed is positive:

$$T_{\mathrm{aux}} = K_{\mathrm{p,aux}}\, \Omega_{\mathrm{s}}|_{\Omega_{\mathrm{s}}>0}, \tag{7.12}$$

with $K_{\mathrm{p,aux}}$ the proportional gain factor for the damping of the auxiliary machine. The control of the auxiliary machine is updated in Section 7.5 Equation (7.14) to add reactive control.

The control of the main generator consists of keeping the speed of the main generator around a setpoint value Ω_{set}. A basic control is a braking torque applied once the actual rotational speed Ω_{main} exceeds this setpoint:

$$T_{\mathrm{main}} = -\min(0,\ \mathrm{K}_{\mathrm{p,main}}(\Omega_{\mathrm{set}} - \Omega_{\mathrm{main}})), \tag{7.13}$$

Table 7.2: The control and mechanical parameters for a first conceptual simulation of the PST in a WEC.

$K_{\mathrm{p,aux}}$ [Nms/rad]	$K_{\mathrm{p,main}}$ [Nms/rad]	n_{set} [rpm]	J_{aux} [kgm^2]	J_{fly} [kgm^2]
10	3	1000	1	5

with $K_{\mathrm{p,main}}$ the proportional gain factor for the damping of the main generator.

$K_{\mathrm{p,main}}(\Omega_{\mathrm{set}} - \Omega_{\mathrm{main}})$ is negative when the speed exceeds the setpoint, thus a minus sign is added to make the electromagnetic torque positive. As stated in Chapter 3 Section 3.1, the convention in this work is that generated power is positive. Thus a positive electromagnetic torque has a braking effect on a positive machine speed. To avoid the flywheel and main generator from being accelerated by an electromagnetic torque, the torque is limited to zero by the minimum operator.

In the simulations, the initial speed of the main generator is set at the setpoint value, but the operation principle allows the acceleration of the main generator to the setpoint value by wave power.

7.4 First simulation results

To explore the working of the PST, the auxiliary and main generator machines have been chosen with an ample available torque. To check the working of the PST in a WEC, control parameters were found on a trial and error basis to result in a situation where the auxiliary machine is prevented from rotating in positive direction to redirect the wave energy to the main generator and flywheel. The used parameters are displayed in Table 7.2.

7.4.1 Bidirectional to unidirectional conversion

One of the aims of the patent [3], is the conversion of the bidirectional rotation towards a unidirectional rotation of the main generator. Fig. 7.3 plots the rotational speeds of carrier, sun and main generator. While the speed of the carrier coming from the pinion changes speed with every wave, it is clear from the bottom graph of Fig. 7.3 that the rotational speed of flywheel and main generator is unidirectional and oscillates due to the oscillating incoming wave power and the fact that energy is extracted from it to convert to electricity. The electromagnetic torque is controlled corresponding to Equation (7.13).

This (preliminary) control strategy tries to retain the auxiliary machine as much as possible from rotation in positive direction during the upwards buoy motion by

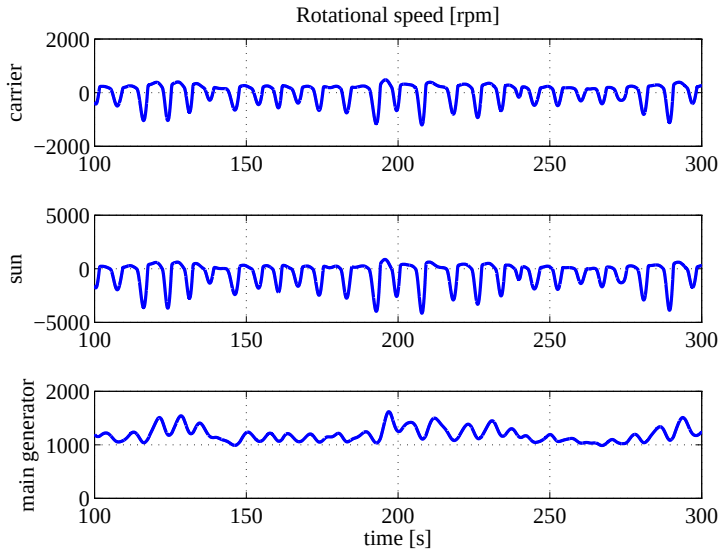

Figure 7.3: Rotational speeds in rpm of carrier, sun and main generator for a SS4 simulation

applying a torque T_{aux}. This torque is also transmitted through the PST to the ring wheel and accelerates the flywheel and main generator. During the downwards buoy movement, the main generator is decelerated. A part of this deceleration is a result of the acceleration torque applied on the auxiliary shaft due to the auxiliary machines rotor inertia and the other contributor to the deceleration is the main generators own electromagnetic torque. As explained before, the acceleration torque of the auxiliary machine should not necessarily be seen as a loss factor, because a corresponding torque is also applied on the shaft to the rack and pinion. As this torque is quasi proportional to the buoys acceleration, it changes the natural frequency of the buoy, which can tune it towards the frequency of the incident waves, thus enabling increased power absorption by the buoy as its motion gets closer to resonance.

7.4.2 Efficiency at operating points

The operating points as a function of actual torque and speed have been plotted above the efficiency maps for an $A1$ machine for the auxiliary machine in Fig. 7.4 and for the main generator in Fig. 7.5. The location of the operation points shows that the main generator indeed operates close to the most efficient region, which could easily be improved by lowering the installed torque which is now over-dimensioned.

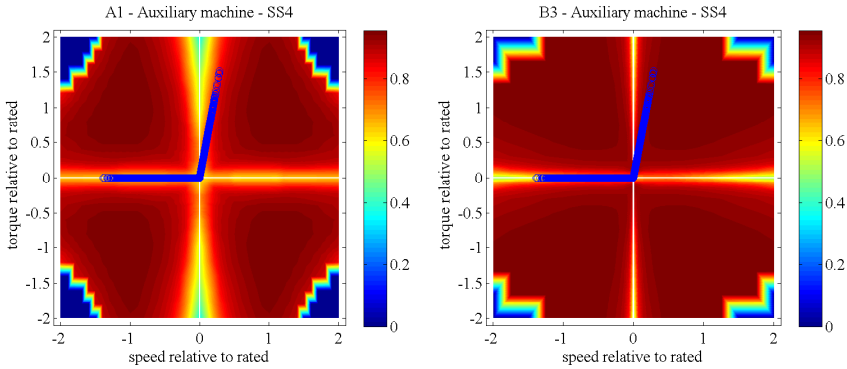

Figure 7.4: Scatter of the operating points of the auxiliary machine with preliminary control for a SS4 above the efficiency maps of an $A1$ machine (left) and a $B3$ machine (right).

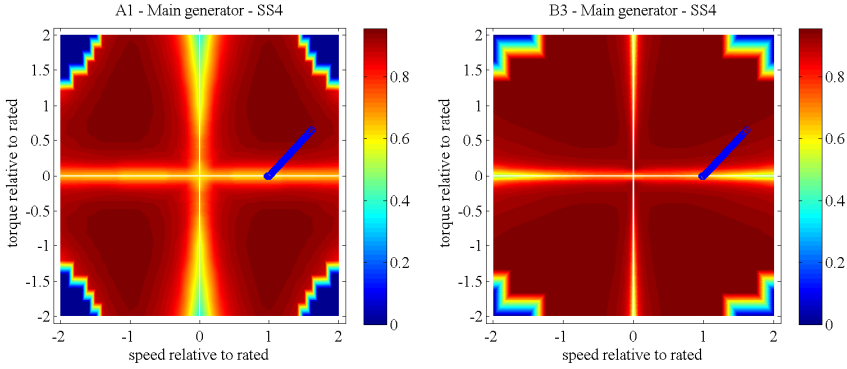

Figure 7.5: Scatter of the operating points of the main generator with preliminary control for a SS4 above the efficiency maps of an $A1$ machine (left) and a $B3$ machine (right).

The auxiliary machine however, operates at the border to low efficiencies, especially with the $A1$ machine (left graph of Fig. 7.4).

7.4.3 Sensitivity of the parameters towards power absorption

The simulation of the previous section is a first step in the proof of concept of a PTO consisting of a PST for wave energy conversion. The main generator rotates in a single direction and could operate at high efficiency zones with optimised control. However, the wave power absorption is not yet evaluated. The simulation of Fig. 7.4 and Fig. 7.5 resulted in a mean absorbed power of 13.3 kW, which is significantly lower than the 24 kW for a drum and cable PTO with an unlimited PTO with tuned control.

The aim is now to assess the influence on the power absorption of the control

and mechanical design parameters of Table 7.2 and how they should be optimised. The easiest to modify are the control parameters. In the current control strategy two control parameters are identified: the proportional gain factor $K_{\mathrm{p,aux}}$ for the damping of the auxiliary machine, and the proportional gain factor $K_{\mathrm{p,main}}$ for the damping of the main generator (a third control parameter is introduced in an updated strategy in Equation (7.14)). The mechanical design parameters, i.e. the inertia of flywheel and main generator J_{fly}, and the inertia of the auxiliary machine J_{aux} are at this stage considered as not variable during operation, although for example a variable inertia is technically possible. Nevertheless, an optimum size for best performance in an average year should be determined in the design process.

In the next subsections, the sensitivity of the control and design parameters is analysed.

7.4.3.1 Influence of auxiliary machine damping

The scatter of the operating points of the auxiliary machine in Fig. 7.4 illustrated that the rotation is already heavily damped, but still permits positive rotation. On the other hand, it is interesting to analyse the impact of a lower damping factor.

For Fig. 7.6, a series of simulations in SS4 were performed where all parameters of Table 7.2 are kept fixed except for the auxiliary machine damping factor $K_{\mathrm{p,aux}}$. To reach the highest absorbed power, it appears that a lower damping factor should be used: compared to the 13.3 kW with a $K_{\mathrm{p,aux}}$ of 10 Nms/rad, an absorbed power of 30 kW can be reached with a $K_{\mathrm{p,aux}}$ of 1 Nms/rad limited by the sinkage constraint. Looking into the resulting electrical power distribution between the main generator and auxiliary machine of Fig. 7.7, this shows that the higher power is due to a higher power absorption by the auxiliary machine. In fact, the auxiliary machine becomes the largest contributor of power. So far, its auxiliary function. While the electrical power with a $K_{\mathrm{p,aux}}$ of 10 Nms/rad was 4.1 kW for the auxiliary machine and 7 kW for the main generator, this is 22.6 kW and 4.5 kW respectively for a $K_{\mathrm{p,aux}}$ of 1 Nms/rad.

7.4.3.2 Influence of main generator damping

The influence of the main generator damping factor $K_{\mathrm{p,main}}$ is studied by setting $K_{\mathrm{p,aux}}$ at the optimal value of 1 Nms/rad found in previous subsection, and maintaining the other parameters as in Table 7.2.

The influence of the main generator damping is significantly less pronounced towards the absorbed power as Fig. 7.8 illustrates. Which can be understood because it does not directly affect the PTO force, but determines the torque with which the main generator is damped. The maximum absorbed power of 30.5 kW is reached at a $K_{\mathrm{p,main}}$ value of 1 Nms/rad, limited by the sinkage constraint, and it only drops to 29.7 kW at a $K_{\mathrm{p,main}}$ of 20 Nms/rad.

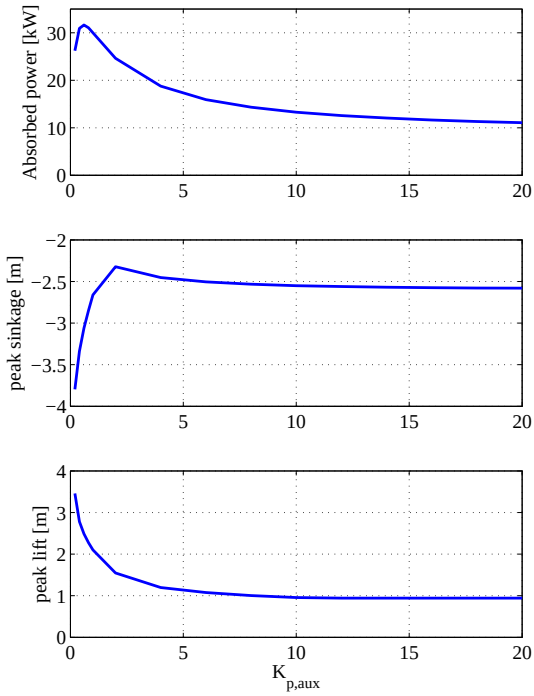

Figure 7.6: Absorbed power for SS4 vs. the auxiliary machine damping $K_{\mathrm{p,aux}}$ [Nms/rad] and the corresponding peak sinkage and peak lift.

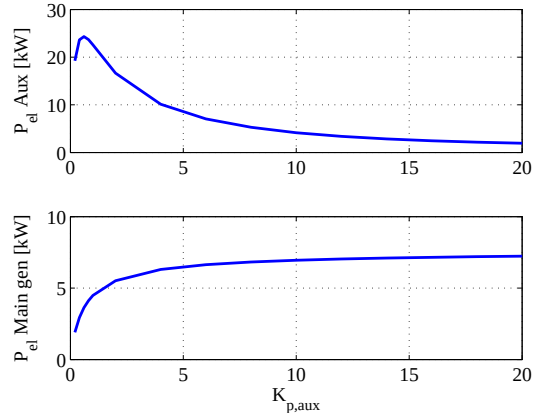

Figure 7.7: Mean electrical power [kW] for SS4 vs. the auxiliary machine damping $K_{\mathrm{p,aux}}$ [Nms/rad] for the auxiliary machine (upper) and main generator (bottom) ($A1$ map).

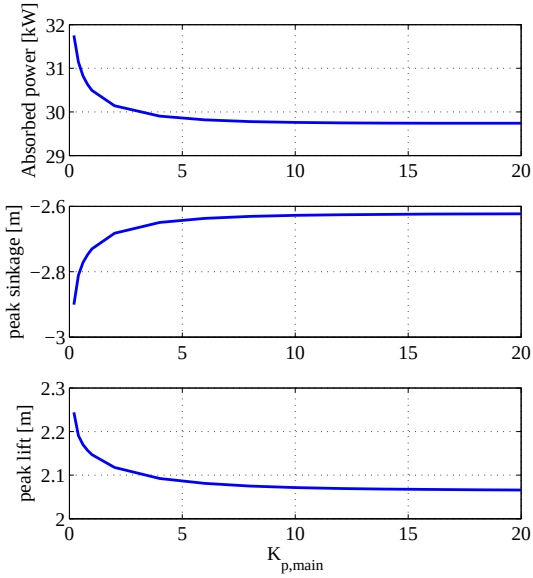

Figure 7.8: Absorbed power for SS4 vs. the main generator damping $K_{\mathrm{p,main}}$ [Nms/rad] and the corresponding peak sinkage and peak lift.

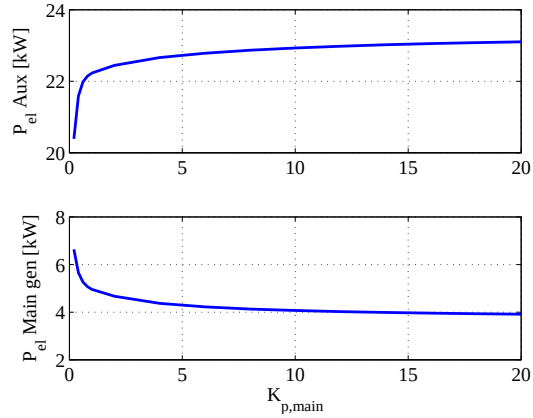

Figure 7.9: Mean electrical power for SS4 vs. the main generator damping $K_{\mathrm{p,main}}$ [Nms/rad] for the auxiliary machine (upper) and main generator (bottom) ($A1$ map).

The contribution of the main generator in the total mean power drops slightly with increasing damping factor as showed in Fig. 7.9.

7.4.3.3 Influence of auxiliary inertia

The inertia of the auxiliary machine J_{aux} affects the hydrodynamic response of the floater by virtually adding mass to it. Even though there is no electromagnetic torque applied during the downwards buoy movement (running idle), the acceleration torque of the rotary inertia is translated to a PTO force quasi proportional to the buoy speed (quasi and not completely because of the interrelated rotary speeds cfr. Equation 7.1, and the main generator speed is not constant). Consequently it influences the hydrodynamic response, and a high sensitivity towards the absorbed power can be expected.

An iteration on the auxiliary inertia J_{aux} has been simulated with $K_{\mathrm{p,aux}}$ = 1 Nms/rad and $K_{\mathrm{p,main}}$ = 1 Nms/rad and the other parameters as in Table 7.2. The expectation is confirmed by the results collected in Fig. 7.10. The absorbed power starts from 11.6 kW with an inertia of 0.2 kgm^2, to reach 30.5 kW limited by the sinkage constraint with an inertia of 1 kgm^2.

The power distribution between the auxiliary machine and main generator seems not affected as Fig. 7.11 demonstrates, both electrical powers are influenced in an identical way.

7.4.3.4 Influence of main generator inertia

The flywheel at the main generator shaft can absorb an amount of wave energy to enable power smoothing towards the electrical output. This is valued as an interesting characteristic, considering the variable nature of wave energy. The inertia of the flywheel J_{fly} is considered a mechanical design parameter in this study. As J_{fly} will be much larger than the rotor inertia of the main generator, it is here the total inertia of the flywheel plus the rotor inertia.

The results of an iteration between 2 kgm^2 and 12 kgm^2 did not reveal a significant influence towards the absorbed power, neither towards the floater constraints or the power distribution between auxiliary and main generator.

However, it is to be expected that the combination of main generator damping and flywheel inertia will affect the wave form of the electrical output power of the main generator.

7.5 Update of the control

The magnitude of the auxiliary inertia has shown to have a substantial influence on the power absorption of the PST PTO, as well as the damping parameter $K_{\mathrm{p,aux}}$. An iteration of these two parameters has been executed to find the optimum - or

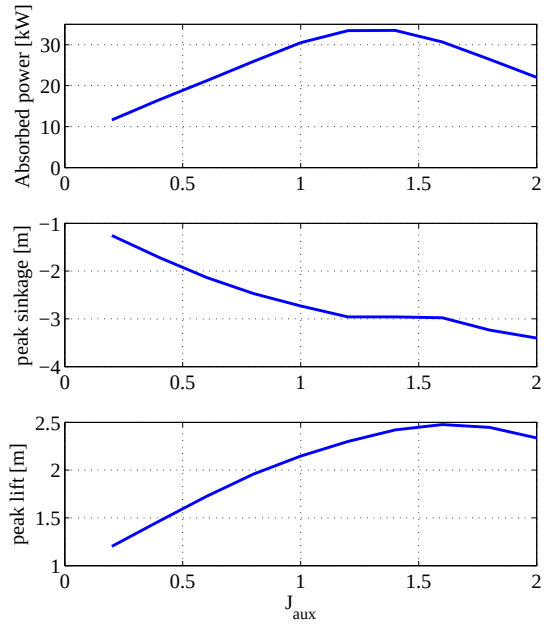

Figure 7.10: Absorbed power for SS4 vs. the auxiliary inertia J_{aux} and the corresponding peak sinkage and peak lift.

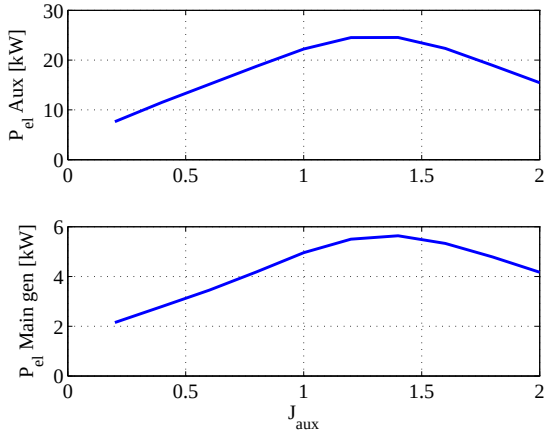

Figure 7.11: Mean electrical power for SS4 vs. the auxiliary inertia J_{aux} for the auxiliary machine (upper) and main generator (bottom) ($A1$ map).

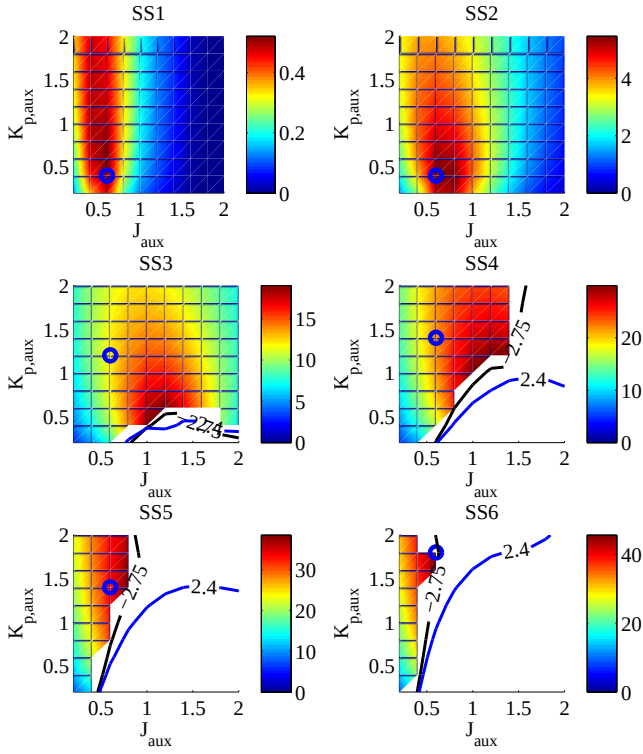

Figure 7.12: Absorbed power [kW] in fuction of the auxiliary inertia J_{aux} and auxiliary damping factor $K_{\mathrm{p,aux}}$ [Nms/rad], contours of peak sinkage (black) and peak lift (blue).

maximum - inertia value for all sea states, and in the mean time, the optimum damping factor for each sea state. The results are displayed in the colour plots of Fig. 7.12 per sea state. The limiting sea state for the inertia appears to be SS6 where the maximum sinkage is reached at an inertia of 0.6 kgm^2. The blue circle in the plot of every SS shows the optimum $K_{\mathrm{p,aux}}$ with the inertia limited at 0.6 kgm^2, but the plots indicate that a higher mean power can be reached in SS3 to SS5 at higher inertia values. Two possibilities rise to tackle this:

1. Using a variable inertia

2. Adding a term proportional to the acceleration to the electromagnetic auxiliary torque: reactive control

Table 7.3: Absorbed power per sea state for a fixed inertia limited to 0.6 kgm^2 (column 2), a variable inertia (column 3) and a fixed inertia complemented with reactive control (column 3).

SS	J fixed	J variable	J fixed with reactive control
	[kW]	[%] of J fixed	[%] of J fixed
1	0.5	100	100
2	5.5	100	100
3	12.0	158	152
4	21.8	137	133
5	33.5	115	113
6	45.6	100	100

7.5.1 Variable inertia

The absorbed powers of a reference case with a fixed (limited) inertia has been presented in the second column of Table 7.3. If the inertia can be varied depending on the actual sea state, the absorbed power increases 15% in SS5, 37% in SS4 and 58% in SS3, compared to the reference case of a fixed inertia. The numbers for all sea states for the variable inertia are collected in the third column of Table 7.3. The results offer an important incentive to check the feasibility of a variable inertia in a further design stage of a PTO, certainly because the power gain is mainly in the sea states contributing significantly to the average yearly yield in all three virtual locations. The feasibility of a variable inertia is however out of scope for this work.

7.5.2 Reactive control

Adding a term to the electromagnetic torque which is proportional to the acceleration, i.e. reactive control, is earlier in this work explained and also called 'motor tuning' or 'tuning'.

By virtually adding inertia to the auxiliary, the mean power rises 152%, 133% and 113% in SS3, SS4 and SS5 respectively (fourth column of Table 7.3) compared to a case where the inertia is fixed and limited to 0.6 kgm^2 (second column), and thus approximating the case of variable inertia.

Hence a new control parameter is introduced to optimise the power output: the supplementary inertia J_{sup}. The electromagnetic torque of the auxiliary machine is consequently updated to:

$$T_{\mathrm{aux}} = K_{\mathrm{p,aux}}\,\Omega_{\mathrm{s}}|_{\Omega_{\mathrm{s}}>0} + J_{\mathrm{sup}}\frac{d\Omega_{\mathrm{s}}}{dt} \tag{7.14}$$

This implies that the auxiliary machine will act as a motor at some instances of the wave cycle.

7.5.3 Auxiliary speed range

A consequence of the lower damping is that the auxiliary machine reaches a higher negative peak speed. The operating points from a lowly damped SS4 are plotted in Fig. 7.13 and can be compared with the operating points from the highly damped SS4 in Fig. 7.4. The negative speed reaches even a higher peak in SS6, illustrated in Fig. 7.14. The design specification for the auxiliary machine should consequently have a high mechanical speed limit. Above 200% of the rated speed, the machine will run idle in any case. When the machine is only damped, the machine runs idle over the complete negative speed range. When reactive control is applied however, as for the simulation resulting in Fig. 7.15, an electromagnetic torque is also applied in negative speed direction to tune the system, but only in the operational range up to 200% of the rated speed.

In positive rotational direction, the control parameters should be choosen to limit the peak speed at 200% of the rated speed. If idle operation would be allowed there, the damping of the floater would suddenly stop as the machine can no longer apply a torque above that limit (in the defined operational torque range for this work). This stop in damping of both floater and auxiliary machine opens the possibility of uncontrolled acceleration and is therefore undesired.

It should be noted that this design condition differs from the PTO topologies from Chapter 5 (drum & cable) and Chapter 6 (rack & pinion) where exceeding of the 200% speed limit was not allowed in none of the directions. The control parameters were determined to respect this prerequisite.

7.6 Power smoothness

One of the aims of the PST in a WEC was to have a smoother power output. By redirecting the absorbed energy to a large inertia, the power could indeed be averaged out by optimising the main generator control. However, the sensitivity analysis on the auxiliary damping factor in Section 7.4.3.1 demonstrated that this strategy - high damping of the auxiliary - results in a very low absorbed power compared to an optimised - and lower - damping of the auxiliary. Moreover, the largest share of the power contribution at optimised damping shifts to the auxiliary machine.

Additionally, the use of reactive control implies power investment and thus a power flow from the grid (or common DC-bus) towards the hydrodynamic system.

Trying to smoothen out the power output as much as possible is not included in this work. First, an exploration of the potential of the PST PTO is at its place, with an assessment of the influence of the installed power.

Considering power smoothing, it is furthermore assumed that the exploitation of a single WEC will be exceptional, and the output of WECs in an array will

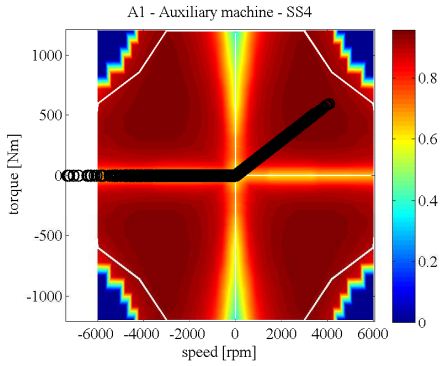

Figure 7.13: Operating points of a lowly damped auxiliary machine in SS4, with negative speeds exceeding the maximum operating limit.

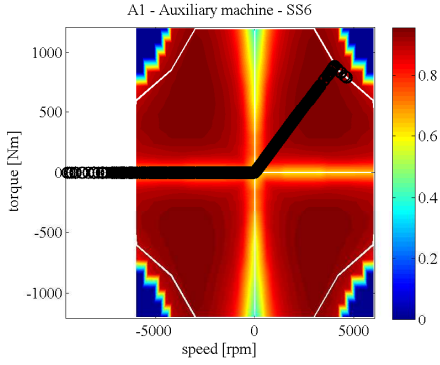

Figure 7.14: Operating points of a lowly damped auxiliary machine in SS6, with negative speeds exceeding the maximum operating limit.

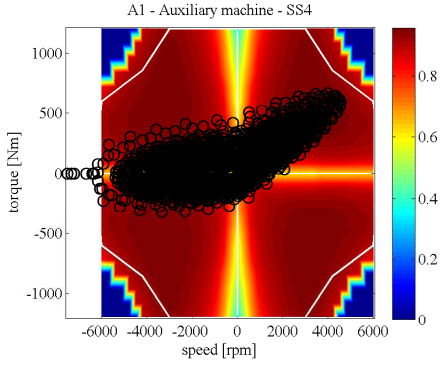

Figure 7.15: Operating points of a lowly damped and tuned auxiliary machine in SS4, with negative speeds exceeding the maximum operating limit.

likely average each other out. However, it should be kept in mind that the higher the power peaks in the electrical output, the higher the installed power of the PTO components will be, which will have an effect on the costs.

7.6.1 Time course of power as a function of control choices

To give an idea of the power output over time, plots have been made for (non-optimised) cases of (i) a highly damped auxiliary in Fig 7.16, (ii) a low damped auxiliary Fig 7.17, (iii) a tuned and low damped auxiliary Fig 7.18 in SS4 with an unlimited PTO.

The first case of a highly damped auxiliary achieves a mean absorbed power of 12.2 kW and has a relatively low peak to mean ratio, the peak power of the auxiliary is around 30 kW, and around 19 kW for the main generator. The total peak power is about 42 kW, which gives a peak-to-mean ratio of only 3.4. The power of the machines is never negative, i.e. always generating.

The second case, a lowly damped auxiliary reaches a mean absorbed power of 20 kW with peaks of the auxiliary machine of up to 220 kW and 10 kW for the main generator. The total peak power is about 225 kW, with a peak-to-mean ratio of 11.3. The power is always positive.

In the third case reactive control (tuning) is applied together with a low damping factor, resulting in a mean absorbed power of 29.4 kW. The auxiliary machine peaks at more than 290 kW when working as generator, and around -170 kW when working as motor. The peak of the main generator is reached at around 12 kW. The total power exceeds 300 kW in generative mode, resulting in a peak-to-mean ratio of 10.2, and the total power reaches a peak around -170 kW in motor mode.

It is reminded that these data are simulated with an unlimited PTO and that the influence of installed power reduction is studied in the next sections. It should also be kept in mind that the control of the main generator can be optimised to have a more steady output.

7.6.2 Potential power averaging with the PST topology

When a constant power output would be a substantial requirement, the topology of the PST PTO with a flywheel offers possibilities. A strategy to flatten the power output could be to store the power peaks generated by the auxiliary machine in the main generator flywheel. To do so, the total power output should be monitored and controlled to correspond to the average produced power. The control can be effectuated by first reducing the power generation of the main generator once the total power exceeds the average produced power, and even using the main generator as motor on moments when the auxiliary power exceeds the average produced power to accelerate the flywheel and store the energy. Some instances later, this

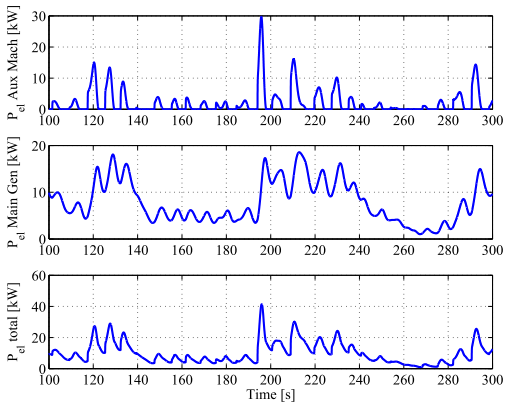

Figure 7.16: Electrical power vs. time for the auxiliary machine, main generator and total electrical power for the case of a highly damped auxiliary machine in SS4.

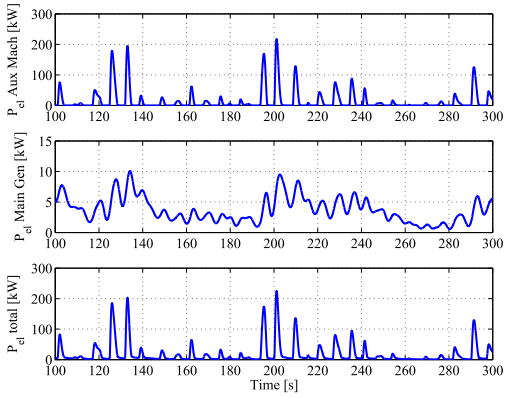

Figure 7.17: Electrical power vs. time for the auxiliary machine, main generator and total electrical power for the case of a low damped auxiliary machine in SS4.

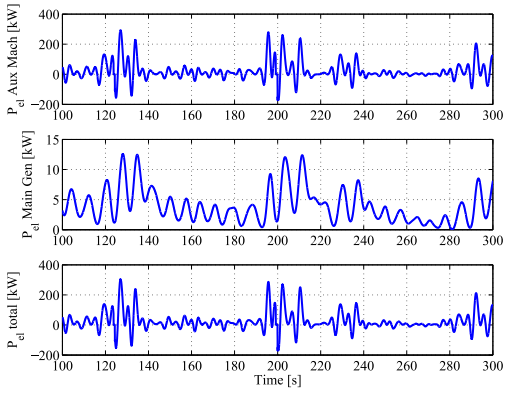

Figure 7.18: Electrical power vs. time for the auxiliary machine, main generator and total power for the case of a tuned and low damped auxiliary machine in SS4.

energy can subsequently be converted to electricity when the output of the auxiliary machine is low (and even negative). The torque of the auxiliary machine will still be controlled to maximise electrical power production, the main generator will control the magnitude of the actual total power output. The main generator's RMS torque will consequently rise significantly, as well as the maximum required torque, and thus its installed power.

This will inevitably lead to a net loss of energy because the stored energy will be converted twice by the main generator with corresponding losses. A cost-benefit analysis should be performed, as well for an alternative power smoothing solution such as ultracapacitors on the DC bus. Ultracapacitors have proven to be a good technical solution in the Wave Pioneer test WEC [77]. Moreover, the question rises whether such a PST system has advantages over another PTO system extended with an extra power smoothing solution. E.g. a rack and pinion PTO could also be extended with an extra machine with a large flywheel, or an ultracapacitor system.

7.7 System definition for further analysis

Based on the above findings a control strategy based on reactive control with optimised damping will be used in the further analyses in this work. The reactive control will also allow negative tuning to virtually reduce the inertia to prevent exceeding of the sinkage constraint which appeared to be an issue in SS5 and SS6. As an extra precaution, the auxiliary machine inertia will be derived from a catalogue of low-inertia machines [78] to enable moderate tuning.

The inertia of the flywheel on the main generator shaft J_{fly} is set at 10 kgm^2 and the main generator damping factor $K_{\mathrm{p,main}}$ at 6 Nms/rad. The setpoint speed n_{set} is set at 1000 rpm.

Hence the only control parameters are the supplementary inertia J_{sup} determining the amount of reactive control, and the damping factor $K_{\mathrm{p,aux}}$ deciding on the degree of damping of the auxiliary machine.

7.8 Influence of PTO installed power

Based on the simulations with an unlimited PTO of the previous sections, an installed power for both the auxiliary machine and main generator have been defined. The required auxiliary machine has a rated power of 188.5 kW with a rated speed of 3000 rpm and the main generator 12.5 kW 1000 rpm. Analogue to the other two studied PTO topologies, six power steps have been defined to investigate the influence of the installed power without varying the rated speed, hence looking at the influence of the available torque. The installed power of the main generator is not changed and remains 12.5 kW in all cases. The power steps of the total installed

Table 7.4: The six power steps [kW] for the sensitivity analysis on rated power. The value represents the total installed power from auxiliary machine and main generator together. The main generator contributes in all cases for 12.5 kW.

	$P1$	$P2$	$P3$	$P4$	$P5$	$P6$
Rated power [kW]	44	75	107	138	170	201

power are displayed in Table 7.4. The power steps do not correspond to available machine sizes, but are a tool to study the influence towards the WEC performance. The inertia of the auxiliary machine is function of the rated torque of the machine and ranges between 0.094 kgm^2 and 0.49 kgm^2, derived from a low inertia machine range [78]. The inertia of the main generator is included in the value of J_{fly}. Unlike the other two studied PTO technologies, the installed machine power is not split up in the simulation model, the PST model comprises one main generator and one auxiliary machine.

For each power step, the optimal values for the control parameters J_{sup} and $K_{\mathrm{p,aux}}$ have been defined at every sea state accounting for the floater and PTO constraints, depicted by the colour plots of Fig. 7.19 as a result of approximately 3000 simulation runs. The PTO constraints include the RMS torque and positive speed limit of the auxiliary machine. As stated in Section 7.5.3, the auxiliary machine is allowed to rotate idle in negative direction above 200% of the rated speed, the peak negative speed reached for the choosen parameter combination is approximately 11 000 rpm. The main generator power of 12.5 kW with a rated speed of 1000 rpm is dimensioned on the requirements of a SS6 with a $P6$ installed power, and might thus be over dimensioned for the other cases, which can be subject for a future optimisation.

The mean power per sea state is subsequently plotted vs. the installed power in Fig. 7.20 together with the values of peak sinkage, lift, RMS torque and speed, normalised to its respective limit. It should be noted that the calculation of the mean power only includes the machine efficiency with an $A1$ map and the drive efficiency, the PST efficiency is not taken into account, an estimation of it will only be considered to calculate the yearly yield as explained in Section 7.2.6. The powers presented here consequently do not have any physical reference, but are used here to visualise the trends influenced by the installed power.

Constraints

Fig. 7.19 and Fig. 7.20 indicate that it is mainly the speed limit that decides on the choice of control parameters, and the sinkage limit from $P4$ on. The chosen speed range of the 3000 rpm might have been too stringent to start with.

The RMS torque is the limiting factor in $P1$, at least for the sea states higher

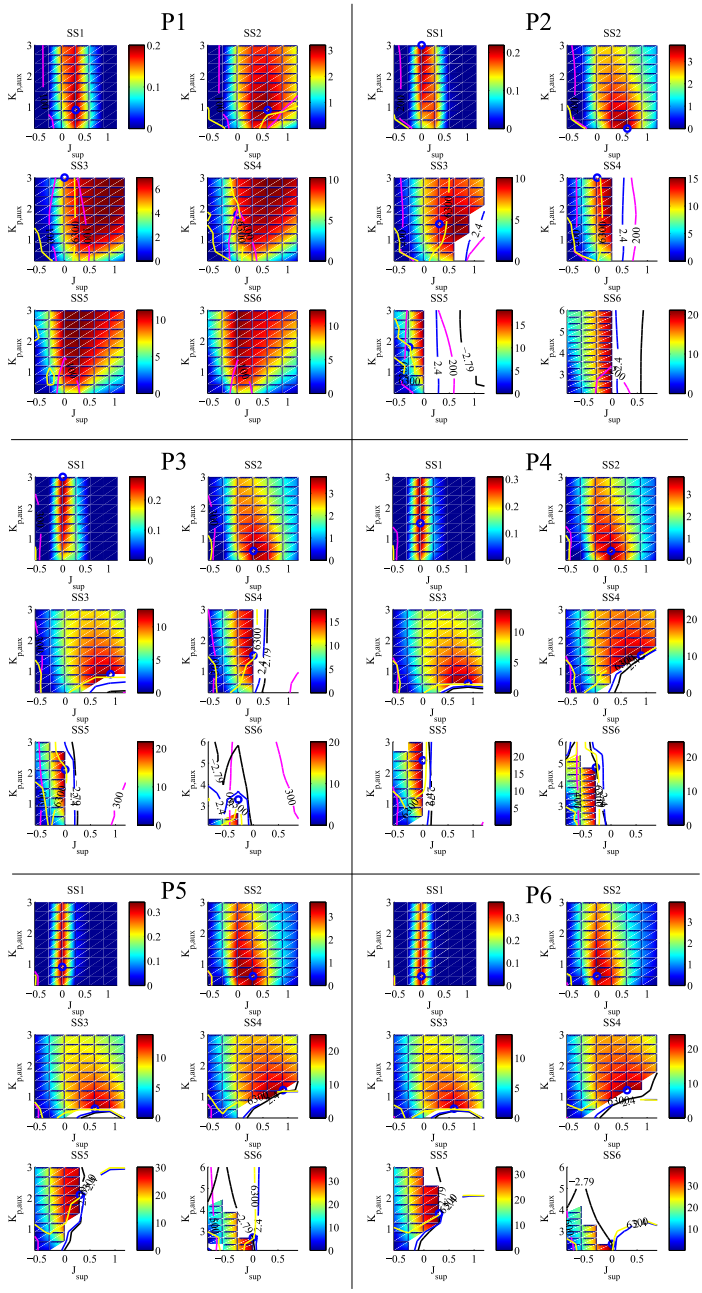

Figure 7.19: Mean power [kW] vs. control parameters J_{sup} [kgm^2] and $K_{\mathrm{p,aux}}$ [Nms/rad] for the 6 steps of PTO power with $A1$ machine efficiency map without accounting for PST efficiency, contours for maximum sinkage (black), speed (yellow), RMS torque (magenta) and lift (blue).

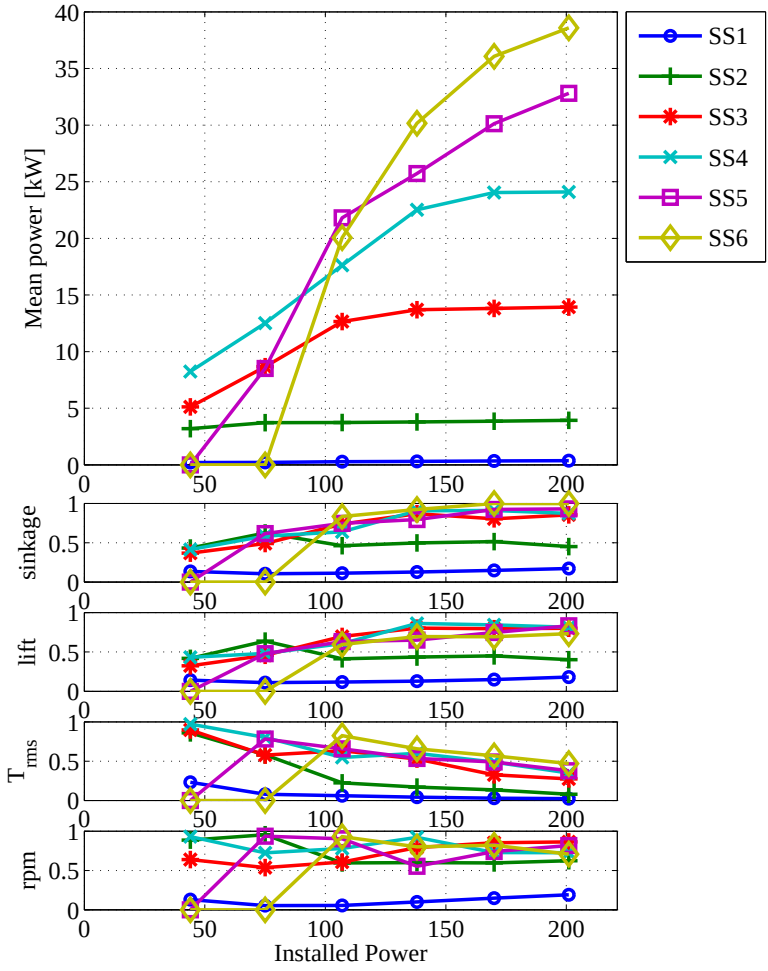

Figure 7.20: Mean power [kW] per sea state vs. installed power [kW] with normalised values in relation to the constraint limits for sinkage, lift, RMS torque and rpm, for an $A1$ machine without accounting for the PST efficiency.

than SS2 where this very small PTO is able to operate. $P1$ does not have enough power on board to handle SS5 and SS6, neither has $P2$ to cope with SS6.

Mean power

The mean power for SS2 is relatively flat, only P1 shows a visible lower mean power for that sea state. The power curves as a function of the installed power for SS3 and SS4 are topped due to reaching of the limits at higher installed powers.

The current configuration of the PST PTO is possibly not optimal to absorb energy at SS5 and SS6, certainly not with installed powers $P1$ to $P4$. As stated before, the study of a PST in a WEC in this work is a first proof of concept, and a better arrangement of the transmission ratios of the additional transmissions, the PST itself and the operational speed range of the machines might improve the system's performance in higher sea states.

Control parameters

The control parameters are sea state dependent as can be seen from the location of the blue circle indicating the feasible optimum. Please note the change in axis limits for some cases. The control parameters J_{sup} and $K_{\mathrm{p,aux}}$ for each sea state are plotted in Fig. 7.21 for the highest installed power $P6$, and for the case $P3$ in Fig. 7.22. The reactive control for $P6$ is purely positive, while with the $P3$ installed power it is necessary to virtually reduce the inertia of the auxiliary machine for SS6 with a negative value for J_{sup}.

The colour plots of Fig. 7.19 show that the iteration range of the control parameters could have been smaller. Care should be taken to define the resolution of the iteration. A first run did not give a workable solution for some cases in the higher sea states, and only after reducing the step of J_{sup} from 0.3 to 0.1 a possible operation point was found.

Average machine efficiency

One of the claimed advantages of the PST PTO is that the machines, or at least the main generator, can operate at or close to its optimal efficiency. Because the contribution of the auxiliary machine exceeds the main generators power contribution, a check of the total average machine and drive efficiency has been done and compared with a direct coupled rack & pinion PTO as studied in the previous chapter. For both the PTOs the results of simulations with a $P6$ installed power have been used with an $A1$ efficiency map.

In Table 7.5 the ratio in [%] of the mean electrical power of the machines over the mean electromagnetic power for each sea state is displayed. The second columns lists the values for the rack & pinion PTO which rise with the sea state between 60% and 88%. In the third column the values of the PST PTO show that the average machine efficiency is indeed higher than with a rack and pinion direct

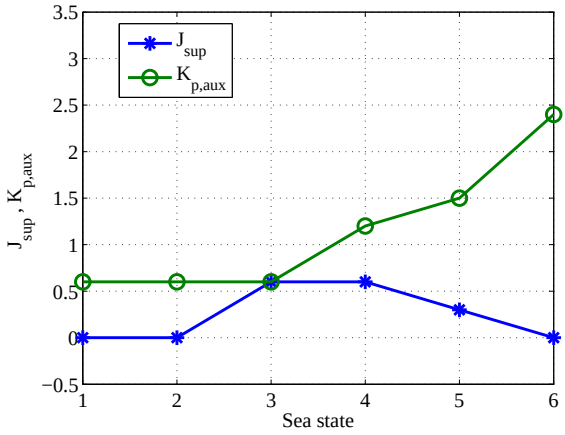

Figure 7.21: Optimal values of the control parameters J_{sup} [kgm^2] and $K_{\mathrm{p,aux}}$ [Nms/rad] vs. sea state for the case $P6$.

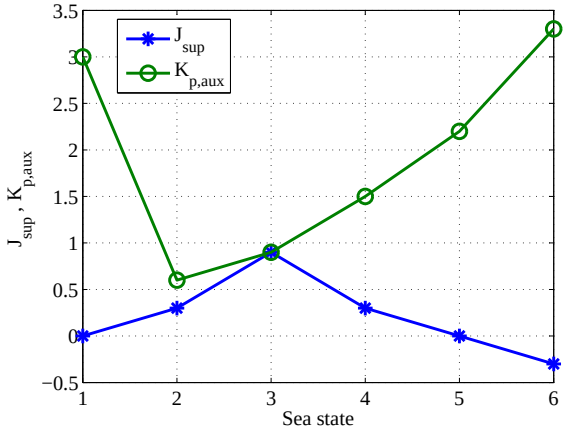

Figure 7.22: Optimal values of the control parameters J_{sup} [kgm^2] and $K_{\mathrm{p,aux}}$ [Nms/rad] vs. sea state for the case $P3$.

Table 7.5: The ratio in [%] of the mean electrical power of the machines over the mean electromagnetic power for each sea state, for the rack & pinion PTO (second column), the PST PTO (third column), and the difference between the two systems (fourth column).

SS	$P_{\mathrm{el}}/P_{\mathrm{em}}$ rack & pinion	$P_{\mathrm{el}}/P_{\mathrm{em}}$ PST	delta
	[%]	[%]	[%]
1	59.6	71.9	12.4
2	74.0	84.4	10.4
3	74.1	77.7	3.6
4	79.9	84.6	4.7
5	85.4	87.5	2.1
6	88.4	91.7	3.3

coupled system, and ranges from 72% to 92% compared to 60% to 88%. This delta has been separately added in the fourth column. The difference is highest in SS1 en SS2 where the machines in a PST environment perform around 10% better. In the higher sea states a substantial 2% to almost 5% are registered.

7.9 Influence of location

The average yearly yield of a WEC equipped with a PST is calculated for the three (virtual) locations (cfr. Section 5.5) for every installed power step and presented in Fig. 7.23. Next to the machine and drive efficiency incorporated in the simulation model, the estimated average PST efficiency has been accounted for to calculate the yearly yield based on the occurrence frequency of the sea states at each location. Due to the poor performance of the lower machine powers in SS5 and SS6, the curves are very steep up to $P4$ for all three locations, note the absence of the bars of SS5 and SS6 representing the contribution per sea state. From $P4$ on, the gradient decreases but the annual yield still rises with increasing installed power. The higher the wave climate at a location, the larger that gradient is, and logically the higher the magnitude. As with the other two studied PTO topologies, the location will decide on the incentive to increase the installed power or not.

In Fig. 7.24, the yearly yield per kW installed power is plotted for all locations. This value, indicated on the left y-axis, can also be read as the equivalent full load hours, i.e. the number of hours that the machines would have to operate at full load to achieve the same amount of energy. Dividing this number by the total number of hours in one year, the capacity factor is obtained, indicated on the right y-axis. The plots clearly indicate the lower performance of the PTO with lower installed power.

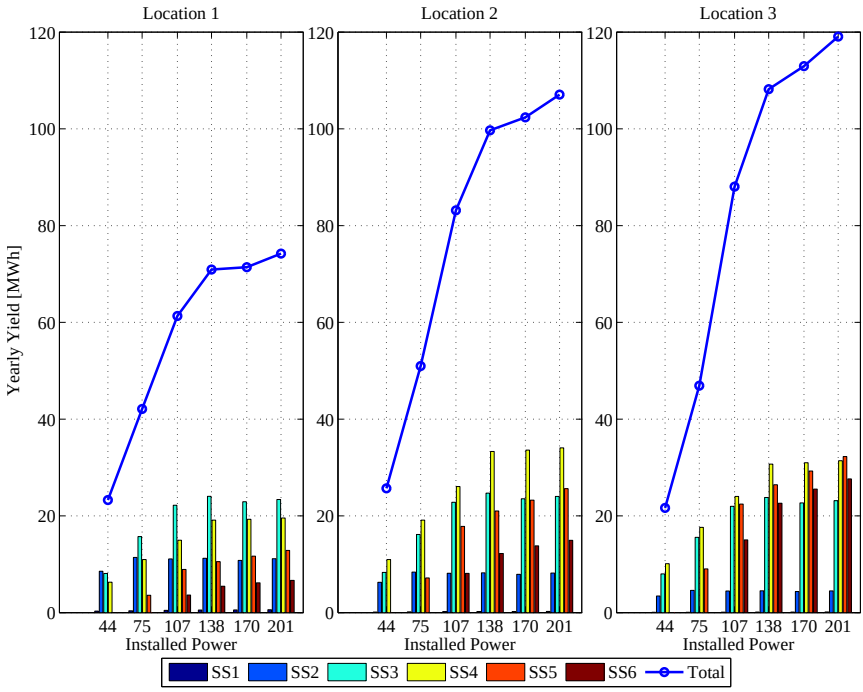

Figure 7.23: Yearly energy yield vs. the installed power [kW] for the 3 locations together with the energy fractions per sea state for the $A1$ efficiency map and estimated PST efficiency.

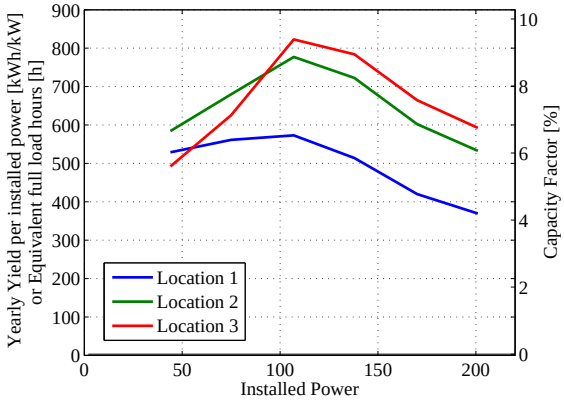

Figure 7.24: The yearly yield per installed power [kWh/kW], or full load hours [h] on the left y-axis, and the capacity factor [%] on the right y-axis vs. the installed power [kW] for the three locations, with an $A1$ efficiency map and estimated PST efficiency.

Table 7.6: The five steps in rotational speed $n1$ to $n5$ in [rpm] and the six steps in torque $T1$ to $T6$ in [Nm] of the auxiliary machine.

	$n1$	$n2$	$n3$	$n4$	$n5$
[rpm]	2200	2400	2600	2800	3000

	$T1$	$T2$	$T3$	$T4$	$T5$	$T6$
[Nm]	100	200	300	400	500	600

7.10 Optimising rated torque and speed

Thirty machine combinations for the auxiliary machine have been analysed to investigate the influence of its size on the average yearly yield. Five steps in rated speed and six steps in rated torque have been defined for the auxiliary machine which are summed up in Table 7.6. The installed power of the main generator is not changed and remains 12.5 kW in all cases, this could be subject of a future optimisation. The total installed power for the $T6$-$n5$ case equals the total installed power of $P6$ of the previous section, i.e. 201 kW. The values are not set at ratings of available machines, but as a tool to illustrate the influence of the available torque and speed. The change in available speed can be effectuated by changing the transmission ratio of the drive train. A $n4$ machine, for example, can be realised with a 3000 rpm machine and a gearbox ratio that is 3000/2800 higher than the $n5$ case. When both have a $T6$ rated torque, the rated torque of the $n4$ machine will in reality be lower than the 600 Nm, to be exact: 2800/3000*600 = 560 Nm.

Because the behaviour of the WEC is highly sensitive to the inertia of the auxiliary machine (cfr. Section 7.4.3.3), the inertia of the auxiliary machine is taken function of the rated torque and ranges between 0.094 kgm^2 and 0.49 kgm^2 [78], unlike the analogue analyses of Chapter 5 and Chapter 6 where the inertia was fixed for the 30 cases. The inertia of the main generator is included in the value of J_{fly}, and is set at 10 kgm^2. The main generator damping $K_{\mathrm{p,main}}$ is set at 6 Nms/rad.

For each of the thirty simulated machines, the control parameters J_{sup} and $K_{\mathrm{p,aux}}$ are selected to optimise the mean power and to respect the constraints. The result of these (approximately 14 000) simulations is plotted for each sea state as a function of the rated torque and rated speed in Fig. 7.25. The value of mean power presented here is calculated accounting for the machine and drive losses, but the estimated PST losses are only considered in the calculation of the average yearly yield.

Similar as with the other two PTO topologies studied, the presented methodology aims at dimensioning the best PTO size based on the average annual energy yield rather than on maximised power production in each sea state. The results of

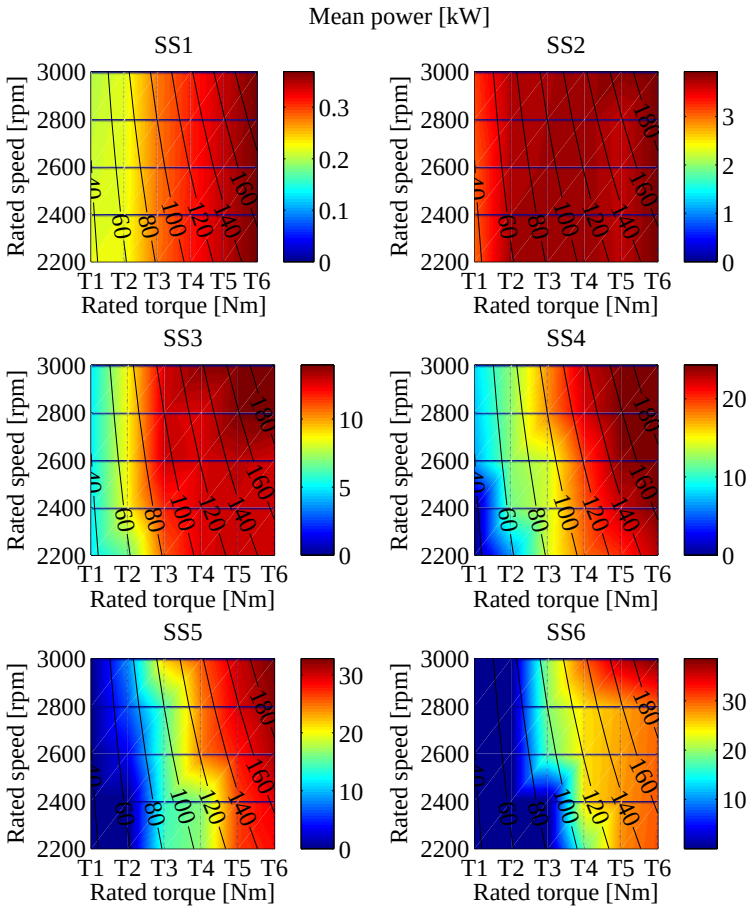

Figure 7.25: Mean power [kW] (only accounting for machine and drive losses) per sea state as a function of the 30 simulated rated torque and speed combinations.

the yields can consequently be used in a techno-economic study to determine the optimum case.

7.10.1 Mean power

The mean power presented in the colour plots of Fig. 7.25 result from simulations considering an $A1$ machine map, but the trend is identical for the $B3$ efficiency map, with slightly higher magnitudes.

The influence of the reducing available speed range is clearly visible from SS3 onwards: the mean power drops with decreasing speed range. The operating

points of the $T6$-$n5$ and $T6$-$n2$ cases are looked at in detail. Fig. 7.26 shows the operating points of SS4 simulations, the upper figures for a $T6$-$n5$ machine, and the figures below for a $T6$-$n2$. In the left figures the operating points are scattered above an $A1$ machine efficiency map, in the right figures above a $B3$ map. The mean power between the two cases barely differs, and indeed, there is no clear shift of the operating points to higher or lower efficiency zones, and the damping is not influenced as can be seen in the upper right quadrant. Still, the ability to apply reactive control is slightly reduced in the $n2$ case at the higher negative speeds. The situation for a SS6 wave condition is somewhat different as illustrated by Fig. 7.27. The $n2$ case is confronted with the need of negative tuning which needs reactive control in contrast to the $n5$ case where the auxiliary machine is simply damped. The path of the operating points is almost perfect for the $B3$ map: the shortest way to the highest efficiency zone. Also for the $A1$ map, most of the operating points - and especially at the higher power values - are located in high efficiency zones. For the $n2$ case, the performance drops significantly due to the need of reactive control as the colour plot of the mean power for SS6 in Fig. 7.25 depicts.

The location of the operating points of the main generator is visibly unaffected between the $T6$-$n5$ and $T6$-$n2$ cases, and is therefore only displayed once for each sea state, in Fig. 7.28.

To tackle the decreasing available torque and speed, for example in the $T4$-$n3$ machine, the damping of the auxiliary machine is increased to prevent exceeding of the speed limit. This is illustrated for a SS4 in Fig. 7.29, the damping is clearly higher than in Fig. 7.26.

7.10.2 Constraints

The normalised values for the limits of sinkage, lift, RMS torque and speed are represented for all 30 machines in Fig. 7.30. The sinkage is clearly the limiting factor for SS6, indicated by the dark red area for $T4$ and above. Relatively high sinkage values are also reached for SS3, SS4 and SS5. The normalised values for the RMS torque constraint show that the thermal capacity for most of the torque-speed combinations is not a limitation. The relative values for the positive peak speed of the auxiliary machine run close to the limit. By applying a finer resolution for the control parameters, a better view on the limiting constraints could be achieved.

7.10.3 Yearly yield

Even though the power split transmission technology in a WEC is in a very early stage, the calculation of the average yearly yield as a function of different combinations of operational range of torque and speed opens a view to potential re-

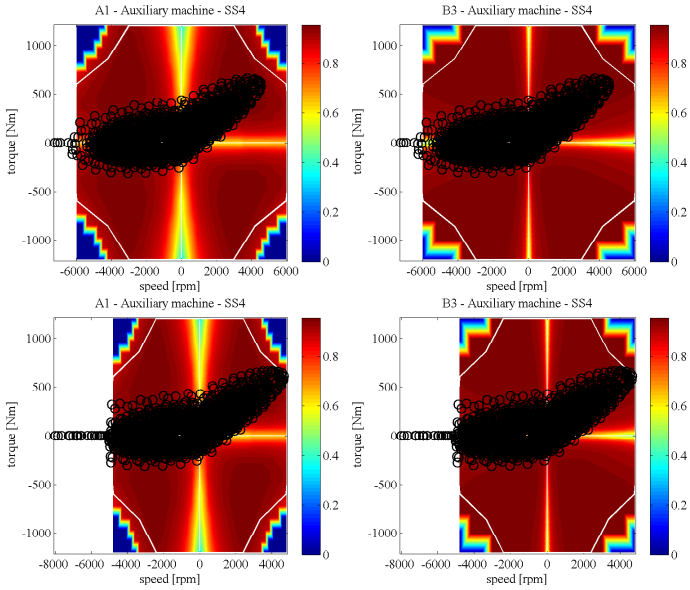

Figure 7.26: Scatter of the SS4 auxiliary machine operating points above an $A1$ (left) and $B3$ (right) efficiency map for a $T6$-$n5$ case (upper) and $T6$-$n2$ case (bottom).

duction of the installed power. Fig. 7.31 presents the yield results accounting for the estimated average PST losses on top of the machine and drive losses. For every location the yield [MWh] as a function of rated torque and speed is plotted together with contours for the total installed power in [kW] in the left figure. The right figures represent the energy per kW installed power, or equivalent full load hours. The figures originate from an $A1$ map, but the trend of the $B3$ yield is substantially identical (with higher magnitudes, cfr. next section) and is therefore not published. Moreover, this level of detail is not relevant at this stage of exploration of the technology. The choice of efficiency map variant is identical for both auxiliary machine and main generator.

What stands out from the yield plots of Fig. 7.31, is that the yield follows the contour lines of the installed power. For the studied cases, a relative reduction in torque has a comparable effect on the yield as the same relative reduction in speed. This is possibly due to the fact that a rated speed of 3000 rpm was already narrow margined.

Table 7.7 compares the yield of every of the thirty combinations with the best performing case at every location. At each of the locations the $T6$-$n5$ case is the best performing option. However, a profitability optimisation could be performed. For example the $T4$-$n3$ outputs only 15.5% less energy with 42% less installed

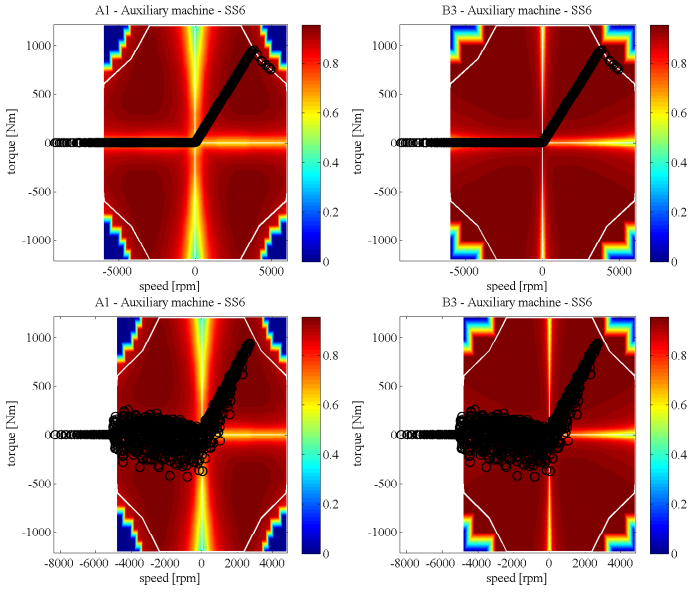

Figure 7.27: Scatter of the SS6 auxiliary machine operating points above an $A1$ (left) and $B3$ (right) efficiency map for a $T6$-$n5$ case (upper) and $T6$-$n2$ case (bottom).

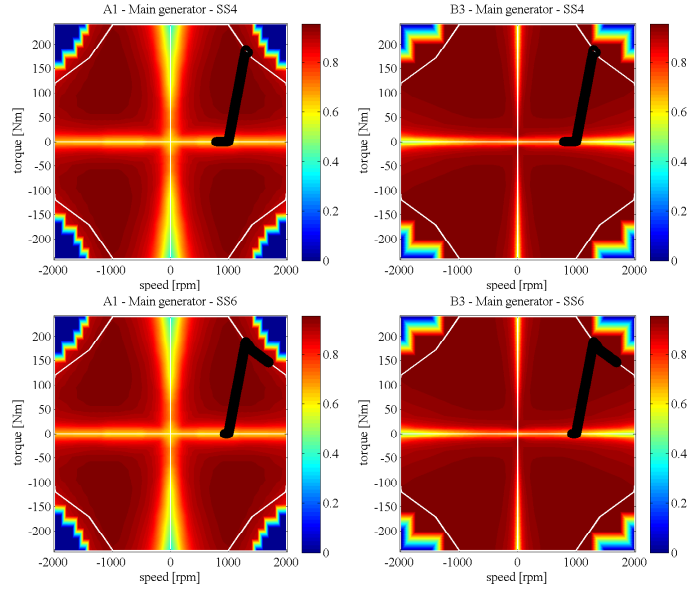

Figure 7.28: Scatter of the main generator operating points above an $A1$ (left) and $B3$ (right) efficiency map for SS4 (upper) and SS6 (bottom).

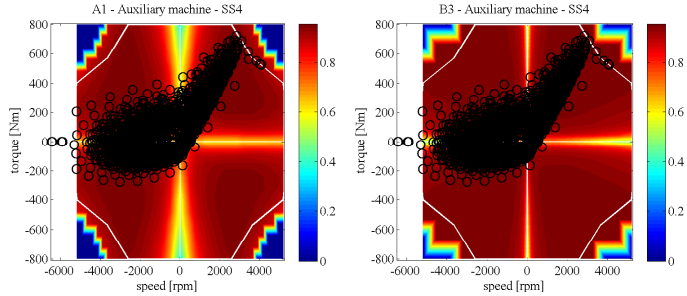

Figure 7.29: Scatter of the SS4 auxiliary machine operating points above an $A1$ (left) and $B3$ (right) efficiency map for a $T4$-$n3$ case, as an example of higher auxiliary machine damping, combined with (positive) reactive control.

Table 7.7: The ratio in [%] relative to the maximum yield at Location 1, 2 and 3 respectively for every rated torque and speed combination for an $A1$ map.

Location 1	$T1$	$T2$	$T3$	$T4$	$T5$	$T6$
$n5$	31.3	56.7	82.6	95.6	96.2	100.0
$n4$	30.6	55.7	78.8	90.2	93.4	97.7
$n3$	29.5	54.0	74.6	87.9	90.2	94.4
$n2$	22.4	51.2	67.1	82.8	87.6	93.6
$n1$	22.0	40.4	65.6	80.5	85.4	91.5
Location 2	$T1$	$T2$	$T3$	$T4$	$T5$	$T6$
$n5$	24.0	47.6	77.7	93.1	95.6	100.0
$n4$	23.2	46.2	72.2	87.3	91.9	96.3
$n3$	22.1	43.7	66.9	84.5	88.9	93.8
$n2$	13.5	40.0	57.6	77.5	85.8	92.6
$n1$	13.2	29.2	56.7	74.2	83.2	89.9
Location 3	$T1$	$T2$	$T3$	$T4$	$T5$	$T6$
$n5$	18.2	39.4	73.9	90.9	94.9	100.0
$n4$	17.5	37.8	67.6	84.0	89.1	94.0
$n3$	16.7	35.0	62.7	81.7	86.3	91.7
$n2$	9.6	31.0	49.1	74.0	83.5	90.4
$n1$	9.4	21.9	48.4	69.3	81.5	88.0

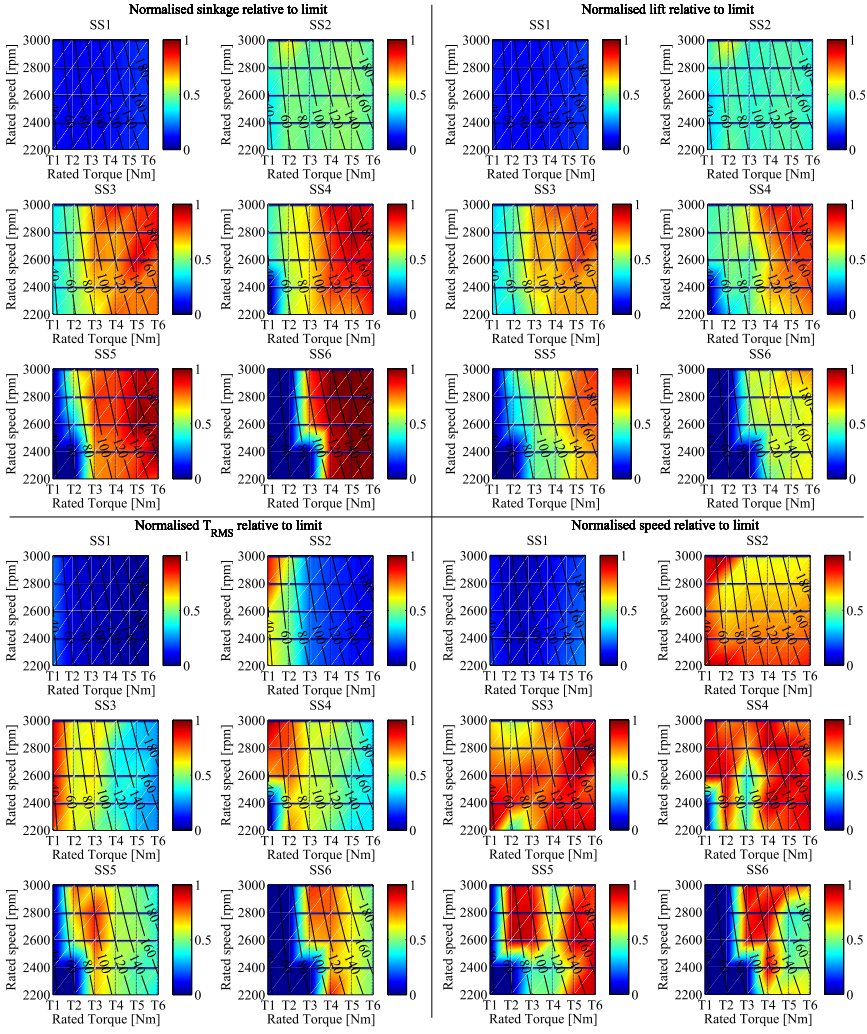

Figure 7.30: Normalised values in relation to the constraint limits for sinkage, lift, RMS torque and speed, for an $A1$ machine and gearbox.

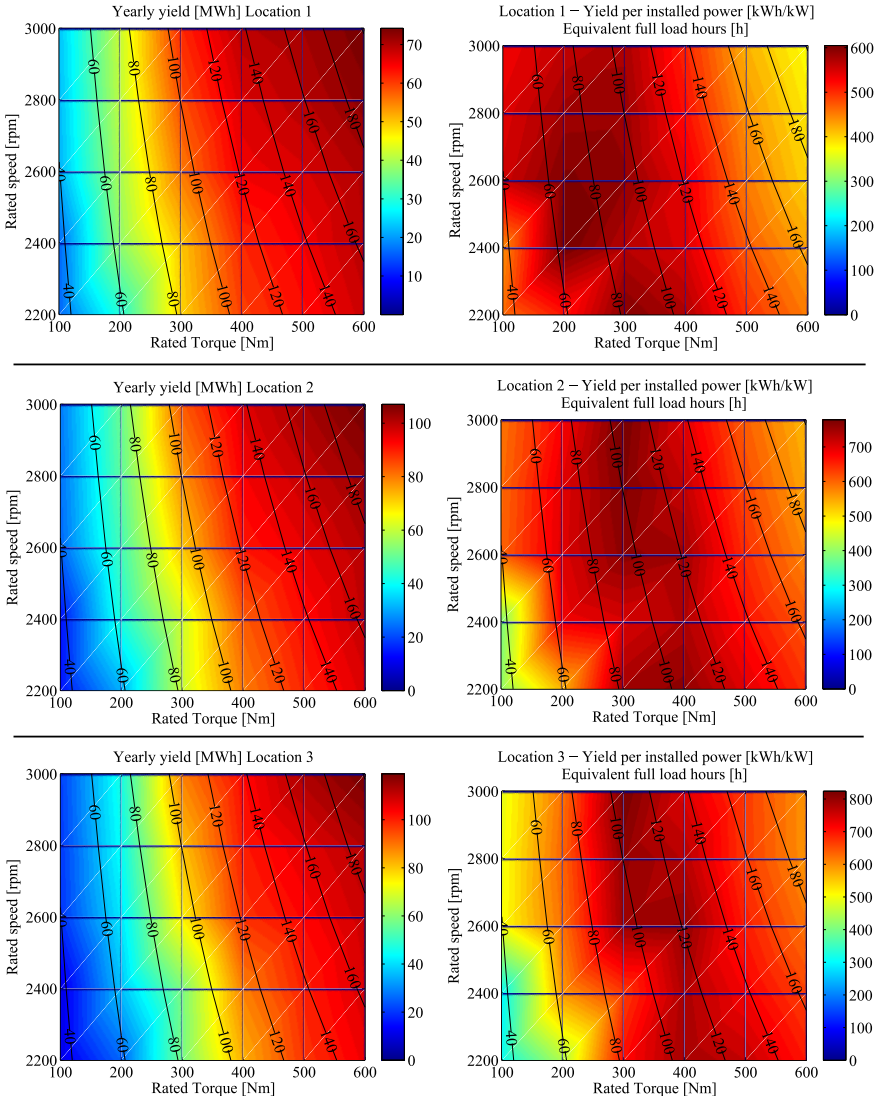

Figure 7.31: Average annual yield [MWh] (left) and yield per installed power [kWh/kW] or equivalent full load hours [h] (right) for each location as a function of rated torque and rated speed. $A1$ map, drive efficiency and estimated average PST efficiency taken into account.

Table 7.8: Comparison of the yearly yield of the $B3$ cases with the $A1$ cases as YY($B3$)/YY($A1$) in [%].

Location 1	$T1$	$T2$	$T3$	$T4$	$T5$	$T6$
$n5$	114	109	106	106	104	104
$n4$	112	108	106	105	105	104
$n3$	112	107	106	105	105	104
$n2$	111	107	105	105	104	104
$n1$	109	108	105	105	104	103
Location 2	$T1$	$T2$	$T3$	$T4$	$T5$	$T6$
$n5$	112	109	105	105	104	104
$n4$	111	108	106	104	104	104
$n3$	110	107	106	104	104	104
$n2$	110	106	105	104	104	103
$n1$	109	108	104	104	103	103
Location 3	$T1$	$T2$	$T3$	$T4$	$T5$	$T6$
$n5$	112	108	105	104	103	103
$n4$	110	107	106	104	104	104
$n3$	109	107	106	104	104	103
$n2$	111	105	105	104	103	103
$n1$	109	108	104	105	103	103

power. Taking these values into account in a total cost and revenue evaluation, the sense or nonsense of a large installed power can be determined.

7.10.4 Yield comparison between $B3$ map and $A1$ map

To assess the influence of the shape of the efficiency map of the electrical machines, the yield results of two different type of machines ($A1$ and $B3$) with equal nominal efficiency have been compared. Table 7.8 lists the ratio of yearly yield of the $B3$ map over the $A1$ yield. The trend is almost uniform across the locations and is dependent on the available rated torque: the difference in performance increases with lower rated torque: 3% to 4% for the $T6$ cases and 9% to 12% for the $T1$ cases.

Although a difference of a few percent can be a substantial difference in energy production, it will depend on the price difference between the two types of machines and their share in the total WEC cost whether there is an incentive to choose for one or the other.

7.11 Conclusion

The research presented in this chapter is a successful exploration of the (planetary) power split transmission (PST) PTO from patent [3] in a WEC. First a simulation model has been set up to mathematically represent the interaction between the three shafts. A first step in that process was to determine which of the torques and speeds are an input to the model - and originating from the control or hydrodynamic submodel - and which of the torques and speeds are an output of the PST submodel to pass along to the hydrodynamic model. The dynamics of the two machines are also taken into consideration. Subsequently the corresponding mathematical expressions were composed to represent a PST PTO consisting of an auxiliary machine on one shaft, a main generator with flywheel on the second, and the third shaft connected to the rack and pinion to exert the PTO force on the floater.

A successful proof-of-concept was confirmed after a first series of simulations using a proposed basic control. By retaining the auxiliary machine from rotating during the upwards buoy motion, wave energy is absorbed and mainly redirected to the main generator with flywheel. The latter is able to maintain a unidirectional rotation while generating electrical power, hence the PST performs a bi- to unidirectional conversion of the rotation.

Subsequently, a series of sensitivity analyses were performed to determine how the power absorption from the waves could be improved. The damping coefficients and inertias of both machines were studied. The auxiliary damping and inertia came forward as the most sensitive parameters. It also came to light that the initial idea of redirecting all - or most - of the wave energy towards the main generator had to be abandoned to maximise the power output. By allowing the auxiliary machine to absorb more wave power than the main generator, the total power absorption is 2.5 times larger. Also the idea of power smoothing was set aside to concentrate on the potential energy production with a PST PTO.

Because the inertia of the auxiliary machine influences the power absorption significantly, it had to be limited as it otherwise caused the floater to exceed the sinkage in the higher sea states. Therefore, it was proposed to add reactive control to the auxiliary electromagnetic torque. By doing so, the performance of the WEC can be improved in the lower sea states without compromising the higher sea states. The reactive control consists of a virtual supplementary inertia multiplied with the auxiliary machine's rotational acceleration. Both positive as negative supplementary inertia values are allowed. An alternative could be to use a variable inertia.

Next, using the optimised damping-tuning strategy, the influence of the installed power on the power and energy output has been studied. For six steps in installed power (in terms of rated torque) the mean power in every sea state has

been obtained from simulations, optimising the control parameters for each case. The two to three lowest installed powers did not have enough power on board to handle high wave conditions, but from the fourth power step and above the PST PTO performs good, with a flattening power curve once the constraints are reached. The poor performance of the low installed powers logically affects the yield curves which show a very steep beginning where the influence of the location is barely noticeable. However, once the installed power increases enough, a high energy location clearly benefits from a higher installed power.

The average machine efficiency has shown to be indeed better in a PST PTO than, for example, in a direct coupled rack & pinion PTO. The operating points appear to be located in better efficiency zones.

Finally, the influence of both rated torque and rated speed has been studied. The initial speed range was already narrow and the maximum speed limit seems to be reached quite easily. An additional reduction of the available torque causes the auxiliary to increase the damping factor as a prevention to cross the speed limit. This increased damping factor, however, results in a lower power output. Nevertheless, many of the simulated combinations of rated torque and speed offer a larger reduction in installed power than the corresponding yield reduction. The door is open for a techno-economic analysis.

What's in a name... By optimising the damping to maximise the WEC performance, the auxiliary machine is promoted to the main contributor of electrical power. The question rises thus to change the used terminology of the machines if the PST PTO is further explored in the future.

The proof-of-concept of a power split transmission PTO for wave energy conversion was successful. The yield results are in the same order of magnitude of the rack and pinion PTO, which is promising for a first exploration of this PST system in wave energy. It should be noted that the PST only damps the motion in the upwards direction and tunes it in both. The transmission ratios used in this work are open to revision, a larger speed range for the auxiliary needs to be researched if the PST technology appears to be a viable alternative to other PTO technologies. For example, it should be studied if a low rated torque and higher rated speed performs better than a comparable installed power with higher torque and lower speed. A multi-parameter optimisation urges to fully understand the potential of the PST topology. Anyhow, attention should be paid to have a sufficient fine resolution for the control parameters.

Future research should also include the performance of a flywheel on the shaft connected to the pinion running on the rack, possibly after a first speed increase. It might be interesting to study the use of a variable inertia, also for the auxiliary shaft.

A point of attention is the relatively high speeds during the idle working cycle of the auxiliary machine, and the possibly higher reciprocating behaviour of

the gearbox compared to a fixed transmission system such as with the rack and pinion PTO of the previous chapter. Another thing is that the system needs two (independently working) machines, which increases the risk of failure.

An added value of the PST technology is the possibility to smoothen the power output. Theoretically, by changing the control and increasing the installed power of the main generator, the presented PST topology can store excess electrical energy from the auxiliary machine in the inertia of the main generator's flywheel in order to output a more or less constant power. The main generator will then act as a motor at these instances, to subsequently convert the kinetic energy back to electricity when the auxiliary machine's power is low.

8

Conclusion and suggestions for future research

To reach the point of competitiveness with other (renewable) energy sources, the cost of a WEC needs to be minimised at all fronts. Even though the PTO only partly contributes in these costs (the share of the PTO cost is estimated at 20% - 30% of the total manufacturing cost of the WEC [30–32]), every bit helps. The methodology and the corresponding analyses in this work want to add to this effort by quantifying the yield for different PTO configurations. The choice of machine topology showed to have an important effect on the yield, where the magnitude of the nominal efficiency is of secondary importance to the shape of the efficiency map. Concerning the machine size, it was most interesting to see that, in some cases a smaller machine size even appeared to result in an increased output because the machine was then used in better efficiency operating zones. Additionally, optimising the rotational inertia of the PTO is shown to help significantly for the performance of the WEC.

To enable the performed tests and simulations, a set of tools needed to be elaborated. Simulation models were built including the PTO's operational range, dynamics and efficiency to assess the performance in different wave climates. Multiple iterations were performed to show trends and sensitivities. A large effort was made behind the scenes in the post-processing of the tens of thousands of simulations and to find an intelligible manner to present them. An appealing and transparent way of presenting the results is believed to convince governments, project developers, other researchers, or whoever person having a keen interest in invest-

ing or assisting in the development of wave energy.

Additionally, a lab setup was developed to be a dry test bench for PTOs in a protected, controllable and accessible environment. The lab setup provides a fully interactive wave emulator where the PTO experiences the same (normalised) torques and speeds as it would in a WEC at sea.

Another contribution made, is the study of the effect of the magnitude and shape of the efficiency map of the electrical machine. The importance is pointed out to evaluate a targeted electrical machine not (only) on the magnitude of its nominal efficiency, but on the shape of the efficiency map over the entire working range. Because of the very variable loads inherent to wave energy, the efficiency across the working range of the machine has a substantial influence on the annual energy yield. This should be kept in mind when comparing machine topologies.

The application of reactive control by means of a supplementary mass by motor tuning was updated. While previously only positive values were used to virtually increase the buoy mass, the optimisation of the physical inertia in the rack and pinion PTO brought an incentive to virtually decrease the inertia in some of the sea states by adding negative supplementary mass.

The influence of the machine size was studied by varying both the rated torque and rated speed and represented in yield maps. The maps offer a starting point for a techno-economic analysis to find the most profitable PTO configuration.

Main conclusions per chapter

This book starts with a chapter explaining an existing hydrodynamic simulation model that was previously implemented in Matlab® and that was for this work translated in Matlab-Simulink® with a significant gain in calculation speed. The model is described in Chapter 2 together with the explanation of the spring-mass analogy on which the reactive control principle is based to maximise the power absorption from the waves. It is pointed out that the control needs to consider the floater's constraints in the selection of the control parameters.

Subsequent to the description of the hydrodynamic mathematical model, the core of the studied rotational electromechanical PTOs is modelled in the third Chapter: the electrical machine. A first step is the inclusion of the dynamic behaviour of the PTO inertia. Next, the operational range is defined to consider the operational limits of the machine in the WEC operation. A first reduction of the installed power is subsequently achieved by super-rated use in both torque as speed range. In this work both torque and speed are used up to 200% of the rated value, resulting in a required installed that can be reduced significantly while maintaining the same maximum PTO force along a large part of the working range.

Another indispensable machine characteristic to achieve a realistic estimation

of the electrical power is its efficiency. A quasi static model is used with efficiency maps as a function of the actual torque and speed of the machine. The quasi static assumption for wave energy simulations is subsequently confirmed by experimental tests on the wave emulator lab setup of Chapter 4. For the simulation work, two different efficiency maps have been defined, the A maps and the B maps, corresponding with two machine topologies (induction machine and permanent magnet synchronous machine) to study the effect of the dissimilarity in efficiency along the operational range. For each of the variants, four subvariants ($A1-4$ and $B1-4$) have been defined to analyse the importance of the magnitude of the nominal efficiency within a certain machine topology. The nominal efficiency value of the $A1$ variant is equal to the nominal efficiency of the $B3$ variant, facilitating the study of the sensitivity of the efficiency shape along the operational range.

The use of a lookup table for the efficiency of the machine instead of a detailed electrical machine model, has the main advantage of resulting in a shorter simulation time.

The efficiency of the variable frequency drive has been entered as a fixed value as the efficiency is relatively similar over the entire working range.

Chapter 4 presents a wave emulator lab setup. The setup is a tool to test a PTO or its components in an accessible, controllable and protected environment to assess their suitability and durability in wave energy converters. The wave emulator enables testing of the PTO at equal (normalised) load conditions as if it were installed in a WEC at sea. The wave emulator responds to PTO actions due to a real-time control by the hydrodynamic floater model.

Calculations with noisy accelerations signals are avoided by representing all mass terms of the floater and hydrodynamic model physically in the setup.

If tests at scale are desired, the WEC can be scaled with Froude scaling while the identical normalised load conditions are maintained. This is accomplished by introducing a compensation method which appoints extra inertia to the setup.

The experimental results of the wave emulator setup have been compared to simulation using equal power take-off forces on the scaled model. The comparison showed good correlation for the motion of the floater for the significant sea states. This makes the proposed Wave Emulator a valuable tool in the development of power take-off systems for wave energy converters. Because the intermittent and reciprocating motion accompanied with wave energy is a considerable challenge for PTO designs, it is advisable to run (long duration) tests on such a setup with realistic loads before employing the PTO for (expensive and less accessible) tests at sea.

In the fifth Chapter, the first of three PTO topologies has been studied consisting of a drum and cable system to convert the heaving motion to rotation. The most

important findings are that the PTO efficiency influences the selection of control parameters, affects the magnitude of the electrical output and that the efficiency along the operational range is of substantial importance to evaluate a PTO system, and more important than the magnitude at nominal load.

Even though the PTO losses diminish the effect of the reactive control due to the bidirectional power flow, applying reactive control still results in an important increase of the electrical yield with the studied electromechanical PTO. Considering the magnitude of the nominal efficiency within the same machine topology it is observed that a difference of 1% in nominal efficiency is amplified to a change of 3% in yearly energy yield. When different machine topologies are compared with identical nominal efficiency but different course over the load range ($B3$ vs. $A1$), the discrepancy is meaningful: at least 20% more energy is generated with a flatter efficiency map, and some cases show a discrepancy of 30% or 40%. This is attributed to the fact that the drum and cable PTO also requires motor actions to keep the cable tense on top of the reactive control. Hence, there is potentially a large incentive to use machines with a flat efficiency map in a drum and cable WEC. The results also reconfirm the need to include the detailed efficiency of the PTO in feasibility assessments.

Next, the influence of the installed power has been studied in the drum & cable PTO with gearbox by both iterating the rated torque and speed. For the $A1$ map, with a relatively peaky efficiency map, the yearly yield even increases with decreasing available speed (and thus lower installed power) because the operating points shift to better performing zones. The yield gain is up to 5% for the highest torque cases, on top of a 20% smaller installed power. Thus it is not necessarily the highest installed power that achieves the maximum yield. For the $B3$ map with a flatter shape, the annual yield drops slightly with decreasing speed range, but the drop of installed power is substantially larger than the loss in yield.

A subsequent analysis was performed on the effect of removing the gearbox losses by using a direct drive rotational machine. Yield gains between 9% and 15% were observed depending on the combination of rated torque and speed. A direct drive machine is assumed to be more expensive, but additionally to the yield gain, the absence of a gearbox might benefit the operational reliability and reduce the maintenance costs.

A last optimisation of Chapter 5 was executed regarding the PTO inertia. An appropriately selected inertia can increase the power absorption as it influences the natural frequency of the system. For this PTO topology, a gain of more than 3% in yield has been observed between the lowest simulated inertia and the optimum.

The model used assumed a purely heaving buoy. In reality this is not the case with a cable between the buoy and the seabed. This might include considerable inaccuracies of the model. Moreover, the system can only absorb energy in upward direction and needs to act as a motor during the downwards motion, leaving

a share of the floater's potential untapped.

The second PTO topology is studied in Chapter 6 and concerns a rack and pinion system to which an electrical machine is connected with or without a gearbox. The rack and pinion offers, in contrast to a drum and cable, energy absorption in both directions and there is no worrying about keeping the cable tense. The rack & pinion also causes the reactive control to have a significantly larger effect because the WEC can be tuned during the whole wave cycle.

A first set of analyses is done on a geared system and includes the efficiencies as in the previous chapter. While the sinkage was the limiting floater constraint for the drum and cable PTO, the peak lift is now reached earlier. This is caused by the fact that the motion of the floater is significantly different due to the damping in both directions.

Once focusing on the electrical output and thus considering the PTO efficiency, the effect of the reactive control is slightly lower than when the absorbed power is maximised, but it still brings a substantial gain in WEC performance. The influence of the nominal efficiency's magnitude is slightly lower than with the drum and cable because there are relatively less motoring actions. A drop of 1% in nominal efficiency decreases the yield with approximately 2% for both the simulated machine topologies (A and B maps). The better average performance of the $B3$ machine, with a flatter efficiency map, brings a yield increase of between 9% and 15% compared with the $A1$ machine, although having an identical nominal efficiency. This gain is also slightly less pronounced than with the previous studied PTO topology, but still clearly emphasises the weight of the efficiency map shape.

The iterations with both rated torque and rated speed showed a large potential to reduce the installed power of the PTO machine. With this PTO topology as well, the $A1$ machines with lower rated speed perform better because they are more often operated in high efficiency zones. As the $B3$ efficiency map is much flatter, the yield does not increase with decreasing speed range, but it does not drop either. Hence a significant installed power reduction can be achieved by adapting the speed range.

At first, the results for the direct drive option were against expectation, because in many cases it performed worse than the geared option. This is however explained by the substantial drop in equivalent PTO mass towards the hydrodynamic system and thus lowering the floater's response. Only for high rated torques, the system benefits from the better PTO efficiency with a yield gain of 15%. Because then the machine has ample torque available to add virtual mass by the reactive control. This is an example of the need to get both the hydrodynamic response right as well as the PTO performance.

The study of the direct drive already revealed the compelling influence of the PTO inertia in the rack and pinion WEC, which was confirmed by an iteration with

a set of inertia values. By optimising the rotary inertia, the motor tuning can be reduced significantly which benefits the net electrical outcome. The optimal inertia results in a substantial gain in annual yield: between 12% and 18% depending on the location, compared to the lowest inertia of the iteration set. For the direct drive option the inertia has not been optimised because this would require an immense amount at low speed.

An update to the control was proposed in the aftermath of the inertia optimisation. The optimal inertia enhanced the overall performance, but was apparently too large for sea state (SS) 6 and thus decreased the mean power in that sea state. As a solution, negative tuning was introduced to virtually reduce the inertia. This led to rise the mean power of SS6 again with 30% and the yearly yield with another 2% to 5%, depending on the location, on top of the already achieved gain due to the optimised inertia.

In Chapter 7 the last of the three studied PTO systems was presented. The PTO consists of a novel idea from patent [3] to insert a power split transmission (PST) in a WEC aiming at a better average machine efficiency and a bidirectional to unidirectional conversion of the rotation. The PST has three shafts of which the speeds and torques are interrelated. By means of controlling an auxiliary machine on one of the three shafts, wave energy should be absorbed from a second shaft and directed to a main generator with flywheel on the third shaft rotating in a single direction.

Firstly, a simulation model has been set up to mathematically represent the interaction between the three shafts of the PST, and the dynamics of the two machines connected to it. The model was then combined with the hydrodynamic simulation model and a successful proof-of-concept was confirmed with a basic control strategy.

A series of sensitivity analyses revealed the most important control and mechanical parameters. On that base, a configuration for the next simulations was defined and the control strategy was adapted to maximise the power output with the consequence that the auxiliary machine becomes the main contributor of energy. A second intervention on the control was done by adding a reactive component to the auxiliary control to improve the hydrodynamic response of the floater and thus the power output. Positive tuning values improved the performance in the lower sea states while negative tuning prevented the WEC from reaching the peak sinkage too easily in the higher sea states and thus also increasing the mean power. An alternative could be the use of a variable inertia.

The average machine efficiency indeed showed to be better in a PST configuration than, for example, in a direct coupled rack & pinion PTO, the operation points appear to be located in better efficiency zones.

In the analysis of the yearly yield versus rated torque and rated speed, many

of the simulated combinations offer a larger reduction in installed power than the corresponding yield reduction. This opens possibilities for a techno-economic optimisation.

The first exploration of the novel PST PTO concept was successful and offers next to the competitive yield, plenty of research opportunities, both in power maximisation and reduction of installed power. And even though the idea of the potential power smoothing was put aside for this work, the configuration lends itself to investigate the opportunities.

As mentioned earlier in the text, the values quantified by the simulations are not meant as absolute assessments of the WEC equipped with a certain PTO configuration, but as a tool to emphasise the sensitivities in dimensioning a power take-off system and to point out where or how the PTO can be optimised, possibly including a potential reduction of installed power. Therefore it was found not appropriate to venture a quantitative comparison between the three studied topologies. Moreover, the only comparison that makes sense, is one that encompasses a complete techno-economic evaluation.

Nevertheless, it is worthwhile to mention some qualitative aspects of the three studied PTO topologies, in particular some points of attention for each of the systems. The drum and cable technology brings the disadvantage of the need to keep the cable tense at all times and the corresponding unidirectional power absorption. Slack on the cable can result in high impact forces which could exceed the maximum tensile strength of the cable. Keeping the cable tensioned requires a higher ratio of power investment. Additionally, the model used here for the drum & cable PTO assumes a pure heaving motion, while the cable will in reality also allow the other motions in all degrees of freedom, including the pitch and roll motions. The model contains therefore a large degree of uncertainty for this topology.

A PTO consisting of a rack and pinion system such as in Chapter 6, but also the PST system of Chapter 7, does not allow other motions but heave, however the guiding system will have to deal with all non-vertical wave forces on the floater, and these are not negligible.

The PST system needs two independently working electrical machines, increasing the risk of failure. Although the two other systems also might consist of a gearbox, it is unsure whether the application as a three shaft PST will jeopardise the life time of a planetary gearbox.

Suggestions for future research

As already stated in the introduction and confirmed by the findings in this work, a holistic approach is necessary in the development of a WEC. Also the floater design needs to be part of this approach to find the most favourable WEC for a

targeted location. Further research could study how to determine the best floater geometry for a targeted location. Does it suffice to compare different floaters with an unlimited PTO (for which the control parameters are optimised for each case) and subsequently optimise the PTO for the best floater, or is it necessary to optimise the PTO for each of the floaters under consideration to find the optimum composition?

The most profitable option is not always the most performing technical option if it needs to be custom designed. In reality - certainly in a market introduction phase - it is a matter of making the right choice in off-the-shelf available components. If different options arise, and detailed efficiency maps are available (and correct), the options can be compared by using the methods presented in this work. If detailed efficiency data are not available, the wave emulator setup described in Chapter 4 can be used. A first option is to test them directly in wave conditions in the wave emulator setup, but then the control parameters might not be optimal for the tested device. Another possibility is that the detailed efficiency map as a function of the actual torque and speed is mapped on the setup first, to be used subsequently in simulations to select the optimal control parameters and evaluate its overall performance according the approach presented here. It is also a matter of applying the less cost intensive optimisations first, such as optimising the rotational inertia.

Once a selection is made, or a selection of eligible components, their durability can be tested on the wave emulator test setup under realistic load conditions in long duration tests. Next to durability, a sustainability assessment should be performed.

The shape of the efficiency map along the entire operational range seems to be a substantial characteristic of a PTO. The sensitivity study thereof was performed by comparing a map based on an induction machine ($A1$ map) with a map based on a permanent magnet synchronous machine (PMSM) ($B3$ map). In this context it should be stated that this was to emphasize the importance of the efficiency over the entire working range, rather than promoting the PMSM topology. Moreover, flux optimisation at lower loads might be an interesting method to improve the efficiency shape of induction machines, and is a valuable path to investigate in the future.

The operational range of the electrical machine used in this work was up to 200% of rated torque and speed. The range to use depends on the capabilities of the selected machine and can differ from type to type. It is probably interesting to use machines that offer a larger peak speed, or might offer it by simply upgrading the bearings.

For the studied cases in this work, the control parameters were optimised for each case and were often restricted to respect the constraints of floater and PTO. The selection made was based on the simulated time series of exciting wave forces.

In real life conditions however, waves might occur where one or more constraints are exceeded with a static control and the set parameters at that moment. Hence a control should be developed to monitor the limits and act to prevent any exceedance if necessary. This can improve the final yield, because now the control parameters could be considered as suboptimal as they are limited by possibly only a single wave where the limits would be exceeded. Additionally, the control can be improved concerning the absorption performance by wave-to-wave control such as in [11] or comparable. And even without wave-to-wave control, the rack & pinion topology might benefit from an asymmetrical damping and tuning for the upwards and downwards movement, which was symmetrical for the simulations performed in this work.

The viability of a certain strategy does not only lie in its possibility to optimise the energy yield in every sea state, but also in its robustness and sensitivity of the control parameters. If a strategy is very sensitive on the control parameters, the yielded energy will drop significantly when parameters are not set appropriately for a certain wave condition.

The yield results for the series of machine combinations can be used as input for a techno-economic analysis. The options that will be subsequently found as economically relevant should be checked on their margins and flexibility in a next phase and the results should be part of a final evaluation. This could possibly be done by formulating a cost function where the different design parameters and simulation outputs are given a weight depending on their importance.

If a drum and cable PTO is going to be pursued, it is advisable to extend the model with the behaviour of the cable to test the winding of the cable and assess the risks and consequences of having slack on the cable. If a rack and pinion PTO is chosen, the horizontal (wave) forces should be taken into account for the durability of the vertical guiding system.

For the PST system many research opportunities remain. As stated, the transmission ratios can be improved and also the control strategy is open to suggestions concerning optimisation of the electrical output. When it comes to power smoothing of the electrical power output, the system inherently offers possibilities, but other power smoothing technologies should be evaluated as well.

In elke druppel trilt de oceaan

In every drop the ocean trembles

Peter Verhelst

Bibliography

[1] P. Immonen, *Energy Efficiency of a Diesel-Electric MobileWorking Machine*. PhD thesis, Lappeenranta University of Technology, Jun. 2013.

[2] S. Derammelaere, S. Dereyne, P. Defreyne, E. Algoet, F. Verbelen, and K. Stockman, "Energy efficiency measurement procedure for gearboxes in their entire operating range," in *IEEE Industry Applications Society Annual Meeting, Proceedings*, IEEE, 2014.

[3] J. Degrieck and W. Van Paepegem, "Wave energy convertor." WO2015055441 (A1), April 23, 2015.

[4] H. Bernhoff, E. Sjstedt, and M. Leijon, "Wave energy resources in sheltered sea areas: A case study of the Baltic Sea," *Renewable Energy*, vol. 31, no. 13, pp. 2164–2170, 2006.

[5] International Energy Agency (IEA), *World Energy Outlook 2009*. Paris, France, 2009.

[6] A. F. de O. Falcão, "Wave energy utilization: A review of the technologies," *Renewable and Sustainable Energy Reviews*, vol. 14, no. 3, pp. 899 – 918, 2010.

[7] J. Weber, F. Mouwen, A. Parrish, and D. Robertson, "Wavebob research & development network and tools in the context of systems engineering," in *8th European Wave Tidal Energy Conference*, 2009.

[8] J. F. Gaspar, M. Kamarlouei, A. Sinha, H. Xu, M. Calvário, F.-X. Faÿ, E. Robles, and C. G. Soares, "Speed control of oil-hydraulic power take-off system for oscillating body type wave energy converters," *Renewable Energy*, vol. 97, pp. 769 – 783, 2016.

[9] R. Waters, M. Stalberg, O. Danielsson, O. Svensson, S. Gustafsson, E. Stromstedt, M. Eriksson, J. Sundberg, and M. Leijon, "Experimental results from sea trials of an offshore wave energy system," *Applied Physics Letters*, vol. 90, no. 3, 2007.

[10] D. Elwood, A. Schacher, K. Rhinefrank, J. Prudell, S. Yim, E. Amon, T. Brekken, and A. von Jouanne, "Numerical modeling and ocean testing of a direct-drive wave energy device utilizing a permanent magnet linear generator for power take-off," *Omae 2009, Vol 4, Pts A and B*, pp. 817–824, 2009.

[11] E. Tedeschi and M. Molinas, "Wave-to-wave buoys control for improved power extraction under electro-mechanical constraints," in *2010 IEEE International Conference on Sustainable Energy Technologies (ICSET)*, 2010.

[12] J. Sjolte, I. Bjerke, E. Hjetland, and G. Tjensvoll, "All-electric wave energy power take off generator optimized by high overspeed," in *European Wave and Tidal Energy Conference (EWTEC11)*, 2011.

[13] "The flansea website (flanders electricity from the sea)." URL: `http://www.flansea.eu/`. Accessed date: December 2015.

[14] A. Bozzetto and E. Tedeschi, "Wave power extraction with constrained power take-off: Single capture vs. double capture point absorbers," in *2014 Ninth International Conference on Ecological Vehicles and Renewable Energies (EVER)*, 2014.

[15] A. Bozzetto, O. C. Spro, and E. Tedeschi, "Impact of technical power take-off constraints on the power extraction of unidirectional and bidirectional point absorbers," *Compel-the International Journal for Computation and Mathematics in Electrical and Electronic Engineering*, vol. 34, no. 6, pp. 1796–1806, 2015.

[16] M. Vantorre, R. Banasiak, and R. Verhoeven, "Modelling of hydraulic performance and wave energy extraction by a point absorber in heave," *Applied Ocean Research*, vol. 26, no. 1-2, pp. 61–72, 2004.

[17] G. De Backer, *Hydrodynamic Design Optimization of Wave Energy Converters Consisting of Heaving Point Absorbers*. PhD thesis, Ghent University, Nov. 2009.

[18] S. Salter, D. Jeffery, and J. Taylor, "The architecture of nodding duck wave power generators," *The Naval Architect*, pp. 21–24, 1976.

[19] K. Budal and J. Falnes, "Optimum operation of improved wave-power converter," *Marine Science Communications*, vol. 3, no. 2, pp. 133–150, 1977.

[20] E. Tedeschi, M. Molinas, M. Carraro, and P. Mattavelli, "Analysis of power extraction from irregular waves by all-electric power take off," in *2010 IEEE Energy Conversion Congress and Exposition*, pp. 2370–2377, 2010.

[21] E. Tedeschi, M. Carraro, M. Molinas, and P. Mattavelli, "Effect of control strategies and power take-off efficiency on the power capture from sea waves," *IEEE Transactions on Energy Conversion*, vol. 26, no. 4, pp. 1088–1098, 2011.

[22] E. Tedeschi and M. Molinas, "Tunable control strategy for wave energy converters with limited power takeoff rating," *IEEE Transactions on Industrial Electronics*, vol. 59, no. 10, pp. 3838–3846, 2012.

[23] M. Stalberg, R. Waters, O. Danielsson, and M. Leijon, "Influence of generator damping on peak power and variance of power for a direct drive wave energy converter," *Journal of Offshore Mechanics and Arctic Engineering-Transactions of the Asme*, vol. 130, no. 3, 2008.

[24] M. Penalba and J. Ringwood, "A review of wave-to-wire models for wave energy converters," *Energies*, vol. 9, no. 7, p. 506, 2016.

[25] E. Ozkop and I. H. Altas, "Control, power and electrical components in wave energy conversion systems: A review of the technologies," *Renewable & Sustainable Energy Reviews*, vol. 67, pp. 106–115, 2017.

[26] M. A. Mueller, H. Polinder, and N. Baker, "Current and novel electrical generator technology for wave energy converters," *IEEE IEMDC 2007: Proceedings of the International Electric Machines and Drives Conference*, pp. 1401–1406, 2007.

[27] B. Czech and P. Bauer, "Wave energy converter concepts design challenges and classification," *IEEE Industrial Electronics Magazine*, vol. 6, no. 2, pp. 4–16, 2012.

[28] I. Lopez, B. Pereiras, F. Castro, and G. Iglesias, "Holistic performance analysis and turbine-induced damping for an owc wave energy converter," *Renewable Energy*, vol. 85, pp. 1155–1163, 2016.

[29] G. Duclos, A. Babarit, and A. H. Clement, "Optimizing the power take off of a wave energy converter with regard to the wave climate," *Journal of Offshore Mechanics and Arctic Engineering-Transactions of the ASME*, vol. 128, no. 1, pp. 56–64, 2006.

[30] A. de Andres, E. Medina-Lopez, D. Crooks, O. Roberts, and H. Jeffrey, "On the reversed LCOE calculation: Design constraints for wave energy commercialization," *International Journal of Marine Energy*, vol. 18, pp. 88–108, 2017.

[31] B. Teillant, R. Costello, J. Weber, and J. Ringwood, "Productivity and economic assessment of wave energy projects through operational simulations," *Renewable Energy*, vol. 48, pp. 220–230, 2012.

[32] SI Ocean, "Ocean energy: Cost of energy and cost reduction opportunities," report, May 2013.

[33] L. Margheritini, A. M. Hansen, and P. Frigaard, "A method for eia scoping of wave energy converters-based on classification of the used technology," *Environmental Impact Assessment Review*, vol. 32, no. 1, pp. 33–44, 2012.

[34] G. De Backer, M. Vantorre, K. De Beule, C. Beels, and J. De Rouck, "Experimental investigation of the validity of linear theory to assess the behaviour of a heaving point absorber at the Belgian continental shelf," *ASME 28th International Conference on Ocean, Offshore and Arctic Engineering (OMAE 2009), Vol. 4*, pp. 1013–1020, 2009.

[35] K. L. De Koker, G. Crevecoeur, B. Meersman, M. Vantorre, and L. Vandevelde, "A wave emulator for ocean wave energy, a froude-scaled dry power take-off test setup," *Renewable Energy*, vol. 105, pp. 712–721, 2017.

[36] K. Hasselmann, T. P. Barnett, E. Bouws, H. Carlson, D. E. Cartwright, K. Enke, J. A Ewing, H. Gienapp, D. E. Hasselmann, P. Kruseman, A. Meerburg, P. Mller, D. Olbers, K. Richter, W. Sell, and H. Walden, "Measurements of wind-wave growth and swell decay during the joint north sea wave project (jonswap)," vol. 8, pp. 1–95, 01 1973.

[37] W. Cummins, "The impulse response function and ship motions," *Schiffstechnik*, vol. 9, pp. 101–109, 1962.

[38] G. Duclos, A. H. Clement, and G. Chatry, "Absorption of outgoing waves in a numerical wave tank using a self-adaptive boundary condition," *International Journal of Offshore and Polar Engineering*, vol. 11, no. 3, pp. 168–175, 2001.

[39] L. Alberti, E. Tedeschi, N. Bianchi, M. Santos, and A. Fasolo, "Effect of the generator sizing on a wave energy converter considering different control strategies," *Compel-the International Journal for Computation and Mathematics in Electrical and Electronic Engineering*, vol. 32, no. 1, pp. 233–247, 2013.

[40] L. Martinelli, B. Zanuttigh, and J. P. Kofoed, "Selection of design power of wave energy converters based on wave basin experiments," *Renewable Energy*, vol. 36, no. 11, pp. 3124–3132, 2011.

[41] R. Genest, F. Bonnefoy, A. H. Clement, and A. Babarit, "Effect of non-ideal power take-off on the energy absorption of a reactively controlled one degree of freedom wave energy converter," *Applied Ocean Research*, vol. 48, pp. 236–243, 2014.

[42] W. Deprez, J. Lemmens, D. Vanhooydonck, W. Symens, K. Stockman, S. Dereyne, and J. Driesen, "Iso efficiency contours as a concept to characterize variable speed drive efficiency," in *XIX International Conference on Electrical Machines - ICEM 2010, Rome*, 2010.

[43] K. Stockman, S. Dereyne, D. Vanhooydonck, W. Symens, J. Lemmens, and W. Deprez, "Iso efficiency contour measurement results for variable speed drives," in *XIX International Conference on Electrical Machines - ICEM 2010, Rome*, 2010.

[44] D. Vanhooydonck, W. Symens, W. Deprez, J. Lemmens, K. Stockman, and S. Dereyne, "Calculating energy consumption of motor systems with varying load using iso efficiency contours," in *XIX International Conference on Electrical Machines (ICEM 2010), Rome*, 2010.

[45] W. Verheirstraeten, "Dynamic efficiency measurements of wave energy generators," Master's thesis, Ghent University, Jun. 2016.

[46] V. Stratigaki, P. Troch, T. Stallard, D. Forehand, J. Kofoed, M. Folley, M. Benoit, A. Babarit, and J. Kirkegaard, "Wave basin experiments with large wave energy converter arrays to study interactions between the converters and effects on other users in the sea and the coastal area," *Energies*, vol. 7, no. 2, pp. 701–734, 2014.

[47] V. Stratigaki, P. Troch, T. Stallard, D. Forehand, M. Folley, J. P. Kofoed, M. Benoit, A. Babarit, M. Vantorre, and J. Kirkegaard, "Sea-state modification and heaving float interaction factors from physical modelling of arrays of wave energy converters," *Journal of Renewable and Sustainable Energy*, vol. 7, no. 6, 2015.

[48] V. Stratigaki, *Experimental study and numerical modelling of intra-array interactions and extra-array effects of wave energy converter arrays.* PhD thesis, Ghent University, Faculty of Engineering and Architecture, Ghent, Belgium, 2014.

[49] A. Van de Sijpe, "Development of a point absorber wave energy converter: realisation of power take-off, optimisation of geometry and installation techniques," Master's thesis, Ghent University, 2012.

[50] W. Froude, *Observations and Suggestions on the Subject of Determining by Experiment the Resistance of Ships*. The Papers of William Froude, 1810-1879, Transactions INA, 1955.

[51] D. Vassalos, "Physical modelling and similitude of marine structures," *Ocean Engineering*, vol. 26, no. 2, pp. 111 – 123, 1998.

[52] Y. Hong, R. Waters, C. Bostrom, M. Eriksson, J. Engstrom, and M. Leijon, "Review on electrical control strategies for wave energy converting systems," *Renewable & Sustainable Energy Reviews*, vol. 31, pp. 329–342, 2014.

[53] A. F. O. Falcão, P. E. R. Pereira, J. C. C. Henriques, and L. M. C. Gato, "Hydrodynamic simulation of a floating wave energy converter by a U-tube rig for power take-off testing," *Ocean Engineering*, vol. 37, no. 14-15, pp. 1253–1260, 2010.

[54] N. J. Baker, M. A. Mueller, L. Ran, P. J. Tavner, and S. McDonald, "Development of a linear test rig for electrical power take off from waves," *Journal of Marine Engineering and Technology*, vol. 6, no. 2, pp. 3–15, 2007.

[55] M. Blanco, M. Lafoz, and L. Garcia Tabares, "Laboratory tests of linear electric machines for wave energy applications with emulation of wave energy converters and sea waves," in *14th European Conf. Power Electronics and Applications, Birmingham, United Kingdom*, 2011.

[56] R. Henderson, "Design, simulation, and testing of a novel hydraulic power take-off system for the Pelamis wave energy converter," *Renewable Energy*, vol. 31, no. 2, pp. 271–283, 2006.

[57] J. Rea, J. Kelly, R. Alcorn, and D. O'Sullivan, "Development and operation of a power take off rig for ocean energy research and testing," in *Proc. 2011 European Wave and Tidal Energy Conf., Southampton, United Kingdom*, 2011.

[58] J. Henriques, R. Gomes, L. Gato, A. Falcão, E. Robles, and S. Ceballos, "Testing and control of a power take-off system for an oscillating-water-column wave energy converter," *Renewable Energy*, vol. 85, pp. 714 – 724, 2016.

[59] J. Henriques, L. Gato, A. Falcão, E. Robles, and F.-X. Faÿ, "Latching control of a floating oscillating-water-column wave energy converter," *Renewable Energy*, vol. 90, pp. 229 – 241, 2016.

[60] K. L. De Koker, G. Crevecoeur, M. Vantorre, and L. Vandevelde, "Design of a Froude scaled PTO lab setup," in *Proceedings of the 11th European Wave and Tidal Energy Conference (EWTEC), Nantes, France*, 2015.

[61] M. Durand, A. Babarit, B. Pettinotti, O. Quillard, J. Toularastel, and A. H. Clément, "Experimental validation of the performances of the SEAREV wave energy converter with real time latching control," in *7th European Wave and Tidal Energy conference, Porto, Portugal*, 2007.

[62] R. Gomes, J. Henriques, L. Gato, and A. Falcão, "Wave power extraction of a heaving floating oscillating water column in a wave channel," *Renewable Energy*, vol. 99, pp. 1262 – 1275, 2016.

[63] K. L. De Koker, G. Crevecoeur, B. Meersman, M. Vantorre, and L. Vandevelde, "A power take-off and control strategy in a test wave energy converter for a moderate wave climate," *Renewable Energy and Power Quality Journal*, vol. 14, no. May 2016, pp. 478–483, 2016.

[64] J. Sjolte, C. M. Sandvik, E. Tedeschi, and M. Molinas, "Exploring the potential for increased production from the wave energy converter lifesaver by reactive control," *Energies*, vol. 6, no. 8, pp. 3706–3733, 2013.

[65] G. De Backer, M. Vantorre, R. Banasiak, J. De Rouck, C. Beels, and H. Verhaeghe, "Performance of a point absorber heaving with respect to a floating platform," in *7th European Wave and Tidal Energy Conference, Porto, Portugal*, 2007.

[66] WEG, "Ecatalog WEG motors." http://ecatalog.weg.net/ , Last access Feb 2017.

[67] Oemer, "Motors catalogue sincrovert series." AC-09/2010 1.0, 2010.

[68] R. Carballo and G. Iglesias, "A methodology to determine the power performance of wave energy converters at a particular coastal location," *Energy Conversion and Management*, vol. 61, pp. 8–18, 2012.

[69] E. Rusu, "Evaluation of the wave energy conversion efficiency in various coastal environments," *Energies*, vol. 7, no. 6, pp. 4002–4018, 2014.

[70] C. Beels, J. Henriques, J. De Rouck, M. Pontes, G. De Backer, and H. Verhaeghe, "Wave energy resource in the north sea," in *Proceedings of the Seventh European Wave and Tidal energy Conference EWTEC, Porto, Portugal*, 2007.

[71] B. Drew, A. R. Plummer, and M. N. Sahinkaya, "A review of wave energy converter technology," in *Proceedings of the Institution of Mechanical Engineers Part a-Journal of Power and Energy*, vol. 223, no. A8, pp. 887–902, 2009.

[72] L. Mangialardi and G. Mantriota, "The advantages of using continuously variable transmissions in wind power systems," *Renewable Energy*, vol. 2, no. 3, pp. 201–209, 1992.

[73] H. Law, "Power generating equipment." EP0120654 (A1), October 03, 1984.

[74] I. Orosz and F. Apro, "Speed stabilizing gear drive system for generating electric power." WO2007042847 (A1), April 19, 2007.

[75] D. Petkovic, Z. Cojbasic, V. Nikolic, S. Shamshirband, M. L. M. Kiah, N. B. Anuar, and A. W. A. Wahab, "Adaptive neuro-fuzzy maximal power extraction of wind turbine with continuously variable transmission," *Energy*, vol. 64, pp. 868–874, 2014.

[76] K. L. De Koker, J. Degrieck, J. De Maeyer, F. Verbelen, T. Verbrugghe, M. Vantorre, and L. Vandevelde, "Modeling of a power sharing transmission in a wave energy converter," in *2016 IEEE 16th International Conference on Environment and Electrical Engineering (EEEIC), Florence, Italy*, June 2016.

[77] K. L. De Koker, G. Crevecoeur, B. Meersman, M. Vantorre, and L. Vandevelde, "Energy storage system for off-grid testing of a wave energy converter," in *2016 IEEE International Energy Conference (ENERGYCON), Leuven, Belgium*, April 2016.

[78] Allen Bradley - Rockwell Automation, "HPK-series high power asynchronous motors - induction motor technology optimized for servo systems." HPK-PP001C-EN-P May 2010, 2010.